Construction of controlled renormalization-group approximations for low-dimensional quantum systems

Von der Fakultät für Mathematik, Informatik und Naturwissenschaften der RWTH Aachen University zur Erlangung des akademischen Grades eines Doktors der Naturwissenschaften genehmigte Dissertation

vorgelegt von

Jan Diekmann, M.Sc.
aus
Paderborn

Berichter: Dr. Severin G. Jakobs
Prof. Dr. Volker Meden

Tag der mündlichen Prüfung: 02.09.2025

Diese Dissertation ist auf den Internetseiten der Universitätsbibliothek verfügbar.

Contents

Eidesstattliche Erklärung **v**

Summary **vii**

1 Introduction **1**

2 Zero-temperature formalism: perturbation theory, generating functionals, FRG **7**
2.1 Introduction 7
2.2 The general model 10
2.3 Definition of Green functions and their generating functional 11
2.4 Discrete integral expression for $Z_\eta[\bar{J}, J]$ 12
2.5 Noninteracting generating functional 14
2.6 Continuous functional-integral notation 14
2.6.1 Constituents of the action 14
2.6.2 Generating functional 15
2.6.3 Free propagator 16
2.7 Diagrammatic expansion of the Green functions 17
2.7.1 Expansion in powers of the two-particle interaction 17
2.7.2 Diagrammatic rules without a single-particle vertex 19
2.7.3 Diagrammatic rules with a single-particle vertex 20
2.8 Frequency representation 22
2.9 Definition of 1PI vertex functions and their generating functional . . 22
2.10 FRG flow equations 23
2.10.1 Flow equations of the generating functionals 24
2.10.2 Flow equations of the 1PI vertex functions 24
2.11 Generalizations of the zero-temperature formalism 25
2.11.1 Infinite system size 25
2.11.2 Common eigenstate of H_0 and H 26
2.11.3 Excited eigenstate of H (for particular vertex structures only) 27
2.12 Conclusion 31

3 Treatment of the X-ray-edge model **33**
3.1 Introduction 33
3.2 The X-ray-edge model 35

3.2.1 Hamiltonian . . . 36
3.2.2 X-ray-absorption rate and the particle-hole susceptibility $\chi(\nu)$ 36
3.2.3 Significance of the model . . . 37
3.3 Diagrammatic perturbation theory . . . 37
3.3.1 Applying the zero-temperature formalism . . . 37
3.3.2 Customizing the diagrammatic rules . . . 39
3.3.3 Expressing $\chi(\nu)$ in terms of the 1PI two-particle vertex γ . . . 43
3.3.4 Setting the renormalized deep level $\tilde{\varepsilon}_d$ to zero . . . 45
3.3.5 Exact calculation of bare bubbles . . . 46
3.3.6 Exact calculation of crossed bubble . . . 48
3.4 Leading-logarithmic parquet approximation of Roulet et al. . . . 50
3.4.1 Leading logarithms . . . 51
3.4.2 List of approximations . . . 52
3.4.3 Approximating the bare bubbles . . . 53
3.4.4 Approximating the crossed bubble . . . 55
3.4.5 Integral equations for γ . . . 57
3.4.6 Result for the X-ray-absorption rate . . . 59
3.5 FRG approach . . . 59
3.5.1 Cutoff and initial conditions . . . 60
3.5.2 Truncation . . . 60
3.5.3 Approximating the flow equation of γ . . . 62
3.6 Comparison between the parquet-based and the FRG approach . . . 65
3.7 Transfer to the Matsubara formalism . . . 66
3.8 Conclusion . . . 67

4 Treatment of the single-impurity Anderson model 71
4.1 Introduction . . . 71
4.2 The single-impurity Anderson model . . . 74
4.2.1 Hamiltonian in real space . . . 75
4.2.2 Reservoirs in momentum space . . . 75
4.2.3 Transforming the reservoirs . . . 76
4.2.4 Wide-band limit . . . 77
4.3 Applying the zero-temperature formalism . . . 78
4.4 Example diagrams . . . 82
4.4.1 Dot-dot bubbles . . . 82
4.4.2 Dot-reservoir bubbles . . . 83
4.4.3 Crossed bubble . . . 86
4.5 Specifying the regime of interest . . . 88
4.5.1 Relation of the SIAM and Kondo Hamiltonians according to Schrieffer and Wolff . . . 89
4.5.2 Parameter and frequency regime for the 1PI two-particle vertex 90
4.6 Leading-logarithmic approximation . . . 92
4.6.1 List of approximations . . . 92
4.6.2 Role of the dot-dot bubbles . . . 94
4.6.3 Approximating the dot-reservoir bubbles . . . 96

4.6.4 Approximating the crossed bubble . . . 98
4.6.5 Relation of the SIAM and the Kondo model from a diagrammatic perspective . . . 99
4.7 Properties of various cutoffs . . . 103
4.8 Linear conductance as observable . . . 106
4.9 Conclusion . . . 108

5 Conclusion and outlook **111**

A Diagonalizing a tight-binding chain **115**

B Properties of the logarithm and dilogarithm **117**
B.1 Logarithm . . . 117
B.2 Dilogarithm . . . 117

C Some useful integrals **119**
C.1 Very simple integrals . . . 119
C.2 Integral over $\mathrm{Log}(x - x_1 - \mathrm{i}\eta)/(x - x_2 - \mathrm{i}\eta)$ . . . 119
C.3 Integral over $\mathrm{Log}(x - x_1 - \mathrm{i}\eta)/(x - x_2 - \mathrm{i}\eta)^2$ . . . 120

D Crossed bubble in the SIAM **123**
D.1 Calculating the exact value . . . 123
D.2 Extracting the leading behavior . . . 127

Bibliography **133**

Eidesstattliche Erklärung

Jan Diekmann

erklärt hiermit, dass diese Dissertation und die darin dargelegten Inhalte die eigenen sind und selbstständig, als Ergebnis der eigenen originären Forschung, generiert wurden.

Hiermit erkläre ich an Eides statt

1. Diese Arbeit wurde vollständig oder größtenteils in der Phase als Doktorand dieser Fakultät und Universität angefertigt;

2. Sofern irgendein Bestandteil dieser Dissertation zuvor für einen akademischen Abschluss oder eine andere Qualifikation an dieser oder einer anderen Institution verwendet wurde, wurde dies klar angezeigt;

3. Wenn immer andere eigene- oder Veröffentlichungen Dritter herangezogen wurden, wurden diese klar benannt;

4. Wenn aus anderen eigenen- oder Veröffentlichungen Dritter zitiert wurde, wurde stets die Quelle hierfür angegeben. Diese Dissertation ist vollständig meine eigene Arbeit, mit der Ausnahme solcher Zitate;

5. Alle wesentlichen Quellen von Unterstützung wurden benannt;

6. Wenn immer ein Teil dieser Dissertation auf der Zusammenarbeit mit anderen basiert, wurde von mir klar gekennzeichnet, was von anderen und was von mir selbst erarbeitet wurde;

7. Ein Teil oder Teile dieser Arbeit wurden zuvor veröffentlicht und zwar in:
   J. Diekmann and S. G. Jakobs. Phys. Rev. B **103**, 155156 (2021).
   J. Diekmann and S. G. Jakobs. Phys. Rev. B **109**, 115134 (2024).

Summary

For low-dimensional condensed-matter systems of interacting fermions, logarithmic divergences are a common problem of perturbation theory. They can appear for example in the perturbative expansion of a power law whose exponent depends on the expansion parameter. Classifying and resumming the leading logarithms allows for approximations with a priori controlled accuracies. For the class of systems where the divergences appear in multiple two-particle channels with one logarithm per diagrammatic bubble, the leading-logarithmic parquet approximation is a well-established tool, specifically designed for this problem.

A prototypical system of this class is the X-ray-edge model, which describes the X-ray-absorption singularity in metals. We devise a one-loop functional renormalization group (FRG) approach to the X-ray-edge model that is fully equivalent, step by step, to the leading-logarithmic parquet approximation. Thus, the one-loop FRG can achieve leading-logarithmic accuracy. This capability is well-known for many lowest-order scaling and RG approaches but has been put into question for the one-loop FRG by recent literature on the X-ray-edge model. In our particular case, the FRG and parquet frameworks can even be interpreted as different perspectives on the exact same approximation. Our study shows a way of controlling the accuracy of FRG truncations in regimes not accessible by perturbation theory, in contrast to merely qualitative justifications that are usually invoked there.

We also investigate the single-impurity Anderson model (SIAM) that describes a quantum dot connecting two reservoirs. From the point of view of an unusual perturbative expansion in both the interaction on the dot and the coupling between the dot and the reservoirs, the SIAM belongs to the same class as the X-ray-edge model, but it is more complicated. We develop an approximation scheme aimed at resumming the leading logarithms of the SIAM in a similar way. We express this scheme in terms of effective diagrammatic rules, which show similarities to the Kondo model. However, our approach needs to be extended before it can properly capture the Kondo physics of the SIAM.

Throughout this thesis we use the zero-temperature formalism. In the context of the X-ray-edge model, it allows for the direct comparison between our FRG approach and the existing leading-logarithmic parquet approximation. It is simpler but more restrictive than the Keldysh and Matsubara formalisms. Since the FRG has never before been used with the zero-temperature formalism, we comprehensively set up the required framework for a general model of interacting fermions in terms of the one-particle irreducible vertex functions.

Chapter 1

Introduction

In condensed-matter systems of interacting fermions, any observable expectation value can be expressed with Green functions. If an exact calculation of the Green functions is not possible, a standard approach is perturbation theory, where one expands in a small parameter, e.g. in the interaction amplitude, and keeps only the lowest few orders. A well-known problem is the occurrence of logarithms that can diverge and render higher orders important, causing the perturbation theory to break down.

Such logarithms can originate from a power law if one expands in a constituent of the exponent. In the diagrammatic representation of the Green functions, the logarithms can arise from bubbles: An integral over two free propagators can produce a logarithm if one of them contributes a $1/x$-shape and the other contributes a step or sign function caused by a sharp Fermi surface.

The terms with the highest number of logarithms in a given order of perturbation theory are dubbed leading logarithms. The terms with a lower number of logarithms are dubbed subleading logarithms. Far from the divergence of the logarithms, the sum of the lowest few orders is still a good approximation. Close to the divergence, the leading logarithms of all orders become important. Even closer to the divergence, subleading logarithms become important as well.

Low-dimensional systems can be classified with respect to their logarithmic structure. In the class with a simple logarithmic structure, one bubble gives only one logarithm. This class comprises mostly zero- and one-dimensional systems like the X-ray-edge model [Mah67], the Kondo model [Abr65], and the one-dimensional Fermi gas model [Sól79]. Special cases of two-dimensional models can also belong to this class, e.g. if they have a nested Fermi surface without Van Hove singularities [BBD03]. In the class with a complicated logarithmic structure, one bubble gives up to two logarithms so identifying the leading logarithms is more difficult. This class comprises mostly two-dimensional systems, see e.g. Refs. [IKK01, Kat09]. The focus of this thesis lies on the class with a simple logarithmic structure.

Early approaches yielding reasonable approximations for systems of this class close to the respective divergence fall into two categories. The first category is formed by applications of the leading-logarithmic parquet approximation. The diagrams of a given model are decomposed into reducible and irreducible parts with respect to

the two-particle channels. These parts are related by exact parquet equations, which are then simplified: a channel that does not produce logarithms is neglected, the totally irreducible vertex is replaced with the bare vertex, and the single-particle Green function is replaced with the free propagator. The remaining diagrams are the parquet diagrams of the logarithmic channels. They are built from bubbles successively inserted into each other; this successive construction corresponds to an iterative solution of the parquet equations. While these diagrams contain all leading logarithms, their exact values are not important. The parquet equations are further approximated, such that the leading logarithms are not affected, and then solved. The leading-logarithmic parquet approximation has been applied to the X-ray-edge model [RGN69], to the Kondo model [Abr65], and to the one-dimensional Fermi gas model [BGD66].

The second category is formed by scaling arguments. Their basic idea is to reduce the description of a system to an effective low-energy model by integrating out its high-energy degrees of freedom. Technically, one varies a scale of the system and monitors the properties of the system as they change. In this category a visualization on the diagrammatic level is not always possible. Examples are Anderson's poor man's scaling for the Kondo model [And70, SZ74], which has also been transferred to the one-dimensional Fermi gas model [Sól79], and renormalization group (RG) approaches to the X-ray-edge model [Sól74], to the Kondo model [AM70, FZ71], and to the one-dimensional Fermi gas model [Kim73, Sól79, Sha94]. The lowest-order, i.e. one-loop, version of each of these approaches reproduced the results of the respective leading-logarithmic parquet approximation. However, in many cases the goal was to go beyond the leading-logarithmic level [GZ74, Sól79, Hew93]. Scaling arguments have led to the concept of universality classes [Kad76, Voi95], which is ubiquitous in condensed-matter physics, and also to Wilson's numerical RG [Wil75], which accurately describes the Kondo effect.

This thesis deals specifically with the functional RG (FRG) in a form that was established by Wetterich [Wet93] and Morris [Mor94]; introductions and reviews are given in Refs. [KBS10, Met+12, PHT13]. While the FRG is typically formulated with generating functionals, it can be illustratively explained with diagrams. In the diagrammatic perturbation theory of the Green functions, one-particle irreducible (1PI) vertex functions can be identified. The Green functions can be reconstructed from the 1PI vertex functions via tree diagrams, which do not produce any new logarithms. A flow parameter is artificially introduced into the free propagator and serves as the variable scale of a system such that the diagrams describe at the start a simplified, solvable system and at the end the actual system. The 1PI vertex functions of the simplified system can be mapped to those of the actual system via flow equations, which are a set of differential equations. With sufficient approximations these flow equations can be solved.

Recently, the relation between the leading-logarithmic parquet approximation and the FRG came into focus in the context of the X-ray-edge model. This model describes the X-ray-absorption singularity in metals [Mah67]. Since the exact solution has been found [ND69], the X-ray-edge model was often used as a test bed for many-body methods [RGN69, NGR69, Sól74, Lan+15, KD18a]. As the electron spin is neglected

and the interacting region is effectively zero-dimensional, this model can be considered as a prototype for the class with a simple logarithmic structure.

A thorough discussion of the X-ray-edge model was performed by Nozières, Roulet, Gavoret, and De Dominicis. They provided all at once the leading-logarithmic parquet approximation [RGN69], a treatment of the subleading logarithms [NGR69], and the exact solution [ND69]. They understood their analysis of the logarithms as a preparation for more complicated models, specifically for the Kondo model.

The leading-logarithmic result for the X-ray-absorption rate has been reproduced with an FRG approach by Lange et al. [Lan+15]. Their work was scrutinized by Kugler and von Delft [KD18c], who argued that this approach has to be corrected in certain ways and that it then includes, with varying weights, only ladder diagrams. Kugler and von Delft ultimately concluded that the success of Ref. [Lan+15] is merely fortuitous as it relies on proportionality relations that hold approximately in the X-ray-edge model between the ladder diagrams and the other parquet diagrams which are equally important at leading logarithmic order. They then developed, at first specifically for the X-ray-edge model, the multiloop FRG, which is a scheme that increases the loop order of an FRG approach via one-loop iterations, thereby yielding the exact sum of all parquet diagrams once convergence is reached [KD18a, KD18b, KD18d].

This appears to invert the historical direction of the methodological development: the RG was initially used to try and overcome the limitations of parquet-based approximations, but the multiloop FRG is now a tool to obtain exact sums of parquet diagrams. For the X-ray-edge model, the analysis of subleading logarithms by Nozières et al. shows that the exact sum of the parquet diagrams does not significantly extend the regime of reliability compared to the leading-logarithmic parquet approximation [NGR69]. However, Kugler and von Delft report that increasing the loop order improves the FRG result [KD18a]. The question arises whether, generally, a one-loop FRG is less accurate than the leading-logarithmic parquet approximation – and by extension less capable than early one-loop RG approximations, which have already reproduced leading-logarithmic results.

We answer this question by devising a one-loop FRG approach to the X-ray-edge model that is fully equivalent to the leading-logarithmic parquet approximation. We thereby reconfirm the widely believed capability of the one-loop RG, including its FRG variant, to capture the leading logarithms for the class of systems with a simple logarithmic structure. Our study of the X-ray-edge model constitutes a direct and detailed comparison between the one-loop FRG and the leading-logarithmic parquet approximation. We find that the individual steps are identical; just the order of the steps differs. So the two approaches can even be understood as different perspectives on the same approximation.

We expect the most interesting applications of the multiloop FRG to lie in other fields, namely those with a specific interest in the exact sum of the parquet diagrams. One such field is the class of systems with a complicated logarithmic structure, which comprises mostly two-dimensional systems. Also for that class, parquet-based approaches are common. But they typically include all channels, use a self-consistently dressed propagator, and calculate the exact sum of the resulting

parquet diagrams [Bic91]. We refer to this procedure as the full parquet approximation, clearly distinguishing it from the leading-logarithmic parquet approximation for the class with a simple logarithmic structure. Since classifying leading-logarithmic and subleading diagrams is more difficult for the class with a complicated logarithmic structure, the focus does then usually not lie on a logarithmic analysis and a controlled accuracy.

After having discussed the X-ray-edge model, we turn to the single-impurity Anderson model (SIAM). Originally, it describes an impurity in a bulk metal [And61]. We consider the modern version of the SIAM that describes a quantum dot connecting two reservoirs [GR88, NL88]. The interacting region of the SIAM is zero-dimensional but, unlike the interacting region of the X-ray-edge model, not structureless because the electron spin cannot be neglected. Solutions with the Bethe ansatz and with numerically exact methods exist, see e.g. Refs. [TW83] and [BCP08].

The electronic transport properties of the SIAM have interesting features [Hew93]. In particular, the SIAM exhibits the Kondo effect, which is an anomalous increase in the resistance of the bulk metal or in the conductance across the dot, respectively. Schrieffer and Wolff have related the SIAM to the Kondo model from the Hamiltonian perspective [SW66]. Many FRG approaches to the SIAM exist, see e.g. Refs. [Hed+04, KEM06, Kar+08, Wen+20], but how to capture the Kondo limit with the FRG remains an open question.

In our approach to the SIAM, we focus on the leading logarithms and use the insights from the X-ray-edge model. We make an unusual choice by expanding in the interaction on the dot and in the coupling between the dot and the reservoirs simultaneously. We can then relate the SIAM to the Kondo model from the diagrammatic perspective. Our goal is to devise an FRG approach that captures the Kondo limit.

For our treatments of both the X-ray-edge model and the SIAM, we set up the perturbation theory in the zero-temperature formalism. It is also known as the ground-state formalism and employs real times; introductions can be found in Refs. [AGD63, FW71, NO88]. The zero-temperature formalism predates the Matsubara and Keldysh formalisms and is simpler, but it is less widely known nowadays and more restrictive. For the X-ray-edge model, we choose it because it was used in Ref. [RGN69], so we can directly compare the one-loop FRG to the leading-logarithmic parquet approximation. For the SIAM we choose it because we can then transfer our insights more directly and avoid complications like the analytic continuation in the Matsubara formalism or the multiple components of Green functions in the Keldysh formalism.

We comprehensively present how to set up the FRG framework in the zero-temperature formalism for a general model of interacting fermions. The FRG was developed in the Matsubara formalism and translated into the Keldysh formalism, see Refs. [GPM07, JMS07, Met+12], but not yet into the zero-temperature formalism. Our discussion of the zero-temperature formalism is based on Ref. [NO88]. But we make adjustments so we can perform the usual FRG derivation via generating functionals and so we can easily apply the general case to the X-ray-edge model and to the SIAM.

The thesis is structured as follows. Chapter 2 covers the zero-temperature FRG for a general model. Chapter 3 discusses the specific one-loop FRG approach to the

X-ray-edge model and gives a detailed comparison to the leading-logarithmic parquet approximation. Chapter 4 discusses our approach to the SIAM, which is another specific implementation of the zero-temperature FRG and uses insights gained from studying the X-ray-edge model. Chapter 5 provides the conclusion. The contents of Chaps. 2 and 3 have been published as Ref. [DJ21], whereas our research into the SIAM is not yet finished.

Chapter 2

Zero-temperature formalism: perturbation theory, generating functionals, FRG

2.1 Introduction

In a system of interacting fermions, any observable quantity is represented by an operator acting on the many-particle Hilbert space. Any such operator can be written as a linear combination of products of creation and annihilation operators, each of which creates or annihilates a fermion in a specific single-particle state. Green functions are expectation values of generic products of creation and annihilation operators. So the expectation value of any observable can be expressed as a linear combination of Green functions. The Green functions of a system completely describe its behavior.

In many cases an exact solution is not known. As the description of a non-interacting system usually reduces to an exactly solvable single-particle problem, the interaction can be identified as the main difficulty. A standard approach for approximations is the perturbation theory where the Green functions are expanded in the interaction amplitude. Calculating and summing up only the lowest few orders can suffice if the interaction amplitude is small compared to other parameters of the system; ultimately, the expansion parameter is of course dimensionless. For efficiency and as a visual aid, a diagrammatic language is commonly used to translate the contributions of the expansion to diagrams. With precise rules one can calculate a given order by constructing all corresponding diagrams and determining their values, i.e. translating them back to nongraphical expressions.

Such a diagrammatic perturbation theory can be set up in different formalisms. The most common ones are the Matsubara formalism and the Keldysh formalism, see e.g. Refs. [NO88] and [HJ96]. In this thesis we work predominantly with the zero-temperature formalism.

The formalisms differ in their requirements and technical details. The Matsubara formalism is suited for equilibrium systems at finite temperature. As it uses Green

functions with imaginary times and discrete imaginary frequencies, obtaining physical quantities often requires an analytic continuation, which can pose a problem, especially in numerical calculations, see e.g. Refs. [JG96, Kar+08]. Performing the limit to vanishing temperature is possible and causes the Matsubara frequencies to become continuous and the corresponding sums to become integrals; however, resolving the issue of convergence can be tricky [KL60, LW60]. The Keldysh formalism is suited not only for equilibrium but also for nonequilibrium systems and uses real times and frequencies on a contour with two branches. Because of these branches, an n-particle Green function has 4^n components. The zero-temperature formalism is suited for systems in their ground state and uses real times and frequencies on a simple contour. No analytic continuation is necessary and each Green function has only a single component. Compared to the Matsubara and Keldysh formalisms, the zero-temperature formalism is more restrictive. But since calculations are simpler, it can facilitate analytic insights and solutions.

Our primary reason for using the zero-temperature formalism is its use in the leading-logarithmic parquet approximation for the X-ray-edge model [RGN69]. When resumming the leading-logarithms with the FRG, we choose the same formalism so that comparing the two approaches constitutes a direct comparison between the general methods of leading-logarithmic parquet approximation and one-loop FRG.

Introductions to the FRG in the Matsubara and Keldysh formalisms are given e.g. in Refs. [Met+12] and [Cam+22]. But we are not aware of any FRG approach using the zero-temperature formalism in the literature. In this chapter we present how to set up the FRG in the zero-temperature formalism for a general model. We ultimately derive flow equations for the 1PI vertex functions, which are the sums of the subdiagrams that would remain connected if any single line was cut. We discuss the important steps explicitly even if they are analogous to the standard literature on the zero-temperature formalism or on the Matsubara and Keldysh FRG. Our goal is to present the zero-temperature FRG in a comprehensive picture.

Early textbooks covering the zero-temperature formalism use the Gell-Mann and Low theorem [AGD63, FW71]. Our take on the zero-temperature formalism is based on the textbook by Negele and Orland [NO88], which uses a damped time evolution instead. But we do several things differently, as we will explain in the next few paragraphs.

By design the zero-temperature formalism deals with systems in their ground state. This field of application is what the formalism has been named after. But in the case of the X-ray-edge model, we occasionally want to prepare the system in an excited eigenstate, e.g. when setting the renormalized deep level to zero. At the end of this chapter, we will generalize the formalism as needed. This generalization was apparently known to the authors of Ref. [RGN69].

We consider a general model of interacting fermions. In addition to a free Hamiltonian that is diagonal and a two-particle interaction, we include a single-particle perturbation into the Hamiltonian. The free Hamiltonian will be synonymously referred to as the noninteracting Hamiltonian, while the sum of all three terms will be referred to as the full or interacting Hamiltonian. Since the sum of all single-particle terms can be considered as a new free Hamiltonian that one can bring into diagonal

form by switching to its single-particle eigenbasis, the single-particle perturbation does not increase the generality of the model and so it is usually omitted in the general description of a formalism. However, for the specific models to which we apply the zero-temperature formalism in this thesis, the explicit treatment will prove useful. We provide two sets of diagrammatic rules with the single-particle perturbation either absorbed into the free propagator or represented by a single-particle vertex.

The Green functions are defined as expectation values in the interacting ground state, whereas their generating functional is defined with an expectation value in the noninteracting ground state. Like Negele and Orland, we bridge this discrepancy via a damped but normalized time evolution [NO88]. They absorb the infinitesimal damping factor into the time integrations so the time contour gets slightly tilted. Motivated by studies of open systems that describe relaxation through non-Hermitian Hamiltonians, see e.g. Ref. [AGU20], we attribute the damping factor to the Hamiltonian instead, where it gives rise to a small anti-Hermitian part. Aside from not having to worry about a tilted time contour when introducing the frequency representation, we find no practical consequences of this different interpretation.

The last and most profound difference to Ref. [NO88] concerns the functional-integral representation of the generating functional. In their derivation Negele and Orland interchange the creation and annihilation operators below the Fermi surface by introducing particle-hole operators. The corresponding coherent states are the common eigenstates of the annihilation operators of the empty single-particle states and the creation operators of the occupied single-particle states. Thereby, Negele and Orland assign the role of the vacuum state to the noninteracting ground state and obtain an elegant functional-integral representation of the noninteracting generating functional, but they do not explicitly discuss the interacting case. Calculating the coherent-state matrix elements of the interaction turns out to be cumbersome. In contrast we use the standard coherent states, which are the common eigenstates of all annihilation operators. The derivation is then straightforward in the interacting case as well as in the noninteracting case. The functional-integral representation of the interacting generating functional is important for deriving the diagrammatic perturbation theory and for deriving the FRG flow equations.

While it is possible to derive FRG flow equations just based on the diagrammatic rules [JMS07], we do it in the standard way via the generating functionals as e.g. in Ref. [Met+12]. Specifically, we proceed in close analogy to Ref. [Jak19]. The flow parameter is introduced into the free propagator, the inverse of which appears in the generating functional of the Green functions. A dependence on the flow parameter is thus carried over into this functional and subsequently also into the generating functional of the 1PI vertex functions. The flow equation of the latter functional results from calculating its derivative with respect to the flow parameter. The flow equations of the 1PI vertex functions are then generated from the flow equation of their generating functional. With these flow equations, the initial 1PI vertex functions describing a simplified system can be mapped to the final 1PI vertex functions describing the actual system.

To a large extent, the contents of this chapter have been published in Ref. [DJ21]. I assure that I am the original author of the many passages with identical wording.

2.2 The general model

We consider a general Hamiltonian for an interacting many-fermion system,

$$H = H_0 + H_{\text{int}} = H_0 + H_{\text{int}}^{(1)} + H_{\text{int}}^{(2)} \tag{2.1a}$$

$$H_0 = \sum_{\alpha} \varepsilon_\alpha a_\alpha^\dagger a_\alpha \tag{2.1b}$$

$$H_{\text{int}}^{(1)} = \sum_{\alpha'\alpha} w_{\alpha'\alpha} a_{\alpha'}^\dagger a_\alpha \tag{2.1c}$$

$$H_{\text{int}}^{(2)} = \frac{1}{4} \sum_{\alpha_1'\alpha_2'\alpha_1\alpha_2} \bar{v}_{\alpha_1'\alpha_2'\alpha_1\alpha_2} a_{\alpha_1'}^\dagger a_{\alpha_2'}^\dagger a_{\alpha_2} a_{\alpha_1}, \tag{2.1d}$$

where $\alpha = 1, 2, \ldots$ numbers the states of an orthonormal single-particle eigenbasis of the noninteracting Hamiltonian H_0 and ε_α denotes their eigenenergies. The $a_\alpha^\dagger$ and a_α are the corresponding standard fermionic creation and annihilation operators, respectively. In the interacting part of the Hamiltonian, H_{int}, we have included the generic single-particle term $H_{\text{int}}^{(1)}$ as well as the general two-particle interaction $H_{\text{int}}^{(2)}$. We will treat their sum H_{int} as a perturbation to the noninteracting Hamiltonian H_0. The amplitude of the two-particle interaction shall be antisymmetric, i.e.

$$\bar{v}_{\alpha_1'\alpha_2'\alpha_1\alpha_2} = -\bar{v}_{\alpha_2'\alpha_1'\alpha_1\alpha_2} = -\bar{v}_{\alpha_1'\alpha_2'\alpha_2\alpha_1} = \bar{v}_{\alpha_2'\alpha_1'\alpha_2\alpha_1}. \tag{2.2}$$

This can easily be achieved and does not limit the generality of the model.

In many specific model Hamiltonians, there is no single-particle perturbation. It is possible to effectively get rid of any such perturbation by diagonalizing the sum of all single-particle terms in the Hamiltonian H and rewriting it in terms of the corresponding basis. This would entail redefining the noninteracting Hamiltonian H_0 and its ground state $|\Phi_0\rangle$. However, there are situations in which it is preferable to work with other bases, see e.g. Secs. 3.3.1 and 4.3. We therefore choose to include $H_{\text{int}}^{(1)}$ and will treat it explicitly in the following.

Following Ref. [NO88] we use a notation suggesting that the described system is finite. Section 2.11.1 shows how to adapt the notation if the system size approaches infinity. We consider the system at a fixed particle number N. Without loss of generality, we assume that the single-particle eigenenergies of H_0 are ordered monotonically $\varepsilon_1 \leq \varepsilon_2 \leq \ldots$ Additionally, we require that there is a gap $\varepsilon_N < \varepsilon_{N+1}$. Then the ground state of the noninteracting Hamiltonian H_0 is nondegenerate and given by

$$|\Phi_0\rangle = a_1^\dagger \ldots a_N^\dagger |0\rangle \tag{2.3}$$

with $|0\rangle$ being the vacuum state. We choose the zero of single-particle energies to lie between ε_N and ε_{N+1} so that the negative levels $\varepsilon_1, \ldots, \varepsilon_N < 0$ are occupied and the positive levels $\varepsilon_{N+1}, \ldots > 0$ are empty in the noninteracting ground state. The corresponding occupation numbers are

$$n_\alpha = \left\langle \Phi_0 \middle| a_\alpha^\dagger a_\alpha \middle| \Phi_0 \right\rangle = \begin{cases} 1, & \alpha \leq N \\ 0, & \alpha > N. \end{cases} \tag{2.4}$$

The normalized ground state of the interacting Hamiltonian H shall be denoted by $|\Psi_0\rangle$. It is assumed to be nondegenerate and not orthogonal to $|\Phi_0\rangle$.

2.3 Definition of Green functions and their generating functional

The time-ordered multi-particle Green functions are defined as

$$\begin{aligned} &G(\alpha_1 t_1, \ldots, \alpha_n t_n | \alpha'_1 t'_1, \ldots, \alpha'_n t'_n) \\ &= (-\mathrm{i})^n \Big\langle \Psi_0 \Big| \mathcal{T} a_{\alpha_1}(t_1) \ldots a_{\alpha_n}(t_n) a^\dagger_{\alpha'_n}(t'_n) \ldots a^\dagger_{\alpha'_1}(t'_1) \Big| \Psi_0 \Big\rangle. \end{aligned} \tag{2.5}$$

Similarly to the discussion in Ref. [NO88], one finds that they can be determined from a damped time evolution. This can formally be realized via $G = \lim_{\eta \to 0^+} G_\eta$ and

$$\begin{aligned} &G_\eta(\alpha_1 t_1, \ldots, \alpha_n t_n | \alpha'_1 t'_1, \ldots, \alpha'_n t'_n) \\ &= (-\mathrm{i})^n \frac{\delta^{2n} \mathcal{G}_\eta[\bar{J}, J]}{\delta \bar{J}_{\alpha_1}(t_1) \ldots \delta \bar{J}_{\alpha_n}(t_n) \delta J_{\alpha'_n}(t'_n) \ldots \delta J_{\alpha'_1}(t'_1)} \bigg|_{\bar{J}=0=J} \end{aligned} \tag{2.6}$$

with the generating functional

$$\mathcal{G}_\eta[\bar{J}, J] = \lim_{t_0 \to \infty} \frac{Z_\eta[\bar{J}, J]}{Z_\eta[0, 0]} \tag{2.7}$$

and

$$Z_\eta[\bar{J}, J] = \big\langle \Phi_0 \big| U^{(\eta)}_{\bar{J}, J}(t_0, -t_0) \big| \Phi_0 \big\rangle. \tag{2.8}$$

In the time evolution operator

$$U^{(\eta)}_{\bar{J}, J}(t_0, -t_0) = \mathcal{T} \exp\bigg(-\mathrm{i} \int_{-t_0}^{t_0} \mathrm{d}t \left\{ (1 - \mathrm{i}\eta) H + \sum_\alpha \left[\bar{J}_\alpha(t) a_\alpha + a^\dagger_\alpha J_\alpha(t) \right] \right\} \bigg), \tag{2.9}$$

source terms with time-dependent, anticommuting Grassmann variables $\bar{J}_\alpha$, J_α were added to the Hamiltonian. Throughout this thesis we use units with $\hbar = 1$.

When $|\Phi_0\rangle$ is expressed in terms of eigenstates of the interacting Hamiltonian H, the factor $1 - \mathrm{i}\eta$ with $\eta > 0$ leads to factors $e^{-t_0 \eta (E_n - E_0)}$ in Eq. (2.6) that suppress the contributions from excited states with eigenenergies E_n compared to the contributions from the ground state with eigenenergy E_0. Only the ground-state expectation value survives the limit $t_0 \to \infty$, as required by the definition (2.5). For this step the requirement that $|\Psi_0\rangle$ and $|\Phi_0\rangle$ are not mutually orthogonal is essential. In contrast to Ref. [NO88], in which a time contour in the complex plane is used, we formally attribute the factor $1 - \mathrm{i}\eta$ not to the time integration, but to the Hamiltonian. This corresponds to the picture that excited states decay because of a non-zero anti-Hermitian part of the Hamiltonian, see e.g. Ref. [AGU20].

The functional derivatives in Eq. (2.6) are not well-defined at equal times. Such cases can be circumvented with infinitesimal shifts. But one has to be careful as

the Green function can be discontinuous at equal times of a creation operator and an annihilation operator. We then infinitesimally increase the time of the $J_{\alpha'}(t')$-derivative to mimic the time-ordering operator in the definition (2.5), which moves the creation operator to the left.

2.4 Discrete integral expression for $Z_\eta[\bar{J}, J]$

We introduce intermediate time steps $\tau_m = -t_0 + m\Delta$ with $\Delta = 2t_0/M$ and $m = 0, 1, \ldots, M$ and insert resolutions of unity into Eq. (2.8) in terms of standard fermionic coherent states

$$|\varphi\rangle = \exp\left(-\sum_\alpha \varphi_\alpha a_\alpha^\dagger\right)|0\rangle, \tag{2.10}$$

where φ stands for the set of Grassmann generators $\{\varphi_1, \varphi_2, \ldots\}$. This yields

$$\begin{aligned} Z_\eta[\bar{J}, J] = \int \left(\prod_{m=0}^{M}\prod_\alpha \mathrm{d}\bar{\varphi}_\alpha^m \mathrm{d}\varphi_\alpha^m e^{-\bar{\varphi}_\alpha^m \varphi_\alpha^m}\right) \langle\Phi_0|\varphi^M\rangle \, \langle\varphi^M|U_{\bar{J},J}^{(\eta)}(\tau_M, \tau_{M-1})|\varphi^{M-1}\rangle \\ \times \ldots \langle\varphi^1|U_{\bar{J},J}^{(\eta)}(\tau_1, \tau_0)|\varphi^0\rangle \, \langle\varphi^0|\Phi_0\rangle, \end{aligned} \tag{2.11}$$

where each $\bar{\varphi}_\alpha^m$ is an additional Grassmann generator that is by definition the conjugate of φ_α^m. The usage of standard coherent states is an important difference to Ref. [NO88]. It will allow for a straightforward derivation of the functional-integral representation of the generating functional in the interacting case, see Eq. (2.31) below. The factors $\langle\Phi_0|\varphi^M\rangle = \varphi_N^M \ldots \varphi_1^M$ and $\langle\varphi^0|\Phi_0\rangle = \bar{\varphi}_1^0 \ldots \bar{\varphi}_N^0$ in Eq. (2.11) are important for the form of the free propagator, see the integration in Eq. (2.14) and the remark at the end of Sec. 2.5. Up to corrections $\propto \Delta^2$, the occurring matrix elements are given by

$$\begin{aligned} &\left\langle\varphi^m\middle|U_{\bar{J},J}^{(\eta)}(\tau_m, \tau_{m-1})\middle|\varphi^{m-1}\right\rangle \\ &= \exp\left(\sum_\alpha \bar{\varphi}_\alpha^m \varphi_\alpha^{m-1}\right) \qquad (2.12a) \\ &\quad \times \left\{1 - \mathrm{i}\Delta\left[(1-\mathrm{i}\eta)H(\bar{\varphi}^m, \varphi^{m-1}) + \sum_\alpha \left(\bar{J}_\alpha^{m-1}\varphi_\alpha^{m-1} + \bar{\varphi}_\alpha^m J_\alpha^m\right)\right]\right\} \\ &= \exp\Bigg\{\sum_\alpha \bar{\varphi}_\alpha^m e^{-(\mathrm{i}+\eta)\varepsilon_\alpha\Delta}\varphi_\alpha^{m-1} \qquad (2.12b) \\ &\qquad - \mathrm{i}\Delta\left[(1-\mathrm{i}\eta)H_{\mathrm{int}}(\bar{\varphi}^m, \varphi^{m-1}) + \sum_\alpha \left(\bar{J}_\alpha^{m-1}\varphi_\alpha^{m-1} + \bar{\varphi}_\alpha^m J_\alpha^m\right)\right]\Bigg\}, \end{aligned}$$

where we used the notation $\bar{J}_\alpha^m = \bar{J}_\alpha(\tau_m)$ and $J_\alpha^m = J_\alpha(\tau_m)$. The expression for $H(\bar{\varphi}^m, \varphi^{m-1})$ can be obtained from Eq. (2.1) by replacing all ladder operators with Grassmann generators according to $a_\alpha^\dagger \to \bar{\varphi}_\alpha^m$ and $a_\alpha \to \varphi_\alpha^{m-1}$. In particular, we have

$$H_{\mathrm{int}}(\bar{\varphi}^m, \varphi^{m-1}) = \sum_{\alpha'\alpha} w_{\alpha'\alpha}\, \bar{\varphi}_{\alpha'}^m \varphi_\alpha^{m-1} + \frac{1}{4}\sum_{\alpha_1'\alpha_2'\alpha_1\alpha_2} \bar{v}_{\alpha_1'\alpha_2'\alpha_1\alpha_2}\, \bar{\varphi}_{\alpha_1'}^m \bar{\varphi}_{\alpha_2'}^m \varphi_{\alpha_2}^{m-1}\varphi_{\alpha_1}^{m-1}. \tag{2.13}$$

(If one uses the particular coherent states of Ref. [NO88] instead, the expression that results for $H_{\rm int}$ is not as simple.) Since none of the matrix elements (2.12) depends on $\bar\varphi^0$ or φ^M, the integrations for $m = 0, M$ in Eq. (2.11) reduce to

$$\begin{aligned}
&\int\biggl(\prod_\alpha \mathrm{d}\bar\varphi_\alpha^0\mathrm{d}\varphi_\alpha^0\, e^{-\bar\varphi_\alpha^0\varphi_\alpha^0}\,\mathrm{d}\bar\varphi_\alpha^M\mathrm{d}\varphi_\alpha^M e^{-\bar\varphi_\alpha^M\varphi_\alpha^M}\biggr)\varphi_N^M\ldots\varphi_1^M\bar\varphi_1^0\ldots\bar\varphi_N^0\, f\bigl(\bar\varphi^M,\varphi^0\bigr)\\
&=\int\biggl(\prod_{\alpha\le N}\mathrm{d}\bar\varphi_\alpha^M\mathrm{d}\varphi_\alpha^M\biggr)\varphi_N^M\ldots\varphi_1^M\biggl(\prod_{\alpha\le N}\mathrm{d}\bar\varphi_\alpha^0\mathrm{d}\varphi_\alpha^0\biggr)\bar\varphi_1^0\ldots\bar\varphi_N^0\\
&\quad\times\biggl[\prod_{\alpha>N}\mathrm{d}\bar\varphi_\alpha^0\mathrm{d}\varphi_\alpha^0\bigl(1-\bar\varphi_\alpha^0\varphi_\alpha^0\bigr)\mathrm{d}\bar\varphi_\alpha^M\mathrm{d}\varphi_\alpha^M\bigl(1-\bar\varphi_\alpha^M\varphi_\alpha^M\bigr)\biggr]f\bigl(\bar\varphi^M,\varphi^0\bigr) \qquad (2.14a)\\
&=(-1)^N\int\biggl(\prod_{\alpha\le N}\mathrm{d}\bar\varphi_\alpha^M\mathrm{d}\varphi_\alpha^0\biggr)f\bigl(\bar\varphi^M,\varphi^0\bigr)\Big|_{\mathcal{B}_>}. \qquad (2.14b)
\end{aligned}$$

The notation in the last line involving the boundary conditions

$$\mathcal{B}_> = \bigl\{\bar\varphi_{\alpha>N}^M = 0, \varphi_{\alpha>N}^0 = 0\bigr\} \qquad (2.15)$$

means that in $f\bigl(\bar\varphi^M,\varphi^0\bigr)$ the generators $\bar\varphi_\alpha^M$, φ_α^0 with $\alpha > N$ are replaced by zero. These boundary conditions reflect that the levels with $\alpha > N$ are empty in the state $|\Phi_0\rangle$. In total one obtains

$$Z_\eta[\bar J, J] = \lim_{M\to\infty}\int D_M(\bar\varphi,\varphi)\, e^{\mathrm{i}S_M(\bar\varphi,\varphi;\bar J,J)} \qquad (2.16)$$

with the Grassmann integration measure

$$D_M(\bar\varphi,\varphi) = (-1)^{MN}\biggl(\prod_{\alpha\le N}\prod_{m=1}^{M}\mathrm{d}\bar\varphi_\alpha^m\mathrm{d}\varphi_\alpha^{m-1}\biggr)\biggl(\prod_{\alpha>N}\prod_{m=1}^{M-1}\mathrm{d}\bar\varphi_\alpha^m\mathrm{d}\varphi_\alpha^m\biggr). \qquad (2.17)$$

The action $S_M(\bar\varphi,\varphi;\bar J, J)$ is the sum of the free part

$$S_M^0(\bar\varphi,\varphi) = \sum_{\alpha',\alpha\le N}\sum_{m'=1}^{M}\sum_{m=0}^{M-1}\bar\varphi_{\alpha'}^{m'}Q_{\alpha'\alpha}^{m'm}\varphi_\alpha^m + \sum_{\alpha',\alpha>N}\sum_{m',m=1}^{M-1}\bar\varphi_{\alpha'}^{m'}Q_{\alpha'\alpha}^{m'm}\varphi_\alpha^m \qquad (2.18)$$

with

$$Q_{\alpha'\alpha}^{m'm} = \mathrm{i}\delta_{\alpha'\alpha}\left[\delta_{m'm} - \delta_{m'-1,m}\, e^{-(\mathrm{i}+\eta)\varepsilon_\alpha\Delta}\right], \qquad (2.19)$$

the interaction part

$$S_M^{\rm int}(\bar\varphi,\varphi) = -(1-\mathrm{i}\eta)\Delta\sum_{m=1}^{M}H_{\rm int}(\bar\varphi^m,\varphi^{m-1})\Big|_{\mathcal{B}_>}, \qquad (2.20)$$

and the source part

$$S_M^{\rm source}(\bar\varphi,\varphi;\bar J,J) = -\Delta\sum_{\alpha\le N}\sum_{m=1}^{M}\bigl(\bar J_\alpha^{m-1}\varphi_\alpha^{m-1}+\bar\varphi_\alpha^m J_\alpha^m\bigr) - \Delta\sum_{\alpha>N}\sum_{m=1}^{M-1}\bigl(\bar J_\alpha^m\varphi_\alpha^m+\bar\varphi_\alpha^m J_\alpha^m\bigr). \qquad (2.21)$$

2.5 Noninteracting generating functional

In the noninteracting case, the integral in Eq. (2.16) is of Gaussian form. We consider Q given by Eq. (2.19) to be a matrix and introduce row vectors $\bar{\varphi}$, $\bar{J}$ and column vectors φ, J. We point out the peculiar ranges of the discrete-time indices, see Eqs. (2.18) and (2.21): In the sector with $\alpha \leq N$, the row index m' of Q runs from 1 to M, whereas its column index m runs from 0 to $M-1$. Correspondingly, the indices of $\bar{\varphi}$ and J run from 1 to M, whereas those of φ and $\bar{J}$ run from 0 to $M-1$. In the sector with $\alpha > N$, all discrete-time indices simply run from 1 to $M-1$. The Gaussian integral evaluates to

$$\int D_M(\bar{\varphi},\varphi)\, e^{\mathrm{i}[\bar{\varphi}Q\varphi - \Delta(\bar{J}\varphi + \bar{\varphi}J)]} = e^{-(\mathrm{i}+\eta)2t_0 \sum_{\alpha\leq N}\varepsilon_\alpha}\; e^{-\mathrm{i}\Delta^2 \bar{J}Q^{-1}J}. \tag{2.22}$$

The result for the noninteracting generating functional is thus

$$\mathcal{G}^0_\eta[\bar{J},J] = \lim_{t_0\to\infty}\lim_{M\to\infty} e^{-\mathrm{i}\Delta^2\bar{J}gJ} \tag{2.23}$$

with the free propagator

$$g^{mm'}_{\alpha\alpha'} = (Q^{-1})^{mm'}_{\alpha\alpha'} = -\mathrm{i}\delta_{\alpha\alpha'}\, e^{-(\mathrm{i}+\eta)\varepsilon_\alpha(\tau_m - \tau_{m'})} \begin{cases} 1-n_\alpha, & M-1 \geq m \geq m' \geq 1 \\ -n_\alpha, & 0 \leq m < m' \leq M. \end{cases} \tag{2.24}$$

The free propagator is purely advanced for $\alpha \leq N$ and purely retarded for $\alpha > N$. The inverse of Q assumes such distinct forms in the two sectors because of the differently restricted ranges of the discrete-time indices. These in turn are a consequence of the integrations over the Grassmann generators at the boundaries, which were performed in Eq. (2.14).

2.6 Continuous functional-integral notation

In the integral expression (2.16) for $Z_\eta[\bar{J},J]$ (and for $\mathcal{G}_\eta[\bar{J},J]$ by extension), we go from the discrete time steps τ_m over to a continuous time variable by formally performing the limit $M\to\infty$. In doing so we gather the Grassmann generators $\bar{\varphi}^m_\alpha$, φ^m_α into functions $\bar{\varphi}_\alpha(t)$, $\varphi_\alpha(t)$ with a formal time dependence.

2.6.1 Constituents of the action

We start by casting the free action (2.18) into either of the following forms

$$S^0_M(\bar{\varphi},\varphi) = \sum_\alpha \Delta \sum_{m=1}^{M} \bar{\varphi}^m_\alpha \left[\mathrm{i}\frac{\varphi^m_\alpha - \varphi^{m-1}_\alpha}{\Delta} - (1-\mathrm{i}\eta)\varepsilon_\alpha \varphi^{m-1}_\alpha\right]\Bigg|_{\mathcal{B}} \tag{2.25a}$$

$$= \sum_\alpha \Delta \sum_{m=0}^{M-1} \left[\mathrm{i}\frac{\bar{\varphi}^m_\alpha - \bar{\varphi}^{m+1}_\alpha}{\Delta} - (1-\mathrm{i}\eta)\varepsilon_\alpha \bar{\varphi}^{m+1}_\alpha\right]\varphi^m_\alpha\Bigg|_{\mathcal{B}}. \tag{2.25b}$$

In Eq. (2.25) some addends were introduced artificially; they evaluate to zero because of the extended boundary conditions

$$\mathcal{B} = \big\{\bar{\varphi}^0_{\alpha\leq N} = 0,\, \bar{\varphi}^M_{\alpha>N} = 0,\, \varphi^M_{\alpha\leq N} = 0,\, \varphi^0_{\alpha>N} = 0\big\}. \tag{2.26}$$

In the limit $M \to \infty$, the free action can thus be written as

$$S^0[\bar{\varphi},\varphi] = \sum_{\alpha'\alpha} \int_{-t_0}^{t_0} \mathrm{d}t' \int_{-t_0}^{t_0} \mathrm{d}t\, \bar{\varphi}_{\alpha'}(t') Q_{\alpha'\alpha}(t',t) \varphi_\alpha(t) \bigg|_{\mathcal{B}} \tag{2.27}$$

with the boundary conditions in continuous form

$$\mathcal{B} = \big\{\bar{\varphi}_{\alpha\leq N}(-t_0) = 0,\, \bar{\varphi}_{\alpha>N}(t_0) = 0,\, \varphi_{\alpha\leq N}(t_0) = 0,\, \varphi_{\alpha>N}(-t_0) = 0\big\} \tag{2.28}$$

and with the differential operator

$$Q_{\alpha'\alpha}(t',t) = \delta_{\alpha'\alpha}\, \delta(t'-t) \big[\mathrm{i}\partial_t - (1-\mathrm{i}\eta)\varepsilon_\alpha\big] \tag{2.29a}$$

or

$$Q_{\alpha'\alpha}(t',t) = \delta_{\alpha'\alpha} \Big[-\mathrm{i}\overleftarrow{\partial}_{t'} - (1-\mathrm{i}\eta)\varepsilon_\alpha\Big] \delta(t'-t) \tag{2.29b}$$

corresponding to the expression (2.25a) or (2.25b), respectively. In the latter version, the time derivative acts to the left.

In the continuum limit, the interaction part and the source part of the action become

$$S^{\mathrm{int}}[\bar{\varphi},\varphi] = -(1-\mathrm{i}\eta) \int_{-t_0}^{t_0} \mathrm{d}t\, H_{\mathrm{int}}\big(\bar{\varphi}(t), \varphi(t^-)\big) \bigg|_{\mathcal{B}} \tag{2.30a}$$

$$S^{\mathrm{source}}[\bar{\varphi},\varphi;\bar{J},J] = -\sum_\alpha \int_{-t_0}^{t_0} \mathrm{d}t\, \big[\bar{J}_\alpha(t)\varphi_\alpha(t) + \bar{\varphi}_\alpha(t) J_\alpha(t)\big] \bigg|_{\mathcal{B}}. \tag{2.30b}$$

Their derivation is analogous to that of the free part.

2.6.2 Generating functional

Here, we employ a matrix notation similar to the one in Sec. 2.5 but with a multi-index $x = (\alpha, t)$. Since the definition (2.7) of the generating functional involves the limit $t_0 \to \infty$, contractions assume the form $\sum_x = \sum_\alpha \int_{-\infty}^{\infty} \mathrm{d}t$. The functional-integral representation then reads

$$\mathcal{G}_\eta[\bar{J},J] = \frac{\int D[\bar{\varphi},\varphi] \exp\big\{\mathrm{i}\bar{\varphi}Q\varphi + \mathrm{i}S^{\mathrm{int}}[\bar{\varphi},\varphi] - \mathrm{i}(\bar{J}\varphi + \bar{\varphi}J)\big\}}{\int D[\bar{\varphi},\varphi] \exp\big\{\mathrm{i}\bar{\varphi}Q\varphi + \mathrm{i}S^{\mathrm{int}}[\bar{\varphi},\varphi]\big\}}, \tag{2.31}$$

where the differential operator Q is given by Eq. (2.29) and where the interaction part of the action can be written as

$$S^{\mathrm{int}}[\bar{\varphi},\varphi] = -\bar{\varphi}w\varphi - \frac{1}{4} \sum_{x'_1 x'_2 x_1 x_2} \bar{v}_{x'_1 x'_2 x_1 x_2}\, \bar{\varphi}_{x'_1} \bar{\varphi}_{x'_2} \varphi_{x_2} \varphi_{x_1} \tag{2.32a}$$

$$w_{x'x} = \delta(t'-t)(1-\mathrm{i}\eta) w_{\alpha'\alpha} \tag{2.32b}$$

$$\bar{v}_{x'_1 x'_2 x_1 x_2} = \delta(t'_1 - t_1)\delta(t'_2 - t_1)\delta(t_2 - t_1)(1-\mathrm{i}\eta)\bar{v}_{\alpha'_1\alpha'_2\alpha_1\alpha_2}. \tag{2.32c}$$

In the diagrammatic language, Eqs. (2.32b) and (2.32c) are the bare single- and two-particle vertex, respectively. We have not carried over the infinitesimal time shifts appearing in Eq. (2.30a) into their expressions because the specific choice for the equal-time value of the free propagator will make these shifts redundant, see below.

2.6.3 Free propagator

There are two ways to derive the continuous form of the free propagator. First, we can define it as the inverse, i.e. Green function, of the differential operator Q given by Eq. (2.29) such that a continuous version of the Gaussian integral Eq. (2.22) holds. By applying particular source derivatives to this continuous version, we can then translate the boundary conditions (2.28) to

$$\begin{aligned} g_{\alpha\leq N}(t,-t_0) &= 0, & g_{\alpha>N}(t,t_0) &= 0, \\ g_{\alpha\leq N}(t_0,t') &= 0, & g_{\alpha>N}(-t_0,t') &= 0. \end{aligned} \tag{2.33}$$

When subjected to these boundary conditions, the inverse of Q is unique in the sense of a distribution, giving us the continuous free propagator. Second, the limit $M\to\infty$ can directly be applied to the discrete form (2.24) of the free propagator. As the distance $\Delta = 2t_0/M$ of the time steps τ_m becomes infinitesimal, the matrix indices m, m' are replaced with continuous time arguments t, t'.

The results of the two ways agree with each other. Only the limit of the discrete form yields a conclusive equal-time value, which we do not carry over though. Following the usual convention [NO88], we choose $g_{\alpha\alpha'}(t,t) = g_{\alpha\alpha'}(t,t^+)$ so the continuous free propagator reads

$$g_{\alpha\alpha'}(t,t') = \delta_{\alpha\alpha'} g_\alpha(t-t') \tag{2.34a}$$

$$g_\alpha(t) = -\mathrm{i}e^{-(\mathrm{i}+\eta)\varepsilon_\alpha t}\big[(1-n_\alpha)\Theta(t-0^+) - n_\alpha\Theta(-t+0^+)\big]. \tag{2.34b}$$

In the limit $t_0\to\infty$, this defines the free propagator for all times. The continuous form of the noninteracting generating functional is given by

$$\mathcal{G}^0_\eta[\bar{J},J] = e^{-\mathrm{i}\bar{J}gJ}, \tag{2.35}$$

where the same matrix notation as in Eq. (2.31) is used. The free propagator coincides with the noninteracting single-particle Green function

$$G^0_\eta(\alpha\, t|\alpha' t') = -\mathrm{i}\,\frac{\delta^2\mathcal{G}^0_\eta[\bar{J},J]}{\delta\bar{J}_\alpha(t)\,\delta J_{\alpha'}(t')}\bigg|_{\bar{J}=0=J} = g_{\alpha\alpha'}(t,t'). \tag{2.36}$$

The equal-time value of the free propagator is mostly irrelevant in the diagrammatic expansion of the Green functions, see Sec. 2.7, because in the time integrations the cases of equal times have measure zero. The equal-time value can matter in only two kinds of situations. First, a free propagator may start and end at the same vertex. Then the equal-time case is actually avoided by the infinitesimal time shifts inherent to the vertex, cf. Eq. (2.30a). These shifts decrease the times of the generators $\varphi_\alpha(t)$

and by extension also the left arguments of the free propagators $g_{\alpha\alpha'}(t,t')$. Thanks to the specific choice in Eq. (2.34), the time shifts at the vertices can be dropped as anticipated in Eqs. (2.32b) and (2.32c). Second, a free propagator may connect two external points that happen to have equal times. The source derivatives used to obtain the Green functions from their generating functional are actually not defined at equal times. As mentioned in Sec. 2.3, one then infinitesimally increases the time of the $J_{\alpha'}(t')$-derivative and by extension the right time argument of $g_{\alpha\alpha'}(t,t')$ to mimic the behavior of the time-ordering operator in the definition of the Green functions. Again, the specific choice in Eq. (2.34) is such that we do not have to worry about applying these infinitesimal shifts and can work with equal-time derivatives instead. For example Eq. (2.36) holds even at equal times thanks to this choice.

2.7 Diagrammatic expansion of the Green functions

In this section we present the diagrammatic perturbation theory for the Green functions. We formulate two sets of rules, which differ in how they treat the single-particle perturbation. One set involves propagator lines implicitly containing the single-particle perturbation, whereas the other set involves explicit single-particle vertices. In both cases a diagram represents a contribution of a given order in the two-particle interaction.

As a first step, we effectively dress the free propagator with the single-particle perturbation by rewriting the interacting generating functional. The functional-integral representation of the interacting generating functional then has a standard form so that a diagrammatic formulation can be derived in the usual way, see e.g. Ref. [Jak19] in the context of the Keldysh formalism and Chap. 2 of Ref. [NO88] in the context of the Matsubara formalism. Note that Chap. 3 of Ref. [NO88] on the zero-temperature formalism does not provide a corresponding expression for the interacting generating functional.

For completeness we present the derivation in a concise way, starting with an expansion in powers of the two-particle interaction. The resulting diagrammatic rules are given in full detail. Based on this first set of rules, we describe how the free propagator and the single-particle perturbation can be unraveled. This leads to a second set of rules with explicit single-particle vertices, which we state in full detail too. We note that one could alternatively choose to derive the two sets of diagrammatic rules in reverse order by first expanding in both the single-particle as well as the two-particle perturbation to obtain the rules with explicit single-particle vertices and only then absorbing the latter into the lines to arrive at the rules without single-particle vertices.

2.7.1 Expansion in powers of the two-particle interaction

We slightly rewrite the expression (2.31) for the generating functional to obtain the alternative functional-integral representation

$$\mathcal{G}_\eta[\bar{J},J] = \frac{\int D[\bar{\varphi},\varphi]\exp\{\mathrm{i}\bar{\varphi}Q^{(w)}\varphi - \frac{\mathrm{i}}{4}\bar{v}_{x_1'x_2'x_1x_2}\bar{\varphi}_{x_1'}\bar{\varphi}_{x_2'}\varphi_{x_2}\varphi_{x_1} - \mathrm{i}(\bar{J}\varphi+\bar{\varphi}J)\}}{\int D[\bar{\varphi},\varphi]\exp\{\mathrm{i}\bar{\varphi}Q^{(w)}\varphi - \frac{\mathrm{i}}{4}\bar{v}_{x_1'x_2'x_1x_2}\bar{\varphi}_{x_1'}\bar{\varphi}_{x_2'}\varphi_{x_2}\varphi_{x_1}\}} \tag{2.37}$$

with the same matrix notation as in Sec. 2.6.2, implicit summation over repeated indices, and

$$Q^{(w)} = Q - w. \tag{2.38}$$

This form of the generating functional is the same as in Ref. [Jak19], but with

$$g^{(w)} = \left[Q^{(w)}\right]^{-1} = \left(g^{-1} - w\right)^{-1} \tag{2.39}$$

playing the role of the free propagator and without a contour index; the following steps are performed in full analogy.

Equation (2.39) can be rather intricate, depending on the details of the single-particle perturbation. If we calculated the inverse of $Q^{(w)}$, we would need to apply boundary conditions to uniquely determine $g^{(w)}$. But translating the boundary conditions (2.33) for g to boundary conditions for $g^{(w)}$ is not straightforward. Since Eq. (2.39) has the form of a Dyson equation, $g^{(w)}$ can alternatively be determined from a Dyson series. A diagrammatic realization of this series is embedded in our second set of rules via explicit single-particle vertices, see Sec. 2.7.3. Compared to g the dressed propagator $g^{(w)}$ can have a more complicated dependence on times (or frequencies) and state indices.

After inserting Eq. (2.37) into Eq. (2.6), we explicitly perform the source derivatives to find the functional-integral representation of the Green functions

$$\begin{aligned} &G_\eta(x_1, \ldots, x_n | x'_1, \ldots, x'_n) \\ &= (-\mathrm{i})^n \frac{\int D[\bar\varphi, \varphi] \exp\{\mathrm{i}\bar\varphi Q^{(w)}\varphi - \frac{\mathrm{i}}{4}\bar v_{x'_1x'_2x_1x_2}\bar\varphi_{x'_1}\bar\varphi_{x'_2}\varphi_{x_2}\varphi_{x_1}\}\varphi_{x_1}\ldots\varphi_{x_n}\bar\varphi_{x'_n}\ldots\bar\varphi_{x'_1}}{\int D[\bar\varphi, \varphi] \exp\{\mathrm{i}\bar\varphi Q^{(w)}\varphi - \frac{\mathrm{i}}{4}\bar v_{x'_1x'_2x_1x_2}\bar\varphi_{x'_1}\bar\varphi_{x'_2}\varphi_{x_2}\varphi_{x_1}\}}. \end{aligned} \tag{2.40}$$

Expanding the numerator in powers of the two-particle interaction amplitude $\bar v$ and subsequently rearranging the Grassmann generators yields

$$\begin{aligned} &G_\eta(x_1, \ldots, x_n | x'_1, \ldots, x'_n) \\ &= \frac{\int D[\bar\varphi, \varphi] \exp\{\mathrm{i}\bar\varphi Q^{(w)}\varphi\}}{\int D[\bar\varphi, \varphi] \exp\{\mathrm{i}\bar\varphi Q^{(w)}\varphi - \frac{\mathrm{i}}{4}\bar v_{x'_1x'_2x_1x_2}\bar\varphi_{x'_1}\bar\varphi_{x'_2}\varphi_{x_2}\varphi_{x_1}\}} \sum_{k=0}^{\infty} \frac{1}{k!} \left(\prod_{l=1}^{k} \frac{\mathrm{i}}{4}\, \bar v_{x'_{l,1}x'_{l,2}x_{l,1}x_{l,2}} \right) \\ &\quad \times \frac{(-\mathrm{i})^{2k+n}}{\int D[\bar\varphi, \varphi] \exp\{\mathrm{i}\bar\varphi Q^{(w)}\varphi\}} \int D[\bar\varphi, \varphi] \exp\{\mathrm{i}\bar\varphi Q^{(w)}\varphi\} \varphi_{x_{1,1}}\varphi_{x_{1,2}}\ldots\varphi_{x_{k,1}}\varphi_{x_{k,2}} \\ &\quad \times \varphi_{x_1}\ldots\varphi_{x_n}\bar\varphi_{x'_n}\ldots\bar\varphi_{x'_1}\bar\varphi_{x'_{k,2}}\bar\varphi_{x'_{k,1}}\ldots\bar\varphi_{x'_{1,2}}\bar\varphi_{x'_{1,1}}. \end{aligned} \tag{2.41}$$

We identify the last two lines as the functional-integral representation of a Green function in the case $\bar v = 0$, cf. Eq. (2.40), and arrive at

$$\begin{aligned} &G_\eta(x_1, \ldots, x_n | x'_1, \ldots, x'_n) \\ &= \frac{\int D[\bar\varphi, \varphi] \exp\{\mathrm{i}\bar\varphi Q^{(w)}\varphi\}}{\int D[\bar\varphi, \varphi] \exp\{\mathrm{i}\bar\varphi Q^{(w)}\varphi - \frac{\mathrm{i}}{4}\bar v_{x'_1x'_2x_1x_2}\bar\varphi_{x'_1}\bar\varphi_{x'_2}\varphi_{x_2}\varphi_{x_1}\}} \sum_{k=0}^{\infty} \frac{1}{k!} \left(\prod_{l=1}^{k} \frac{\mathrm{i}}{4}\, \bar v_{x'_{l,1}x'_{l,2}x_{l,1}x_{l,2}} \right) \\ &\quad \times G_\eta^{(\bar v=0)}(x_{1,1}, x_{1,2}, \ldots, x_{k,1}, x_{k,2}, x_1, \ldots, x_n | x'_{1,1}, x'_{1,2}, \ldots, x'_{k,1}, x'_{k,2}, x'_1, \ldots, x'_n). \end{aligned} \tag{2.42}$$

We have thus expressed the full Green functions in terms of the Green functions $G_\eta^{(\bar{v}=0)}(\ldots) = G_\eta(\ldots)\big|_{\bar{v}=0}$ describing the system with the single-particle perturbation but without the two-particle interaction. Note that the inverse ratio of the functional integrals remaining in Eq. (2.42) could be expanded in exactly the same way, just without the external Grassmann generators $\varphi_{x_1} \ldots \bar{\varphi}_{x_1'}$; this inverse ratio will cancel with all vacuum diagrams.

2.7.2 Diagrammatic rules without a single-particle vertex

In order to translate the expansion (2.42) of the Green functions into a diagrammatic language, we employ the Wick theorem

$$G_\eta^{(\bar{v}=0)}(x_1,\ldots,x_n|x_1',\ldots,x_n') = (-\mathrm{i})^n \frac{\delta^{2n} e^{-\mathrm{i}\bar{J}g^{(w)}J}}{\delta\bar{J}_{x_1}\ldots\delta\bar{J}_{x_n}\delta J_{x_n'}\ldots\delta J_{x_1'}}\bigg|_{\bar{J}=0=J} \tag{2.43a}$$

$$= \sum_{P\in S_n} \operatorname{sgn}(P)\, g^{(w)}_{x_{P(n)}x_n'} \ldots g^{(w)}_{x_{P(1)}x_1'}, \tag{2.43b}$$

where S_n is the set of all permutations of the numbers $1,\ldots,n$. In Eq. (2.43a) we used an expression for $\mathcal{G}_\eta^{(\bar{v}=0)}[\bar{J},J]$ that is analogous to the noninteracting generating functional (2.35), where $w=0$ as well as $\bar{v}=0$. Both cases feature a quadratic action in the respective functional-integral representation and differ only in replacing $Q \to Q^{(w)}$ and $g \to g^{(w)}$.

We use the Wick theorem (2.43) to express $G_\eta^{(\bar{v}=0)}$ in Eq. (2.42) in terms of products of $g^{(w)}$. For each permutation P appearing in the Wick theorem, one can then draw a diagram with external points x_i, x_i' and two-particle vertices $\bar{v}$ connected by directed lines $g^{(w)}$. The sign of the permutation can conveniently be determined by examining in which way the external points are connected to each other and by counting the number of closed loops. The parts of the diagrams that are not connected to the external points, i.e. the vacuum diagrams, can be separated and cancel with the remaining ratio of functional integrals so that it suffices to consider only diagrams where each vertex is connected to the external points. One can represent multiple diagrams having the same value by just a single diagram if one drops the labels of the legs of the vertices; this cancels the factors $1/4$ except in cases with equivalent lines. Similarly, one can drop the remaining labels numbering the vertices; this cancels the factor $1/k!$ unless the diagram is symmetric. More details on these simplifications of the diagrammatic rules can be found in Ref. [Jak19].

We arrive at the following diagrammatic rules for the Green functions. On the semantic level, these rules are the same as the ones in Ref. [Jak19]; even the wording is partly identical.

Diagrammatic rules for the Green functions

The contribution of order $\bar{v}^k$ to the Green function $G_\eta(x_1,\ldots,x_n|x_1',\ldots,x_n')$ is the sum of all distinct diagrams constructed in the following way. Draw n external starting points x_i', n external end points x_i, and k unlabeled two-particle vertices and connect them with directed lines. Do not draw internal

connections within the vertices yet. Consider only diagrams in which each vertex is connected via lines and vertices to at least one of the external points.

An individual diagram is evaluated as follows. Let n_{eq} be the number of pairs of equivalent lines; two lines are equivalent if they connect the same vertices in the same direction. Assign labels $1, \ldots, k$ to the vertices. Determine the symmetry factor S as the number of permutations of these labels that map the diagram onto itself, including the identity permutation. Now draw internal connections within each vertex between the incoming and the outgoing legs in a one-to-one relation. Let n_{loop} be the number of closed loops formed by the lines. Determine the permutation P such that x'_i is connected via lines to $x_{P(i)}$. Assign multi-indices $x_{n+1}, x_{n+2}, \ldots$ to the incoming legs of the vertices and $x'_{n+1}, x'_{n+2}, \ldots$ to their outgoing legs. A directed line running from some index x' to some index x has the value $g^{(w)}_{xx'}$. A vertex has the value $\bar{v}_{x'_i x'_j x_i x_j}$ where x'_i, x'_j are the indices of its outgoing legs and x_i, x_j are the indices of its incoming legs such that x_i is internally connected to x'_i. The value of the diagram is

$$\frac{\mathrm{sgn}(P)(-1)^{n_{\mathrm{loop}}}}{2^{n_{\mathrm{eq}}} S} \Big[\prod g^{(w)}\Big] \Big(\prod \mathrm{i}\bar{v}\Big) \tag{2.44}$$

with implicit summation over all internal multi-indices.

In the above version of the diagrammatic rules, the propagator lines are dressed with the single-particle perturbation via $g^{(w)} = (g^{-1} - w)^{-1}$. For models without a single-particle perturbation, their value is identical to the free propagator g. In time representation the values of g, w, and $\bar{v}$ are given by Eqs. (2.34), (2.32b), and (2.32c), respectively. In frequency representation they are given by Eqs. (2.47), (2.48a), and (2.48b) instead.

2.7.3 Diagrammatic rules with a single-particle vertex

We now refer to the diagrams from Sec. 2.7.2 as the original ones. Each of them can be decomposed into new diagrams in which the number of w-insertions in the form of single-particle vertices is specified for each original line. In the following we call an original line with a specified number of w-insertions a sequence (of lines and single-particle vertices) and define its length to be the number of single-particle vertices it contains. A diagram of this new kind is not only of a certain order in $\bar{v}$ but also of a certain order in w. The value of a new diagram is essentially given by the value of its original diagram. But the value of an original line is now replaced by $gwg \ldots wg$, depending on the length of the respective sequence.

There is, however, one special case in which we must correct the prefactor of the diagram. If in the new diagram two sequences with different lengths connect the same two-particle vertices in the same direction, this represents two possibilities for distributing the w-factors among the original lines. Therefore, the value of the new diagram picks up a factor 2, which cancels the factor 1/2 that accounts for the fact that the two original lines were equivalent. We can accommodate for this change of the prefactor by defining that two sequences with different lengths cannot

be equivalent. On the other hand, if in the new diagram two sequences with equal lengths connect the same two-particle vertices in the same direction, this represents only one possibility for distributing the w-factors among the original lines. Then the prefactor does not change compared to the original diagram and we consider the sequences to be equivalent.

Using the new diagrams, we can formulate the following diagrammatic rules, which are still quite similar to those of Ref. [Jak19].

Diagrammatic rules for the Green functions

The contribution of order $w^m \bar{v}^k$ to the Green function $G_\eta(x_1, \ldots, x_n | x'_1, \ldots, x'_n)$ is the sum of all distinct diagrams constructed in the following way. Draw n external starting points x'_i, n external end points x_i, m unlabeled single-particle vertices, and k unlabeled two-particle vertices and connect them with directed lines. Do not draw internal connections within the vertices yet. Consider only diagrams in which each vertex is connected via lines and vertices to at least one of the external points.

An individual diagram is evaluated as follows. Let n_{eq} be the number of pairs of equivalent sequences of lines and single-particle vertices; two such sequences are equivalent if they connect the same two-particle vertices in the same direction and contain the same number of single-particle vertices. Assign labels $1, \ldots, k$ to the two-particle vertices. Determine the symmetry factor S as the number of permutations of these labels that map the diagram onto itself, including the identity permutation. Now draw internal connections within each vertex between the incoming and the outgoing legs in a one-to-one relation. Let n_{loop} be the number of closed loops formed by the lines. Determine the permutation P such that x'_i is connected via lines to $x_{P(i)}$. Assign multi-indices $x_{n+1}, x_{n+2}, \ldots$ to the incoming legs of the vertices and $x'_{n+1}, x'_{n+2}, \ldots$ to their outgoing legs. A directed line running from some index x' to some index x has the value $g_{xx'}$. A single-particle vertex having its outgoing and incoming leg labeled with some index x' and x, respectively, has the value $w_{x'x}$. A two-particle vertex has the value $\bar{v}_{x'_i x'_j x_i x_j}$ where x'_i, x'_j are the indices of its outgoing legs and x_i, x_j are the indices of its incoming legs such that x_i is internally connected to x'_i. The value of the diagram is

$$\frac{\mathrm{sgn}(P)(-1)^{n_{\mathrm{loop}}}}{2^{n_{\mathrm{eq}}} S} \Big(\prod g\Big)\Big(\prod w\Big)\Big(\prod \mathrm{i}\bar{v}\Big) \tag{2.45}$$

with implicit summation over all internal multi-indices.

In time representation the values of the free propagator g, the single-particle vertex w, and the two-particle vertex $\bar{v}$ are given by Eqs. (2.34), (2.32b), and (2.32c), respectively. In frequency representation they are given by Eqs. (2.47), (2.48a), and (2.48b) instead.

2.8 Frequency representation

Here, we describe the Fourier transformation used to go from time arguments in the diagrammatic expansion over to frequency arguments. Since the Green functions (2.5), the free propagator (2.34), and the bare vertices (2.32b) and (2.32c) are time-translationally invariant, it is advantageous to work in frequency representation, where each of these quantities becomes frequency conserving and where convolutions of time that occur in the diagrams are transformed into simple products. We note that the limit $t_0 \to \infty$ has to be performed first so that the boundaries of the Fourier integrals $\int_{-\infty}^{\infty} \mathrm{d}t\, e^{\pm \mathrm{i}\omega t} \ldots$ can be infinite. In frequency representation sums over multi-indices have the form $\sum_x = \sum_\alpha \int_{-\infty}^{\infty} \mathrm{d}\omega/2\pi$.

The frequency-dependent free propagator is defined as

$$g_{\alpha\alpha'}(\omega,\omega') = \int_{-\infty}^{\infty} \mathrm{d}t \int_{-\infty}^{\infty} \mathrm{d}t' e^{\mathrm{i}(\omega t - \omega' t')} g_{\alpha\alpha'}(t,t'). \tag{2.46}$$

The integrals converge thanks to the positive infinitesimal η that was introduced in the context of the generating functional, see Eq. (2.9). The result is

$$g_{\alpha\alpha'}(\omega,\omega') = 2\pi\delta(\omega-\omega')\delta_{\alpha\alpha'} g_\alpha(\omega) \tag{2.47a}$$

$$g_\alpha(\omega) = \frac{e^{\mathrm{i}\omega\eta'}}{\omega - \varepsilon_\alpha + \mathrm{i}\eta\,\mathrm{sgn}\,\varepsilon_\alpha}, \tag{2.47b}$$

where we made the replacement $\eta\varepsilon_\alpha \to \eta\,\mathrm{sgn}\,\varepsilon_\alpha$. The positive infinitesimal η' is necessary to obtain the correct equal-time value $g_{\alpha\alpha'}(t,t)$ from the inverse Fourier transformation. It is relevant only for Hartree-type propagator loops. The single-particle vertex and the two-particle vertex are Fourier transformed into

$$w_{\alpha'\alpha}(\omega',\omega) = 2\pi\delta(\omega'-\omega)(1-\mathrm{i}\eta) w_{\alpha'\alpha} \tag{2.48a}$$

$$\bar{v}_{\alpha_1'\alpha_2'\alpha_1\alpha_2}(\omega_1',\omega_2',\omega_1,\omega_2) = 2\pi\delta(\omega_1'+\omega_2'-\omega_1-\omega_2)(1-\mathrm{i}\eta)\bar{v}_{\alpha_1'\alpha_2'\alpha_1\alpha_2}. \tag{2.48b}$$

The frequency-dependent interacting Green functions

$$G(\omega_1,\ldots|\ldots,\omega_n') = \int_{-\infty}^{\infty} \mathrm{d}t_1 \ldots \int_{-\infty}^{\infty} \mathrm{d}t_n' e^{\mathrm{i}(\omega_1 t_1 + \cdots - \omega_n' t_n')} G(t_1,\ldots|\ldots,t_n') \tag{2.49a}$$

$$\propto \delta(\omega_1 + \cdots + \omega_n - \omega_1' - \cdots - \omega_n') \tag{2.49b}$$

are well-defined whenever long-term correlations decay so that the Fourier integrals converge. They can be calculated by applying the diagrammatic rules from Sec. 2.7 to obtain G_η and finally taking the limit $G = \lim_{\eta\to 0^+} G_\eta$.

2.9 Definition of 1PI vertex functions and their generating functional

In the following we outline how to arrive at the generating functional for the 1PI vertex functions, starting from $\mathcal{G}_\eta[\bar{J}, J]$. We will use matrix notation with multi-indices $x = (\alpha, t)$ or $x = (\alpha, \omega)$, depending on the chosen representation.

Let us define

$$\mathcal{W}_\eta[\bar{J}, J] = \ln \mathcal{G}_\eta[\bar{J}, J] = \lim_{t_0 \to \infty} \ln \frac{Z_\eta[\bar{J}, J]}{Z_\eta[0, 0]}, \tag{2.50}$$

which can be shown to be the generating functional of the connected Green functions via the replica technique. Next, we define the so-called effective action as the Legendre transform of $\mathcal{W}_\eta[\bar{J}, J]$,

$$\mathcal{U}_\eta[\bar{\psi}, \psi] = -\bar{J}\psi + \bar{\psi}J + \mathcal{W}_\eta[\bar{J}, J], \tag{2.51}$$

where $\bar{J} = \bar{J}[\bar{\psi}, \psi]$ and $J = J[\bar{\psi}, \psi]$ are the inverse relations to the definitions of the new variables

$$\bar{\psi}_{x'}[\bar{J}, J] = \frac{\delta \mathcal{W}_\eta}{\delta J_{x'}}, \qquad \psi_x[\bar{J}, J] = \frac{\delta \mathcal{W}_\eta}{\delta \bar{J}_x}. \tag{2.52}$$

Note that this (standard) notation is misleading as $\bar{\psi}$ and ψ are not conjugated to each other even if $\bar{J}$ and J are. Lastly, we define the generating functional of the 1PI vertex functions as

$$\Gamma_\eta[\bar{\psi}, \psi] = \mathcal{U}_\eta[\bar{\psi}, \psi] - \mathrm{i}\bar{\psi}Q^{(w)}\psi \tag{2.53a}$$

or

$$\Gamma_\eta[\bar{\psi}, \psi] = \mathcal{U}_\eta[\bar{\psi}, \psi] - \mathrm{i}\bar{\psi}Q\psi, \tag{2.53b}$$

depending on whether we want to work with dressed propagator lines, see Sec. 2.7.2, or with explicit single-particle vertices, see Sec. 2.7.3. The only effect of the difference between these two definitions is that, in the latter case, the single-particle vertex is an explicit part of the self-energy.

The 1PI vertex functions are generated via

$$\gamma_\eta(x'_1, \ldots, x'_n | x_1, \ldots, x_n) = (-1)^n \, \mathrm{i} \, \frac{\delta^{2n} \Gamma_\eta[\bar{\psi}, \psi]}{\delta\bar{\psi}_{x'_1} \ldots \delta\bar{\psi}_{x'_n} \delta\psi_{x_n} \ldots \delta\psi_{x_1}}\bigg|_{\bar{\psi}=0=\psi}. \tag{2.54}$$

Diagrammatically, they are the sums of all one-particle irreducible diagrams, which cannot be disconnected by removing any single propagator line and which are evaluated with an additional prefactor i^{1-n} compared to the values (2.44) or (2.45) of the diagrams for the Green functions. Like for the Green functions, we ultimately consider the limit $\gamma = \lim_{\eta \to 0^+} \gamma_\eta$.

2.10 FRG flow equations

In the 1PI FRG formalism, the problem of determining the 1PI vertex functions is recast into the task to solve a set of differential equations that map the 1PI vertex functions for an easily solvable system to the ones for the system of interest. We now present a concise derivation of these flow equations. The procedure is analogous to the one in the Matsubara and Keldysh formalisms, see e.g. Refs. [Met+12, PHT13] and [GPM07, Jak19].

2.10.1 Flow equations of the generating functionals

The starting point is the introduction of a flow parameter λ into the free propagator $g \to g_\lambda$. Then also the functional $Z_\eta[\bar{J}, J]$ acquires a λ-dependence through the inverse free propagator $Q \to Q_\lambda$. Its flow equation reads

$$\dot{Z} = \mathrm{i} \frac{\delta}{\delta J} \dot{Q} \frac{\delta}{\delta \bar{J}} Z. \tag{2.55}$$

For conciseness we have suppressed all dependences, used the shorthand notation $\dot{Z} = \mathrm{d}Z/\mathrm{d}\lambda$, and considered $\delta/\delta J$ as a row vector and $\delta/\delta \bar{J}$ as a column vector. Since the definition of $Z_\eta[\bar{J}, J]$ does not contain the limit $t_0 \to \infty$ as it would otherwise diverge, see Eq. (2.22), the time integrations in Eq. (2.55) are restricted to the finite interval $[-t_0, t_0]$. This is not the case for the other equations in this section. For the generating functional of the connected Green functions $\mathcal{W}_\eta[\bar{J}, J]$, one obtains the flow equation

$$\dot{\mathcal{W}} = \mathrm{i} \left(\frac{\delta \mathcal{W}}{\delta J} \dot{Q} \frac{\delta \mathcal{W}}{\delta \bar{J}} - \operatorname{Tr} \dot{Q} \frac{\delta^2 \mathcal{W}}{\delta \bar{J} \delta J} \right) - \operatorname{Tr} \dot{Q} G, \tag{2.56}$$

where G stands for the single-particle Green function and the second derivatives $\delta^2 \mathcal{W} / \delta \bar{J}_x \delta J_{x'}$ form a matrix with row index x and column index x'. This in turn leads to the flow equation of the generating functional of the 1PI vertex functions

$$\dot{\Gamma} = -\mathrm{i} \operatorname{Tr} \dot{Q} \big(u^{-1} \big)_{++} - \operatorname{Tr} \dot{Q} G \tag{2.57}$$

with the matrix

$$u_{XX'} = \frac{\delta^2 \mathcal{U}}{\delta \psi_X \delta \psi_{\bar{X}'}}, \tag{2.58}$$

for which the multi-index was extended to $X = (c, x)$ with $c = \pm$ and we defined $\bar{X} = (-c, x)$, $\psi_{(+,x)} = \bar{\psi}_x$, and $\psi_{(-,x)} = \psi_x$.

2.10.2 Flow equations of the 1PI vertex functions

The flow equations of the 1PI vertex functions result from Eq. (2.57). With the same notation, they can be written as

$$\dot{\gamma}(x_1', \ldots, x_n' | x_1, \ldots, x_n) = (-1)^n \operatorname{Tr} \dot{Q} \left(\frac{\delta^{2n} u^{-1}}{\delta \bar{\psi}_{x_1'} \ldots \delta \psi_{x_1}} \bigg|_{\bar{\psi} = 0 = \psi} \right)_{++}. \tag{2.59}$$

The right-hand side of each of these flow equations corresponds to a sum over ring diagrams composed of 1PI m-particle vertex functions with $m = 2, \ldots, n+1$ that are connected by full single-particle Green functions and one single-scale propagator

$$S = -G \dot{Q} G = G g^{-1} \dot{g} g^{-1} G. \tag{2.60}$$

As the instances with $n = 1$ and $n = 2$ of Eq. (2.59), we obtain the flow equations of the self-energy and of the 1PI two-particle vertex function. If we return to explicitly

writing all dependences again but retain the shorthand notation $\dot{\gamma} = \mathrm{d}\gamma/\mathrm{d}\lambda$, these equations read

$$\dot{\Sigma}_\eta^\lambda(x'|x) = -\mathrm{i}\sum_{yy'} \gamma_\eta^\lambda(x'y'|xy) S_\eta^\lambda(y|y') \tag{2.61}$$

and

$$\begin{aligned}\dot{\gamma}_\eta^\lambda(x'y'|xy) = &-\mathrm{i}\sum_{aa'} \gamma_\eta^\lambda(x'y'a'|xya) S_\eta^\lambda(a|a') \\ &+\mathrm{i}\sum_{aa'bb'} \Big\{ \gamma_\eta^\lambda(x'y'|ab) S_\eta^\lambda(a|a') G_\eta^\lambda(b|b') \gamma_\eta^\lambda(a'b'|xy) \\ &\qquad + \gamma_\eta^\lambda(x'b'|ay)\big[S_\eta^\lambda(a|a')G_\eta^\lambda(b|b') + S_\eta^\lambda(b|b')G_\eta^\lambda(a|a')\big]\gamma_\eta^\lambda(a'y'|xb) \\ &\qquad - \gamma_\eta^\lambda(y'b'|ya)\big[S_\eta^\lambda(a|a')G_\eta^\lambda(b|b') + S_\eta^\lambda(b|b')G_\eta^\lambda(a|a')\big]\gamma_\eta^\lambda(a'x'|bx)\Big\}.\end{aligned} \tag{2.62}$$

Since the flow equation of the 1PI n-particle vertex function contains the 1PI $(n+1)$-particle vertex function, all of the flow equations are coupled. To find an approximate solution for a given model, we have to truncate this infinite hierarchy in some way. One possibility is to neglect the 1PI three-particle vertex function in Eq. (2.62). Because of Dyson's equation $G = 1/(g^{-1} - \Sigma)$, we would then be left with the task of solving a closed set of differential equations for the self-energy and for the 1PI two-particle vertex function.

2.11 Generalizations of the zero-temperature formalism

In this section we discuss how the zero-temperature formalism can be generalized with regard to the models and states that can be studied. We formulate these generalizations in the context of a general model of interacting fermions. We do not exhaust all possible ways to generalize the formalism. Instead, we focus on the generalizations that are relevant for the X-ray-edge model and the SIAM.

2.11.1 Infinite system size

We have discussed the zero-temperature formalism for the general Hamiltonian (2.1), in which the free part has a discrete single-particle spectrum with eigenenergies $\varepsilon_1 \leq \varepsilon_2 \leq \ldots$ But many specific models feature a continuous spectrum and an infinite number of particles. Here, we consider only continuous models that can be interpreted as describing the limit of a finite system for size approaching infinity. The zero-temperature formalism is applicable to the finite case, provided the noninteracting and interacting ground states are nondegenerate and not mutually orthogonal. The limit of infinite system size can then be thought of as the final step of any calculation. So these continuous models can be treated with the zero-temperature formalism.

This situation applies to the X-ray-edge model and the SIAM, see Secs. 3.2.1 and 4.2.2. We assume both models to feature electron bands with constant densities of states. These densities of states just approximate rather dense but discrete spectra because in any real-world application of these models the number of momentum eigenstates is finite.

To anticipate the eventual limit of infinite system size, we can slightly adapt the notation of the zero-temperature formalism. Instead of distinguishing $\alpha \leq N$ and $\alpha > N$, we then distinguish whether α is occupied or unoccupied in $|\Phi_0\rangle$. The gap between the occupied and unoccupied states can become infinitesimal. When appropriate, a sum over α can be replaced with an integral.

2.11.2 Common eigenstate of H_0 and H

Let us consider the case that we want to study the system in a common eigenstate of the noninteracting Hamiltonian H_0 and the full Hamiltonian H given in Eq. (2.1). We assume only that this state can be written in the form

$$\big|\tilde{\Phi}\big\rangle = a_{\tilde{1}}^\dagger \dots a_{\tilde{N}}^\dagger |0\rangle, \tag{2.63}$$

where $\tilde{1}, \dots, \tilde{N}$ enumerate some states of the chosen orthonormal single-particle eigenbasis of H_0. The zero-temperature formalism can be applied to this situation without further requirements. With respect to either Hamiltonian, $|\tilde{\Phi}\rangle$ can be a ground or excited state with a degenerate or nondegenerate eigenenergy. In particular, we do not require $\{\tilde{1}, \dots, \tilde{N}\} = \{1, \dots, N\}$.

In this case performing a damped time evolution as described in Sec. 2.3 is not necessary. In order to compute an arbitrary Green function of the system

$$\begin{aligned} &\tilde{G}(\alpha_1 t_1, \dots, \alpha_n t_n | \alpha_1' t_1', \dots, \alpha_n' t_n') \\ &= (-i)^n \big\langle \tilde{\Phi} \big| \mathcal{T} a_{\alpha_1}(t_1) \dots a_{\alpha_n}(t_n) a_{\alpha_n'}^\dagger(t_n') \dots a_{\alpha_1'}^\dagger(t_1') \big| \tilde{\Phi} \big\rangle, \end{aligned} \tag{2.64}$$

we define the generating functional without the damping η and without the limit $t_0 \to \infty$, cf. Eqs. (2.7) to (2.9),

$$\tilde{\mathcal{G}}[\bar{J}, J] = \frac{\tilde{Z}[\bar{J}, J]}{\tilde{Z}[0, 0]} \tag{2.65a}$$

$$\tilde{Z}[\bar{J}, J] = \big\langle \tilde{\Phi} \big| \tilde{U}_{\bar{J},J}(t_0, -t_0) \big| \tilde{\Phi} \big\rangle \tag{2.65b}$$

$$\tilde{U}_{\bar{J},J}(t_0, -t_0) = \mathcal{T} \exp\bigg(-\mathrm{i} \int_{-t_0}^{t_0} \mathrm{d}t \left\{ H + \sum_\alpha \left[\bar{J}_\alpha(t) a_\alpha + a_\alpha^\dagger J_\alpha(t) \right] \right\} \bigg). \tag{2.65c}$$

One can directly show that the Green function (2.64) can be generated from $\tilde{\mathcal{G}}[\bar{J}, J]$ via source derivatives analogously to Eq. (2.6). For this to work, the interval $[-t_0, t_0]$ has to contain all time arguments of the Green function which is satisfied by the choice $t_0 > \max\{|t_1|, \dots, |t_n|, |t_1'|, \dots, |t_n'|\}$.

The continuous functional-integral expression for the interacting generating functional and the diagrammatic rules for the Green functions can be derived in full analogy to Secs. 2.4 to 2.7. Instead of distinguishing $\alpha \leq N$ and $\alpha > N$, one now distinguishes whether $\alpha \in \{\tilde{1}, \dots, \tilde{N}\}$ or not. Throughout the entire derivation, no η appears. Since all time integrations have the finite boundaries $\pm t_0$, they converge and so the values of the diagrams are well-defined in time representation.

Only in connection with the frequency representation, we introduce dampings such that the free propagator $\tilde{g}_{\alpha\alpha'}(t, t')$ decays for large time differences. To this

end we insert a factor $e^{\pm\eta t}$ into $\tilde{g}_\alpha(t)$ for states α that are occupied or empty in $|\tilde{\Phi}\rangle$, respectively. Thanks to these convergence factors, the time integrations in diagrams are well-defined even in the limit $t_0 \to \infty$. The Fourier transformations of the Green functions and of the diagrammatic elements are then analogous to Sec. 2.8. In this case the frequency-dependent free propagator reads

$$\tilde{g}_{\alpha\alpha'}(\omega,\omega') = 2\pi\delta(\omega-\omega')\delta_{\alpha\alpha'}\tilde{g}_\alpha(\omega) \tag{2.66a}$$

$$\tilde{g}_\alpha(\omega) = e^{\mathrm{i}\omega\eta'}\begin{cases}(\omega-\varepsilon_\alpha+\mathrm{i}\eta)^{-1}, & \alpha\notin\{\tilde{1},\dots,\tilde{N}\}\\ (\omega-\varepsilon_\alpha-\mathrm{i}\eta)^{-1}, & \alpha\in\{\tilde{1},\dots,\tilde{N}\}\end{cases} \tag{2.66b}$$

and the expressions for the vertices are

$$\tilde{w}_{\alpha'\alpha}(\omega',\omega) = 2\pi\delta(\omega'-\omega)w_{\alpha'\alpha} \tag{2.67a}$$

$$\tilde{\bar{v}}_{\alpha_1'\alpha_2'\alpha_1\alpha_2}(\omega_1',\omega_2',\omega_1,\omega_2) = 2\pi\delta(\omega_1'+\omega_2'-\omega_1-\omega_2)\bar{v}_{\alpha_1'\alpha_2'\alpha_1\alpha_2}. \tag{2.67b}$$

2.11.3 Excited eigenstate of H (for particular vertex structures only)

Suppose we want to study the system in a given excited eigenstate $|\tilde{\Psi}\rangle$ of the full Hamiltonian H. In general the zero-temperature formalism cannot be applied to this situation. We show how the formalism can still be employed under certain conditions. In the X-ray-edge model, these conditions can be fulfilled to describe the case of X-ray emission.

We require that a state

$$\big|\tilde{\Phi}\big\rangle = a_{\tilde{1}}^\dagger\dots a_{\tilde{N}}^\dagger|0\rangle \tag{2.68}$$

exists such that $|\tilde{\Psi}\rangle$ is the lowest-energy eigenstate of H having a nonzero overlap with $|\tilde{\Phi}\rangle$ and that $|\tilde{\Psi}\rangle$ is unique in this respect. Here, $\tilde{1},\dots,\tilde{N}$ enumerate some states of the chosen orthonormal single-particle eigenbasis of H_0. So $|\tilde{\Phi}\rangle$ is necessarily an eigenstate of H_0, but it does not have to be the ground state, i.e. we do not require $\{\tilde{1},\dots,\tilde{N}\} = \{1,\dots,N\}$.

Analogously to Sec. 2.3, the Green functions of the system are defined as

$$\begin{aligned}&G(\alpha_1 t_1,\dots,\alpha_n t_n|\alpha_1' t_1',\dots,\alpha_n' t_n')\\ &= (-\mathrm{i})^n\big\langle\tilde{\Psi}\big|\mathcal{T}a_{\alpha_1}(t_1)\dots a_{\alpha_n}(t_n)a_{\alpha_n'}^\dagger(t_n')\dots a_{\alpha_1'}^\dagger(t_1')\big|\tilde{\Psi}\big\rangle\end{aligned} \tag{2.69}$$

and they can be obtained via source derivatives and via the limit $\eta\to 0^+$ from the generating functional

$$\tilde{\mathcal{G}}_\eta[\bar{J},J] = \lim_{t_0\to\infty}\frac{\tilde{Z}_\eta[\bar{J},J]}{\tilde{Z}_\eta[0,0]} \tag{2.70a}$$

$$\tilde{Z}_\eta[\bar{J},J] = \big\langle\tilde{\Phi}\big|U_{\bar{J},J}^{(\eta)}(t_0,-t_0)\big|\tilde{\Phi}\big\rangle \tag{2.70b}$$

$$U_{\bar{J},J}^{(\eta)}(t_0,-t_0) = \mathcal{T}\exp\!\left(-\mathrm{i}\int_{-t_0}^{t_0}\mathrm{d}t\left\{(1-\mathrm{i}\eta)H+\sum_\alpha\left[\bar{J}_\alpha(t)a_\alpha+a_\alpha^\dagger J_\alpha(t)\right]\right\}\right). \tag{2.70c}$$

The considerations in Sec. 2.3 about the damped time evolution still apply – one just has to replace $|\Psi_0\rangle$ and $|\Phi_0\rangle$ with $|\tilde{\Psi}\rangle$ and $|\tilde{\Phi}\rangle$, respectively. In fact, the requirement that $|\tilde{\Psi}\rangle$ is the unique lowest-energy eigenstate of H having a nonzero overlap with $|\tilde{\Phi}\rangle$ is necessary and sufficient for the damped time evolution to work as described. There are no additional requirements concerning the ground states of H_0 and H.

We can derive a continuous functional-integral representation of the interacting generating functional and diagrammatic rules for the Green functions in full analogy to Secs. 2.4 to 2.7. Here, we consider the version of the diagrammatic rules with an explicit single-particle vertex such that the propagator lines in diagrams are not dressed. Instead of distinguishing between $\alpha \leq N$ and $\alpha > N$, we now distinguish between whether $\alpha \in \{\tilde{1}, \ldots, \tilde{N}\}$ or not. In general, however, the values of the diagrams are not well-defined because the internal time integrations are not guaranteed to converge. The free propagator

$$\tilde{g}_{\alpha\alpha'}(t,t') = \delta_{\alpha\alpha'}\tilde{g}_\alpha(t-t') \tag{2.71a}$$

$$\tilde{g}_\alpha(t) = -\mathrm{i}e^{-(\mathrm{i}+\eta)\varepsilon_\alpha t}\begin{cases}\Theta(t-0^+), & \alpha \notin \{\tilde{1}, \ldots, \tilde{N}\} \\ -\Theta(-t+0^+), & \alpha \in \{\tilde{1}, \ldots, \tilde{N}\}\end{cases} \tag{2.71b}$$

diverges for single-particle states with $\varepsilon_\alpha < 0$ that are unoccupied in $|\tilde{\Phi}\rangle$ and for those with $\varepsilon_\alpha > 0$ that are occupied in $|\tilde{\Phi}\rangle$. We cannot avoid all these divergences by shifting the reference point for the single-particle energies unless $|\tilde{\Phi}\rangle$ happens to be the ground state of H_0. Anyway, the value of a diagram ultimately depends only on differences $\varepsilon_\alpha - \varepsilon_{\alpha'}$ and so choosing this reference point has no actual effect regarding the convergence of time integrations.

To better understand the issue of convergence for the time integrations in diagrams, let us consider an arbitrary diagram of a Green function and fix all appearing state indices α, i.e. we deal with a particular summand of the sum over all internal α-indices. Each propagator line then has a fixed direction of time. This allows us to identify vertices with a "locally minimal time", where only backward running propagators enter and only forward running propagators leave; vertices with a "locally maximal time" are defined the other way around. When calculating the value of the diagram, we choose to integrate over these times first. For example the integral for a single-particle vertex with a locally minimal time has the form

$$\int_{-\infty}^{\infty} \mathrm{d}\tilde{t}\, \tilde{g}_{\alpha'}(\tilde{t}-t')\tilde{g}_\alpha(t-\tilde{t}) = \int_{-\infty}^{\min\{t',t\}} \mathrm{d}\tilde{t}\, e^{-(\mathrm{i}+\eta)\varepsilon_{\alpha'}(\tilde{t}-t')}\, e^{-(\mathrm{i}+\eta)\varepsilon_\alpha(t-\tilde{t})} \tag{2.72a}$$

$$\propto e^{-(\mathrm{i}+\eta)\varepsilon_{\alpha'}(\min\{t',t\}-t')}\, e^{-(\mathrm{i}+\eta)\varepsilon_\alpha(t-\min\{t',t\})}, \tag{2.72b}$$

where $\alpha^{(\prime)}$ refers to a state that is unoccupied (occupied) in $|\tilde{\Phi}\rangle$ and $\varepsilon_{\alpha'} < \varepsilon_\alpha$ is necessary and sufficient for convergence. Similarly, the integral for a two-particle

vertex with a locally maximal time has the form

$$\begin{aligned}
&\int_{-\infty}^{\infty} \mathrm{d}\tilde{t}\, \tilde{g}_{\alpha_1'}(\tilde{t}-t_1')\tilde{g}_{\alpha_2'}(\tilde{t}-t_2')\tilde{g}_{\alpha_1}(t_1-\tilde{t})\tilde{g}_{\alpha_2}(t_2-\tilde{t}) \\
&= \int_{t_\mathrm{max}}^{\infty} \mathrm{d}\tilde{t}\, e^{-(\mathrm{i}+\eta)\varepsilon_{\alpha_1'}(\tilde{t}-t_1')}\, e^{-(\mathrm{i}+\eta)\varepsilon_{\alpha_2'}(\tilde{t}-t_2')}\, e^{-(\mathrm{i}+\eta)\varepsilon_{\alpha_1}(t_1-\tilde{t})}\, e^{-(\mathrm{i}+\eta)\varepsilon_{\alpha_2}(t_2-\tilde{t})} \qquad (2.73a) \\
&\propto e^{-(\mathrm{i}+\eta)\varepsilon_{\alpha_1'}(t_\mathrm{max}-t_1')}\, e^{-(\mathrm{i}+\eta)\varepsilon_{\alpha_2'}(t_\mathrm{max}-t_2')}\, e^{-(\mathrm{i}+\eta)\varepsilon_{\alpha_1}(t_1-t_\mathrm{max})}\, e^{-(\mathrm{i}+\eta)\varepsilon_{\alpha_2}(t_2-t_\mathrm{max})}, \qquad (2.73b)
\end{aligned}$$

where t_max stands for $\max\{t_1', t_2', t_1, t_2\}$, $\alpha_1^{(\prime)}$ and $\alpha_2^{(\prime)}$ refer to states that are occupied (unoccupied) in $|\tilde{\Phi}\rangle$, and $\varepsilon_{\alpha_1} + \varepsilon_{\alpha_2} < \varepsilon_{\alpha_1'} + \varepsilon_{\alpha_2'}$ is necessary and sufficient for convergence. The results are always products of factors $e^{-(\mathrm{i}+\eta)\varepsilon_\alpha t}$ that mimic the time dependence of the free propagator (2.71b): $\alpha \notin \{\tilde{1}, \ldots, \tilde{N}\}$ implies $t \geq 0$, whereas $\alpha \in \{\tilde{1}, \ldots, \tilde{N}\}$ implies $t \leq 0$. Subsequently, we can again identify locally minimal and maximal times and we continue to integrate over them until there are only integrals left that are bounded by the external times of the Green function. The latter integrals obviously converge. All other integrals, i.e. the ones over locally minimal or maximal times, are essentially analogous to the examples (2.72) and (2.73). But they can assume the form of integrals for effective n-particle vertices with $n = 1, 2, \ldots$ because of the results of previous time integrations. For each of these effective n-particle vertices with a locally minimal or maximal time, the respective integral converges if and only if the sum of the appearing ε_α with $\alpha \in \{\tilde{1}, \ldots, \tilde{N}\}$ is less than the sum of the appearing ε_α with $\alpha \notin \{\tilde{1}, \ldots, \tilde{N}\}$. This would be fulfilled if $|\tilde{\Phi}\rangle$ was the ground state of H_0 and if that ground state was nondegenerate. But in general the convergence is not guaranteed.

In the following we formulate the condition for the convergence of time integrations in more intuitive terms. We still consider an arbitrary diagram of a Green function, which essentially represents a contribution to a time-ordered expectation value $\langle\tilde{\Phi}|\ldots|\tilde{\Phi}\rangle$ of ladder operators $a_\alpha^{(\dagger)}(t)_{H_0}$ with integration over the internal times and summation over the internal α-indices. Note that the Heisenberg picture is with respect to the free Hamiltonian at this stage because one has already expanded in the single-particle and two-particle perturbation. As we did above, we fix all α-indices in the diagram, thereby fixing the time direction of the lines and ordering the times of the vertices and external points. Between each consecutive pair of these times, we can identify an intermediate state of the system. Such a state is always an eigenstate of H_0 because it results from acting with all ladder operators at greater times to the left on $\langle\tilde{\Phi}|$ or, equivalently, from acting with all ladder operators at smaller times to the right on $|\tilde{\Phi}\rangle$.

We revisit the example of a two-particle vertex with a locally maximal time $\tilde{t}$, which has been discussed in Eq. (2.73). For simplicity we here assume $\tilde{t}$ to even be the globally maximal time. Then the expectation value, which the diagram contributes

to, has the form

$$\begin{aligned}&\int \mathrm{d}\tilde{t}\,\big\langle\tilde{\Phi}\big|a^\dagger_{\alpha_1}(\tilde{t})_{H_0}a^\dagger_{\alpha_2}(\tilde{t})_{H_0}a_{\alpha'_1}(\tilde{t})_{H_0}a_{\alpha'_2}(\tilde{t})_{H_0}\overset{\downarrow}{\ldots}\big|\tilde{\Phi}\big\rangle\\ &=\int \mathrm{d}\tilde{t}\,e^{-(\mathrm{i}+\eta)(\varepsilon_{\alpha'_1}+\varepsilon_{\alpha'_2}-\varepsilon_{\alpha_1}-\varepsilon_{\alpha_2})\tilde{t}}\,\big\langle\tilde{\Phi}\big|a^\dagger_{\alpha_1}a^\dagger_{\alpha_2}a_{\alpha'_1}a_{\alpha'_2}\overset{\downarrow}{\ldots}\big|\tilde{\Phi}\big\rangle. \qquad (2.74)\end{aligned}$$

At the position indicated by the arrow, the system is in the intermediate state $|\tilde{\Phi}'\rangle = a^\dagger_{\alpha'_2}a^\dagger_{\alpha'_1}a_{\alpha_2}a_{\alpha_1}|\tilde{\Phi}\rangle$. Requiring that the $\tilde{t}$-integral converges is equivalent to requiring that $|\tilde{\Phi}\rangle$ is energetically favored over $|\tilde{\Phi}'\rangle$. In both cases the necessary and sufficient condition is $\varepsilon_{\alpha_1}+\varepsilon_{\alpha_2} < \varepsilon_{\alpha'_1}+\varepsilon_{\alpha'_2}$.

This argument works analogously for all effective n-particle vertices with locally minimal or maximal times. For the diagrammatic expansion to be well-defined, $|\tilde{\Phi}\rangle$ must be energetically favored over all intermediate states that can occur at times beyond the external times. Put in other words, we require the vertex structure to be such that clusters of vertices can realize neither a relaxation of $|\tilde{\Phi}\rangle$ at infinite negative times nor a re-excitation to $|\tilde{\Phi}\rangle$ at infinite positive times. Even intermediate states with the same energy as $|\tilde{\Phi}\rangle$ must be avoided at infinite times.

Now, we describe a special case that satisfies the above requirement on the vertex structure; it is relevant to the emission case in the X-ray-edge model. We define a set M_1 of state indices $\alpha \notin \{\tilde{1},\ldots,\tilde{N}\}$ such that a line with $\alpha \in M_1$ can be connected via single-particle vertices only to other lines with respective $\alpha \in M_1$. The resulting sequences of lines and single-particle vertices run only forward in time. They cannot form closed loops; otherwise a diagram would immediately evaluate to zero. Even Hartree-Fock-type loops of forward running lines are impossible because the respective equal-time value of the free propagator vanishes. First, we assume that each two-particle vertex has at least one incoming and one outgoing leg with a respective index $\alpha \in M_1$. As a consequence the times of all two-particle vertices are bounded by the times of the external points. Second, we assume that the structure of the single-particle vertex is such that for any pair of indices $\alpha \in \{\tilde{1},\ldots,\tilde{N}\}$ and $\alpha' \notin \{\tilde{1},\ldots,\tilde{N}\}$ appearing anywhere along the same sequence of lines and single-particle vertices, the condition $\varepsilon_\alpha < \varepsilon_{\alpha'}$ is fulfilled. This guarantees convergence when we successively integrate over all locally minimal or maximal times, which can appear only at single-particle vertices. All remaining integrals are bounded by the external times and thus trivially converge. In total the values of diagrams are well-defined.

In the reverse case, these considerations work analogously. We define a set M_2 of state indices $\alpha \in \{\tilde{1},\ldots,\tilde{N}\}$ such that lines with $\alpha \in M_2$ can be connected via single-particle vertices only to other lines with respective $\alpha \in M_2$ and we assume that each two-particle vertex has at least one incoming and one outgoing leg with a respective index $\alpha \in M_2$. The resulting sequences of lines and single-particle vertices run only backward in time and connect the two-particle vertices to the external points, restricting the respective time integrations. However, the time of a two-particle vertex can also be unrestricted if its legs with $\alpha \in M_2$ are directly connected. This is possible because the equal-time value of the free propagator is nonzero in this case. We successively integrate over all locally minimal or maximal times, which can appear

at these two-particle vertices with Hartree-Fock loops as well as at the single-particle vertices. To guarantee convergence we assume that the condition $\varepsilon_\alpha < \varepsilon_{\alpha'}$ is fulfilled for any pair of indices $\alpha \in \{\tilde{1}, \ldots, \tilde{N}\}$ and $\alpha' \notin \{\tilde{1}, \ldots, \tilde{N}\}$ appearing anywhere along the same sequence of lines, single-particle vertices, and two-particle vertices with Hartree-Fock loops; the indices in the loops themselves are not subject to this condition. All remaining integrals converge too because they are bounded by the external times. The values of diagrams are thus well-defined also in this case.

2.12 Conclusion

The zero-temperature formalism is tailored to interacting fermionic systems in their ground states and allows to set up a diagrammatic perturbation theory. The Green functions of a system are thereby expanded in powers of the interaction and contributions of different orders are represented by diagrams. These diagrams are constructed and evaluated according to specific rules. In this chapter, we have formulated the diagrammatic rules for a general model of interacting fermions that features a single-particle perturbation as well as a two-particle interaction. We have either absorbed the former into the propagator lines or expressed it as a single-particle vertex.

While our discussion of the zero-temperature formalism was based on Ref. [NO88], we used standard coherent states instead of those corresponding to particle-hole operators and derived a functional-integral representation of the generating functional of the Green functions not only in the noninteracting but also in the interacting case. We could then perform the standard derivation of the FRG, in full analogy to the Matsubara and Keldysh cases, see Refs. [Met+12] and [GPM07, Jak19]: the flow equations of the various generating functionals were determined and subsequently used to obtain the flow equations of the 1PI vertex functions. In total we have comprehensively set up the FRG framework in the zero-temperature formalism for a general model of interacting fermions.

In its original form, the formalism is used for systems at vanishing temperature and requires that the interacting and noninteracting ground states are nondegenerate and not mutually orthogonal. We have presented generalizations that loosen these requirements or describe how the formalism can be adapted to other specific situations. For example in some cases a system can be studied in an excited eigenstate. We have focused on those generalizations that we need to treat the X-ray-edge model and the SIAM. Likely, others are possible and the applicability of the zero-temperature formalism can be extended further.

For any concrete FRG approach to a specific model, the following steps remain to be done. The dependence of the free propagator on the flow parameter has to be specified. There is a significant freedom of choice involved, but the initial value of the flow parameter has to correspond to a simplified system and the final value to the actual system. The initial values of the 1PI vertex functions have to be calculated, at least approximately. The infinite hierarchy of flow equations has to be truncated to become a closed set of differential equations. Approximations can also target other aspects of the flow equations. The approximated flow equations have to be solved, yielding the final values of the remaining 1PI vertex functions. Finally, the Green

functions have to be reconstructed from the 1PI vertex functions, in principle giving access to any observable expectation value. In Chap. 3 these steps are performed for the X-ray-edge model and in Chap. 4 we prepare a zero-temperature FRG approach to the SIAM.

The zero-temperature formalism is more restricted in its applicability than the Matsubara and Keldysh formalisms. But since it uses real times and frequencies on a simple contour, no analytic continuation is needed like in the Matsubara formalism and the Green functions do not have multiple components like in the Keldysh formalism. Choosing the zero-temperature formalism can through its simplicity facilitate analytic insights or save computational cost in numerical studies. The Matsubara FRG and Keldysh FRG have proven to be successful tools for the study of condensed-matter systems of interacting fermions. We hope that the zero-temperature FRG will, beyond the scope of this thesis, be found useful as well.

Chapter 3

Treatment of the X-ray-edge model

3.1 Introduction

When a material is exposed to X-rays, its electrons can be excited through the absorption of photons. The discrete energy levels of an atom or molecule allow only for specific transitions and thus lead to a characteristic absorption spectrum. In bulk metals, where the discrete levels form energy bands, the X-ray-absorption spectrum exhibits features that cannot be attributed to the individual atoms. Some singularities occur at vanishing temperature and correspond to transitions involving the conduction band.

The X-ray-edge model is used to study this type of singularity. It describes a basic metal with a conduction band and just one lower-energy band. The latter is flat and is represented by a single so-called deep state. Since, additionally, only the interband Coulomb interaction is considered explicitly, the interacting region is zero-dimensional. The electron spin is neglected. The X-ray-absorption rate is studied as a function of the frequency of an external X-ray field that induces interband transitions. If the system is prepared in its ground state, a threshold frequency exists at which the absorption rate exhibits a power-law divergence with an exponent that depends on the interaction. This power-law behavior was conjectured by Mahan [Mah67] and confirmed by Nozières and collaborators [RGN69, ND69].

Let us briefly mention that X-ray emission can be studied as well, namely if the system is prepared with an empty deep state. But we study only X-ray absorption because the calculations turn out to be analogous within the considered approximations [RGN69], see also Sec. 2.11.3 for the necessary generalization of the zero-temperature formalism.

The interaction in the X-ray-edge model does not alter the deep-state occupancy and either vanishes or constitutes a mere scattering potential for the conduction electrons, depending on whether the deep state is occupied or empty. Even though the exact solution is therefore accessible via a one-body scattering approach [ND69], studying the X-ray-edge model with many-body approaches is instructive. The power-law divergence of the X-ray-absorption rate causes logarithmic divergences to appear in arbitrarily high orders of perturbation theory. Logarithms arise in two of the two-particle channels: the exchange particle-hole bubble and the particle-particle

bubble each give one logarithm. The leading logarithms of the 1PI two-particle vertex function are contained in the parquet diagrams that result from crossing these channels [RGN69]. Being spinless and effectively zero-dimensional, the X-ray-edge model is as simple a model as possible that has such an interesting logarithmic structure.

Aside from the exact solution [ND69], Nozières and his collaborators performed the leading-logarithmic parquet approximation [RGN69] and even investigated the subleading logarithms [NGR69]. Lange et al. studied the X-ray-edge model with the FRG [Lan+15]. Using multi-channel Hubbard-Stratonovich transformations, i.e. introducing bosonic fields that mediate the interaction between the fermions, they reproduced the leading-logarithmic result for the particle-hole susceptibility from which the X-ray-absorption rate is calculated. Kugler and von Delft achieved the same by treating the particle-hole susceptibility as a photon self-energy [KD18c]. They compared in detail the work of Lange et al. to their own: After some technical inaccuracies of Ref. [Lan+15] have been corrected, these two approaches arrive at the exact same flow equations for a bosonic self-energy and a 1PI three-point vertex; the flow of the other 1PI vertices has been neglected. These flow equations generate only ladder diagrams but assign different weights that make up for the missing parquet diagrams. (Compared to the parquet diagrams of the 1PI two-particle vertex, the parquet diagrams of the particle-hole susceptibility have an extra bubble and a three-point vertex at either side, see Fig. 3.1.) Since this is possible only because of approximate proportionality relations between diagrams in the X-ray-edge model, Kugler and von Delft concluded that the successful reproduction of the leading-logarithmic result by these low-order FRG approaches is fortuitous [KD18c].

Kugler and von Delft then developed in a purely fermionic framework the multiloop FRG, with which they successively increased the loop order [KD18a]. After reaching convergence their approach amounts to an exact resummation of the parquet diagrams that contain the leading logarithms. Kugler and von Delft reported strong numerical deviations between the results from their one-loop FRG and the converged results from multiloop FRG [KD18a]. So they concluded that the multiloop extension is needed to reproduce parquet results, referring to the exact sum of the parquet diagrams obtained from numerically solving the parquet equations. But the exact sum of the parquet diagrams does not improve the regime of reliability and is in this sense not better than the leading-logarithmic parquet approximation [NGR69]. The question arises whether a one-loop FRG is less accurate than the leading-logarithmic parquet approximation. This would contradict the conventional understanding of a one-loop approximation as one which correctly treats the leading logarithmic terms in the perturbation series of the 1PI two-particle vertex [Kat09].

In this chapter we devise an FRG approach to the X-ray-edge model with a one-loop truncation, i.e. neglecting the influence of the three-particle vertex entirely, and design it to be as similar as possible to the parquet-based approach of Roulet et al. [RGN69]. For instance we too choose the zero-temperature formalism for the underlying diagrammatic perturbation theory. We perform exact calculations for key example diagrams to show how the leading logarithms arise and we recap the approximations made in Ref. [RGN69]. When presenting our FRG approach, we

relate the individual approximation steps to those of the leading-logarithmic parquet approximation.

Our approach reproduces the leading-logarithmic result of Ref. [RGN69], so it captures the leading logarithms. On top of that, we show that this one-loop FRG approach is fully equivalent to the leading-logarithmic parquet approximation on a detailed level. Even the introduction of the flow parameter has an equivalent. Just the order of the steps differs.

For the entire class of systems for which the X-ray-edge model is prototypical, the multiloop extension is not expected to be helpful for the reproduction of results from the leading-logarithmic parquet approximation. In the context of logarithmic divergences in perturbation theory, we expect the multiloop FRG to be useful rather for the class of mostly two-dimensional systems where the logarithmic structure is more complicated and a controlled accuracy is usually not pursued. So the expected field of application of the multiloop FRG coincides with that of the full parquet approximation, which typically includes all channels, uses a self-consistently dressed propagator, and calculates the exact sum of the resulting parquet diagrams [Bic91].

Reasons for choosing the full parquet approximation are e.g. that it has no bias for the different two-particle channels, respects crossing symmetry [Bic91, VT97], and fulfills one-particle conservation laws [KD18d]. Also, it should satisfy the Mermin-Wagner theorem [BS92, VT97]. One can extend the full parquet approximation by using an approximation for the totally irreducible vertex other than the bare vertex. The dynamical vertex approximation [TKH07], for instance, uses the local totally irreducible vertex obtained from an impurity solver when studying the Hubbard model. Through the parquet equations, it includes long-range correlations and constitutes a systematic improvement over dynamical mean-field theory [TKH07, Roh+18].

With the multiloop FRG, the full parquet approximation or extensions thereof can be performed by way of solving flow equations. Kugler and von Delft have formulated the multiloop FRG for general models, using free propagators or self-consistently dressed propagators and using nontrivial approximations of the totally irreducible vertex [KD18b, KD18d]. The multiloop FRG has been applied to the two-dimensional Hubbard model [Tag+19, Hil+20b, Hil+20a] and to the two- and three-dimensional Heisenberg model in a pseudo-fermion representation [Tho+20, Kie+22]. In both cases the multiloop scheme is viewed as an improvement for the FRG. In the presence of pseudo-fermion propagators, the numerical implementation is more feasible than a direct iterative solution of the parquet equations [Tho+20].

To a large extent, the contents of this chapter have been published in Ref. [DJ21]. I assure that I am the original author of the many passages with identical wording.

3.2 The X-ray-edge model

In this section we briefly introduce the X-ray-edge model, which is a basic model that describes the X-ray-absorption singularity in metals. It is essentially taken from Ref. [RGN69], where more details can be found.

3.2.1 Hamiltonian

The model comprises two electronic bands: the conduction band and some lower-energy band. The latter is assumed to be flat as it typically originates from atomic orbitals that are more localized. As such it can be represented by a single so-called deep state. The effect of the intraband Coulomb interaction, which leads to long-lasting quasi-particle states, is assumed to be already accounted for by effective single-particle parameters. The interaction that is considered explicitly is an attractive one between the conduction electrons and a hole at the deep state. The electron spin is neglected. This physical model is described by the Hamiltonian

$$H = \sum_k \varepsilon_k a_k^\dagger a_k + \varepsilon_d a_d^\dagger a_d - \frac{U}{V} \sum_{kk'} a_{k'}^\dagger a_k a_d a_d^\dagger. \tag{3.1}$$

Here, $a_d^\dagger$ creates an electron in the deep state and $a_k^\dagger$ creates an electron with momentum k and energy ε_k in the conduction band, which shall have a constant density of states ρ and a bandwidth $2\xi_0$. We set the zero of single-particle energy in the middle of the conduction band such that $\varepsilon_k \in [-\xi_0, \xi_0]$. Then the deep-state eigenenergy is $\varepsilon_d < -\xi_0$. The interaction amplitude $U > 0$ is assumed to be momentum independent and thus describes a local interaction in real space. V denotes the volume. We study the system at vanishing temperature $T = 0$ and with a half-filled conduction band, i.e. the Fermi energy is $\varepsilon_F = 0$. In the resulting ground state, the deep level is occupied as long as the interaction strength is not too large.

3.2.2 X-ray-absorption rate and the particle-hole susceptibility $\chi(\nu)$

As an external perturbation, an X-ray field with frequency ν is coupled to the system with momentum-independent amplitude W,

$$H_X(t) = \frac{W}{\sqrt{V}} \sum_k e^{-\mathrm{i}\nu t} a_k^\dagger a_d + \text{H.c.} \tag{3.2}$$

$H_X(t)$ is chosen to describe only interband transitions because these are, in conjunction with the sharp Fermi surface and the flat lower band, responsible for the absorption singularity. Correspondingly, we consider the X-ray frequency to be of the order of $|\varepsilon_d|$.

A physical observable of interest is the X-ray-absorption rate $R(\nu)$ or, equivalently, the excitation rate of the deep state. When ν approaches the threshold frequency ν_c, the leading behavior of $R(\nu)$ is a power-law divergence $\propto [\xi_0/(\nu - \nu_c)]^{2g}$ with $g = \rho U/V$. This was conjectured by Mahan [Mah67] based on the terms up to third order of an expansion in powers of the interaction and later confirmed by Nozières and collaborators [RGN69, ND69]. In linear response and for sufficiently small $|W|^2/V$, the absorption rate can be accessed with many-body techniques via $R(\nu) = -2|W|^2 \operatorname{Im} \chi(\nu)$, where

$$\chi(\nu) = -\mathrm{i} \frac{1}{V} \sum_{kk'} \int_{-\infty}^{\infty} \mathrm{d}t \, e^{\mathrm{i}\nu t} \langle \mathcal{T} a_d^\dagger(t) a_k(t) a_{k'}^\dagger(0) a_d(0) \rangle \tag{3.3}$$

is a particle-hole susceptibility. Here, $\langle . \rangle$ denotes the ground-state expectation value, $a^{(\dagger)}_{k/d}(t)$ are the ladder operators in the Heisenberg picture with respect to the Hamiltonian (3.1), and $\mathcal{T}$ is the time-ordering operator.

A diagrammatic expansion of χ results in a power series in U/V. Effectively, however, one obtains an expansion in powers of the dimensionless parameter $g = \rho U/V$ because for every additional interaction vertex in a diagram there is also one more independent momentum summation $\sum_k = \rho \int_{-\xi_0}^{\xi_0} \mathrm{d}\varepsilon$.

3.2.3 Significance of the model

We note that a many-body approach is not necessary to treat this model. In fact, it has been solved exactly with a one-body scattering theory [ND69]. This is possible because the particular interaction term in Eq. (3.1) does not alter the deep-state occupancy and acts just as a single-particle potential for the conduction states when the deep level is empty. However, if one chooses to treat this model with many-body perturbation theory, one encounters the interesting problem of logarithmic divergences in two distinct channels, see also Sec. 3.4.1. Being spinless and effectively zero-dimensional, it is probably the most basic model with this important feature. Therefore, it was repeatedly used as a test bed to refine and compare various many-body approaches [RGN69, NGR69, Sól74, Lan+15, KD18a]. Having an exact solution for comparison was then an additional advantage of this model.

3.3 Diagrammatic perturbation theory

In this section we recap the most important features of a perturbative approach to the X-ray-edge model. Following largely Roulet et al. [RGN69], we choose the zero-temperature formalism as framework for the diagrammatic expansion, see Chap. 2. Our one-loop FRG approach developed in Sec. 3.5 is also formulated in the realm of this formalism. This makes a detailed comparison between the parquet-based approach of Ref. [RGN69] and the one-loop FRG approach possible.

3.3.1 Applying the zero-temperature formalism

In the following we map the X-ray-edge model to the general model discussed in Chap. 2 and conclude that the requirements to use the zero-temperature formalism are fulfilled. We rewrite the Hamiltonian (3.1) of the X-ray-edge model in two respects. First, we move the deep-state creation operator in the interaction to the left, producing a single-particle term for the conduction states in the process. Second, we add and subtract a term $g\xi_0 a_d^\dagger a_d$. This step will be motivated in the next paragraph. Using the same notation as for the general Hamiltonian (2.1), we define the noninteracting and interacting parts as follows,

$$H = \underbrace{\sum_k \varepsilon_k a_k^\dagger a_k + (\varepsilon_d + g\xi_0) a_d^\dagger a_d}_{H_0} \underbrace{- \frac{U}{V} \sum_{kk'} a_{k'}^\dagger a_k - g\xi_0 a_d^\dagger a_d}_{H_{\mathrm{int}}^{(1)}} + \underbrace{\frac{U}{V} \sum_{kk'} a_d^\dagger a_{k'}^\dagger a_k a_d}_{H_{\mathrm{int}}^{(2)}}. \quad (3.4)$$

In this case the single-particle perturbation has the amplitude

$$w_{\alpha'\alpha} = -\frac{U}{V}\delta_{\alpha' c}\delta_{\alpha c} - g\xi_0\delta_{\alpha' d}\delta_{\alpha d}, \tag{3.5}$$

where a Kronecker delta $\delta_{\alpha c}$ restricts the index α to refer to a conduction state but does not restrict the momentum thereof. The two-particle interaction is characterized by the antisymmetric amplitude

$$\begin{aligned}\bar{v}_{\alpha'_1\alpha'_2\alpha_1\alpha_2} = \frac{U}{V}\big(&\delta_{\alpha'_1 d}\,\delta_{\alpha'_2 c}\,\delta_{\alpha_1 d}\,\delta_{\alpha_2 c} - \delta_{\alpha'_1 c}\,\delta_{\alpha'_2 d}\,\delta_{\alpha_1 d}\,\delta_{\alpha_2 c}\\ &- \delta_{\alpha'_1 d}\,\delta_{\alpha'_2 c}\,\delta_{\alpha_1 c}\,\delta_{\alpha_2 d} + \delta_{\alpha'_1 c}\,\delta_{\alpha'_2 d}\,\delta_{\alpha_1 c}\,\delta_{\alpha_2 d}\big).\end{aligned} \tag{3.6}$$

We have chosen to let the term $+g\xi_0 a_d^\dagger a_d$ renormalize the deep level to

$$\tilde{\varepsilon}_d = \varepsilon_d + g\xi_0 \tag{3.7}$$

and to treat the term $-g\xi_0 a_d^\dagger a_d$ as a single-particle perturbation. This renormalized deep level will replace ε_d as the position of the logarithmic divergences in individual diagrams. It provides a better estimate for the threshold frequency of the X-ray-absorption singularity [RGN69]. By design the deep-state single-particle perturbation will cancel out with the deep-state Hartree diagram. This procedure incorporates the deep-state Hartree diagram into the free propagator. It is the technical basis allowing us to introduce the cutoff around $\tilde{\varepsilon}_d$ in our FRG approach, see Sec. 3.5.1.

The free propagator has acquired an implicit dependence on the interaction strength. This implicit dependence will be ignored in the nomenclature of diagrams: we will classify each diagram as a contribution of a specific order that refers only to the number of vertices.

As the density of states is constant inside the conduction band, the free Hamiltonian features a spectrum with a continuous part and the number of its momentum eigenstates is infinite. This does not hinder the application of the zero-temperature formalism, see Sec. 2.11.1.

We study the system in the state

$$|\Phi\rangle = a_d^\dagger\left(\prod_{k\,\text{with}\,\varepsilon_k<0} a_k^\dagger\right)|0\rangle, \tag{3.8}$$

where the deep level and the lower half of the conduction band are occupied. Since this is a common eigenstate of H_0 and H, the requirements for the slightly adapted version of the zero-temperature formalism presented in Sec. 2.11.2 are fulfilled. As we explained there in detail, we do not perform a damped time evolution and introduce the infinitesimal η only in the context of the frequency representation. In contrast to Sec. 2.11.2, we drop the tildes.

We note that if $\tilde{\varepsilon}_d < 0$ and if the interaction strength U is not too large, the standard requirements for the zero-temperature formalism are fulfilled as well: the ground state of H_0 is nondegenerate, the system is studied in the nondegenerate ground state of H, and these two states are not mutually orthogonal. In fact, they

are identical and given by Eq. (3.8). This is the case for the X-ray-edge model as we introduced it in Sec. 3.2.1. However, as a mathematical trick, we will later set $\tilde{\varepsilon}_d$ to zero. We will then still study the system in the state $|\Phi\rangle$ even though it may not be the ground state of either Hamiltonian anymore. Since $|\Phi\rangle$ will remain a common eigenstate of H_0 and H, the zero-temperature formalism will still be applicable. In Ref. [RGN69] this shift of the deep level is performed too, but its impact on the requirements of the formalism is not discussed.

3.3.2 Customizing the diagrammatic rules

In this section we formulate efficient diagrammatic rules specific to the X-ray-edge model. Our starting point is the set of rules given in Sec. 2.7.3, which applies to Green functions of the general model and features an explicit single-particle vertex. For the diagrammatic elements, we use the frequency representation, see Sec. 2.8. As the X-ray-absorption rate is primarily determined from the 1PI two-particle vertex function, see Ref. [RGN69] and our Secs. 3.2.2 and 3.3.3, we directly discuss the diagrammatic rules for the 1PI vertex functions. These rules are analogous to those for the Green functions but have (amputated) external legs instead of external points, allow only one-particle irreducible diagrams, and feature an additional prefactor i^{1-n} for an n-particle function.

In the following we customize the diagrammatic rules in several ways. The lines and vertices contain many delta functions and Kronecker deltas, which allow us to reduce the number of integrals and sums per diagram. We choose to visually distinguish deep-state propagators from conduction-state propagators and absorb the momentum sums into the latter. The Hartree diagrams and the single-particle vertices cancel out.

The free propagator is given by

$$g_{\alpha\alpha'}(\omega,\omega') = 2\pi\delta(\omega-\omega')\delta_{\alpha\alpha'}g_\alpha(\omega) \tag{3.9a}$$

$$g_d(\omega) = \frac{e^{\mathrm{i}\omega\eta'}}{\omega-\tilde{\varepsilon}_d-\mathrm{i}\eta} \tag{3.9b}$$

$$g_k(\omega) = \frac{e^{\mathrm{i}\omega\eta'}}{\omega-\varepsilon_k+\mathrm{i}\eta\,\mathrm{sgn}\,\varepsilon_k}. \tag{3.9c}$$

In the deep-state subspace, it is analytic in the lower half plane and thus purely advanced. This implies that loops of two or more free deep-state propagators evaluate to zero. In time representation it is directed backward in time. The same holds for the full deep-state propagator, which takes the form

$$G_d(t,t') = -\mathrm{i}\left\langle\Phi\middle|\mathcal{T}a_d(t)a_d^\dagger(t')\middle|\Phi\right\rangle = \mathrm{i}\Theta(t'-t)\left\langle\Phi\middle|a_d^\dagger a_d(t-t')\middle|\Phi\right\rangle. \tag{3.10}$$

This expression can be interpreted as creating and subsequently annihilating a hole at the deep-state.

The free propagator (3.9) is diagonal in its frequency arguments and state indices. This causes half of the integrals and sums in diagrams to collapse immediately. From now on we shall assign only a single frequency ω and a single state index α to each line, which then represents a factor $g_\alpha(\omega)$.

The above step has exploited the frequency conservation of lines so diagrams presently involve a single frequency integration $\int \mathrm{d}\omega/(2\pi)$ for each line. Now we exploit the frequency conservation of vertices. Each vertex contains a factor $2\pi\delta(\ldots)$ guaranteeing that the sum of the outgoing frequencies equals the sum of the incoming frequencies. Many of the frequency integrations collapse over these delta functions, always leading to a factor $2\pi\delta(\omega_1' + \ldots + \omega_n' - \omega_1 - \ldots - \omega_n)$ that ensures overall frequency conservation for the 1PI vertex functions.

In a given diagram, we choose a set of independent internal and external frequencies. Respecting frequency conservation at each vertex, we express all other frequencies as linear combinations of these independent ones. The frequency at each line and external leg shall be written explicitly in the diagram. Vertices shall not contain the factors $2\pi\delta(\ldots)$ anymore. Only the independent internal frequencies shall be integrated over. The value of the diagram is then a function of the chosen independent external frequencies. The overall frequency conservation regarding the external legs is explicitly fulfilled. The value of a 1PI vertex function is given by $2\pi\delta(\omega_1' + \ldots + \omega_n' - \omega_1 - \ldots - \omega_n)$ times the sum of all diagrams.

Let each state index of a 1PI vertex function be specified such that it refers either to the deep state or to a conduction state and consider an arbitrary contributing diagram, which we will refer to as the old diagram. We shall visualize all state indices by drawing dashed lines for the deep-state and full lines for the conduction states. The old diagram is thereby replaced by multiple diagrams corresponding to the various possibilities in its internal sums. But often the stroke style of a line is fixed by the external legs and properties of the vertices: the single-particle vertex conserves the stroke style and the two-particle vertex has one incoming and one outgoing dashed line and one incoming and one outgoing full line.

The number of diagrams can be further reduced in two cases. If the old diagram involves a pair of equivalent lines, it contains a prefactor $1/2$ and its internal sums decompose into two equal-valued parts differing in which of the two lines represents a deep-state propagator and which one represents a conduction-state propagator. By using dashed and full lines, we initially represent the two possibilities by two diagrams that can be deformed to coincide completely. We shall draw only one of these diagrams and define its value without the prefactor $1/2$. If the old diagram is symmetric under permutations of the vertices, it contains a prefactor $1/S$ and its internal sums decompose into S equal-valued parts. When using dashed and full lines, we shall draw only one of the possible diagrams and define its value without the prefactor $1/S$. In summary we draw only distinct diagrams with dashed and full lines. Their values are analogous to the value of the old diagram but no prefactors $1/2^{n_{\mathrm{eq}}}$ and $1/S$ appear.

The vertices do not actually depend on the momenta of conduction states, see Eqs. (3.5) and (3.6), so the momentum summations in diagrams are independent and can be precalculated. We absorb each momentum summation into the respective conduction-state line and we additionally absorb a factor $1/V$ to achieve the form of a Fourier transform. Thus, a full line shall represent the local conduction-electron

propagator

$$g_c(\omega) = \frac{1}{V}\sum_k g_k(\omega) \tag{3.11a}$$

$$= \frac{1}{V}\sum_k \frac{e^{\mathrm{i}\omega\eta'}}{\omega - \varepsilon_k + \mathrm{i}\eta\,\mathrm{sgn}\,\varepsilon_k} \tag{3.11b}$$

$$= e^{\mathrm{i}\omega\eta'}\frac{\rho}{V}\left[\ln\frac{|\xi_0+\omega|}{|\xi_0-\omega|} - \mathrm{i}\pi\,\mathrm{sgn}(\omega)\,\Theta(\xi_0-|\omega|)\right]. \tag{3.11c}$$

In this sense the X-ray-edge model is effectively zero-dimensional. [In the exact analytic evaluation of diagrams, e.g. of the Hartree diagram (3.14) and of the bare bubbles (3.30) and (3.32), it can still be helpful to integrate over frequencies before summing over momenta.]

The factors $1/V$ absorbed into the conduction-state lines are taken from the vertices: we change their values according to

$$w_{k'k} = -U/V \qquad \to \qquad w_{cc} = -U \tag{3.12a}$$

$$\bar{v}_{dk'|dk} = U/V \qquad \to \qquad \bar{v}_{dc|dc} = U. \tag{3.12b}$$

In total this reduces the number of factors $1/V$ in a given diagram by n_c, which is half the number of external conduction-state legs. We correct this discrepancy with a global factor $1/V^{n_c}$ when determining the value of a 1PI vertex function from its contributing diagrams.

Using the simplifications and conventions discussed above, we evaluate all first-order diagrams contributing to the self-energy and show that they cancel out. No Fock contributions arise in the X-ray-edge model: they would involve a free propagation between the deep state and a conduction state, which is not admitted by the free Hamiltonian. The diagrams consisting of just one single-particle vertex are



$$= -g\xi_0, \qquad = -U. \tag{3.13}$$

The deep-state Hartree diagram is given by

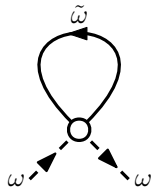

$$= -\mathrm{i}U\int_{-\infty}^{\infty}\frac{\mathrm{d}\tilde{\omega}}{2\pi}\,g_c(\tilde{\omega}) = -\mathrm{i}U\frac{1}{V}\sum_k\int_{-\infty}^{\infty}\frac{\mathrm{d}\tilde{\omega}}{2\pi}\,\frac{e^{\mathrm{i}\tilde{\omega}\eta'}}{\tilde{\omega}-\varepsilon_k+\mathrm{i}\eta\,\mathrm{sgn}\,\varepsilon_k} = g\xi_0, \tag{3.14}$$

where we closed the $\tilde{\omega}$-integral in the upper half plane and applied the residue theorem. Analogously, the conduction-state Hartree diagram is given by

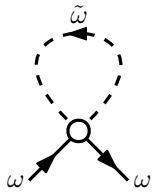

$$= -\mathrm{i}U\int_{-\infty}^{\infty}\frac{\mathrm{d}\tilde{\omega}}{2\pi}\,g_d(\tilde{\omega}) = -\mathrm{i}U\int_{-\infty}^{\infty}\frac{\mathrm{d}\tilde{\omega}}{2\pi}\,\frac{e^{\mathrm{i}\tilde{\omega}\eta'}}{\tilde{\omega}-\tilde{\varepsilon}_d-\mathrm{i}\eta} = U. \tag{3.15}$$

Two diagrams that differ only by replacing a single-particle vertex with a Hartree subdiagram have opposite values and cancel out. We shall therefore consider only diagrams with no single-particle vertices and no Hartree loops. The convergence factors $e^{\mathrm{i}\omega\eta'}$ from the free propagators can then safely be dropped.

For the deep state, this cancellation is deliberate. We have added and subtracted a term in the Hamiltonian (3.4) to effectively incorporate the deep-state Hartree diagram into the free propagator. For the conduction states, this cancellation reflects that electrons in the conduction band do not interact with an electron occupying the deep state but only with a hole at the deep state. For this reason any (time-dependent) expectation value $\langle\Phi|\ldots|\Phi\rangle$ involving only conduction-state ladder operators is not affected by the interaction from Eq. (3.1). For example the interacting single-particle Green function and the free propagator are identical for the conduction states,

$$G_{k|k'}(\omega|\omega') = g_{kk'}(\omega,\omega'). \tag{3.16}$$

When evaluating a diagram, we have to draw internal connections into the two-particle vertices to determine their signs and the sign of the prefactor. We shall always make the intuitive choice of connecting the dashed legs to each other and the full legs to each other. Then the value of a vertex is always $\bar{v}_{dc|dc} = \bar{v}_{cd|cd} = U$ and never $\bar{v}_{cd|dc} = \bar{v}_{dc|cd} = -U$.

In summary we arrive at the following diagrammatic rules for the 1PI vertex functions.

Diagrammatic rules for the 1PI vertex functions

Consider a 1PI vertex function $\gamma_{\alpha'_1\ldots\alpha'_n|\alpha_1\ldots\alpha_n}(\omega'_1,\ldots,\omega'_n|\omega_1,\ldots,\omega_n)$ with specified indices $\alpha_i^{(\prime)} = d$ or $\alpha_i^{(\prime)} = k_i^{(\prime)}$. Let n_c be half the number of conduction-state indices $k_i^{(\prime)}$. The contribution of order U^l to the 1PI vertex function is given by

$$2\pi\delta(\omega'_1 + \ldots + \omega'_n - \omega_1 - \ldots - \omega_n)\,\frac{1}{V^{n_c}} \tag{3.17}$$

times the sum of all distinct diagrams constructed in the following way.

Choose a set of $2n-1$ independent external frequencies and use it to express $\omega'_1,\ldots,\omega_n$. Draw l unlabeled vertices, each having one incoming and one outgoing dashed leg and one incoming and one outgoing full leg. Designate n of the incoming legs as external ones and label them with the expressions for $\omega_1,\ldots,\omega_n$. Designate n of the outgoing legs as external ones and label them with the expressions for $\omega'_1,\ldots,\omega'_n$. The dashed stroke style is reserved for the deep state and the full stroke style for the conduction states. Connect the vertices with directed lines, respecting the stroke style. A line must not start and end at the same vertex. Draw only one-particle irreducible diagrams, which cannot be disconnected by removing a single line. Successively label each line with a frequency, respecting the frequency conservation at vertices. If the frequency of a line is fixed, express it in terms of the existing frequencies; otherwise introduce a new frequency variable.

Two diagrams are distinct if they cannot be deformed into each other. The

order of the external legs as well as the direction and stroke style of lines matter. But the internal frequency labels are irrelevant when comparing diagrams.

An individual diagram is evaluated as follows. Consider the dashed legs of a vertex to be internally connected and its full legs to be internally connected. Let n_{loop} be the number of closed loops formed by the lines. Determine the permutation P such that the i-th incoming external leg is connected via lines to the $P(i)$-th outgoing external leg. Dashed and full lines have the respective values

$$g_d(\omega) = \frac{1}{\omega - \tilde{\varepsilon}_d - \mathrm{i}\eta} \tag{3.18a}$$

$$g_c(\omega) = \frac{1}{V}\sum_k \frac{1}{\omega - \varepsilon_k + \mathrm{i}\eta\,\mathrm{sgn}\,\varepsilon_k} = \frac{\rho}{V}\left[\ln\frac{|\xi_0+\omega|}{|\xi_0-\omega|} - \mathrm{i}\pi\,\mathrm{sgn}(\omega)\,\Theta(\xi_0-|\omega|)\right]. \tag{3.18b}$$

The value of the diagram is

$$\mathrm{sgn}(P)(-1)^{n_{\text{loop}}}\,\mathrm{i}^{1-n+l}\,U^l \int\ldots\int \prod g, \tag{3.19}$$

where $\int\ldots\int$ indicates that we perform an integral $\int_{-\infty}^{\infty}\mathrm{d}\omega/(2\pi)$ for each internal frequency variable.

3.3.3 Expressing $\chi(\nu)$ in terms of the 1PI two-particle vertex γ

We now discuss which 1PI vertex functions are needed to determine the X-ray-absorption rate. Since we have already related it to the particle-hole susceptibility $\chi(\nu)$ in Sec. 3.2.2, we here express $\chi(\nu)$ in terms of the 1PI vertex functions, finding that only the self-energy and the 1PI two-particle vertex function appear. Roulet et al. [RGN69] essentially used the same expression, neglected the self-energy, and focused their approach on the 1PI two-particle vertex function.

Let us repeat the definition (3.3) of the particle-hole susceptibility for convenience,

$$\chi(\nu) = -\mathrm{i}\frac{1}{V}\sum_{kk'}\int_{-\infty}^{\infty}\mathrm{d}t\,e^{\mathrm{i}\nu t}\big\langle\Phi\big|\mathcal{T}\,a_d^\dagger(t)a_k(t)a_{k'}^\dagger(0)a_d(0)\big|\Phi\big\rangle, \tag{3.20}$$

where the state $|\Phi\rangle$ of the system is given by Eq. (3.8). Under the influence of the time-ordering operator, the ladder operators can be anticommuted such that the expectation value matches the definition (2.5) of the Green functions,

$$\big\langle\Phi\big|\mathcal{T}\,a_d^\dagger(t)a_k(t)a_{k'}^\dagger(0)a_d(0)\big|\Phi\big\rangle = G_{dk|dk'}(0,t|t,0). \tag{3.21}$$

We go over to frequency representation via the inverse Fourier transformation

$$\begin{aligned} &G_{dk|dk'}(0,t|t,0) \\ &= \int_{-\infty}^{\infty}\frac{\mathrm{d}\omega_d}{2\pi}\int_{-\infty}^{\infty}\frac{\mathrm{d}\omega_c}{2\pi}\int_{-\infty}^{\infty}\frac{\mathrm{d}\omega_d'}{2\pi}\int_{-\infty}^{\infty}\frac{\mathrm{d}\omega_c'}{2\pi}\,e^{-\mathrm{i}\omega_c t}\,e^{\mathrm{i}\omega_d' t}\,G_{dk|dk'}(\omega_d,\omega_c|\omega_d',\omega_c'). \end{aligned} \tag{3.22}$$

We then insert the standard relation between the two-particle Green function and the 1PI two-particle vertex function, see e.g. Ref. [Jak19],

$$\begin{aligned} &G_{dk|dk'}(\omega_d,\omega_c|\omega_d',\omega_c') \\ &= G_{d|d}(\omega_d|\omega_d')\,G_{k|k'}(\omega_c|\omega_c') + \mathrm{i}\sum_{\tilde{k}\tilde{k}'}\int_{-\infty}^{\infty}\frac{\mathrm{d}\tilde{\omega}_d}{2\pi}\int_{-\infty}^{\infty}\frac{\mathrm{d}\tilde{\omega}_c}{2\pi}\int_{-\infty}^{\infty}\frac{\mathrm{d}\tilde{\omega}_d'}{2\pi}\int_{-\infty}^{\infty}\frac{\mathrm{d}\tilde{\omega}_c'}{2\pi} \\ &\times G_{d|d}(\omega_d|\tilde{\omega}_d')\,G_{k|\tilde{k}'}(\omega_c|\tilde{\omega}_c')\,\gamma_{d\tilde{k}'|d\tilde{k}}(\tilde{\omega}_d',\tilde{\omega}_c'|\tilde{\omega}_d,\tilde{\omega}_c)\,G_{d|d}(\tilde{\omega}_d|\omega_d')\,G_{\tilde{k}|k'}(\tilde{\omega}_c|\omega_c'), \end{aligned} \tag{3.23}$$

where we used that the interaction conserves the number of electrons in the deep state.

We use shorthand notations for the 1PI two-particle vertex function and the single-particle Green function. $\gamma_{dk'|dk}$ does not actually depend on the momenta k', k – just like the bare vertex. We define

$$\gamma_{dc|dc} = V\gamma_{dk'|dk}, \tag{3.24}$$

which mirrors the definition (3.12b) for the bare vertex. For the single-particle Green function, we write

$$G_{d|d}(\omega|\omega') = 2\pi\delta(\omega-\omega')\,G_d(\omega) \tag{3.25a}$$

$$\frac{1}{V}\sum_{kk'}G_{k|k'}(\omega|\omega') = 2\pi\delta(\omega-\omega')\,g_c(\omega). \tag{3.25b}$$

We have used that the single-particle Green function and the free propagator are identical in the conduction-state case, see Eqs. (3.11a) and (3.16). The particle-hole susceptibility now reads

$$\begin{aligned} \chi(\nu) = -\mathrm{i}&\int_{-\infty}^{\infty}\mathrm{d}t\,e^{\mathrm{i}\nu t}\int_{-\infty}^{\infty}\frac{\mathrm{d}\omega_d}{2\pi}\int_{-\infty}^{\infty}\frac{\mathrm{d}\omega_c}{2\pi}\,e^{-\mathrm{i}\omega_c t}\,e^{\mathrm{i}\omega_d t}\,G_d(\omega_d)\,g_c(\omega_c) \\ &+\int_{-\infty}^{\infty}\mathrm{d}t\,e^{\mathrm{i}\nu t}\int_{-\infty}^{\infty}\frac{\mathrm{d}\omega_d}{2\pi}\int_{-\infty}^{\infty}\frac{\mathrm{d}\omega_c}{2\pi}\int_{-\infty}^{\infty}\frac{\mathrm{d}\omega_d'}{2\pi}\int_{-\infty}^{\infty}\frac{\mathrm{d}\omega_c'}{2\pi}\,e^{-\mathrm{i}\omega_c' t}\,e^{\mathrm{i}\omega_d t} \\ &\times G_d(\omega_d')\,g_c(\omega_c')\,\gamma_{dc|dc}(\omega_d',\omega_c'|\omega_d,\omega_c)\,G_d(\omega_d)\,g_c(\omega_c). \end{aligned} \tag{3.26}$$

We introduce a notation for the frequency arguments of the 1PI two-particle vertex function $\gamma_{dc|dc}(\omega_d',\omega_c'|\omega_d,\omega_c)$. Because of frequency conservation, only three of its frequencies are independent. We always use the deep-state frequencies ω_d, ω_d'. As the third independent frequency, we choose either the total frequency $\Omega = \omega_d+\omega_c = \omega_d'+\omega_c'$ or the exchange frequency $X = \omega_c' - \omega_d = \omega_c - \omega_d'$. These two cases are distinguished via

$$\gamma_{dc|dc}(\omega_d',\omega_c'|\omega_d,\omega_c) = 2\pi\delta(\omega_d'+\omega_c'-\omega_d-\omega_c)\,\hat{\gamma}(\omega_d,\omega_d';\Omega) \tag{3.27a}$$

$$= 2\pi\delta(\omega_d'+\omega_c'-\omega_d-\omega_c)\,\bar{\gamma}(\omega_d,\omega_d';X). \tag{3.27b}$$

The order of ω_d, ω_d' in $\bar{\gamma}(\omega_d,\omega_d';X)$ has been chosen to match the order of the frequencies in Fig. 3.1.

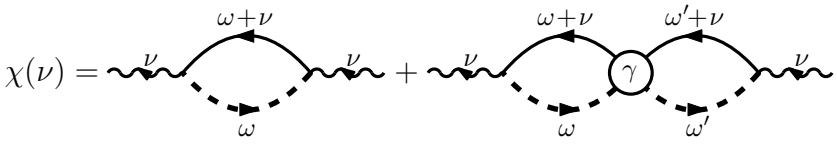

Figure 3.1: Diagrammatic translation of Eq. (3.28). Full lines refer to local conduction-electron propagators g_c, fat dashed lines to deep-state propagators G_d. The circle stands for the 1PI two-particle vertex function. The three-leg vertices involving each a full, dashed, and wavy line conserve frequency but do not contribute any factor.

With this notation we arrive at the relation

$$\chi(\nu) = -\mathrm{i}\int_{-\infty}^{\infty}\frac{\mathrm{d}\omega}{2\pi}\,G_d(\omega)\,g_c(\omega+\nu) + \int_{-\infty}^{\infty}\frac{\mathrm{d}\omega}{2\pi}\int_{-\infty}^{\infty}\frac{\mathrm{d}\omega'}{2\pi}\,G_d(\omega)\,g_c(\omega+\nu)\,\bar{\gamma}(\omega,\omega';\nu)\,G_d(\omega')\,g_c(\omega'+\nu). \quad (3.28)$$

It allows to calculate the particle-hole susceptibility once the self-energy and the 1PI two-particle vertex function are known. Figure 3.1 is a translation into diagrammatic language.

The functions $\hat{\gamma}(\omega,\omega';\Omega) = \bar{\gamma}(\omega,\omega';X)$ will be important in the remaining discussion of the X-ray-edge model. They are given by the sum of all diagrams defined in the rule set on page 42; they do not contain the factor $2\pi\delta(\ldots)/V$. The parquet approach of Roulet et al. and our FRG approach focus on calculating these functions approximately.

3.3.4 Setting the renormalized deep level $\tilde{\varepsilon}_d$ to zero

In the remaining calculations for the X-ray-edge model, we set the renormalized deep level to $\tilde{\varepsilon}_d = 0$. This is equivalent to measuring the X-ray frequency ν relative to $|\tilde{\varepsilon}_d|$, which is our estimate for the threshold frequency. While our renormalized deep level accounts only for the Hartree self-energy, the value of the threshold frequency is actually affected also by other real, static contributions of the self-energy; they could be treated similarly. However, our focus does not lie on the specific value of the threshold frequency. Setting the renormalized deep level to zero is a convenient way to eliminate one of the parameters; the same was done by Roulet et al. [RGN69]. We present the reasoning behind this step by relating it to a Ward identity.

Let us consider a diagram contributing to $\chi(\nu) = \chi(\nu,\tilde{\varepsilon}_d)$ which arises when diagrams for the 1PI vertex function and for the full deep-state lines are inserted into Fig. 3.1. We may choose the frequencies of the internal lines in accordance with frequency conservation such that the external frequency ν appears as addend in the frequency argument of every conduction-state propagator but not of any deep-state propagator. Subtracting a frequency α from the frequency arguments of all conduction- and deep-state propagators respects frequency conservation and does not alter the value of the diagram. Then ν appears only in the conduction-state propagators,

always in the form $\nu - \alpha$, and $\tilde{\varepsilon}_d$ appears only in the deep-state propagators, always in the form $\tilde{\varepsilon}_d + \alpha$. This proves the Ward identity

$$\chi(\nu, \tilde{\varepsilon}_d) = \chi(\nu - \alpha, \tilde{\varepsilon}_d + \alpha), \tag{3.29}$$

which results from frequency conservation (i.e. time-translational invariance) and the conservation of the numbers of conduction- and deep-state electrons.

Equation (3.29) relates the susceptibilities of two models with respective values $\tilde{\varepsilon}_d$ and $\tilde{\varepsilon}_d + \alpha$ of the renormalized deep level. These susceptibilities are defined in the state $|\Phi\rangle$ given by Eq. (3.8), in which the deep level and the lower half of the conduction band are occupied. For the model with $\tilde{\varepsilon}_d + \alpha$ and for sufficiently large α, this state is not the ground state of the interacting Hamiltonian; for even larger α, it is not even the ground state of the noninteracting Hamiltonian. Nonetheless, the zero-temperature formalism allows to compute expectation values in the state $|\Phi\rangle$ because it is a common eigenstate of the noninteracting and interacting Hamiltonian, see Sec. 2.11.2. When χ is determined accordingly, the identity (3.29) holds for all real frequencies α and even on the level of individual diagrams. As a special case, we obtain $\chi(\nu - \tilde{\varepsilon}_d, \tilde{\varepsilon}_d) = \chi(\nu, 0)$, where ν is now the deviation of the X-ray frequency from the threshold frequency $|\tilde{\varepsilon}_d|$.

3.3.5 Exact calculation of bare bubbles

We now discuss the second-order diagrams of the 1PI vertex function $\gamma_{dc|dc}$ and determine their exact values. These diagrams are the bare bubbles in the exchange particle-hole channel and in the particle-particle channel. We do not discuss the direct particle-hole bubble, which does not contribute to $\gamma_{dc|dc}$ but only to $\gamma_{dd|dd}$. We will often refer to the exchange particle-hole channel simply as the particle-hole channel.

The following calculations serve as examples for applying the diagrammatic rules of Sec. 3.3.2. More importantly, they are crucial for understanding the breakdown of naive perturbation theory. The bare bubbles are the lowest-order diagrams that exhibit logarithmic divergences. The exact values of these diagrams will later help to validate the approximations made in Ref. [RGN69].

Regarding the choice of independent external frequencies, we use the notation introduced in Sec. 3.3.3. The diagrams discussed here are exactly the second-order contributions to $\hat{\gamma}(\omega, \omega'; \Omega) = \bar{\gamma}(\omega, \omega'; X)$. We choose the exchange frequency X as one of the independent frequencies for the particle-hole bubble, whereas we choose the total frequency Ω for the particle-particle bubble. This is the natural choice, see below.

The particle-hole bubble is given by

$$B^{(\mathrm{ph})}(X) = \tag{3.30a}$$

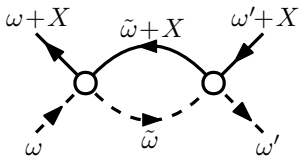

$$= \mathrm{i}U^2 \int_{-\infty}^{\infty} \frac{\mathrm{d}\tilde{\omega}}{2\pi}\, g_d(\tilde{\omega})\, g_c(\tilde{\omega}+X) \tag{3.30b}$$

$$= \mathrm{i}\frac{U^2}{V} \sum_k \int_{-\infty}^{\infty} \frac{\mathrm{d}\tilde{\omega}}{2\pi} \frac{1}{\tilde{\omega}-\mathrm{i}\eta} \frac{1}{\tilde{\omega}+X-\varepsilon_k+\mathrm{i}\eta\,\mathrm{sgn}\,\varepsilon_k}. \tag{3.30c}$$

This diagram depends only on the exchange frequency X, which is consequently the natural frequency of the exchange particle-hole channel. It is convenient to not precalculate the momentum sum and to instead integrate over $\tilde{\omega}$ first. By closing the integral in the lower half plane and applying the residue theorem, we find that only the unoccupied conduction states contribute. The exact value of the particle-hole bubble is

$$B^{(\mathrm{ph})}(X) = \frac{U^2}{V} \sum_k \Theta(\varepsilon_k) \frac{1}{-X+\varepsilon_k-2\mathrm{i}\eta} \tag{3.31a}$$

$$= \frac{U^2\rho}{V} \int_0^{\xi_0} \mathrm{d}\varepsilon \left[\mathcal{P}\frac{1}{\varepsilon-X} + \mathrm{i}\pi\delta(\varepsilon-X)\right] \tag{3.31b}$$

$$= -g^2\frac{V}{\rho}\left[\ln\frac{|X|}{|\xi_0-X|} - \mathrm{i}\pi\Theta(\xi_0-X)\Theta(X)\right] \tag{3.31c}$$

$$\approx -g^2\frac{V}{\rho}\ln\frac{|X|}{\xi_0} \qquad \text{for } |X| \ll \xi_0. \tag{3.31d}$$

The last line states the leading behavior in a specific regime and serves as a reference for Sec. 3.4.3, where we will use approximations aimed at capturing the leading logarithms.

The particle-particle bubble is given by

$$B^{(\mathrm{pp})}(\Omega) = \tag{3.32a}$$

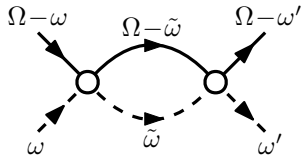

$$= \mathrm{i}U^2 \int_{-\infty}^{\infty} \frac{\mathrm{d}\tilde{\omega}}{2\pi}\, g_d(\tilde{\omega})\, g_c(\Omega-\tilde{\omega}) \tag{3.32b}$$

$$= \mathrm{i}\frac{U^2}{V} \sum_k \int_{-\infty}^{\infty} \frac{\mathrm{d}\tilde{\omega}}{2\pi} \frac{1}{\tilde{\omega}-\mathrm{i}\eta} \frac{1}{\Omega-\tilde{\omega}-\varepsilon_k+\mathrm{i}\eta\,\mathrm{sgn}\,\varepsilon_k}. \tag{3.32c}$$

This diagram depends only on the total frequency Ω, which is consequently the natural frequency of the particle-particle channel. Again, it is convenient to first integrate over $\tilde{\omega}$. In this case only those conduction states contribute that are, like the

deep state, occupied. So the particle-particle channel is strictly speaking a hole-hole channel. The exact value of the particle-particle bubble is

$$B^{(\mathrm{pp})}(\Omega) = \frac{U^2}{V}\sum_k \Theta(-\varepsilon_k)\,\frac{-1}{\Omega-\varepsilon_k-2\mathrm{i}\eta} \tag{3.33a}$$

$$= g^2\frac{V}{\rho}\left[\ln\frac{|\Omega|}{|\xi_0+\Omega|} - \mathrm{i}\pi\Theta(\xi_0+\Omega)\Theta(-\Omega)\right] \tag{3.33b}$$

$$\approx g^2\frac{V}{\rho}\ln\frac{|\Omega|}{\xi_0} \qquad \text{for } |\Omega| \ll \xi_0. \tag{3.33c}$$

Again, the last line serves as a reference for Sec. 3.4.3.

3.3.6 Exact calculation of crossed bubble

We consider the particular third-order diagram of the 1PI vertex function $\gamma_{dc|dc}$ that results from replacing the left vertex in the particle-hole bubble (3.30) with the particle-particle bubble (3.32). As this diagram is an example of crossing the two channels, we refer to it as the crossed bubble. (Similar diagrams exist that could also be called crossed bubbles.) In this section we determine the exact value of the crossed bubble and its leading behavior in a certain regime.

The crossed bubble will serve as a key example for showing the approximations of Roulet et al. aimed at capturing the leading logarithms in the diagrammatic expansion of the 1PI two-particle vertex function, see Sec. 3.4.4. The leading behavior of the crossed bubble, which we here determine from its exact value, will be used there for comparison.

Since the particle-hole bubble is the outer one, the crossed bubble inherits the exchange frequency X as a natural external frequency. In the notation of Sec. 3.3.3, the crossed bubble is a third-order contribution to $\bar{\gamma}(\omega,\omega';X)$.

The crossed bubble is given by

$B^{(\mathrm{c})}(X,\omega) =$ 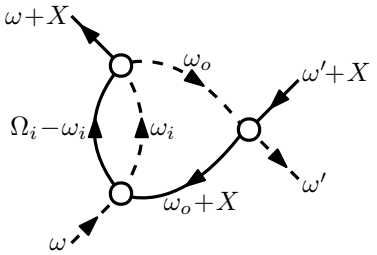

with $\Omega_i = \omega_o+\omega+X$ (3.34a)

$$= \mathrm{i}^2U^3\int_{-\infty}^{\infty}\frac{\mathrm{d}\omega_o}{2\pi}\int_{-\infty}^{\infty}\frac{\mathrm{d}\omega_i}{2\pi}\,g_d(\omega_o)\,g_c(\omega_o+X)\,g_d(\omega_i)\,g_c(\Omega_i-\omega_i) \tag{3.34b}$$

$$= -\frac{U^3}{V^2}\sum_{k_ok_i}\int_{-\infty}^{\infty}\frac{\mathrm{d}\omega_o}{2\pi}\int_{-\infty}^{\infty}\frac{\mathrm{d}\omega_i}{2\pi}\,\frac{1}{\omega_o-\mathrm{i}\eta}\,\frac{1}{\omega_o+X-\varepsilon_{k_o}+\mathrm{i}\eta\,\mathrm{sgn}\,\varepsilon_{k_o}}$$
$$\times\,\frac{1}{\omega_i-\mathrm{i}\eta}\,\frac{1}{\Omega_i-\omega_i-\varepsilon_{k_i}+\mathrm{i}\eta\,\mathrm{sgn}\,\varepsilon_{k_i}}. \tag{3.34c}$$

Similarly to the frequency integrals in the bare bubbles, we close the integrals in the

lower half plane and apply the residue theorem to obtain

$$B^{(\mathrm{c})}(X,\omega) = -\frac{U^3}{V^2}\sum_{k_o k_i}\Theta(\varepsilon_{k_o})\Theta(-\varepsilon_{k_i})\,\frac{1}{\varepsilon_{k_o}-X-2\mathrm{i}\eta}\,\frac{1}{\varepsilon_{k_o}-\varepsilon_{k_i}+\omega-3\mathrm{i}\eta} \tag{3.35a}$$

$$= -g^3\frac{V}{\rho}\int_0^{\xi_0}\mathrm{d}\varepsilon_o\int_{-\xi_0}^{0}\mathrm{d}\varepsilon_i\,\frac{1}{\varepsilon_o-X-\mathrm{i}\eta}\,\frac{1}{\varepsilon_o-\varepsilon_i+\omega-\mathrm{i}\eta}. \tag{3.35b}$$

We consider also the remaining two integrals as contour integrals in the complex plane. In the last step, we have neglected the factors 2 and 3 in the η-terms because these terms merely specify on which side of a pole or branch cut a contour passes; the result remains unchanged.

The ε_i-integral can be read as a contour integral over $1/z$, see Appendix C.1. Using the principal branch of the complex logarithm, see Appendix B.1, we get

$$B^{(\mathrm{c})}(X,\omega) = -g^3\frac{V}{\rho}\int_0^{\xi_0}\mathrm{d}\varepsilon_o\,\frac{\mathrm{Log}(\varepsilon_o+\xi_0+\omega-\mathrm{i}\eta)-\mathrm{Log}(\varepsilon_o+\omega-\mathrm{i}\eta)}{\varepsilon_o-X-\mathrm{i}\eta}. \tag{3.36}$$

A generic integral that is applicable to each of the two summands is solved in Appendix C.2 in terms of the principle branch of the dilogarithm $\mathrm{Li}_2(z)$. The definition and relevant properties of $\mathrm{Li}_2(z)$ can be found in Ref. [DLMF: §25.12(i)] and are stated in Appendix B.2 for convenience. The exact value of the crossed bubble is

$$\begin{aligned} &B^{(\mathrm{c})}(X,\omega) \qquad\qquad (3.37)\\ &= -g^3\frac{V}{\rho}\Big\{\big[\mathrm{Log}(X+\xi_0+\omega-\mathrm{i}\eta)-\mathrm{Log}(X+\omega-\mathrm{i}\eta)\big]\big[\mathrm{Log}(\xi_0-X-\mathrm{i}\eta)-\mathrm{Log}(-X-\mathrm{i}\eta)\big]\\ &\quad-\mathrm{Li}_2\Big(\frac{\xi_0-X-\mathrm{i}\eta}{-\xi_0-\omega-X}\Big)+\mathrm{Li}_2\Big(\frac{-X-\mathrm{i}\eta}{-\xi_0-\omega-X}\Big)+\mathrm{Li}_2\Big(\frac{\xi_0-X-\mathrm{i}\eta}{-\omega-X}\Big)-\mathrm{Li}_2\Big(\frac{-X-\mathrm{i}\eta}{-\omega-X}\Big)\Big\}. \end{aligned}$$

(We exclude the special cases $-\xi_0-\omega-X=0$ and $-\omega-X=0$; they have measure zero anyway when one finally integrates over ω to obtain a contribution to the particle-hole susceptibility.)

Now, we extract the leading behavior of the crossed bubble to later compare it with the leading-logarithmic parquet approximation of Roulet et al. in Sec. 3.4.4. There, the relevant regime is identified as $|X|<|\omega|\ll\xi_0$.

The first and second dilogarithms in Eq. (3.37) are $O(1)$ because $\mathrm{Li}_2(z)$ diverges only for $|z|\to\infty$. By using the exact relation (B.7b), we can rewrite the divergence of $\mathrm{Li}_2(z)$ for $|z|\to\infty$ as a diverging term $-\mathrm{Log}^2(-z)/2$; the leading contribution comes specifically from the square of the real part of the logarithm, while the influence of the imaginary part is subleading. The third and fourth dilogarithms in Eq. (3.37) are thus

$$\mathrm{Li}_2\Big(\frac{\xi_0-X-\mathrm{i}\eta}{-\omega-X}\Big) = -\frac{1}{2}\ln^2\frac{|X+\omega|}{\xi_0}+O\Big(\ln\frac{|X+\omega|}{\xi_0}\Big) \tag{3.38a}$$

$$\mathrm{Li}_2\Big(\frac{-X-\mathrm{i}\eta}{-\omega-X}\Big) = -\Theta\big(|X|-|X+\omega|\big)\,\frac{1}{2}\ln^2\frac{|X|}{|X+\omega|}+O\Big(1,\ln\frac{|X|}{|X+\omega|}\Big). \tag{3.38b}$$

In the second line, we have made no assumptions on the relation between X and $X+\omega$. The first term constitutes the leading behavior if the dilogarithm diverges. To describe the dropped terms in this line, we have stretched the meaning of the big O notation: constants a and b exist such that these terms are bounded by a or $b\ln(|X|/|X+\omega|)$ for all X and ω.

When we insert the approximations for the dilogarithms in Eq. (3.37), we distinguish two cases because of the step function from Eq. (3.38b). The cases can be written simultaneously through the use of maxima such that the value of the crossed bubble for $|X|, |\omega| \ll \xi_0$ reads

$$B^{(\mathrm{c})}(X,\omega) = -g^3\frac{V}{\rho}\left[\ln\frac{\max\{|X|,|X+\omega|\}}{\xi_0}\ln\frac{|X|}{\xi_0} - \frac{1}{2}\ln^2\frac{\max\{|X|,|X+\omega|\}}{\xi_0} + O\left(\ln\frac{|X+\omega|}{\xi_0}, \ln\frac{|X|}{\xi_0}\right)\right]. \tag{3.39}$$

Anticipating the form of the leading logarithms obtained in Sec. 3.4.4, we rewrite this expression further. The condition $|X| < |\omega|$ implies

$$\frac{|\omega|}{2} \leq \max\{|X|,|X+\omega|\} < 2|\omega|, \tag{3.40}$$

so replacing the maximum with $|\omega|$ is correct within a factor of 2. With regard to the logarithms in Eq. (3.39), the error of this replacement is subleading. In total the value of the crossed bubble for $|X| < |\omega| \ll \xi_0$ is given by

$$B^{(\mathrm{c})}(X,\omega) = -g^3\frac{V}{\rho}\left[\ln\frac{|\omega|}{\xi_0}\ln\frac{|X|}{\xi_0} - \frac{1}{2}\ln^2\frac{|\omega|}{\xi_0} + O\left(\ln\frac{|X+\omega|}{\xi_0}, \ln\frac{|X|}{\xi_0}\right)\right] \tag{3.41a}$$

$$= g^3\frac{V}{\rho}\left[\ln\frac{|\omega|}{|X|}\ln\frac{|\omega|}{\xi_0} - \frac{1}{2}\ln^2\frac{|\omega|}{\xi_0} + O\left(\ln\frac{|X+\omega|}{\xi_0}, \ln\frac{|X|}{\xi_0}\right)\right]. \tag{3.41b}$$

3.4 Leading-logarithmic parquet approximation of Roulet et al.

In this section we discuss in detail the leading-logarithmic parquet approximation of Roulet et al. [RGN69]. Their diagrammatic expansion is essentially the same as the one in Sec. 3.3.2. The insights gained into the parquet approach will be used to develop our FRG approach in Sec. 3.5. Roulet et al. formulated and approximated parquet equations, whereas we will work with FRG flow equations. We will compare the two approaches in Sec. 3.6.

We start by discussing the occurrence of logarithmic divergences in the diagrammatic expansion. One distinguishes leading and subleading terms based on their order in the interaction and their power of diverging logarithms. The purpose of the leading-logarithmic parquet approximation is to account for all so-called leading logarithms. We then list all approximations that Roulet et al. made on the level of the parquet equations and demonstrate them for key example diagrams, namely for the bare bubbles and the crossed bubble. Roulet et al. solved the approximated

parquet equations to obtain the 1PI two-particle vertex function. Using this result, they determined the imaginary part of the particle-hole susceptibility and thereby the X-ray-absorption rate.

3.4.1 Leading logarithms

Importantly, the values (3.31) and (3.33) of the bubbles in the particle-hole and particle-particle channel feature a logarithmic divergence as their natural frequency X or Ω approaches zero. [There are also divergences for $X \to \xi_0$ and $\Omega \to -\xi_0$. Those, however, turn out to be not important for $\chi(\nu)$ at small ν.]

It is known that such logarithmic divergences appear for all powers of the interaction. For the 1PI two-particle vertex function, the *leading* logarithms have the form $g^n \ln^{n-1}$ while subleading contributions contain at least one logarithm less. Here, the arguments of the logarithms are essentially $|X|/\xi_0$ or $|\Omega|/\xi_0$ depending on the channel. The arguments can also depend on the other independent frequencies ω, ω' if the corresponding external deep-state leg is not attached to the same vertex as one of the external conduction-state legs, see e.g. the crossed bubble (3.34) and its leading behavior (3.41). All of the leading logarithms are contained within the parquet diagrams without any self-energy insertions (except for static contributions absorbed into $\tilde{\varepsilon}_d$) [RGN69]. These diagrams can be constructed by starting with a single vertex and successively replacing any vertex with the particle-hole bubble (3.30) or particle-particle bubble (3.32).

This construction naturally leads to a strict partial order of the bubbles in a parquet diagram. If a vertex at an end of some bubble is replaced by a bubble of the opposite channel, then we call the old bubble the outer one and the new bubble the inner one. Additionally, the new bubble inherits the list of outer bubbles from the old bubble. If a vertex at an end of some bubble is replaced by a bubble of the same channel, then these two bubbles are incomparable and the new bubble inherits the list of outer bubbles from the old bubble. A given parquet diagram can often be constructed in different ways, but the answer to the question whether a bubble is inner to another bubble is the same for all these ways. In total, the relation "being inner to" is a strict partial order because it is well-defined, irreflexive, and transitive. As far as the leading logarithms are concerned, we will see that the internal frequency variables in a parquet diagram satisfy a related order.

The leading logarithms appearing in the expansion of the particle-hole susceptibility $\chi(\nu)$, which directly follow from those of γ via Eq. (3.28), assume the form $g^n \ln^{n+1}(|\nu|/\xi_0)$. In comparison to the 1PI two-particle vertex function, two additional powers of the logarithm arise from the two external bubbles in the right diagram in Fig. 3.1. Close to the threshold $\nu = 0$ where $g \ln(|\nu|/\xi_0)$ is not much smaller than one, these terms are significant for arbitrary powers n even though g itself is small. To approximate the behavior of $\chi(\nu)$ in a reasonable way, it is then necessary to resum the leading logarithms of all orders. Even closer to the threshold, i.e. as ν goes to zero, $g \ln(|\nu|/\xi_0)$ increases further until also subleading logarithms become large and must be included. However, in this thesis we discuss only the resummation of the leading logarithms.

It is important to note that it is not necessary to include the exact value of any given parquet diagram in the resummation scheme to obtain a valid leading-logarithmic approximation. Instead, one can make further approximations as long as they do not influence the leading logarithms. That the parquet diagrams indeed contain subleading contributions is already obvious from the exact results (3.31c) and (3.33b) for the bubbles, where e.g.

$$\ln \frac{|X|}{|\xi_0 - X|} = \ln \frac{|X|}{\xi_0} - \ln \frac{|\xi_0 - X|}{\xi_0}. \tag{3.42}$$

3.4.2 List of approximations

Here, we give a complete summary of the approximation steps performed by Roulet et al. [RGN69]. To later refer to the individual steps, we group them into five labeled points. For the justification, especially of steps (i) and (ii), which neglect entire classes of diagrams, we refer to the discussion of the subleading logarithms in Ref. [NGR69]. The justification of steps (iii)-(v), which affect the calculation of the remaining diagrams, will become evident also in Secs. 3.4.3 and 3.4.4, where we apply the approximations to the bare bubbles and the crossed bubble. Together, the approximations (i)-(v) form the leading-logarithmic parquet approximation.

(i) consider only the parquet diagrams in the exchange particle-hole and particle-particle channel

After identifying the two singular bubbles, Roulet et al. decomposed the 1PI two-particle vertex function into three contributions that are reducible in the exchange particle-hole channel, reducible in the particle-particle channel, or irreducible in both channels. They formulated exact parquet equations in terms of these contributions and called the last one the "totally irreducible interaction", which still contains all diagrams reducible in the direct particle-hole channel. Roulet et al. retained only the lowest-order term of the totally irreducible interaction, namely the bare vertex. The parquet equations then produce exactly the parquet diagrams in the exchange particle-hole and particle-particle channel. The direct particle-hole channel has been removed, while self-energy insertions are still fully included.

(ii) neglect the self-energy

For the conduction states, the self-energy vanishes from the start, see Eq. (3.16). For the deep state, neglecting the self-energy is an approximation.

Roulet et al. accounted for real, static contributions of the self-energy that renormalize the deep level. We technically incorporated the Hartree self-energy into the free propagator in Sec. 3.3.1, obtaining the renormalized deep level $\tilde{\varepsilon}_d = \varepsilon_d + g\xi_0$. We could treat other real, static contributions in a similar way, obtaining a slightly different renormalized deep level. The absolute value of the fully renormalized deep level is equal to the threshold frequency ν_c, which in turn constitutes the position of the divergence of $\chi(\nu)$ [RGN69]. Based on the Hartree self-energy, the estimate for

the threshold frequency is $\nu_c \approx |\tilde{\varepsilon}_d| = -\varepsilon_d - g\xi_0$. Anyway, in Sec. 3.3.4 we have set the renormalized deep level to zero, just like Roulet et al.

The focus does not lie on the value of the threshold frequency but only on the shape of $\chi(\nu)$ near threshold. Roulet et al. argued that all remaining self-energy contributions are negligible in leading logarithmic order. In summary the diagrams left after step (i) now have no self-energy insertions.

(iii) neglect the imaginary part of g_d and the real part of g_c

The imaginary part of the free deep-state propagator and the real part of the local conduction-electron propagator are neglected. The dashed and full lines now have the values

$$g_d(\omega) = \mathcal{P}\frac{1}{\omega} \tag{3.43a}$$

$$g_c(\omega) = -\mathrm{i}\pi\frac{\rho}{V}\,\mathrm{sgn}(\omega)\Theta(\xi_0 - |\omega|). \tag{3.43b}$$

These remaining parts cause the divergences of the bubbles, see Eqs. (3.44) and (3.45).

(iv) neglect small shifts of the integration boundaries

Each bubble appearing in a parquet diagram has one independent frequency variable ω. If this variable is chosen to be the frequency of the dashed line, the full line contributes a step function $\Theta(\xi_0 - |\omega + X|)$ or $\Theta(\xi_0 - |\Omega - \omega|)$ that leads to integration boundaries $\pm\xi_0 - X$ or $\pm\xi_0 + \Omega$. Roulet et al. replaced these boundaries by $\pm\xi_0$. Here, X or Ω is the natural frequency of the bubble and always turns out to be much smaller than ξ_0 [even if it is a linear combination of multiple independent frequencies, see e.g. Eq. (3.47)].

(v) logarithmic approximation

A bubble or series of bubbles of either channel depends on its natural frequency via slowly varying logarithms. If such a bubble or series of bubbles is embedded in a bubble of the other channel, this natural frequency is a linear combination of independent frequency variables. Roulet et al. replaced the linear combination with the maximum of the absolute values of these variables, see Eq. (3.51) for a concrete example. This approximation step has been named logarithmic approximation by Roulet et al., while (i)-(v) are together known as the leading-logarithmic parquet approximation.

3.4.3 Approximating the bare bubbles

Using the approximation scheme of Roulet et al., we calculate the values of the particle-hole and particle-particle bubbles. Specifically, these calculations are examples of the

steps (iii) and (iv). In the case of the particle-hole bubble (3.30), the approximations lead to

$$B^{(\mathrm{ph})}(X) = \mathrm{i}U^2 \int_{-\infty}^{\infty} \frac{\mathrm{d}\tilde{\omega}}{2\pi}\, g_d(\tilde{\omega})\, g_c(\tilde{\omega}+X) \tag{3.44a}$$

$$\overset{\text{(iii)}}{\approx} \frac{U^2\rho}{2V} \int_{-\infty}^{\infty} \mathrm{d}\tilde{\omega}\, \mathcal{P}\frac{1}{\tilde{\omega}}\, \mathrm{sgn}(\tilde{\omega}+X)\Theta(\xi_0 - |\tilde{\omega}+X|) \tag{3.44b}$$

$$\overset{\text{(iv)}}{\approx} \frac{U^2\rho}{2V} \int_{-\xi_0}^{\xi_0} \mathrm{d}\tilde{\omega}\, \mathcal{P}\frac{1}{\tilde{\omega}}\, \mathrm{sgn}(\tilde{\omega}+X) \tag{3.44c}$$

$$\overset{|X|\leq\xi_0}{=} g^2 \frac{V}{\rho} \int_{|X|}^{\xi_0} \mathrm{d}|\tilde{\omega}|\, \frac{1}{|\tilde{\omega}|} \tag{3.44d}$$

$$= -g^2 \frac{V}{\rho} \ln \frac{|X|}{\xi_0}. \tag{3.44e}$$

In the case of the particle-particle bubble (3.32), the approximations lead to

$$B^{(\mathrm{pp})}(\Omega) = \mathrm{i}U^2 \int_{-\infty}^{\infty} \frac{\mathrm{d}\tilde{\omega}}{2\pi}\, g_d(\tilde{\omega})\, g_c(\Omega-\tilde{\omega}) \tag{3.45a}$$

$$\overset{\text{(iii)}}{\approx} \frac{U^2\rho}{2V} \int_{-\infty}^{\infty} \mathrm{d}\tilde{\omega}\, \mathcal{P}\frac{1}{\tilde{\omega}}\, \mathrm{sgn}(\Omega-\tilde{\omega})\Theta(\xi_0 - |\Omega-\tilde{\omega}|) \tag{3.45b}$$

$$\overset{\text{(iv)}}{\approx} \frac{U^2\rho}{2V} \int_{-\xi_0}^{\xi_0} \mathrm{d}\tilde{\omega}\, \mathcal{P}\frac{1}{\tilde{\omega}}\, \mathrm{sgn}(\Omega-\tilde{\omega}) \tag{3.45c}$$

$$\overset{|\Omega|\leq\xi_0}{=} -g^2 \frac{V}{\rho} \int_{|\Omega|}^{\xi_0} \mathrm{d}|\tilde{\omega}|\, \frac{1}{|\tilde{\omega}|} \tag{3.45d}$$

$$= g^2 \frac{V}{\rho} \ln \frac{|\Omega|}{\xi_0}. \tag{3.45e}$$

Let us compare the above results to the exact values determined in Sec. 3.3.5. The approximate result (3.44e) of the particle-hole bubble matches the leading behavior (3.31d) of the exact value. And the approximate result (3.45e) of the particle-particle bubble matches the leading behavior (3.33c) of the exact value. Thus, the approximations (iii) and (iv) capture the leading logarithms of the bubbles. This capability is decisive for the general justification of these approximations because the bubbles are the building blocks of all relevant diagrams.

We now determine the region of the internal deep-state frequency $\tilde{\omega}$ that gives rise to the leading logarithm in Eq. (3.44). On the one hand, for $|\tilde{\omega}| < |X|$ contributions from positive and negative $\tilde{\omega}$ cancel out thanks to the principal value; for $|\tilde{\omega}| > |X|$ the sign function prevents this cancellation. On the other hand, the region $\xi_0/10 < |\tilde{\omega}| < \xi_0$ yields only the constant term $g^2 V \ln(10)/\rho$. In conclusion, $|X| < |\tilde{\omega}| \ll \xi_0$ is the relevant region for the leading logarithm of the particle-hole bubble. Analogously, $|\Omega| < |\tilde{\omega}| \ll \xi_0$ is the relevant region for the leading logarithm of the particle-particle bubble.

3.4.4 Approximating the crossed bubble

We calculate the crossed bubble via the approximation scheme of Roulet et al. Steps (iii) and (iv) are used as for the bare bubbles. Here, we additionally demonstrate step (v), which applies to all parquet diagrams with crossed channels, i.e. to all non-ladder parquet diagrams. We verify that these approximations reproduce the leading behavior of the crossed bubble, which is obtained in Sec. 3.3.6 via an expansion of the exact value.

Let us copy the definition (3.34) of the crossed bubble for convenience,

$B^{(\mathrm{c})}(X,\omega) =$ 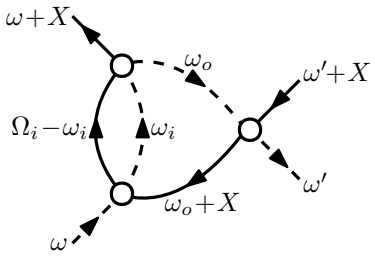

with $\Omega_i = \omega_o + \omega + X$ (3.46a)

$$= \mathrm{i}^2 U^3 \int_{-\infty}^{\infty} \frac{\mathrm{d}\omega_o}{2\pi} \int_{-\infty}^{\infty} \frac{\mathrm{d}\omega_i}{2\pi}\, g_d(\omega_o)\, g_c(\omega_o + X)\, g_d(\omega_i)\, g_c(\Omega_i - \omega_i). \quad (3.46\mathrm{b})$$

As this diagram is an example for the crossing of the channels, the bubbles influence each other through their frequency variables. In leading logarithmic order, we expect that each bubble contributes one logarithmic factor $g\ln$ to the value of the diagram [RGN69].

At this point the mechanism that justifies approximations (iii) and (iv) even for non-ladder parquet diagrams becomes transparent. We use the insights obtained in Sec. 3.4.3 about which frequency region gives rise to the leading logarithm of a single bubble. Let us first discuss the external frequencies. If we insert the crossed bubble for the 1PI two-particle vertex function in Fig. 3.1, which is the diagrammatic representation of $\chi(\nu)$, then X is equal to the X-ray frequency ν. We are interested in the behavior near threshold, i.e. $|X| = |\nu| \ll \xi_0$. The leading logarithms of the two extra bubbles with deep-state frequencies ω, ω' that appear in Fig. 3.1 come from the regions $|X| < |\omega^{(\prime)}| \ll \xi_0$. So we want to approximate the crossed bubble for $|X| < |\omega| \ll \xi_0$.

The leading logarithm of the outer bubble comes from $|X| < |\omega_o| \ll \xi_0$. The conditions $|\omega_o|, |\omega|, |X| \ll \xi_0$ together imply

$$|\Omega_i| = |\omega_o + \omega + X| \ll \xi_0. \quad (3.47)$$

The leading logarithm of the inner bubble then comes from $|\Omega_i| < |\omega_i| \ll \xi_0$.

In Sec. 3.4.3 we have seen that approximations (iii) and (iv) capture the leading behavior of a single bubble if its natural frequency is $\ll \xi_0$. Here, this condition is satisfied for both the outer and the inner bubble. Performing these approximations

yields

$$B^{(\mathrm{c})}(X,\omega) \overset{\text{(iii)}}{\approx} \frac{U^3\rho^2}{4V^2}\int_{-\infty}^{\infty}\mathrm{d}\omega_o\int_{-\infty}^{\infty}\mathrm{d}\omega_i\,\mathcal{P}\frac{1}{\omega_o}\operatorname{sgn}(\omega_o+X)\Theta(\xi_0-|\omega_o+X|) \\ \times\mathcal{P}\frac{1}{\omega_i}\operatorname{sgn}(\Omega_i-\omega_i)\Theta(\xi_0-|\Omega_i-\omega_i|) \tag{3.48a}$$

$$\overset{\text{(iv)}}{\approx} \frac{U^3\rho^2}{4V^2}\int_{-\xi_0}^{\xi_0}\mathrm{d}\omega_o\int_{-\xi_0}^{\xi_0}\mathrm{d}\omega_i\,\mathcal{P}\frac{1}{\omega_o}\operatorname{sgn}(\omega_o+X)\,\mathcal{P}\frac{1}{\omega_i}\operatorname{sgn}(\Omega_i-\omega_i). \tag{3.48b}$$

The integral of the inner bubble is

$$\int_{-\xi_0}^{\xi_0}\mathrm{d}\omega_i\,\mathcal{P}\frac{1}{\omega_i}\operatorname{sgn}(\Omega_i-\omega_i) = \Theta(\xi_0-|\Omega_i|)\,2\ln\frac{|\Omega_i|}{\xi_0}. \tag{3.49}$$

We drop the step function $\Theta(\xi_0-|\Omega_i|)$ because we have already verified $|\Omega_i|\ll\xi_0$ as far as the leading logarithms are concerned, see Eq. (3.47). Alternatively, the step function $\Theta(\xi_0-|\Omega_i|)=\Theta(\xi_0-|\omega_o+\omega+X|)$ can be interpreted as a small shift of the integration boundaries for ω_o so approximation (iv) is applicable. Either way, we obtain

$$B^{(\mathrm{c})}(X,\omega)\approx\frac{g^3V}{2\rho}\int_{-\xi_0}^{\xi_0}\mathrm{d}\omega_o\,\mathcal{P}\frac{1}{\omega_o}\operatorname{sgn}(\omega_o+X)\ln\frac{|\omega_o+\omega+X|}{\xi_0}. \tag{3.50}$$

As the final step, we apply the logarithmic approximation (v) by replacing

$$|\omega_o+\omega+X|\to\max\{|\omega_o|,|\omega|,|X|\}. \tag{3.51}$$

This replacement is wrong by more than a factor $O(1)$ only in a small integration region that gives a negligible contribution to the leading logarithm of the outer bubble [RGN69]. Straightforwardly solving the remaining integral, we arrive at the leading behavior of the crossed bubble for $|X|<|\omega|\ll\xi_0$,

$$B^{(\mathrm{c})}(X,\omega)\approx g^3\frac{V}{\rho}\left(\ln\frac{|\omega|}{|X|}\ln\frac{|\omega|}{\xi_0}-\frac{1}{2}\ln^2\frac{|\omega|}{\xi_0}\right). \tag{3.52}$$

This expression agrees with the expansion (3.41) of the exact value, confirming that approximations (iii)-(v) capture the leading logarithms of the crossed bubble. From this example it is evident that the justification can be transferred to higher-order parquet diagrams with more and more nested bubbles.

We conclude the discussion of the crossed bubble with an observation about the internal frequency variables. Within leading logarithmic order, we have seen that $|\Omega_i|<|\omega_i|$ and we have replaced $|\Omega_i|$ with $\max\{|\omega_o|,|\omega|,|X|\}$. As a consequence we find that $|\omega_o|<|\omega_i|$: the absolute value of the deep-state frequency of the outer bubble is less than the absolute value of the deep-state frequency of the inner bubble. This relation can be generalized to all parquet diagrams, see Sec. 3.4.5.

3.4.5 Integral equations for γ

As a preparation for a comparison with our FRG approach, we discuss how Roulet et al. proceeded to manipulate the parquet equations. Starting from the exact parquet equations, they applied approximations (i)-(v) and obtained [RGN69: Eq. (34)]

$$\gamma_1(t_1,t_2,\alpha) = -\nu_0 \int_0^\alpha \mathrm{d}t_i\, I_1(\min\{t_1,t_i\}) \left[I_1(\min\{t_2,t_i\}) + \gamma_1(t_i,t_2,\alpha)\right] \tag{3.53a}$$

$$\bar{\gamma}_2(t_1,t_2,\beta) = \nu_0 \int_0^\beta \mathrm{d}t_i\, \bar{I}_2(\min\{t_1,t_i\}) \left[\bar{I}_2(\min\{t_2,t_i\}) + \bar{\gamma}_2(t_i,t_2,\beta)\right] \tag{3.53b}$$

$$I_1(t) = V + \bar{\gamma}_2(t) \tag{3.53c}$$

$$\bar{I}_2(t) = V + \gamma_1(t). \tag{3.53d}$$

In this entire Sec. 3.4.5, we use the original notation of Ref. [RGN69], which will be explained in the following paragraphs. On the level of individual diagrams, we have seen that the approximations significantly simplify the calculations. On the level of the parquet equations, the approximations allow for an analytical solution: Roulet et al. solved Eq. (3.53) without further approximations.

The basic structure of the parquet equations is still recognizable in the approximated form (3.53). The underlying idea is the following [RGN69]. Decompose the 1PI two-particle vertex function γ into $\gamma_1 + \gamma_2 + R$, where γ_1 is reducible in the particle-particle channel, γ_2 is reducible in the exchange particle-hole channel, and R is irreducible in either channel. The last part has been replaced with the bare vertex, $R = V$, see approximation (i). To get the parquet equation for γ_1, identify in each contributing diagram the first outermost bubble from the left. When all these diagrams are added up, the irreducible part $I_1 = V + \gamma_2$ appears to the left of the selected bubble while the full γ appears to the right. The deep-state frequency of the selected bubble remains to be integrated over. To get the parquet equation for γ_2, proceed analogously. Obviously, the two equations are coupled.

Let us explain the notation in Eq. (3.53) in more detail. As the independent frequency arguments of the reducible parts, Roulet et al. use the incoming deep-state frequency, the outgoing deep-state frequency, and the natural frequency of the respective channel. Similar to our convention from Eq. (3.27), the overbar indicates which frequency is used as the third argument: γ_1 depends on the total frequency Ω, while $\bar{\gamma}_2$ depends on the exchange frequency X. In the approximated parquet equations, γ_1 and $\bar{\gamma}_2$ are independent of their first two frequency arguments as long as these are smaller than the third frequency argument in terms of absolute values. Because of the logarithmic approximation (v), this is the case whenever the channels are crossed and Roulet et al., as a shorthand notation, then dropped the first two frequency arguments.

Furthermore, each frequency variable ω is transformed into a logarithmic variable $t = \ln(\xi_0/|\omega|)$. The logarithmic variables α and β correspond to the frequencies Ω and X. Note that $t(|\omega|)$ is a strictly decreasing function so the maximum introduced in approximation (v) becomes a minimum in Eq. (3.53). Each explicit bubble integral involves a deep-state propagator and a local conduction-electron propagator, the values

of which have been absorbed into the integration variable and into the integration boundaries.

From the parquet equations (3.53), we derive a strict partial order of the deep-state frequencies. To this end we consider formally solving these equations by successively inserting them into their right-hand sides. The nesting of the integrals mimics the construction of the parquet diagrams via successive insertions of bubbles, see Sec. 3.4.1: each newly inserted integral corresponds to a newly inserted bubble, which has replaced a bare vertex. Regarding a nesting with opposite channels, the old integral corresponds to the outer bubble and the new integral to the inner bubble. The integration variable t_{outer} is greater than or equal to the minima that appear as arguments of the irreducible parts I_1 or $\bar{I}_2$. These minima then take on the role of the third argument of the inner bubble and thus appear as upper boundary for the integration variable t_{inner} so that $t_{\text{outer}} > t_{\text{inner}}$. Equivalently, the absolute value of the frequency of the outer bubble is a lower bound for the absolute value of the frequency of the inner bubble, $|\omega_{\text{outer}}| < |\omega_{\text{inner}}|$. The new bubble automatically inherits the lower bounds from the old bubble, just like it inherits the list of outer bubbles. Regarding a nesting with equal channels, neither the old nor the new bubble is inner to the other. In this case the integration regions are identical, so the new and old integration variables are not bounded by each other. In terms of absolute values of frequencies, the new bubble thereby inherits the lower bounds from the old bubble, just like it inherits the list of outer bubbles.

In summary, we find a strict partial order of the deep-state frequencies that mimics the strict partial order "being inner to" of the bubbles: Whenever a bubble is inner to another bubble, the integration region is restricted by

$$|\omega_{\text{outer}}| < |\omega_{\text{inner}}| \tag{3.54}$$

as far as the leading logarithms are concerned. Similar observations are described in Refs. [Abr65, BBD03]. This property of the leading logarithms is the reason why they are captured by a one-loop truncation in our FRG approach.

In the solution of the approximated parquet equations (3.53), a central step is what Roulet et al. referred to as a "trick by Abrikosov and Sudakov" [Sud56, Abr65]. This trick is a way of rewriting the basic structure of the parquet equations, which we have briefly described above. Instead of singling out the first outermost bubble from the left, one identifies the outermost bubble with the smallest absolute value of the deep-state frequency, which we denote by $|\omega_{\text{min}}|$. Because of the partial order discussed above, $|\omega_{\text{min}}|$ is the smallest absolute value of all deep-state frequencies. When all diagrams reducible in a given channel are added up, the full $\gamma = \gamma_1 + \gamma_2 + R$ appears to both sides of the bubble. The absolute values of all deep-state frequencies appearing in these factors γ are then restricted to be $\geq |\omega_{\text{min}}|$.

Roulet et al. performed this trick in terms of the logarithmic variables, i.e. they identified the bubble with the greatest t. The rewritten parquet equations read

[RGN69: Eqs. (A1) and (A2)]

$$\gamma_1(t_1,t_2,\alpha) = -\nu_0 \int_0^\alpha \mathrm{d}t \left[I_1(\min\{t_1,t\}) + \gamma_1(t_1,t,t)\right]\left[I_1(\min\{t_2,t\}) + \gamma_1(t,t_2,t)\right] \tag{3.55a}$$

$$\bar{\gamma}_2(t_1,t_2,\beta) = \nu_0 \int_0^\beta \mathrm{d}t \left[\bar{I}_2(\min\{t_1,t\}) + \bar{\gamma}_2(t_1,t,t)\right]\left[\bar{I}_2(\min\{t_2,t\}) + \bar{\gamma}_2(t,t_2,t)\right]. \tag{3.55b}$$

They are equivalent to Eqs. (3.53a) and (3.53b).

3.4.6 Result for the X-ray-absorption rate

Here, we briefly sketch how Roulet et al. proceeded to determine the X-ray-absorption rate. We return to using our own notation.

Roulet et al. solved the integral equations (3.55) exactly by performing a case distinction for the logarithmic variables and obtained the 1PI two-particle vertex function γ. They inserted this result into an equation conforming with our Eq. (3.28) to get the particle-hole susceptibility $\chi(\nu)$. In the two additional bubble integrals, they applied the same approximations, specifically (ii)-(v), as in the parquet equations. The result for the particle-hole susceptibility is [RGN69: Eq. (42)]

$$\chi(\nu) = -\frac{\rho}{2gV}\left[\left(\frac{\xi_0}{|\nu|}\right)^{2g} - 1\right]. \tag{3.56}$$

However, Eq. (3.56) is only the leading-logarithmic approximation of the real part $\operatorname{Re}\chi(\nu)$. It accounts for all terms of the form $g^n \ln^{n+1}(|\nu|/\xi_0)$. The leading contributions to the imaginary part have one logarithm less and have been neglected. Roulet et al. described how to reconstruct the leading-logarithmic approximation of $\operatorname{Im}\chi(\nu)$ from Eq. (3.56), e.g. via a Kramers-Kronig relation.

Finally, the equation $R(\nu) = -2\,|W|^2 \operatorname{Im}\chi(\nu)$ gives the X-ray-absorption rate

$$R(\nu) = 2\pi \frac{\rho}{V}\,|W|^2 \left(\frac{\xi_0}{\nu}\right)^{2g} \Theta(\nu). \tag{3.57}$$

This leading approximation of $R(\nu)$ has been verified by an exact solution of the X-ray-edge model [ND69].

3.5 FRG approach

In the following we devise a specific one-loop 1PI FRG approach to the X-ray-edge model that is based on the zero-temperature formalism, see Chap. 2. The goal is to obtain the correct leading-logarithmic result for the X-ray-absorption rate. To achieve this we perform approximations analogous to those of Roulet et al. [RGN69], which are listed in Sec. 3.4.2. We discuss why a *one-loop* truncation suffices to capture the leading logarithms. In fact, we show that the parquet-based scheme by Roulet et al. and the following FRG approach are completely equivalent.

3.5.1 Cutoff and initial conditions

We choose to employ a sharp frequency cutoff that is inserted only into the real part of the free deep-state propagator

$$g_d^\lambda(\omega) = \Theta(|\omega| - \lambda)\frac{1}{\omega} + \mathrm{i}\pi\delta(\omega). \tag{3.58}$$

No cutoff is introduced into the conduction-state propagator. For the initial value of the flow parameter, we will consider the limit $\lambda_{\text{ini}} \to \infty$. At the final value $\lambda_{\text{fin}} = 0$, the original model is recovered.

In the following we determine the initial values of the 1PI vertex functions, starting with the first order of the self-energy. The deep-state Hartree diagram (3.14), which consists of a single conduction-state loop, is not affected by the cutoff. At λ_{ini} the conduction-state Hartree diagram (3.15) evaluates to

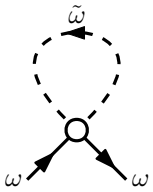

$$= -\mathrm{i}U\int_{-\infty}^{\infty}\frac{\mathrm{d}\tilde{\omega}}{2\pi}\, g_d^{\lambda_{\text{ini}}}(\tilde{\omega}) = -\mathrm{i}U\int_{-\infty}^{\infty}\frac{\mathrm{d}\tilde{\omega}}{2\pi}\, e^{\mathrm{i}\tilde{\omega}\eta'}\left[\frac{\Theta(|\tilde{\omega}| - \lambda_{\text{ini}})}{\tilde{\omega}} + \mathrm{i}\pi\delta(\tilde{\omega})\right] = U, \tag{3.59}$$

which is the same as without cutoff. In Eq. (3.59) a convergence factor $e^{\mathrm{i}\tilde{\omega}\eta'}$ with $\eta' \to 0^+$ has been included as part of the free deep-state propagator, as required for Hartree-type propagator loops, see Eq. (2.47b). Here, it is important to take the limit $\eta' \to 0^+$ before the limit $\lambda_{\text{ini}} \to \infty$. The Hartree diagrams still exactly cancel with the single-particle vertices (3.13). So we have to account for neither Hartree diagrams nor single-particle vertices in the remaining calculation of the initial values.

Let us now consider an arbitrary 1PI diagram with at least two two-particle vertices and conclude that its initial value is negligible. If it contains a deep-state propagator that connects two different vertices, this propagator is replaced by its delta-function part at λ_{ini}. The result is negligible in leading logarithmic order according to Roulet et al. [RGN69]. If the diagram does not contain any such deep-state propagator, then all its external legs are deep-state ones. But a 1PI subdiagram of this form does not enter the parquet diagrams that contain the leading logarithms, see Sec. 3.4.1.

In the leading-logarithmic approximation, the initial conditions are thus fully determined by diagrams with only one two-particle vertex. Consequently, the initial value of the 1PI two-particle vertex is given by the bare two-particle vertex,

$$\hat{\gamma}_{\lambda_{\text{ini}}}(\omega, \omega'; \Omega) = U = \bar{\gamma}_{\lambda_{\text{ini}}}(\omega, \omega'; X), \tag{3.60}$$

while the initial values of all other 1PI vertex functions, including the self-energy, vanish.

3.5.2 Truncation

In order to truncate and solve the set of FRG flow equations, we neglect the flow of the self-energy and of the 1PI three-particle vertex so that the values of both remain

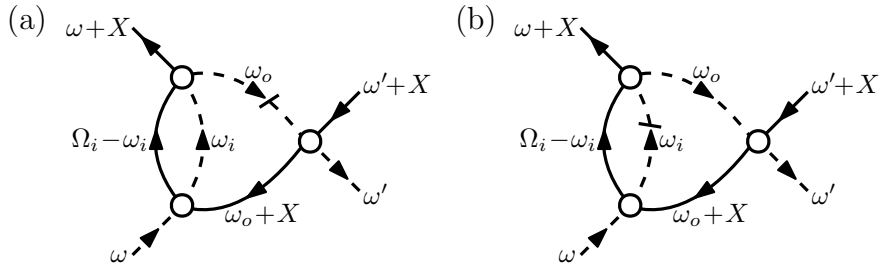

Figure 3.2: The diagrammatic contributions to $\mathrm{d}\gamma_\lambda/\mathrm{d}\lambda$ that result from taking the derivative of the crossed bubble (3.34). Again, Ω_i stands for $\omega_o + \omega + X$. In each diagram the crossed-out dashed line represents the differentiated deep-state propagator. (a) A leading contribution. Removing the crossed-out line, which is in the outer bubble, would render the diagram one-particle reducible. (b) A subleading contribution. Removing the crossed-out line, which is in the inner bubble, would leave the diagram one-particle irreducible.

zero. This means that we set the right-hand side of Eq. (2.61) to zero and neglect the first addend on the right-hand side of Eq. (2.62). Neglecting the self-energy for the leading-logarithmic approximation is a step directly carried over from the diagrammatic discussion of Roulet et al. [RGN69].

Let us clarify why the 1PI three-particle vertex does not affect the leading logarithmic order of the 1PI two-particle vertex via the flow equations. The argument is based on the properties of individual diagrams. In the diagrammatic derivation of the flow equation for the 1PI two-particle vertex γ_λ, see Ref. [JMS07], the derivative with respect to the flow parameter acts on each of the contributing diagrams. In each diagram, according to the product rule, every deep-state propagator needs to be differentiated. Therefore, $\mathrm{d}\gamma_\lambda/\mathrm{d}\lambda$ is represented by a sum of diagrams in each of which the derivative acts on some particular dashed line; examples for this type of diagram are shown in Fig. 3.2. Let us now consider any such diagram that results from differentiating one of the parquet diagrams as those contain all of the important contributions. Because of the sharp cutoff (3.58), the frequency of the differentiated propagator satisfies $|\omega| = \lambda$. With regard to the real parts of the deep-state propagators, this frequency has the smallest absolute value of all deep-state frequencies. As far as the leading logarithms are concerned, the differentiated propagator then has to be in one of the outermost bubbles because of the strict partial order discussed in Sec. 3.4.5. Removing this propagator would render the diagram one-particle *reducible*. In contrast all diagrams contributing to $\mathrm{d}\gamma_\lambda/\mathrm{d}\lambda$ that stem from the 1PI three-particle vertex, i.e. that represent the first term in Eq. (2.62), would remain one-particle *irreducible* if the respective differentiated propagator was removed. Consequently, the leading logarithmic contributions cannot originate from the 1PI three-particle vertex so that it can indeed be neglected. This shows that, for a sharp frequency cutoff in the deep-state propagator, a *one-loop* truncation already captures all important contributions of the parquet diagrams even though it does not account for the exact values of these diagrams.

As an example we illustrate the above argument for the crossed bubble (3.34).

Its derivative with respect to λ is the sum of the two diagrams shown in Fig. 3.2. If we removed the respective differentiated propagator, diagram (a) would become one-particle reducible, whereas diagram (b) would remain one-particle irreducible, i.e. the latter stems from the 1PI three-particle vertex. In diagram (a) the frequencies (of the real parts of the deep-state propagators) satisfy $|\omega_o| = \lambda \leq |\omega_i|$ and in diagram (b) they satisfy $|\omega_o| \geq \lambda = |\omega_i|$. Since we have shown in Sec. 3.4.4 that only the integration region $|\omega_o| < |\omega_i|$ gives rise to the leading logarithms of the crossed bubble, the contribution to the flow represented by diagram (b) is negligible.

3.5.3 Approximating the flow equation of γ

Following Roulet et al. [RGN69], we approximate the propagators by neglecting the imaginary part of the free deep-state propagator and the real part of the local conduction-electron propagator because they do not give rise to the logarithmic divergence in a bubble, cf. Sec. 3.4.3. This step can be performed only after the evaluation of Eq. (3.59) for the initial conditions, where the imaginary part of the free deep-state propagator contributes half of the result. Within these approximations the local conduction-electron propagator does not depend on the flow parameter and is given by

$$g_c(\omega) = -\mathrm{i}\pi \frac{\rho}{V} \operatorname{sgn}(\omega) \Theta(\xi_0 - |\omega|) \tag{3.61}$$

and the single-scale propagator assumes the form

$$S_d^\lambda(\omega) = \frac{\mathrm{d}}{\mathrm{d}\lambda} g_d^\lambda(\omega) = -\frac{\delta(|\omega| - \lambda)}{\omega}. \tag{3.62}$$

There remains to be solved the flow equation of the 1PI two-particle vertex. While its general form is as stated in Eq. (2.62), it now assumes the closed form

$$\begin{aligned}
&\frac{\mathrm{d}}{\mathrm{d}\lambda} \hat{\gamma}_\lambda(\omega, \omega'; \Omega) \\
&= \frac{\mathrm{d}}{\mathrm{d}\lambda} \bar{\gamma}_\lambda(\omega, \omega'; X) && \text{(3.63a)} \\
&= -\frac{\rho}{2V} \int_{-\infty}^{\infty} \mathrm{d}\tilde{\omega}\, \delta(|\tilde{\omega}| - \lambda) \frac{1}{\tilde{\omega}} \Big[\hat{\gamma}_\lambda(\omega, \tilde{\omega}; \Omega)\, \hat{\gamma}_\lambda(\tilde{\omega}, \omega'; \Omega) \operatorname{sgn}(\Omega - \tilde{\omega}) \Theta(\xi_0 - |\Omega - \tilde{\omega}|) \\
&\quad + \bar{\gamma}_\lambda(\omega, \tilde{\omega}; X)\, \bar{\gamma}_\lambda(\tilde{\omega}, \omega'; X) \operatorname{sgn}(\tilde{\omega} + X) \Theta(\xi_0 - |\tilde{\omega} + X|) \Big], && \text{(3.63b)}
\end{aligned}$$

where the frequency arguments are related via $\Omega - X = \omega + \omega'$. The diagrammatic representation of this equation is shown in Fig. 3.3. In writing Eq. (3.63) we consider the flow only of $\gamma^\lambda_{dc|dc}$ because it is the sole part of the 1PI vertex needed to calculate the particle-hole susceptibility (3.28). We do not consider the flow of $\gamma^\lambda_{cc|cc}$ because it does not influence the flow of $\gamma^\lambda_{dc|dc}$: the single-scale propagator, which has only deep-state indices, cannot be attached to $\gamma^\lambda_{cc|cc}$. We neither consider the flow of $\gamma^\lambda_{dd|dd}$. Its flow equation and its contribution to the flow of $\gamma^\lambda_{dc|dc}$ both involve a bubble with two deep-state propagators. Consequently, its influence is subleading, see Sec. 3.4.1. As a result of neglecting $\gamma^\lambda_{dd|dd}$, the direct particle-hole channel is absent in Eq. (3.63).

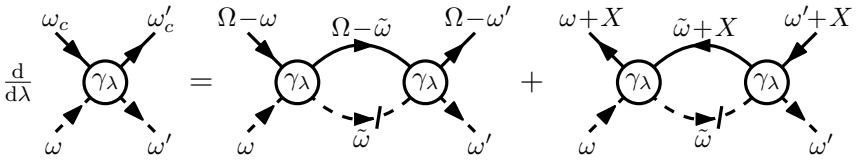

Figure 3.3: Diagrammatic representation of the flow equation (3.63) of the 1PI two-particle vertex. The crossed-out dashed line stands for the single-scale propagator S_d^λ. The first term represents the particle-particle channel while the second term represents the (exchange) particle-hole channel. The external frequencies are related via $\omega_c = \Omega - \omega = \omega' + X$ and $\omega_c' = \Omega - \omega' = \omega + X$.

We perform a channel decomposition by defining $\mathrm{d}\hat{\gamma}_\lambda^{\mathrm{pp}}(\omega,\omega';\Omega)/\mathrm{d}\lambda$ as the first addend on the right-hand side of Eq. (3.63) and $\mathrm{d}\bar{\gamma}_\lambda^{\mathrm{ph}}(\omega,\omega';X)/\mathrm{d}\lambda$ as the second addend. For the choice $\hat{\gamma}_{\lambda_{\mathrm{ini}}}^{\mathrm{pp}}(\omega,\omega';\Omega) = 0 = \bar{\gamma}_{\lambda_{\mathrm{ini}}}^{\mathrm{ph}}(\omega,\omega';X)$, a formal integration of the flow equation leads to the decomposition of the 1PI two-particle vertex

$$\hat{\gamma}_\lambda(\omega,\omega';\Omega) = \bar{\gamma}_\lambda(\omega,\omega';X) = U + \hat{\gamma}_\lambda^{\mathrm{pp}}(\omega,\omega';\Omega) + \bar{\gamma}_\lambda^{\mathrm{ph}}(\omega,\omega';X), \tag{3.64}$$

where $\Omega - X = \omega + \omega'$. Equation (3.63) can then be rewritten in terms of the two coupled flow equations

$$\begin{aligned}
\frac{\mathrm{d}}{\mathrm{d}\lambda}\hat{\gamma}_\lambda^{\mathrm{pp}}(\omega,\omega';\Omega) = &-\frac{\rho}{2V}\sum_{\tilde{\omega}=\pm\lambda}\frac{1}{\tilde{\omega}}\,\mathrm{sgn}(\Omega-\tilde{\omega})\Theta(\xi_0-|\Omega-\tilde{\omega}|)\\
&\times\Big[U+\hat{\gamma}_\lambda^{\mathrm{pp}}(\omega,\tilde{\omega};\Omega)+\bar{\gamma}_\lambda^{\mathrm{ph}}(\omega,\tilde{\omega};\Omega-\omega-\tilde{\omega})\Big] \qquad (3.65a)\\
&\times\Big[U+\hat{\gamma}_\lambda^{\mathrm{pp}}(\tilde{\omega},\omega';\Omega)+\bar{\gamma}_\lambda^{\mathrm{ph}}(\tilde{\omega},\omega';\Omega-\tilde{\omega}-\omega')\Big]\\
\frac{\mathrm{d}}{\mathrm{d}\lambda}\bar{\gamma}_\lambda^{\mathrm{ph}}(\omega,\omega';X) = &-\frac{\rho}{2V}\sum_{\tilde{\omega}=\pm\lambda}\frac{1}{\tilde{\omega}}\,\mathrm{sgn}(\tilde{\omega}+X)\Theta(\xi_0-|\tilde{\omega}+X|)\\
&\times\Big[U+\hat{\gamma}_\lambda^{\mathrm{pp}}(\omega,\tilde{\omega};\omega+\tilde{\omega}+X)+\bar{\gamma}_\lambda^{\mathrm{ph}}(\omega,\tilde{\omega};X)\Big] \qquad (3.65b)\\
&\times\Big[U+\hat{\gamma}_\lambda^{\mathrm{pp}}(\tilde{\omega},\omega';\tilde{\omega}+\omega'+X)+\bar{\gamma}_\lambda^{\mathrm{ph}}(\tilde{\omega},\omega';X)\Big].
\end{aligned}$$

These are the contributions to the flow in the particle-particle and particle-hole channel, respectively. In the diagrammatic language, Eq. (3.65a) gives rise to diagrams that can be disconnected by cutting two parallel lines, whereas the diagrams resulting from Eq. (3.65b) can be disconnected by cutting two antiparallel lines. Since a diagram of one type can appear as a subdiagram in diagrams of the other type, the two differential equations are coupled. For the contribution from each channel, we have employed the notation that features the respective natural frequency, see Eqs. (3.27), (3.30), and (3.32).

Next, we replace the step functions $\Theta(\xi_0-|\Omega\mp\lambda|)$ and $\Theta(\xi_0-|\pm\lambda+X|)$ occurring in Eq. (3.65) with $\Theta(\xi_0-\lambda)$. When compared with the parquet-based scheme by Roulet et al. [RGN69], this corresponds to neglecting small shifts of the boundaries for the frequency integrations of the bubbles. To motivate this approximation here,

consider integrating the flow equations by applying $-\int_0^{\lambda_{\mathrm{ini}}} \mathrm{d}\lambda \ldots$ The resulting λ-integrals take on the role of the frequency integrals of the bubbles. Provided that $|\Omega| \ll \xi_0$ or $|X| \ll \xi_0$, respectively, the replacement above is wrong only for certain $\lambda \approx \xi_0$, but the leading contribution that builds the logarithm comes from $\lambda \ll \xi_0$. Indeed, said conditions are satisfied: For the particle-hole susceptibility (3.28) near threshold, the values of $\hat{\gamma}^{\mathrm{pp}}_{\lambda=0}(\omega, \omega'; \omega + \omega' + \nu)$ and $\bar{\gamma}^{\mathrm{ph}}_{\lambda=0}(\omega, \omega'; \nu)$ are important only for $|\omega|, |\omega'|, |\nu| \ll \xi_0$; it follows that the values of $\hat{\gamma}^{\mathrm{pp}}_{\lambda}$ and $\bar{\gamma}^{\mathrm{ph}}_{\lambda}$ are relevant only with all frequency arguments being small – even for the cross-feedback terms in Eq. (3.65), analogously to Eq. (3.47) in the context of the crossed bubble. Consequently, the error made by replacing the step functions is negligible. Because of the factors $\Theta(\xi_0 - \lambda)$, the actual flow now starts at $\lambda = \xi_0$.

We now make an assumption that we will later show to be correct within logarithmic accuracy based on a self-consistency argument: We assume that the relations

$$\hat{\gamma}^{\mathrm{pp}}_{\lambda}(\omega, \omega'; \Omega) = \hat{\gamma}^{\mathrm{pp}}_{\lambda}(|\omega|, |\omega'|; \max\{\lambda, |\Omega|\}) \tag{3.66a}$$

$$\bar{\gamma}^{\mathrm{ph}}_{\lambda}(\omega, \omega'; X) = \bar{\gamma}^{\mathrm{ph}}_{\lambda}(|\omega|, |\omega'|; \max\{\lambda, |X|\}) \tag{3.66b}$$

hold, which are trivially satisfied at the start of the flow. We use these relations to rewrite the vertex functions appearing on the right-hand side of the flow equations (3.65).

In the terms representing the cross feedback, we subsequently approximate the third frequency argument. For example, in the term $\hat{\gamma}^{\mathrm{pp}}_{\lambda}(\omega, \pm\lambda; \omega \pm \lambda + X) = \hat{\gamma}^{\mathrm{pp}}_{\lambda}(|\omega|, \lambda; \max\{\lambda, |\omega \pm \lambda + X|\})$ appearing in Eq. (3.65b), we approximate

$$\max\{\lambda, |\omega \pm \lambda + X|\} \approx \max\{\lambda, |\omega|\}. \tag{3.67}$$

This step corresponds to what Roulet et al. [RGN69] called the logarithmic approximation. Here, it can be justified as follows. For $\lambda \geq |X|$ the approximation (3.67) is correct within a factor of three. Such a factor is negligible because, based on the considerations of Roulet et al., we expect $\hat{\gamma}^{\mathrm{pp}}_{\lambda}$ to be a slowly varying function of its arguments; this expectation will be confirmed by the final result. For $\lambda < |X|$ the two summands for $\tilde{\omega} = \pm\lambda$ cancel each other at least to a large extent because the factor $\mathrm{sgn}(\pm\lambda + X)$ does not cancel the sign of $1/(\pm\lambda)$ anymore. Consequently, the final part with $\lambda < |X|$ of the flow in the particle-hole channel does not contribute to building the leading logarithms. This corresponds to the observation that small frequencies with $|\tilde{\omega}| < |X|$ do not contribute to the logarithmic divergence of the bare particle-hole bubble, see Sec. 3.4.3. For the other cross-feedback terms in the flow equations, we apply approximations analogous to Eq. (3.67). The justification is similar. This constitutes our last approximation.

Since the vertex functions occurring in the flow equations do not depend on the sign of $\tilde{\omega} = \pm\lambda$ anymore, we can easily perform the sums over $\tilde{\omega}$ in Eq. (3.65), e.g.

$$\sum_{\tilde{\omega}=\pm\lambda} \frac{1}{\tilde{\omega}} \mathrm{sgn}(\tilde{\omega} + X) = \frac{2}{\lambda} \Theta(\lambda - |X|). \tag{3.68}$$

A formal integration with respect to the flow parameter, starting from λ_{ini} down to some value λ, then leads to

$$\begin{aligned}\hat{\gamma}_{\lambda}^{\mathrm{pp}}(\omega,\omega';\Omega) = -\frac{\rho}{V}\int_{\max\{\lambda,|\Omega|\}}^{\xi_0}\frac{\mathrm{d}\lambda'}{\lambda'}\Big[U+\hat{\gamma}_{\lambda'}^{\mathrm{pp}}(|\omega|,\lambda';\lambda')+\bar{\gamma}_{\lambda'}^{\mathrm{ph}}(|\omega|,\lambda';\max\{\lambda',|\omega|\})\Big]\\ \times\Big[U+\hat{\gamma}_{\lambda'}^{\mathrm{pp}}(\lambda',|\omega'|;\lambda')+\bar{\gamma}_{\lambda'}^{\mathrm{ph}}(\lambda',|\omega'|;\max\{\lambda',|\omega'|\})\Big] \qquad (3.69a)\\ \bar{\gamma}_{\lambda}^{\mathrm{ph}}(\omega,\omega';X) = \frac{\rho}{V}\int_{\max\{\lambda,|X|\}}^{\xi_0}\frac{\mathrm{d}\lambda'}{\lambda'}\Big[U+\hat{\gamma}_{\lambda'}^{\mathrm{pp}}(|\omega|,\lambda';\max\{\lambda',|\omega|\})+\bar{\gamma}_{\lambda'}^{\mathrm{ph}}(|\omega|,\lambda';\lambda')\Big]\\ \times\Big[U+\hat{\gamma}_{\lambda'}^{\mathrm{pp}}(\lambda',|\omega'|;\max\{\lambda',|\omega'|\})+\bar{\gamma}_{\lambda'}^{\mathrm{ph}}(\lambda',|\omega'|;\lambda')\Big] \qquad (3.69b)\end{aligned}$$

for $\xi_0 > \lambda, |\Omega|, |X|$. As claimed above, the relations (3.66) follow from these flow equations and are thus validated within logarithmic accuracy: On the right-hand side of Eq. (3.69a), only the absolute values of ω and ω' enter and only $\max\{\lambda,|\Omega|\}$ appears with no separate dependence on λ or Ω; the analogue holds for the particle-hole channel. For this reason we can from now on even write $\hat{\gamma}_0^{\mathrm{pp}}$ and $\bar{\gamma}_0^{\mathrm{ph}}$ instead of $\hat{\gamma}_{\lambda'}^{\mathrm{pp}}$ and $\bar{\gamma}_{\lambda'}^{\mathrm{ph}}$ in the integrands in Eq. (3.69). Furthermore, the flow equations (3.69), in conjunction with the vanishing initial conditions, imply that $\hat{\gamma}_{\lambda}^{\mathrm{pp}}(\omega,\omega';\Omega)$ does not depend on $\omega^{(\prime)}$ if $|\omega^{(\prime)}| \leq |\Omega|$ and the same for $\bar{\gamma}_{\lambda}^{\mathrm{ph}}(\omega,\omega';X)$ if $|\omega^{(\prime)}| \leq |X|$. It is therefore reasonable to introduce the shorthand notation

$$\hat{\gamma}_{\lambda}^{\mathrm{pp}}(\Omega) = \hat{\gamma}_{\lambda}^{\mathrm{pp}}(\omega,\omega';\Omega) \qquad \text{if } |\omega|,|\omega'| \leq |\Omega| \qquad (3.70a)$$

$$\bar{\gamma}_{\lambda}^{\mathrm{ph}}(X) = \bar{\gamma}_{\lambda}^{\mathrm{ph}}(\omega,\omega';X) \qquad \text{if } |\omega|,|\omega'| \leq |X|. \qquad (3.70b)$$

With this the integrated flow equations at $\lambda_{\mathrm{fin}} = 0$ assume the form

$$\begin{aligned}\hat{\gamma}_{0}^{\mathrm{pp}}(\omega,\omega';\Omega) = -\frac{\rho}{V}\int_{|\Omega|}^{\xi_0}\frac{\mathrm{d}\lambda}{\lambda}\Big[U+\hat{\gamma}_{0}^{\mathrm{pp}}(|\omega|,\lambda;\lambda)+\bar{\gamma}_{0}^{\mathrm{ph}}(\max\{\lambda,|\omega|\})\Big]\\ \times\Big[U+\hat{\gamma}_{0}^{\mathrm{pp}}(\lambda,|\omega'|;\lambda)+\bar{\gamma}_{0}^{\mathrm{ph}}(\max\{\lambda,|\omega'|\})\Big] \qquad (3.71a)\\ \bar{\gamma}_{0}^{\mathrm{ph}}(\omega,\omega';X) = \frac{\rho}{V}\int_{|X|}^{\xi_0}\frac{\mathrm{d}\lambda}{\lambda}\Big[U+\hat{\gamma}_{0}^{\mathrm{pp}}(\max\{\lambda,|\omega|\})+\bar{\gamma}_{0}^{\mathrm{ph}}(|\omega|,\lambda;\lambda)\Big]\\ \times\Big[U+\hat{\gamma}_{0}^{\mathrm{pp}}(\max\{\lambda,|\omega'|\})+\bar{\gamma}_{0}^{\mathrm{ph}}(\lambda,|\omega'|;\lambda)\Big]. \qquad (3.71b)\end{aligned}$$

3.6 Comparison between the parquet-based and the FRG approach

The integrated flow equations (3.71) are, aside from notation, identical to the integral equations (A1) and (A2) of Roulet et al. [RGN69], which we have discussed in Sec. 3.4.5. From these equations Roulet et al. derived the X-ray-absorption rate as outlined in Sec. 3.4.6 and we adopt those steps. In conclusion our FRG approach leads to the same result as the leading-logarithmic parquet approximation. In particular, our FRG approach captures the leading logarithms.

Even the ways are equivalent, in which the parquet-based approach of Roulet et al. and our FRG approach derive these integral equations. Let us discuss this equivalence step by step, following the order used in Sec. 3.4.2.

In step (i) of the parquet approach, the diagrams under consideration are reduced to the parquet diagrams in the exchange particle-hole and particle-particle channel. Correspondingly, neglecting the three-particle vertex in the FRG approach reduces the diagrams to the parquet diagrams and neglecting $\gamma_{dd|dd}$ gets rid of the direct particle-hole channel. Note that neglecting the three-particle vertex in the presence of the sharp frequency cutoff additionally means that the integration regions of the frequencies are restricted. In the parquet approach, the same restriction appears as a by-product after all approximation steps have been applied, see the discussion of the strict partial order in Sec. 3.4.5.

Steps (ii) and (iii), which state that the self-energy and the real or imaginary parts of the free propagators are neglected, have been transferred one-to-one to the FRG approach. Step (iv) states that small shifts of the integration boundaries resulting from step functions are neglected; it is applied in the FRG approach as well – with the flow parameter taking on the role of the integration variable. The logarithmic approximation (v) is realized in the FRG approach through Eq. (3.67).

Finally, the parquet approach invokes the "trick by Abrikosov and Sudakov", which we have briefly described in Sec. 3.4.5. Identifying the smallest frequency and integrating over it corresponds to introducing the sharp frequency cutoff and formally integrating the flow equations. Figure 13 of Ref. [RGN69] illustrates this trick and can be understood as a precursor of our Fig. 3.3, which is the diagrammatic representation of the FRG flow equation of the 1PI two-particle vertex function. When comparing the figures, note that Fig. 13 of Ref. [RGN69] has wrongly directed deep-state lines, shows only the particle-particle channel, and only sketches how the irreducible parts I_1 are assembled into vertex functions γ on both sides.

In summary the two approaches are fully equivalent. Only the point at which the cutoff is introduced differs. The parquet approach uses the cutoff at the very end after all approximations have been applied to the parquet equations, whereas our FRG approach starts with the cutoff and applies the same approximations to the flow equations.

The detailed equivalence of our FRG approach to the parquet approach of Roulet et al. is possible only for the particular choice of cutoff. For other cutoffs that regularize the divergences of the bare bubbles during the entire flow, a one-loop truncation can be expected to capture the leading logarithms. But for ill-conceived cutoffs, the three-particle vertex is likely important already in the leading logarithmic order.

3.7 Transfer to the Matsubara formalism

The Matsubara formalism is the standard for FRG studies of condensed-matter systems. Reference [DJ24] transfers our approach from the zero-temperature formalism to the Matsubara formalism. This transfer is beyond the scope of this thesis, but we briefly summarize it in the following. The central point of Ref. [DJ24] is that also

a one-loop Matsubara FRG can capture the leading logarithms in the X-ray-edge model.

Within the Matsubara formalism, the temperature and the renormalized deep level have a regularizing effect on the logarithmic divergences. To allow for a comparison with our approach, Ref. [DJ24] focuses on the limit of vanishing temperature. The proper way to obtain results at vanishing temperature is to evaluate diagrams at finite temperature using discrete Matsubara frequencies and then take the limit. But for the parquet diagrams without self-energy insertions, aside from the already included single-particle perturbation and Hartree diagrams, one can instead take the limit of the propagators and then evaluate diagrams using continuous Matsubara frequencies.

Reference [DJ24] proceeds by setting the renormalized deep level to zero to make the logarithmic divergences clearly visible already on the imaginary frequency axis and not only after the analytic continuation to the real axis. Even though the ground state might not feature an occupied deep level anymore, Ref. [DJ24] shows that the parquet diagrams with the limit propagators and the renormalized deep level set to zero can be analytically continued to the diagrams in the zero-temperature formalism with respect to an occupied deep level. Our Ward identity within the zero-temperature formalism thus provides the relation to the physically relevant case, also for the respective susceptibilities as sums of these diagrams.

Furthermore, an approximation to the local conduction-electron propagator, which is shown to not affect the leading logarithms, causes the expressions for the diagrams on the imaginary frequency axis to become identical to the corresponding expressions in the zero-temperature formalism on the real frequency axis. This conformance is different from the well-known analytic continuation. So evaluating the parquet diagrams within leading-logarithmic accuracy in the Matsubara formalism boils down to computing the exact same expressions as in the zero-temperature formalism. The remaining approximations and the procedure to determine the X-ray-absorption rate are then analogous.

3.8 Conclusion

The X-ray-edge model is used to describe singularities in the X-ray-absorption rate of a simple metal that are caused by transitions of bound electrons into the conduction band at low temperature. The gap to the sharp Fermi surface leads to a threshold X-ray frequency, at which the absorption rate exhibits a power-law divergence with the exponent depending on the interband Coulomb interaction [ND69]. Any perturbation theory with the interaction as expansion parameter is therefore plagued by logarithmic divergences at all orders. We discussed the resummation of the leading logarithms with the leading-logarithmic parquet approximation and with the FRG.

We recapped the leading-logarithmic parquet approximation to the X-ray-edge model by Roulet et al. [RGN69]. Like them we employed the zero-temperature formalism. The absorption rate was expressed in terms of the 1PI two-particle vertex via a particle-hole susceptibility. The renormalized deep level was set to zero. While this shift potentially changes the ground state of the system, the zero-temperature formalism still describes the original ground state because it is a common eigenstate

of the noninteracting Hamiltonian and the full Hamiltonian. A Ward identity, which holds for each individual diagram, proves that the shift effectively offsets the frequency axis such that the X-ray frequency is measured relative to the threshold frequency. We listed all approximations made by Roulet et al. in detail. Using a few low-order diagrams as examples, we described how the leading logarithms are contained in the exact values of the parquet diagrams built by crossing the exchange particle-hole channel and the particle-particle channel and how these leading logarithms are captured by the listed further approximations.

We then formulated our FRG approach, choosing to introduce a sharp frequency cutoff in the real part of the deep-state propagator, to perform a one-loop truncation, and to employ a channel decomposition for the 1PI two-particle vertex. We transferred the approximations of Roulet et al. to the FRG framework. We could justify some of them directly within the flow equations. The formally integrated FRG flow equations for the 1PI two-particle vertex are identical to the integral equations that Roulet et al. obtained from approximating the parquet equations; they produce the same correct leading-logarithmic result for the X-ray-absorption rate. The two approaches are fully equivalent, step by step with the only difference lying in the order of the steps, and they can be thought of as different perspectives on the same approximation scheme.

This difference relates to the cutoff. To obtain the integral equations in their final form, Roulet et al. employ after having applied all their approximations the "trick by Abrikosov and Sudakov", which singles out the smallest deep-state frequency in the outermost bubbles of a parquet diagram in terms of the absolute value. Because of the strict partial order that we found within leading-logarithmic accuracy, the singled-out frequency is the smallest of all deep-state frequencies of the parquet diagram. This last step of Ref. [RGN69] corresponds exactly to the first steps of our FRG approach, namely the sharp frequency cutoff in the deep-state propagator and the one-loop truncation. The contributions to the flow of the parquet diagram from the 1PI three-particle vertex are subleading as they put the single-scale propagator and thus the smallest deep-state frequency into some inner bubble. We thereby gave the explicit reason why the one-loop truncation captures the leading logarithms in our FRG approach. A similar argument is presented in Ref. [BBD03].

Using the zero-temperature formalism facilitated a direct comparison between the given leading-logarithmic parquet approximation of Ref. [RGN69] and the one-loop FRG. But nowadays the Matsubara formalism is the standard for studying condensed-matter systems – in particular in the context of the FRG, which was originally developed within that formalism. The therefore important transfer of our approach to the Matsubara formalism is achieved in Ref. [DJ24].

Reference [DJ24] confirms our conclusion in regard to the multiloop Matsubara FRG study of the X-ray-edge model by Kugler and von Delft [KD18a]: the multiloop extension is not needed to reproduce parquet results – at least not the results from the leading-logarithmic parquet approximation. The multiloop FRG scheme of Ref. [KD18a] effectively produces the exact sum of the parquet diagrams in two of the two-particle channels, which contains the leading logarithms but does not constitute a controlled improvement over leading-logarithmic accuracy. According to the very recent Ref. [Gie+25], a full parquet approximation to the X-ray-edge model can

consistently capture the next-to-leading logarithms, but it has to involve all three channels. Note that while these next-to-leading logarithms are a meaningful correction, the product of expansion parameter and logarithm still has to be $|g \ln(|\nu|/\xi_0)| \leq 1$. To fully capture the exponent of the power law of the X-ray-absorption rate to second order in the Coulomb interaction, one would have to extend the regime of reliability to $|g^2 \ln(|\nu|/\xi_0)| \leq 1$, see also the discussion of the subleading logarithms by Nozières et al. [NGR69].

The logarithmic divergences are regularized in Ref. [KD18a] as the temperature and the deep level, which the authors do not renormalize, are kept finite. The numerical nature of the results then makes it difficult to judge whether the various one-loop schemes studied in Ref. [KD18a] miss some leading contributions or whether the observed improvements by the multiloop scheme are subleading. With respect to the leading-logarithmic result for the particle-hole susceptibility, the deviations of the one-loop results are actually not larger than the deviation of the multiloop result, see Ref. [DJ24] for a detailed comparison. Since we know the latter deviation to be subleading, the multiloop improvements can very well be subleading too – even though the chosen cutoffs do not seem optimal from a one-loop perspective [DJ24]. An advantage of the multiloop scheme is that, provided convergence can be achieved, it guarantees the capture of the leading logarithms for all cutoffs, even those ill-suited for the problem at hand.

Our study of the X-ray-edge model reconfirms that low-order RG, including low-order FRG, approximations can reproduce results from the leading-logarithmic parquet approximation. While the full equivalence we found between the one-loop FRG and the leading-logarithmic parquet approximation relies on the specific cutoff, we expect that the one-loop FRG can achieve leading-logarithmic accuracy also with other sensible cutoffs so long as they properly regularize the divergences during the flow. Roulet, Nozières, and Gavoret understood their study of the X-ray-edge model as a preparation for more complicated models like the Kondo model [RGN69, NGR69]. We too want to use the insights about the leading logarithms we gained from the X-ray-edge model to develop controlled approximations for more complicated models that also display divergences in some appropriate perturbation theory. For the SIAM we perform a first step within the zero-temperature formalism in Chap. 4.

Chapter 4

Treatment of the single-impurity Anderson model

4.1 Introduction

In its original version, the SIAM describes an impurity in a bulk metal [And61]. The conduction electrons can tunnel to two impurity states, one for each spin projection. The Coulomb interaction is treated explicitly only as an on-site interaction at the impurity.

We study the quantum-dot version of the SIAM where a dot comprising two interacting single-particle states is tunnel-coupled to two noninteracting reservoirs. This case has first been studied in the context of electronic transport through a barrier that contains many such localized states [GR88, NL88]. But devices have since been realized that amount to a single quantum dot between two reservoirs and that can reasonably be described with the SIAM, see e.g. Ref. [Wie+00]. The dot levels can be manipulated through a gate voltage and a magnetic field; we consider these parameters to be near the particle-hole symmetric point. For the reservoirs we employ the momentum representation and the wide-band limit.

The SIAM is more complicated than the X-ray-edge model. We can consider the reservoirs of the SIAM to correspond to the conduction band of the X-ray-edge model and the impurity or dot to correspond to the deep state. But the electron spin is crucial for an adequate description of the interaction, whereas in the X-ray-edge model the spin can be neglected. So the impurity or dot is represented by two interacting states in contrast to the single deep state. Moreover, the electrons can freely tunnel between the impurity or dot and the reservoirs, whereas in the X-ray-edge model the electrons can occupy or leave the deep state only via external X-rays. The electronic transport properties of the SIAM have interesting features, like e.g. the Coulomb blockade [PG04]. The SIAM continues to be extensively studied in the literature, see Ref. [YJ22] for a rather broad discussion and also the many references below.

A prominent example of these features is the Kondo effect: In the original version of the SIAM, strong correlations between the impurity and the conduction band can cause an anomalously increased resistance. In the quantum-dot version, strong correlations between the dot and the reservoirs can instead cause an anomalously

increased conductance across the dot. The characteristic energy scale for this anomaly is called the Kondo temperature; it becomes exponentially small as the interaction increases. A review of the Kondo effect in quantum dots is for example given by Ref. [PG04]. The Kondo effect has been experimentally observed in quantum-dot devices, see Refs. [Gol+98, Wie+00], and its emergence in the SIAM has been the subject of many theoretical studies, e.g. using the Bethe ansatz [TW83], the numerical RG [BCP08], or the quantum Monte Carlo method [HH07] to name a few.

These last three methods are exact or numerically exact. They give a satisfactory description of the properties of the SIAM, at least in equilibrium. The exact solvability is a reason why the SIAM is often used for benchmarking novel approaches. But the applicability of the exact methods diminishes as one considers more general models, e.g. with an impurity or dot having multiple orbitals. Such complicated situations arise in dynamical mean-field theory calculations for lattice models, where the solution of an impurity problem is required as a central step [Geo+96, Hel07]. The FRG is a good candidate for a versatile and efficient impurity solver [KH13]; the challenge lies in reaching an acceptable accuracy.

Before summarizing the many FRG approaches that have been developed for the SIAM, let us first mention that the FRG has also been applied to the Kondo model, where the impurity or dot consists of just a spin degree of freedom. Treating this local spin is a problem because the standard FRG is set up for fermions and bosons. The approaches of Refs. [SW10, Ren16, Die17] represent the spin operator in terms of fermionic and bosonic operators. Reference [Ren16] gives a detailed comparison of various representations and their difficulties, which include the violation of particle number conservation and the introduction of unphysical states to the Hilbert space. In contrast, Ref. [TKK18] uses a recently developed implementation of the FRG to work with the spin operator directly. All these FRG approaches demonstrate satisfying accuracy when the temperature or bias voltage is much greater than the Kondo temperature, e.g. by explicitly reproducing the poor man's scaling equations, see Ref. [And70]. The physics below the Kondo temperature, on the other hand, are not captured. However, in the FRG framework, more elaborate approaches are conceivable.

Most FRG approaches to the SIAM are based on the Matsubara formalism. A simple static approach is promising as it already finds some signatures of the Kondo effect and gives quite an accurate estimate of the Kondo temperature [KEM06, And+08]. The early Refs. [Hed+04, Kar+08] can be seen as extending this approach by keeping the frequency dependence of the 1PI vertex functions. While the agreement with numerically exact benchmark data is improved at small to intermediate interaction, no accurate results are obtained at large interaction, where both references report numerical uncertainty regarding the frequency parametrization. (The reference scale for the interaction is the hybridization of the dot states from the noninteracting case.) The more elaborate approach even no longer captures some aspects of the Kondo effect that are captured in the static approximation [Kar+08]. Recently, Ref. [Wen+20] focused on developing a parametrization scheme that properly incorporates the high-frequency domain of the vertex functions, allowing to effectively include the full frequency dependence, see also Ref. [Cha+22]. But the FRG is still

not accurate at large interaction.

Several non-straightforward or unusual ideas have been employed in the FRG treatment of the SIAM. Among them are Hubbard-Stratonovich transformations [Bar+09, Isi+10, SIK13], the functional generalization of the so-called field-theoretical RG [FC12], and the 2PI FRG [RMJ16]. The latter is formulated in terms of two-particle irreducible instead of the usual one-particle irreducible vertex functions. Again, a simple static approach gives good results, in particular the same estimate of the Kondo temperature as the simple 1PI approach of Ref. [KEM06], but overall the 2PI FRG schemes studied in Ref. [RMJ16] perform worse than 1PI FRG schemes. Furthermore, while most approaches truncate the FRG flow equations at the one-loop level and incorporate at most a certain two-loop correction via the Katanin substitution, see Ref. [Kat04], Ref. [Cha+22] applies the multiloop FRG, effectively performing the full parquet approximation. However, the inherent scheme that successively increases the loop order does not converge at large interaction.

The above Matsubara-based approaches are restricted to the equilibrium case. Transport properties can be studied only in linear response, a prominent example being the linear conductance across the dot. References [GPM07, Jak10, JPS10] present FRG approaches to the SIAM based on the Keldysh formalism and discuss the nonequilibrium case at finite bias voltage. In Ref. [Ge+24], which studies the SIAM only in equilibrium, the Keldysh formalism is chosen mainly to avoid the numerically ill-posed problem of analytic continuation.

None of the mentioned FRG approaches captures the full Kondo physics with accurate results across the entire parameter regime. Often, significant deviations from benchmark data or even fundamental problems arise at large interaction. Reference [SIK13] can be regarded as the only exception, accurately reproducing the exponential interaction-dependence of the Kondo temperature. But it uses several Ward identities and introduces four parameters that are fitted to known results from opposite regimes. Such a procedure cannot readily be generalized to more complicated models where no exact results are known from other methods. All in all, understanding the Kondo physics of the SIAM with FRG remains an active field of study.

In most perturbation-based approaches to the SIAM, including the aforementioned FRG approaches, the expansion parameter is the on-site interaction. This is the reason why the approaches typically are accurate at small interaction, whereas they struggle at large interaction. The reservoirs are commonly integrated out in the functional-integral formalism and so the coupling between the dot and the reservoirs is treated nonperturbatively. This procedure is possible because the reservoir and coupling parts of the Hamiltonian are only quadratic.

The only FRG approach to the SIAM that sticks out in regard to the underlying perturbation theory is Ref. [Kin+13]. It uses the Matsubara formalism, includes the frequency dependence of the 1PI vertex functions, and truncates the flow equations at the one-loop level (but employs the Katanin substitution). The model is divided into a core system comprising the dot and up to three nearest reservoir sites and the remaining reservoir. The core system is solved exactly and integrated out. As a result the connected Green functions of the core system with arbitrarily many particles act as effective vertices, but only the single- and two-particle vertices are kept. While the

effective interaction is local on the first remaining reservoir site, the other reservoir sites are still noninteracting and are integrated out as well. So the effective theory takes place on only one site. The flow parameter, which is originally introduced into the coupling between the core and the remaining reservoir, turns on the vertices during the flow. Even though this approach is inherently nonperturbative in the original interaction, the deviations from benchmark data are, against the hope of the authors, significant at large interaction. Reference [Kin+13] finds that aspects of the Kondo effect are captured qualitatively but not quantitatively, in particular the exponential behavior of the Kondo temperature is not reproduced. In fact, the accuracy is comparable to that of the conventional FRG approaches of Refs. [Kar+08, JPS10].

For our approach we choose to expand simultaneously in the coupling as well as in the interaction. This choice is motivated by the work of Schrieffer and Wolff [SW66], who have shown that, in a certain limit, the SIAM Hamiltonian is unitarily equivalent to the Kondo Hamiltonian, with the effective Kondo interaction being of second order in the coupling. Our aim is to relate the SIAM to the Kondo model in diagrammatic perturbation theory, with a focus on the leading logarithms. To directly use the insights we gained from studying the X-ray-edge model, we use the zero-temperature formalism. Thereby, we restrict the discussion to the equilibrium case at vanishing temperature, which still allows us to study the electron transport in linear response. Calculations are simpler than they would be in other formalisms. We perform exact calculations for key example diagrams to see how logarithms arise in the SIAM. Like for the X-ray-edge model, we identify important diagrams and devise convenient approximations that capture their leading logarithms. These approximations lead to effective diagrammatic rules that reveal some similarities to the Kondo model.

However, our research into the SIAM is not yet finished. A resummation of the approximated diagrams, either via FRG flow equations or via parquet equations, remains to be done. In its current form, our approach does not seem to correctly capture the Kondo physics; at the end of this chapter, we discuss possible extensions.

4.2 The single-impurity Anderson model

The SIAM describes an electronic system featuring a quantum dot with on-site interaction. The dot is coupled to two noninteracting reservoirs.

This setup allows for a current to flow through the dot if a bias voltage is applied. However, we will look only at linear-response properties, specifically the linear conductance. We will study the system in equilibrium at half filling and vanishing temperature. Without loss of generality, the electric potential in the reservoirs is then set to zero.

The dot consists of two levels denoted by

$$\varepsilon_{d,\sigma} = -\frac{U}{2} + V_g + \sigma B. \tag{4.1}$$

Here, the spin-projection $\sigma = \uparrow, \downarrow$ is identified with $\sigma = \pm$; later, we will write $\bar{\sigma}$ to denote the opposite of σ. Furthermore, U is the on-site interaction, V_g is the gate

voltage, and B is the magnetic field on the dot after having absorbed the g-factor and the Bohr magneton, $g\mu_B B/2 \to B$. The first term in Eq. (4.1) is a convention so that the particle-hole symmetric point is $V_g = 0$.

4.2.1 Hamiltonian in real space

In real space the Hamiltonian of the SIAM is given by

$$H = H_{\text{dot}} + H_{\text{res}} + H_{\text{coup}} \tag{4.2a}$$

$$H_{\text{dot}} = H_{\text{dot},0} + H_{\text{dot, int}} = \sum_{\sigma=\uparrow,\downarrow} \varepsilon_{d,\sigma}\, d_\sigma^\dagger d_\sigma + U d_\uparrow^\dagger d_\uparrow d_\downarrow^\dagger d_\downarrow \tag{4.2b}$$

$$H_{\text{res}} = -t \sum_{r=L,R} \sum_{s=1}^{\infty} \sum_{\sigma=\uparrow,\downarrow} \left(c_{r,s,\sigma}^\dagger c_{r,s+1,\sigma} + \text{H.c.} \right) \tag{4.2c}$$

$$H_{\text{coup}} = -\tau \sum_{r=L,R} \sum_{\sigma=\uparrow,\downarrow} \left(c_{r,1,\sigma}^\dagger d_\sigma + \text{H.c.} \right). \tag{4.2d}$$

The operator $d_\sigma^\dagger$ creates an electron with spin-projection σ on the dot. The interaction $H_{\text{dot, int}}$ represents the Coulomb repulsion on the dot. A doubly occupied dot is associated with an energy cost $U > 0$.

The left and the right reservoir ($r = L, R$) are modeled as semi-infinite tight-binding chains. The operator $c_{r,s,\sigma}^\dagger$ creates an electron in reservoir r at site s with spin-projection σ. Since the electric potential in the reservoirs is zero, the reservoir Hamiltonian H_{res} consists just of the kinetic term. The nearest-neighbor hopping amplitude $t > 0$ is the same for both reservoirs.

The dot is coupled to the first site of each reservoir through H_{coup} with the coupling amplitude $\tau > 0$. Also this parameter is the same for both reservoirs, i.e. the coupling to the reservoirs is symmetric.

4.2.2 Reservoirs in momentum space

We change the single-particle basis to an eigenbasis of the reservoir Hamiltonian H_{res}. To this end we go from the site index s over to a momentum index k.

The details of this basis change follow from Appendix A, where we diagonalize the Hamiltonian of a spinless tight-binding chain. There, the number of sites is kept finite and denoted by M. We will take the limit $M \to \infty$ to recover the infinitely large reservoirs. The ends of the chain we consider in Appendix A are not linked. This property matters for the SIAM because only the first site of each reservoir couples to the dot.

Let us now transform the Hamiltonian (4.2) of the SIAM. The reservoir part becomes diagonal with eigenenergies

$$\varepsilon_k = -2t\cos(k), \qquad k \in (0, \pi). \tag{4.3}$$

For the coupling part, we use

$$c_{r,1,\sigma}^\dagger = \sum_k \langle r, k, \sigma | r, 1, \sigma \rangle\, c_{r,k,\sigma}^\dagger = \sqrt{\frac{2}{M+1}} \sum_k \sin(k)\, c_{r,k,\sigma}^\dagger \tag{4.4}$$

and introduce the momentum-dependent coupling amplitude

$$\tau_k = \sqrt{\frac{2}{M+1}}\,\sin(k)\,\tau. \tag{4.5}$$

So while the dot part of the Hamiltonian remains unchanged, the reservoir and coupling parts become

$$H_{\text{res}} = \sum_{r=L,R}\sum_{k}\sum_{\sigma=\uparrow,\downarrow} \varepsilon_k\, c^\dagger_{r,k,\sigma} c_{r,k,\sigma} \tag{4.6a}$$

$$H_{\text{coup}} = -\sum_{r=L,R}\sum_{k}\sum_{\sigma=\uparrow,\downarrow} \tau_k \big(c^\dagger_{r,k,\sigma} d_\sigma + \text{H.c.}\big). \tag{4.6b}$$

The discrete momenta found in Appendix A approach a continuum as $M \to \infty$. The momentum sums will then take the form of Riemann integrals

$$\frac{\pi}{M+1}\sum_k f(k) = \frac{\pi}{M+1}\sum_{l=1}^{M} f\left(\frac{\pi l}{M+1}\right) \overset{M\to\infty}{=} \int_0^\pi \mathrm{d}k\, f(k) = \int_{-2t}^{2t} \mathrm{d}\varepsilon\, \rho(\varepsilon)\, f\big(k(\varepsilon)\big). \tag{4.7}$$

In the last step, we have inverted the dispersion (4.3) and introduced the density of states

$$\rho(\varepsilon) = \frac{\mathrm{d}k}{\mathrm{d}\varepsilon} = \frac{1}{\sqrt{4t^2-\varepsilon^2}}, \qquad \varepsilon \in (-2t, 2t). \tag{4.8}$$

4.2.3 Transforming the reservoirs

Since we have defined the model without a bias voltage and with the parameters t and τ being independent of the reservoir, the Hamiltonian is symmetric under swapping the indices $L \leftrightarrow R$. As a consequence the left and the right reservoir can be transformed into one reservoir that couples to the dot and one reservoir that decouples completely, see e.g. Ref. [PG04] in the context of Kondo quantum dots.

Technically, this is achieved by changing the single-particle basis according to

$$c_L = \frac{c_{\text{even}} + c_{\text{odd}}}{\sqrt{2}}, \qquad c_R = \frac{c_{\text{even}} - c_{\text{odd}}}{\sqrt{2}}, \tag{4.9}$$

where we have omitted the other quantum numbers, which are not transformed. In momentum space and with transformed reservoirs, the Hamiltonian assumes the form

$$H = H_{\text{even}} + H_{\text{odd}} \tag{4.10a}$$
$$H_{\text{even}} = H_{\text{dot}} + H_{\text{even, res}} + H_{\text{coup}} \tag{4.10b}$$
$$H_{\text{dot}} = H_{\text{dot},0} + H_{\text{dot, int}} = \sum_{\sigma=\uparrow,\downarrow} \varepsilon_{d,\sigma}\, d_\sigma^\dagger d_\sigma + U d_\uparrow^\dagger d_\uparrow d_\downarrow^\dagger d_\downarrow \tag{4.10c}$$
$$H_{\text{even, res}} = \sum_k \sum_{\sigma=\uparrow,\downarrow} \varepsilon_k\, c_{\text{even},k,\sigma}^\dagger c_{\text{even},k,\sigma} \tag{4.10d}$$
$$H_{\text{coup}} = -\sum_k \sum_{\sigma=\uparrow,\downarrow} \bar{\tau}_k \big(c_{\text{even},k,\sigma}^\dagger d_\sigma + \text{H.c.}\big) \tag{4.10e}$$
$$H_{\text{odd}} = \sum_k \sum_{\sigma=\uparrow,\downarrow} \varepsilon_k\, c_{\text{odd},k,\sigma}^\dagger c_{\text{odd},k,\sigma} \tag{4.10f}$$

with $\bar{\tau}_k = \sqrt{2}\,\tau_k$.

We now divide the single-particle Hilbert space into two sectors: an even sector that consists of the dot states $|\uparrow\rangle$, $|\downarrow\rangle$ as well as the states $|\text{even}, k, \sigma\rangle$ and an odd sector that consists of the states $|\text{odd}, k, \sigma\rangle$. H_{even} affects only the electrons in the even sector, whereas H_{odd} affects only the electrons in the odd sector.

We will consider the system with fixed numbers of electrons in these sectors. Since H_{odd} is noninteracting, the ground state $|\Psi_0\rangle$ of the full system features a simple Fermi sea in the odd sector. In ground-state expectation values, one can then easily calculate the effect from the odd sector, see Sec. 4.8 for the concrete example of the linear conductance. But for the even sector, a proper many-particle approach will be necessary.

4.2.4 Wide-band limit

We use the wide-band limit to simplify calculations. This is common in studies of the SIAM [KEM06, Kin+13]. The band width $2W$ is assumed to be by far the greatest energy scale of the model. The density of states and the coupling amplitude are approximated as constant inside the band. They are set to the respective values at the Fermi surface with $\varepsilon_F = 0$ and $k_F = \pi/2$, i.e.

$$\rho(\varepsilon) = \frac{1}{2t}, \qquad \varepsilon \in (-W, W) \tag{4.11a}$$
$$\bar{\tau}_k = \frac{2\tau}{\sqrt{M+1}}. \tag{4.11b}$$

In our situation we can motivate the wide-band limit as follows. The momentum sums appear in diagrams always in the form

$$\sum_k \bar{\tau}_k^2\, g_{k\sigma}(\omega) = \frac{4\tau^2}{\pi} \int_{-W}^{W} \mathrm{d}\varepsilon\, \rho(\varepsilon) \sin^2\big(k(\varepsilon)\big) \frac{1}{\omega - \varepsilon + \operatorname{sgn}(\varepsilon)\mathrm{i}\eta}. \tag{4.12}$$

With regard to the leading logarithms, the discontinuity of the imaginary part of Eq. (4.12) at $\omega = 0$ is crucial. For the X-ray-edge model, we have found that the real

part of the conduction-electron propagator can be neglected and that the leading logarithms arise only from integration regions where the frequency argument of each conduction-electron propagator is close to the Fermi energy, see Sec. 3.4.3; for the SIAM we will find the same, see Sec. 4.6.3. For the imaginary part of Eq. (4.12) at such frequencies, the density of states and the coupling amplitude are evaluated at $\varepsilon = \omega$ close to the Fermi surface. So the error of the approximation (4.11) is negligible.

In the wide-band limit, different ways are conceivable to define the value of the half band width. It can for example be set to $W = 2t$ so that it matches the original value or to $W = \pi t$ so that the total number of states is unchanged. For the purpose of studying the leading logarithms, only $W \approx t$ is relevant.

4.3 Applying the zero-temperature formalism

We apply the zero-temperature formalism from Chap. 2 to the SIAM. We consider the system at half filling, in equilibrium, at vanishing temperature, and near the particle-hole symmetric point.

We make use of the transformation to an even and odd reservoir, see Sec. 4.2.3. The Hamiltonian does not couple the even and odd sectors nor does it couple the spin-↑ and spin-↓ sectors. We prepare the system with a fixed number of electrons in each of these sectors, choosing a balanced distribution. Specifically, we assume that the number M of sites per reservoir and spin is even and set the particle numbers to

$$N_{\mathrm{even},\uparrow} = N_{\mathrm{even},\downarrow} = \frac{M}{2} + 1, \qquad N_{\mathrm{odd},\uparrow} = N_{\mathrm{odd},\downarrow} = \frac{M}{2}. \tag{4.13}$$

The odd sector is noninteracting and easy to solve.

We apply the formalism only to the even sector, dropping the index "even" in the following. Aside from the trivial generalization to an infinite system size, see Sec. 2.11.1, we use the zero-temperature formalism in its original form: The Green functions are defined in the ground state $|\Psi_0\rangle$ of the full Hamiltonian H, while the generating functional is defined with the ground state $|\Phi_0\rangle$ of the noninteracting Hamiltonian H_0. The ground states are required to be nondegenerate and not mutually orthogonal. We will check these requirements below.

But first we have to choose how to decompose the Hamiltonian into a noninteracting part and a perturbation, $H = H_0 + H_{\mathrm{int}}$. The terms that are quadratic in ladder operators can be treated as single-particle perturbations or not. As a guide we try to make the structure as similar to the X-ray-edge model as possible so that we can harness our insights from Chap. 3. The dot states can be thought of as a deep state with a spin degree of freedom, while the reservoir corresponds to a conduction band. This motivates the choice

$$H_0 = H_{\mathrm{dot},0} + H_{\mathrm{res}} = \sum_{\sigma=\uparrow,\downarrow} \varepsilon_{d,\sigma}\, d_\sigma^\dagger d_\sigma + \sum_k \sum_{\sigma=\uparrow,\downarrow} \varepsilon_k\, c_{k,\sigma}^\dagger c_{k,\sigma} \tag{4.14a}$$

$$H_{\mathrm{int}} = H_{\mathrm{coup}} + H_{\mathrm{dot,\,int}} = -\sum_k \sum_{\sigma=\uparrow,\downarrow} \bar{\tau}_k \big(c_{k,\sigma}^\dagger d_\sigma + \mathrm{H.c.}\big) + U d_\uparrow^\dagger d_\uparrow d_\downarrow^\dagger d_\downarrow, \tag{4.14b}$$

see the even part of Eq. (4.10).

The single-particle eigenstates of H_0 are the dot states $|\sigma\rangle$ and the momentum states $|k,\sigma\rangle$. As for the X-ray-edge model, we will find that the momentum sums appearing in diagrams can be precalculated. If we had assigned the coupling term to the noninteracting part, the eigenstates would instead have been superpositions of dot and reservoir states.

By treating the coupling term as a perturbation, we expand in the coupling amplitude τ as well as in the interaction U. This will help us to investigate the regime where the SIAM resembles the Kondo model, see Sec. 4.5 and Ref. [SW66], in a controlled fashion. There, the leading contributions feature two factors τ for every factor U.

The ground state of the noninteracting Hamiltonian is given by a Fermi sea built from the single-particle eigenstates. We consider the dot levels to be well below the middle of the reservoir band, $\varepsilon_{d,\sigma} < 0$, so the dot states are occupied. The Fermi energy is $\varepsilon_F = 0$; note that there is no momentum state with $\varepsilon_k = 0$ because the number of sites per spin is even. The ground state of H_0 reads

$$|\Phi_0\rangle = d_\uparrow^\dagger d_\downarrow^\dagger \left(\prod_{k \text{ with } \varepsilon_k<0} c_{k,\uparrow}^\dagger c_{k,\downarrow}^\dagger \right) |0\rangle. \tag{4.15}$$

It is nondegenerate. The interacting ground state $|\Psi_0\rangle$ is known from the Bethe-ansatz solution to the SIAM; it is nondegenerate as well [Hew93].

To get an idea of how the interacting ground state looks like, it is instructive to consider a simplified model where the reservoir is replaced with just a single state per spin. We set the energy level of this state to the Fermi energy $\varepsilon_F = 0$ of the original model; since we study the SIAM at half filling, the Fermi energy matches the energy level of the reservoir sites in the real-space formulation. We set the dot levels to $\varepsilon_{d,\sigma} = -U/2$ so we are at the particle-hole symmetric point and we prepare the system with one $\uparrow$- and one $\downarrow$-electron. With respect to the many-particle basis

$$\left\{ c_\uparrow^\dagger d_\downarrow^\dagger |0\rangle,\ c_\downarrow^\dagger d_\uparrow^\dagger |0\rangle,\ c_\uparrow^\dagger c_\downarrow^\dagger |0\rangle,\ d_\uparrow^\dagger d_\downarrow^\dagger |0\rangle \right\}, \tag{4.16}$$

the Hamiltonian is then represented by the matrix

$$H^{(\mathrm{simp})} \doteq \begin{pmatrix} -U/2 & 0 & -\bar{\tau} & -\bar{\tau} \\ 0 & -U/2 & \bar{\tau} & \bar{\tau} \\ -\bar{\tau} & \bar{\tau} & 0 & 0 \\ -\bar{\tau} & \bar{\tau} & 0 & 0 \end{pmatrix}. \tag{4.17}$$

Its ground state is nondegenerate and reads

$$\left|\Psi_0^{(\mathrm{simp})}\right\rangle \doteq \begin{pmatrix} -E_0^{(\mathrm{simp})} \\ E_0^{(\mathrm{simp})} \\ 2\bar{\tau} \\ 2\bar{\tau} \end{pmatrix} \qquad \text{with } E_0^{(\mathrm{simp})} = -\frac{U}{4} - \sqrt{\frac{U^2}{16} + 4\bar{\tau}^2}. \tag{4.18}$$

Naively, one might expect that the interacting ground state is degenerate as the system favors a singly occupied dot, which can be realized with either an $\uparrow$- or a

↓-electron. But from the simplified model, we infer that the coupling between the dot and the reservoir lifts this degeneracy. Anyway, we can use a magnetic field $B \neq 0$ to avoid any spin degeneracy; the case $B = 0$ can then be obtained from the limit $B \to 0$. As a side remark, the limiting case

$$\left|\Psi_0^{(\mathrm{simp})}\right\rangle \doteq \begin{pmatrix} U/2 \\ -U/2 \\ 0 \\ 0 \end{pmatrix} \qquad \text{for } U \gg \tau \tag{4.19}$$

corresponds to the Kondo singlet [PG04].

The final requirement is that $|\Psi_0\rangle$ and $|\Phi_0\rangle$ are not orthogonal. Since $|\Psi_0\rangle$ favors a singly occupied dot, while $|\Phi_0\rangle$ features a doubly occupied dot, the overlap is guaranteed to be small. But, crucially, the full Hamiltonian is not block diagonal with respect to the subspaces with singly occupied dot and with doubly occupied dot. These many-particle subspaces are coupled through the coupling between the dot and the reservoir. The simplified Hamiltonian (4.17) illustrates this well and its ground state (4.18) indeed has a nonzero overlap with the fourth basis state, which represents a doubly occupied dot. In summary all requirements are fulfilled for applying the zero-temperature formalism.

The formalism provides diagrammatic rules for the Green functions, see Sec. 2.7.3. In the following we customize the diagrammatic rules specifically for the SIAM. Since this procedure is similar to the one for the X-ray-edge model, see Sec. 3.3.2, we will describe only briefly how we arrive at the specific diagrammatic elements. We will refrain from explicitly stating the final rule set.

Instead of Green functions, we will consider 1PI vertex functions, where the external points and propagators are amputated and diagrams must be one-particle irreducible. The values of the diagrams then have an additional prefactor i^{1-n} for an n-particle function.

We work in frequency representation and exploit the frequency conservation of the lines and vertices. Most frequency integrals collapse immediately then. Each internal line and external leg has a single frequency argument. We express these in terms of a set of independent frequencies such that the frequency conservation at each line and vertex is explicitly fulfilled. In doing so we drop a factor $2\pi\delta(\ldots)$ which represents the overall frequency conservation of a diagram. The independent internal frequencies are still integrated over.

With respect to the state index α, the free propagator is diagonal. Half of the sums collapse so each internal line and external leg has a single state index. The state index α is a multi-index: it distinguishes between the dot and the reservoir and between spin ↑ and spin ↓; in the reservoir case, it additionally involves the momentum index k.

We visually distinguish dot propagators from reservoir propagators by using dotted and full lines. The two lines attached to a single-particle vertex must have different stroke styles. All four lines attached to a two-particle vertex must be dotted. Since we will consider only diagrams that are one-particle irreducible and contain a two-particle vertex, the stroke style of every line is fixed unambiguously.

The momentum sums are independent and can be precalculated. There is one sum for every reservoir propagator and any two reservoir propagators are always separated by a dot propagator. We let the reservoir propagator absorb its associated momentum sum and also a factor $2/\sqrt{M+1}$ from each of the two adjacent single-particle vertices. Through this redefinition the individual diagrammatic elements are well-defined for $M \to \infty$, i.e. for an infinite reservoir. Note that the vertices do not depend on momenta within the wide-band limit.

Regarding the spin indices, we exploit the structure of the vertices. All vertices conserve spin. At the two-particle vertex, the incoming legs have opposite spins and the outgoing legs have opposite spins. Many spin sums collapse over the corresponding Kronecker deltas. We express all spin indices in a diagram in terms of a set of independent spin indices such that the structure of the vertices is explicitly fulfilled. In doing so we neglect all diagrammatic contributions with impossible spin structures; they evaluate to zero anyway. The independent internal spin indices are still summed over.

Lastly, we further reduce the number of labels in diagrams. Since the single-particle vertex conserves frequency and spin, all labels along a sequence of lines and single-particle vertices are identical. So it suffices to label an entire sequence with a single frequency and spin.

In summary we obtain the following diagrammatic elements. With regard to direction, stroke style, frequency, and spin, only the presented structures are possible. The free propagator is given by

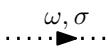

$$= g_{d\sigma}(\omega) = \frac{1}{\omega - \varepsilon_{d,\sigma} - \mathrm{i}\eta} \tag{4.20a}$$

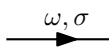

$$= g_r(\omega) = \frac{4}{M+1} \sum_k \frac{1}{\omega - \varepsilon_k + \mathrm{i}\eta \operatorname{sgn} \varepsilon_k} \tag{4.20b}$$

$$= \frac{2}{\pi t} \int_{-W}^{W} \mathrm{d}\varepsilon \, \frac{1}{\omega - \varepsilon + \mathrm{i}\eta \operatorname{sgn} \varepsilon} \tag{4.20c}$$

$$= \frac{2}{\pi t} \left[\ln \frac{|W+\omega|}{|W-\omega|} - \mathrm{i}\pi \operatorname{sgn}(\omega) \Theta(W - |\omega|) \right]. \tag{4.20d}$$

In the step leading to Eq. (4.20c), we have performed the limit $M \to \infty$ by using Eq. (4.7) and we have performed the wide-band limit by using the density of states (4.11a). Since we will only consider diagrams without Hartree-Fock loops, we have written the free propagator without the convergence factor $e^{\mathrm{i}\omega\eta'}$. The vertices are given by

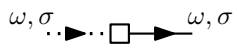

$$= -\tau \tag{4.21a}$$

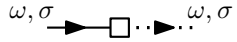

$$= -\tau \tag{4.21b}$$

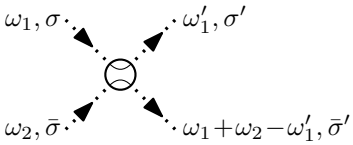

$$= U\sigma'\sigma. \tag{4.21c}$$

Here, we have drawn the internal connections in the two-particle vertex to fix its value.

4.4 Example diagrams

In this section we discuss some low-order diagrams of the 1PI two-particle vertex function. Primarily, we consider bubble diagrams, starting with the simplest possible version and then inserting single-particle vertices. We also discuss a crossed bubble that closely resembles the one we discussed for the X-ray-edge model, see Sec. 3.3.6.

For each bubble we use the natural frequency of the respective two-particle channel. If the order of the incoming and outgoing frequencies is given by ω_1, ω_2 and ω_1', ω_2', this natural frequency is for the particle-particle channel the total frequency

$$\Omega = \omega_1 + \omega_2 = \omega_1' + \omega_2', \tag{4.22a}$$

for the exchange particle-hole channel the exchange frequency

$$X = \omega_2' - \omega_1 = \omega_2 - \omega_1', \tag{4.22b}$$

and for the direct particle-hole channel the direct frequency

$$D = \omega_1' - \omega_1 = \omega_2 - \omega_2'. \tag{4.22c}$$

Since all legs of the two-particle vertex have the same stroke style, some diagrams differ only in the order of their incoming legs or in the order of their outgoing legs but are otherwise identical. In those cases we discuss only one of the diagrams. The values of the other diagrams can be obtained by renaming the external frequencies and spins and by keeping track of the permutation that describes the connection of the incoming to the outgoing legs. This applies to the distinction between the exchange particle-hole channel and the direct particle-hole channel. We will therefore distinguish only between the particle-particle channel and the particle-hole channel.

After calculating the exact values of diagrams, we look for logarithmic divergences to which we can later apply our insights from the X-ray-edge model. In a particular kind of bubble, which we call dot-reservoir bubble, we find logarithms that are reminiscent of the ones in the X-ray-edge model. We observe that these logarithms diverge if we restrict the parameters and external frequencies in a particular way. In Sec. 4.5 we will motivate these restrictions.

We expand the exact values in this regime. In Sec. 4.6 we will develop an approximation scheme aimed at capturing the leading logarithms. We will then check that scheme against the expansions.

4.4.1 Dot-dot bubbles

The first diagrams we discuss are the simplest ones of the 1PI two-particle vertex function, aside from a bare vertex. These are the bubble diagrams with no single-particle vertices. We call them dot-dot bubbles because both internal lines are free dot propagators.

The dot-dot particle-particle bubble reads

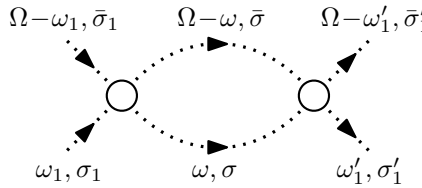

$$= \frac{\mathrm{i}}{2}\, U^2 \sigma_1' \sigma_1 \int_{-\infty}^{\infty} \frac{\mathrm{d}\omega}{2\pi} \sum_{\sigma} g_{d\bar{\sigma}}(\Omega - \omega)\, g_{d\sigma}(\omega) \tag{4.23a}$$

$$= \frac{\mathrm{i}}{2} U^2 \sigma_1' \sigma_1 \int_{-\infty}^{\infty} \frac{\mathrm{d}\omega}{2\pi} \sum_{\sigma} \frac{1}{\Omega - \omega - \varepsilon_{d,\bar{\sigma}} - \mathrm{i}\eta}\, \frac{1}{\omega - \varepsilon_{d,\sigma} - \mathrm{i}\eta} \tag{4.23b}$$

$$= -U^2 \sigma_1' \sigma_1\, \frac{1}{\Omega - \varepsilon_{d,\uparrow} - \varepsilon_{d,\downarrow} - \mathrm{i}\eta}, \tag{4.23c}$$

where we have used the residue theorem after closing the integral at infinity and we have used that η is infinitesimal. To determine the sign of the prefactor, we have considered the ω_1'-leg as the first outgoing leg and the ω_1-leg as the first incoming leg. This convention applies also to the following diagrams.

The dot-dot particle-hole bubble reads

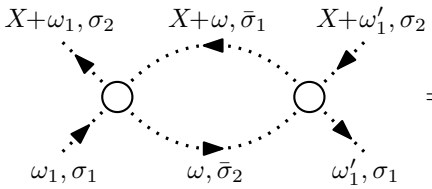

$$= \mathrm{i}U^2 \int_{-\infty}^{\infty} \frac{\mathrm{d}\omega}{2\pi}\, g_{d\bar{\sigma}_1}(X + \omega)\, g_{d\bar{\sigma}_2}(\omega) \tag{4.24a}$$

$$= \mathrm{i}U^2 \int_{-\infty}^{\infty} \frac{\mathrm{d}\omega}{2\pi}\, \frac{1}{X + \omega - \varepsilon_{d,\bar{\sigma}_1} - \mathrm{i}\eta}\, \frac{1}{\omega - \varepsilon_{d,\bar{\sigma}_2} - \mathrm{i}\eta} \tag{4.24b}$$

$$= 0. \tag{4.24c}$$

This result is obvious in time representation: as the free dot propagators represent only hole propagations, they are directed backward in time and thus lead to contradicting requirements on the times of the two vertices. There is one other particle-hole bubble that differs only in the order of its outgoing legs; it, too, evaluates to zero.

There are no logarithmic divergences in the dot-dot bubbles. The dot-dot particle-particle bubble diverges as $1/x$ at $\Omega = \varepsilon_{d,\uparrow} + \varepsilon_{d,\downarrow}$, but a different region of the external frequency Ω will later be of interest. So we will consider the dot-dot bubbles to be subleading.

4.4.2 Dot-reservoir bubbles

Next, we modify the bubbles by letting one particle (or hole) tunnel into the reservoir and back again. We call these diagrams the dot-reservoir bubbles. They will play a central role for our approximation scheme in Sec. 4.6.

The dot-reservoir particle-particle bubble is

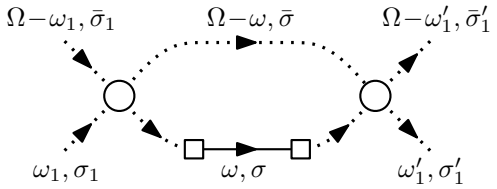

$$= \mathrm{i}\tau^2 U^2 \sigma_1' \sigma_1 \int_{-\infty}^{\infty} \frac{\mathrm{d}\omega}{2\pi} \sum_{\sigma} g_{d\bar{\sigma}}(\Omega - \omega)\, g_r(\omega) \big[g_{d\sigma}(\omega)\big]^2 \tag{4.25a}$$

$$= \mathrm{i}\frac{2\tau^2}{\pi t}\, U^2 \sigma_1' \sigma_1 \int_{-\infty}^{\infty} \frac{\mathrm{d}\omega}{2\pi} \int_{-W}^{W} \mathrm{d}\varepsilon \sum_{\sigma} \frac{1}{\Omega - \omega - \varepsilon_{d,\bar{\sigma}} - \mathrm{i}\eta}\, \frac{1}{\omega - \varepsilon + \mathrm{i}\eta \operatorname{sgn}\varepsilon}\, \frac{1}{(\omega - \varepsilon_{d,\sigma} - \mathrm{i}\eta)^2} \tag{4.25b}$$

$$= \mathrm{i}\frac{2\tau^2}{\pi t}\, U^2 \sigma_1' \sigma_1 \sum_{\sigma} I_{\sigma}^{(\mathrm{pp})}(\Omega). \tag{4.25c}$$

In the last line we have defined $I_{\sigma}^{(\mathrm{pp})}(\Omega)$, which denotes the frequency dependence of the diagram. We will call this quantity the dot-reservoir particle-particle bubble, just as the actual diagram.

The dot-reservoir particle-hole bubble is

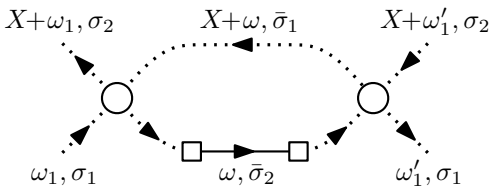

$$= \mathrm{i}\tau^2 U^2 \int_{-\infty}^{\infty} \frac{\mathrm{d}\omega}{2\pi}\, g_{d\bar{\sigma}_1}(X + \omega)\, g_r(\omega) \big[g_{d\bar{\sigma}_2}(\omega)\big]^2 \tag{4.26a}$$

$$= \mathrm{i}\frac{2\tau^2}{\pi t}\, U^2 \int_{-\infty}^{\infty} \frac{\mathrm{d}\omega}{2\pi} \int_{-W}^{W} \mathrm{d}\varepsilon\, \frac{1}{X + \omega - \varepsilon_{d,\bar{\sigma}_1} - \mathrm{i}\eta}\, \frac{1}{\omega - \varepsilon + \mathrm{i}\eta \operatorname{sgn}\varepsilon}\, \frac{1}{(\omega - \varepsilon_{d,\bar{\sigma}_2} - \mathrm{i}\eta)^2} \tag{4.26b}$$

$$= \mathrm{i}\frac{2\tau^2}{\pi t}\, U^2 I_{\bar{\sigma}_1 \bar{\sigma}_2}^{(\mathrm{ph})}(X). \tag{4.26c}$$

There are three other particle-hole bubbles that differ only in the order of their incoming legs or in the order of their outgoing legs; their values are fully analogous.

Now, we calculate the exact values of these bubbles. For the dot-reservoir particle-particle bubble, we close the ω-integral in the lower half plane and apply the residue theorem,

$$I_{\sigma}^{(\mathrm{pp})}(\Omega) = \mathrm{i} \int_{-W}^{W} \mathrm{d}\varepsilon \Bigg[- \frac{1}{\varepsilon - \Omega + \varepsilon_{d,\bar{\sigma}} + \mathrm{i}\eta - \mathrm{i}\eta \operatorname{sgn}\varepsilon}\, \frac{1}{(\Omega - \varepsilon_{d,\uparrow} - \varepsilon_{d,\downarrow} - 2\mathrm{i}\eta)^2} + \Theta(\varepsilon)\, \frac{1}{\varepsilon - \Omega + \varepsilon_{d,\bar{\sigma}}}\, \frac{1}{(\varepsilon - \varepsilon_{d,\sigma} - 2\mathrm{i}\eta)^2} \Bigg]. \tag{4.27}$$

In the second term, we use the partial fraction decomposition

$$\frac{1}{\varepsilon - z_1}\,\frac{1}{(\varepsilon - z_2)^2} = \frac{1}{\varepsilon - z_1}\,\frac{1}{(z_1 - z_2)^2} - \frac{1}{\varepsilon - z_2}\,\frac{1}{(z_1 - z_2)^2} - \frac{1}{(\varepsilon - z_2)^2}\,\frac{1}{z_1 - z_2} \tag{4.28}$$

with $z_1 = \Omega - \varepsilon_{d,\bar{\sigma}}$ and $z_2 = \varepsilon_{d,\sigma} + 2\mathrm{i}\eta$.

For $\varepsilon > 0$ the first term in Eq. (4.27) cancels with the first term in Eq. (4.28). Note that the ε-dependent denominators lack an imaginary part so we could not have integrated over these terms individually. This cancellation of problematic terms would have taken place also if the imaginary parts of the denominators of the free propagators had not been unified through the replacement $\eta\varepsilon_\alpha \to \eta \operatorname{sgn}\varepsilon_\alpha$ in Eq. (2.47) – and even if these imaginary parts had been treated as independent in Eq. (4.25).

In the remaining expression for the dot-reservoir particle-particle bubble, we drop the factors 2 in front of the infinitesimal η and use $\varepsilon_{d,\sigma} < 0$ to obtain

$$\begin{aligned} I_\sigma^{(\mathrm{pp})}(\Omega) = {} & \frac{-\mathrm{i}}{(\Omega - \varepsilon_{d,\uparrow} - \varepsilon_{d,\downarrow} - \mathrm{i}\eta)^2}\left(\int_{-W}^{0} \mathrm{d}\varepsilon\, \frac{1}{\varepsilon - \Omega + \varepsilon_{d,\bar{\sigma}} + \mathrm{i}\eta} + \int_0^W \mathrm{d}\varepsilon\, \frac{1}{\varepsilon - \varepsilon_{d,\sigma}}\right) \\ & - \frac{\mathrm{i}}{\Omega - \varepsilon_{d,\uparrow} - \varepsilon_{d,\downarrow} - \mathrm{i}\eta} \int_0^W \mathrm{d}\varepsilon\, \frac{1}{(\varepsilon - \varepsilon_{d,\sigma})^2}. \end{aligned} \tag{4.29}$$

We solve the first integral using the principal branch of the complex logarithm, see Appendices B.1 and C.1. We arrive at the exact result

$$\begin{aligned} I_\sigma^{(\mathrm{pp})}(\Omega) = {} & \frac{-\mathrm{i}}{(\Omega - \varepsilon_{d,\uparrow} - \varepsilon_{d,\downarrow} - \mathrm{i}\eta)^2}\left[\operatorname{Log}(-\Omega + \varepsilon_{d,\bar{\sigma}} + \mathrm{i}\eta) - \operatorname{Log}(-W - \Omega + \varepsilon_{d,\bar{\sigma}} + \mathrm{i}\eta)\right. \\ & \left. + \ln\frac{W - \varepsilon_{d,\sigma}}{-\varepsilon_{d,\sigma}}\right] + \frac{\mathrm{i}}{\Omega - \varepsilon_{d,\uparrow} - \varepsilon_{d,\downarrow} - \mathrm{i}\eta}\left(\frac{1}{W - \varepsilon_{d,\sigma}} + \frac{1}{\varepsilon_{d,\sigma}}\right). \end{aligned} \tag{4.30}$$

For the dot-reservoir particle-hole bubble, we again close the ω-integral in the lower half plane and apply the residue theorem,

$$I_{\sigma'\sigma}^{(\mathrm{ph})}(X) = -\mathrm{i}\int_{-W}^{W} \mathrm{d}\varepsilon\, \Theta(\varepsilon)\, \frac{1}{\varepsilon + X - \varepsilon_{d,\sigma'} - 2\mathrm{i}\eta}\, \frac{1}{(\varepsilon - \varepsilon_{d,\sigma} - 2\mathrm{i}\eta)^2}. \tag{4.31}$$

Again, we use the partial fraction decomposition (4.28), now with $z_1 = -X + \varepsilon_{d,\sigma'} + 2\mathrm{i}\eta$ and $z_2 = \varepsilon_{d,\sigma} + 2\mathrm{i}\eta$, we drop the factors 2 in front of the infinitesimal η, and we use $\varepsilon_{d,\sigma} < 0$ to obtain

$$\begin{aligned} I_{\sigma'\sigma}^{(\mathrm{ph})}(X) = {} & \frac{-\mathrm{i}}{(X - \varepsilon_{d,\sigma'} + \varepsilon_{d,\sigma})^2}\int_0^W \mathrm{d}\varepsilon\left(\frac{1}{\varepsilon + X - \varepsilon_{d,\sigma'} - \mathrm{i}\eta} - \frac{1}{\varepsilon - \varepsilon_{d,\sigma}}\right) \\ & - \frac{\mathrm{i}}{X - \varepsilon_{d,\sigma'} + \varepsilon_{d,\sigma}} \int_0^W \mathrm{d}\varepsilon\, \frac{1}{(\varepsilon - \varepsilon_{d,\sigma})^2}. \end{aligned} \tag{4.32}$$

After solving the remaining integrals, we arrive at the exact result

$$\begin{aligned} I_{\sigma'\sigma}^{(\mathrm{ph})}(X) = {} & \frac{-\mathrm{i}}{(X - \varepsilon_{d,\sigma'} + \varepsilon_{d,\sigma})^2}\left[\operatorname{Log}(W + X - \varepsilon_{d,\sigma'} - \mathrm{i}\eta) - \operatorname{Log}(X - \varepsilon_{d,\sigma'} - \mathrm{i}\eta)\right. \\ & \left. - \ln\frac{W - \varepsilon_{d,\sigma}}{-\varepsilon_{d,\sigma}}\right] + \frac{\mathrm{i}}{X - \varepsilon_{d,\sigma'} + \varepsilon_{d,\sigma}}\left(\frac{1}{W - \varepsilon_{d,\sigma}} + \frac{1}{\varepsilon_{d,\sigma}}\right). \end{aligned} \tag{4.33}$$

Let us look at the divergences of the dot-reservoir bubbles. The particle-particle bubble diverges at $\Omega = \varepsilon_{d,\uparrow} + \varepsilon_{d,\downarrow}$. This point will turn out to be irrelevant. The particle-hole bubble appears to diverge at $X = \varepsilon_{d,\sigma'} - \varepsilon_{d,\sigma}$. However, this point is just a removable singularity.

Additional divergences are caused by the logarithms. We will be interested in the values of the dot-reservoir bubbles at $|\Omega - \varepsilon_{d,\bar{\sigma}}| \ll |\varepsilon_{d,\sigma}| \ll W$ and $|X - \varepsilon_{d,\sigma'}| \ll |\varepsilon_{d,\sigma}| \ll W$, respectively, see Sec. 4.5. At the center of these regions, the bubbles feature logarithmic divergences. The expansions of the exact values have the leading terms

$$I_{\sigma}^{(\mathrm{pp})}(\Omega) \approx \frac{-\mathrm{i}}{\varepsilon_{d,\sigma}^2} \ln \frac{|\Omega - \varepsilon_{d,\bar{\sigma}}|}{|\varepsilon_{d,\sigma}|} \qquad \text{for } |\Omega - \varepsilon_{d,\bar{\sigma}}| \ll |\varepsilon_{d,\sigma}| \ll W \tag{4.34a}$$

$$I_{\sigma'\sigma}^{(\mathrm{ph})}(X) \approx \frac{\mathrm{i}}{\varepsilon_{d,\sigma}^2} \ln \frac{|X - \varepsilon_{d,\sigma'}|}{|\varepsilon_{d,\sigma}|} \qquad \text{for } |X - \varepsilon_{d,\sigma'}| \ll |\varepsilon_{d,\sigma}| \ll W. \tag{4.34b}$$

These logarithmic divergences are analogous to the ones in the X-ray-edge model, see Eqs. (3.33c) and (3.31d), respectively. But here the dot levels replace the band width appearing in those expressions. In Sec. 4.6.3 we will show that this difference can be attributed to the two dot propagators of the longer sequence, which have no analogue in a bubble of the X-ray-edge model.

4.4.3 Crossed bubble

The last diagram we discuss results from replacing the left vertex in the dot-reservoir particle-hole bubble (4.26) with the dot-reservoir particle-particle bubble (4.25). We refer to this diagram as the crossed bubble. It will serve as a key example for the relevant higher-order diagrams for our approximation scheme in Sec. 4.6.

The crossed bubble is given by

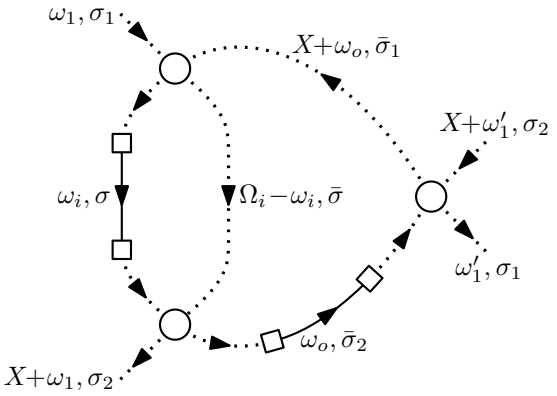

with $\Omega_i = X + \omega_1 + \omega_o$

$$= -\tau^4 U^3 \int_{-\infty}^{\infty} \frac{\mathrm{d}\omega_o}{2\pi} \int_{-\infty}^{\infty} \frac{\mathrm{d}\omega_i}{2\pi} \sum_{\sigma} g_{d\bar{\sigma}_1}(X+\omega_o)\, g_r(\omega_o) \big[g_{d\bar{\sigma}_2}(\omega_o)\big]^2$$
$$\times\, g_{d\bar{\sigma}}(X+\omega_1+\omega_o-\omega_i)\, g_r(\omega_i) \big[g_{d\sigma}(\omega_i)\big]^2 \tag{4.35a}$$
$$= -\frac{8\tau^4}{\pi^2 t^2} U^3 \int_{-\infty}^{\infty} \frac{\mathrm{d}\omega_o}{2\pi} \int_{-\infty}^{\infty} \frac{\mathrm{d}\omega_i}{2\pi} \int_{-W}^{W} \mathrm{d}\varepsilon_o \int_{-W}^{W} \mathrm{d}\varepsilon_i \, \frac{1}{X+\omega_o-\varepsilon_d-\mathrm{i}\eta} \, \frac{1}{\omega_o-\varepsilon_o+\mathrm{i}\eta\,\mathrm{sgn}\,\varepsilon_o}$$
$$\times\, \frac{1}{(\omega_o-\varepsilon_d-\mathrm{i}\eta)^2} \, \frac{1}{X+\omega_1+\omega_o-\omega_i-\varepsilon_d-\mathrm{i}\eta} \, \frac{1}{\omega_i-\varepsilon_i+\mathrm{i}\eta\,\mathrm{sgn}\,\varepsilon_i} \, \frac{1}{(\omega_i-\varepsilon_d-\mathrm{i}\eta)^2} \tag{4.35b}$$
$$= -\frac{8\tau^4}{\pi^2 t^2} U^3 C(X, \omega_1). \tag{4.35c}$$

In the last line, we have defined $C(X, \omega)$, which we will also call the crossed bubble. To make the calculation less cumbersome we have set $\varepsilon_{d,\uparrow} = \varepsilon_d = \varepsilon_{d,\downarrow}$. Nonetheless, the calculation is still tedious. It is performed in Appendix D.1; the exact value of the crossed bubble is given by Eq. (D.7).

In Appendix D.2 we extract from the exact value the leading behavior under certain assumptions. Since this leading behavior is important and will serve as a reference, we copy the result (D.17) here,

$$C(X,\omega) \approx \frac{1}{2\varepsilon_d^4} \begin{cases} 2\ln\frac{|\omega|}{|\varepsilon_d|} \ln\frac{|X-\varepsilon_d|}{|\varepsilon_d|} - \ln^2\frac{|\omega|}{|\varepsilon_d|}, & |\omega| \geq |X-\varepsilon_d| \\ \ln^2\frac{|X-\varepsilon_d|}{|\varepsilon_d|}, & |\omega| \leq |X-\varepsilon_d|. \end{cases} \tag{4.36}$$

It is based on assuming

$$|X-\varepsilon_d|, |\omega+X-\varepsilon_d| \ll |\varepsilon_d| \ll \frac{|\omega+X-\varepsilon_d|^3}{|\varepsilon_d|^3} W \tag{4.37a}$$
$$\frac{|\omega+X-\varepsilon_d|}{|\varepsilon_d|} \ln^2\frac{W}{|\varepsilon_d|} \ll 1 \tag{4.37b}$$

and on assuming that none of the factors

$$\ln\frac{W}{|X-\varepsilon_d|}, \ \ln\frac{W}{|\omega+X-\varepsilon_d|}, \ \ln\frac{W}{|\omega|} \tag{4.38}$$

is so large that it can change the relations if it is inserted somewhere in Eq. (4.37a).

These assumptions are stricter than the regime of interest we will formulate in Sec. 4.5. They were partly made to keep the calculation manageable; we did not investigate how much they can be loosened without altering the leading behavior (4.36) to a more general expression. For example the assumptions were made to render certain terms negligible compared to $1/\varepsilon_d^4$, but it would have been enough if those terms were negligible compared to $\ln^2/\varepsilon_d^4$ with two large logarithms.

The logarithmic divergences in the approximate result (4.36) are analogous to the ones of the crossed bubble that we investigated for the X-ray-edge model, see Eq. (3.41). There, only the first case has been considered. But, as for the dot-reservoir bubbles, here the dot levels replace the band width appearing in that expression.

4.5 Specifying the regime of interest

In this section we discuss the regime in which we study the SIAM. We make assumptions in addition to the ones already stated in Secs. 4.2 and 4.3, which are most notably equilibrium, half filling, vanishing temperature, wide-band limit, and vicinity to the particle-hole symmetric point. Regarding the model, we want to capture its Kondo physics. For example we want to determine the exponentially small scale at which the anomalous rise of the linear conductance across the dot can be observed as the gate voltage or the magnetic field are decreased. Regarding the method, we want to carry over the insights from our treatment of the X-ray-edge model, i.e. the concept of identifying and resumming leading logarithms.

We briefly recap the parameter regime studied by Schrieffer and Wolff [SW66]. They describe how the SIAM Hamiltonian can be approximated by the Kondo Hamiltonian.

However, we do not perform any approximations on the Hamiltonian level. Approaching from an FRG and parquet angle, we investigate 1PI vertices and perform approximations during calculations thereof. We make assumptions on the frequency arguments of the 1PI vertices as well as on the system parameters.

We find logarithmic divergences with respect to frequencies in certain bubble diagrams of the 1PI two-particle vertex. To facilitate a leading-logarithmic analysis similar to the one for the X-ray-edge model, we assume that the frequencies are close to these divergences and that the prefactor of these logarithms is small. The latter assumption coincides with the parameter regime of Schrieffer and Wolff.

We restrict the discussion to the 1PI *two-particle* vertex, expecting that it plays a central role in accessing observables like the linear conductance. But we do not provide the necessary formulas; an attempt at relating the 1PI two-particle vertex in the even sector to the linear conductance is briefly described in Sec. 4.8. There, we find that the linear conductance naturally depends on single-particle, not two-particle, correlation functions, similar to the linear conductance in the Kondo model [PG04]. So it is unclear how important other 1PI vertices are and how well our assumptions on the frequencies are justified. The motivation for these assumptions is so far a technical one and lies in making a leading-logarithmic analysis viable.

4.5.1 Relation of the SIAM and Kondo Hamiltonians according to Schrieffer and Wolff

In their paper [SW66], Schrieffer and Wolff treat the original version of the SIAM. They consider a bulk metal, which has a conduction band formed by s-orbitals, with an impurity atom, which provides a single d-orbital. We consider the quantum-dot version of the SIAM with two reservoirs but have already transformed them such that only one reservoir couples to the dot, see Sec. 4.2.3. So the Hamiltonian studied by Schrieffer and Wolff corresponds to the one studied in this thesis, see the even part of Eq. (4.10); the conduction band and the d-orbital correspond to the reservoir and the dot. Reference [SW66] does not include a magnetic field, i.e. $\varepsilon_{d,\sigma} = \varepsilon_d$.

Schrieffer and Wolff define

$$\varepsilon_+ = \varepsilon_d + U, \qquad \varepsilon_- = \varepsilon_d, \qquad \Gamma_\pm = \pi N(\varepsilon_\pm)|V_{kd}|^2_{\mathrm{AVE}}, \tag{4.39}$$

where $N(\varepsilon)$ denotes the density of states, V_{kd} denotes the coupling amplitude, and the average is over the states with energy $\varepsilon_\pm$, respectively. They consider the case $\varepsilon_+ > 0$, $\varepsilon_- < 0$ and define the limit of small s-d mixing as $\Gamma_\pm/|\varepsilon_\pm| \ll 1$.

In our case the definitions translate to

$$\varepsilon_\pm = \pm\frac{U}{2} + V_g, \qquad \Gamma_\pm = (M+1)\rho(\varepsilon_\pm)|-\bar{\tau}_k|^2_{\mathrm{AVE}} = \frac{2\tau^2}{t}. \tag{4.40}$$

We have taken into account that Schrieffer and Wolff presumably define the density of states by $\sum_k = \int \mathrm{d}\varepsilon\, N(\varepsilon)$, whereas we define it by $[\pi/(M+1)]\sum_k = \int \mathrm{d}\varepsilon\, \rho(\varepsilon)$, see Eq. (4.7); additionally, we have used the wide-band limit, see Sec. 4.2.4. Since we consider the system close to the particle-hole symmetric point, we have $\varepsilon_\pm \approx \pm U/2$. So in our notation their limit of small s-d mixing can be written as $\tau^2 U/(t\varepsilon_d^2) \ll 1$.

Schrieffer and Wolff proceed by rewriting the Hamiltonian with a unitary transformation. This transformation is designed to eliminate the original coupling term, which is of first order in the coupling amplitude, at the cost of introducing higher-order terms. Under the conditions above, Schrieffer and Wolff argue that the system favors a singly occupied d-orbital and that almost all of the newly introduced coupling terms are negligible. The only important coupling term is an s-d exchange interaction of the Kondo form. A modern interpretation of the Schrieffer-Wolff transformation as a form of perturbation theory is given in Ref. [BDL11]; the above procedure corresponds to the lowest-order truncation.

Schrieffer and Wolff have thus approximated the SIAM Hamiltonian with the Kondo Hamiltonian [SW66]

$$\begin{aligned} H_{\mathrm{Kondo}} = &\sum_{k\sigma} \varepsilon_k\, c^\dagger_{k,\sigma} c_{k,\sigma} \\ &- \frac{1}{4}\sum_{k'k} J_{k'k}\left(2\, c^\dagger_{k',\uparrow} c_{k,\downarrow} d^\dagger_\downarrow d_\uparrow + 2\, c^\dagger_{k',\downarrow} c_{k,\uparrow} d^\dagger_\uparrow d_\downarrow + \sum_{\sigma_1\sigma_2} \sigma_1\sigma_2\, c^\dagger_{k',\sigma_1} c_{k,\sigma_1} d^\dagger_{\sigma_2} d_{\sigma_2}\right). \end{aligned} \tag{4.41}$$

Here, we use our own notation. This expression involves restricting the system to the subspace with a singly occupied d-orbital; the constant term ε_d has been dropped.

If the effective coupling strength $J_{k'k}$ is approximated with a constant matching its value at the Fermi surface, it is [SW66]

$$J = \frac{8\tau^2 U}{(M+1)\varepsilon_d(\varepsilon_d + U)} < 0. \tag{4.42}$$

Formulated in terms of this coupling strength, the limit of small s-d mixing reads

$$|N(0)J| = \left| \frac{M+1}{\pi} \rho(0) J \right| \ll 1 \tag{4.43}$$

and is also known as the weak-coupling regime.

4.5.2 Parameter and frequency regime for the 1PI two-particle vertex

Let us now discuss our assumptions for calculating the 1PI two-particle vertex. They involve not only the system parameters but also the frequency region. Our goal is to make a leading-logarithmic analysis viable.

We assume that the influence of the magnetic field on the dot levels is rather small. So as long as we roughly compare the energy scales of the model, we use $\varepsilon_{d,\sigma} \approx \varepsilon_d$. Furthermore, the band width $2W$ is assumed to be by far the greatest energy scale. We have already made this assumption to perform the eponymous wide-band limit, see Sec. 4.2.4. This implies that the dot levels lie relatively close to the middle of the reservoir band, $|\varepsilon_d| \ll W$.

In Sec. 4.4 we have calculated the exact values of some low-order diagrams of the 1PI two-particle vertex. We have found logarithms in the dot-reservoir bubbles, see Eqs. (4.30) and (4.33). They diverge as the respective natural frequency approaches $-W + \varepsilon_{d,\sigma}$ or $\varepsilon_{d,\sigma}$ for some spin σ. We are not interested in the former kind of divergence as it is associated with the edge of the reservoir band. For our leading-logarithmic analysis, we focus on the latter kind of divergence, i.e. we want the natural frequencies to be close to the dot levels, $|\Omega - \varepsilon_d| \ll |\varepsilon_d|$ or $|X - \varepsilon_d| \ll |\varepsilon_d|$.

We will investigate both these cases, i.e. the divergences of both channels. Regarding the target external frequency region of the 1PI two-particle vertex, we actually do not know if these cases apply because we have no formula relating this vertex directly to an observable. But we assume that the external frequencies are close to the divergence of at least one channel. We expect that the divergence of the other channel is then just as relevant: Provided the leading-logarithmic approximation works as for the X-ray-edge model, see Sec. 3.4, the important diagrams will be the parquet diagrams and even for inner bubbles the natural frequency will be close to the respective divergence.

For the above assumptions, we have already given the leading behavior of the dot-reservoir bubbles in Eq. (4.34). If we include the inherent prefactors of the diagrams that were excluded from the definitions of $I_\sigma^{(\mathrm{pp})}(\Omega)$ and $I_{\sigma'\sigma}^{(\mathrm{ph})}(X)$, see Eqs. (4.25) and (4.26), the leading behavior of the dot-reservoir particle-particle bubble and of the

dot-reservoir particle-hole bubble reads

$$\mathrm{i}\frac{2\tau^2}{\pi t}\,U^2\sigma_1'\sigma_1\sum_\sigma I_\sigma^{(\mathrm{pp})}(\Omega) \approx \frac{2\tau^2}{\pi t}\,U^2\sigma_1'\sigma_1\sum_\sigma \frac{1}{\varepsilon_{d,\sigma}^2}\ln\frac{|\Omega-\varepsilon_{d,\bar\sigma}|}{|\varepsilon_{d,\sigma}|} \tag{4.44a}$$

$$\mathrm{i}\frac{2\tau^2}{\pi t}\,U^2 I_{\bar\sigma_1\bar\sigma_2}^{(\mathrm{ph})}(X) \approx -\frac{2\tau^2}{\pi t}\,U^2\frac{1}{\varepsilon_{d,\bar\sigma_2}^2}\ln\frac{|X-\varepsilon_{d,\bar\sigma_1}|}{|\varepsilon_{d,\bar\sigma_2}|}. \tag{4.44b}$$

We require that the absolute values of these expressions are close to but less than the absolute value of the bare vertex. If the absolute values would be greater, subleading logarithms would become important. If the absolute values would be much smaller, low-order perturbation theory would suffice and no resummation would be necessary. This requirement translates to an interplay between the frequencies and the prefactors in Eq. (4.44). Although we want the frequencies to be close to the divergences, they must not be too close. Meanwhile, the factor $\tau^2U/(t\varepsilon_d^2)$ must be small.

Also, we might want to assume that U and τ are small to make other diagrams less important when compared to the parquet diagrams built from dot-reservoir bubbles. For example, dot-only subdiagrams with more and more vertices feature more and more factors U. The dot-dot bubbles from Sec. 4.4.1 fall into this category; in Sec. 4.6.2 we will discuss their role in more detail, finding that they effectively renormalize U as they depend only weakly on frequencies. And bubbles with more and more reservoir propagators feature more and more factors τ^2. To find out how small τ has to be for such diagrams to be less important, a discussion similar to the one that we will perform in Sec. 4.6.3 for the dot-reservoir bubbles could be helpful.

Anyway, we can argue that, to an extent, the requirement that U and τ are small is already quantified by the requirement that $\tau^2U/(t\varepsilon_d^2)$ is small. The latter requirement exactly matches the regime considered by Schrieffer and Wolff, see Sec. 4.5.1. In their Hamiltonian view, the effective Kondo interaction is $\propto \tau^2U$ and all other interaction terms are negligible. In our diagrammatic view, the parquet diagrams built from dot-reservoir bubbles can be understood as parquet diagrams built with effective Kondo vertices that are $\propto \tau^2U$; this idea is discussed in more detail in Sec. 4.6.5. Hoping that the argument by Schrieffer and Wolff can be transferred to the diagrammatic level, we expect that all diagrams representing other combinations of U and τ are negligible. However, this is not the whole story: First, in the regime of interest, one of the dot-dot bubbles, which are not built with effective Kondo vertices, is not small compared to the dot-reservoir bubbles. But since the dot-dot bubbles depend only weakly on frequencies, they do not seem to be as important, see Sec. 4.6.2. Second, Schrieffer and Wolff's effective Kondo interaction has an additional U-dependence in the denominator, see Eq. (4.42). We will take a closer look at this second point in Sec. 4.6.5.

In the discussion above, we have treated the interaction strength U and the dot levels ε_d as independent. However, we impose $\varepsilon_d \approx -U/2$ because we want to study the system close to the particle-hole symmetric point. Because of this restriction, the requirement that $\tau^2U/(t\varepsilon_d^2)$ is small actually favors large U.

Let us summarize our assumptions for calculating the 1PI two-particle vertex. For the frequencies, we assume that the total frequency Ω, the exchange frequency

X, or the direct frequency D is close to the dot levels, i.e. at least one of the cases

$$|\Omega - \varepsilon_d| \ll |\varepsilon_d|, \qquad |X - \varepsilon_d| \ll |\varepsilon_d|, \text{ or} \qquad |D - \varepsilon_d| \ll |\varepsilon_d| \tag{4.45}$$

is satisfied. For the system parameters, we assume

$$|\varepsilon_d| \ll W \qquad \text{and} \qquad \frac{\tau^2 U}{t\varepsilon_d^2} \ll 1. \tag{4.46}$$

Here, we have written ε_d as a placeholder for $\varepsilon_{d,\uparrow}$ or $\varepsilon_{d,\downarrow}$ because we assume that the influence of the magnetic field on the dot levels is rather small, but we do not neglect the magnetic field. Since we study the SIAM near the particle-hole symmetric point, the second assumption in Eq. (4.46) translates to $\Gamma \ll U$ when expressed in terms of the hybridization $\Gamma = 2\tau^2/t$, which coincides with Schrieffer and Wolff's definition of $\Gamma_\pm$.

4.6 Leading-logarithmic approximation

We formulate an approximation scheme for the SIAM with the goal of resumming the leading logarithms. Our focus lies on the 1PI two-particle vertex in the regime described in Sec. 4.5.2.

We start by listing the individual approximation steps. These include the restriction to parquet diagrams built from dot-reservoir bubbles.

Next, we discuss the role of the dot-dot bubbles. In the regime of interest, one of their values is so large that it does not seem negligible. However, they depend only weakly on frequencies and effectively renormalize U. As the dot-dot bubbles contain no logarithms, we neglect their effect.

Given the restriction to certain diagrams, we justify the remaining approximations, using the dot-reservoir bubbles from Sec. 4.4.2 and the crossed bubble from Sec. 4.4.3 as key examples. Each result is validated against the respective exact value.

Based on our approximation steps, we formulate effective diagrammatic rules, which we then use to relate the SIAM and the Kondo model. We thereby provide a diagrammatic perspective that is complementary to the Hamiltonian perspective of Ref. [SW66].

4.6.1 List of approximations

We give a complete summary of our approximation steps to calculate the 1PI two-particle vertex. These steps are very similar to the ones for the X-ray-edge model, see Sec. 3.4.2, which in turn were adopted from Ref. [RGN69]. To emphasize this similarity, we again group the steps into five labeled points. In the following the focus lies on the aspects that are different or new.

(i) consider only the parquet diagrams

We have found singular bubbles in the particle-particle, exchange particle-hole, and direct particle-hole channels, see Sec. 4.4.2. Here, even the direct particle-hole channel

appears; since the bare two-particle vertex has only dot legs, the difference between the direct and the exchange particle-hole channels concerns only the order of the external legs. We neglect the diagrams and subdiagrams that are irreducible with respect to all channels, except the bare two-particle vertex. The remaining diagrams are the parquet diagrams in all three channels.

(ii) impose self-energy insertions to form dot-reservoir bubbles

We neglect all self-energy contributions that involve a two-particle vertex. In each bubble of the parquet diagrams, we impose that one sequence (of lines and single-particle vertices) has two single-particle vertices and the other sequence has none. The remaining diagrams are the parquet diagrams built from the dot-reservoir bubbles (4.25) and (4.26). We require these bubbles to be oriented such that each two-particle vertex has one incoming and one outgoing long sequence and one incoming and one outgoing short sequence, see Sec. 4.6.5 for a detailed explanation. The only exception to this rule are the external legs.

(iii.a) neglect the imaginary part of $g_{d\sigma}$ and the real part of g_r

The imaginary part of the free dot propagator and the real part of the free reservoir propagator are neglected. The dotted and full lines now have the values

$$g_{d\sigma}(\omega) = \mathcal{P}\frac{1}{\omega - \varepsilon_{d,\sigma}} \tag{4.47a}$$

$$g_r(\omega) = -\mathrm{i}\frac{2}{t}\,\mathrm{sgn}(\omega)\Theta(W - |\omega|). \tag{4.47b}$$

(iii.b) replace the free dot propagators of each longer sequence with a step function

Let us consider each dot-reservoir bubble individually. The previous step is targeted at the free dot propagator constituting the shorter sequence (of lines and single-particle vertices). We perform a much more drastic replacement for the two identical free dot propagators of the longer sequence, namely

$$\big[g_{d\sigma}(\omega)\big]^2 \to \frac{\Theta(|\varepsilon_{d,\sigma}| - |\omega|)}{\varepsilon_{d,\sigma}^2}. \tag{4.48}$$

This step function overrides the step function from the free reservoir propagator because it is more specific.

(iv) neglect small shifts of the integration boundaries

The step function above selects a window for the independent frequency variable of a bubble. If this variable is the frequency of the longer sequence, the integration boundaries are $\pm|\varepsilon_{d,\sigma}|$. In the course of variable transformations, the integration boundaries will be shifted by $\Omega - \varepsilon_{d,\bar{\sigma}}$ or $X - \varepsilon_{d,\sigma'}$. These shifts are small and we neglect them.

(v) logarithmic approximation

If a bubble is embedded in a bubble of the other channel, the natural frequency of the former bubble is a linear combination of independent frequency variables. We replace the linear combination with the maximum of the absolute values of these frequencies. The natural frequency of a bubble appears always as $\Omega - \varepsilon_{d,\sigma}$ or $X - \varepsilon_{d,\sigma}$ and is thus effectively measured against one of the dot levels, which are nonzero in contrast to the renormalized deep level in the X-ray-edge model. Depending on the choice of independent frequencies, the logarithmic approximation can be performed in different ways. Concrete examples can be seen in Eqs. (4.60) and (4.62). In leading logarithmic order, the result turns out to be independent of the choice.

We do not sufficiently justify steps (i) and (ii) for the SIAM. They are similar to the respective steps for the X-ray-edge model, see Sec. 3.4.2, and are designed to include those diagrams in which we found logarithmic divergences. The dot-dot bubbles are among the neglected diagrams because they feature no logarithms; in Sec. 4.6.2 we discuss additional reasons that diminish their importance. Still, which diagrams contain the leading contributions remains an open question.

Step (ii) describes a rather peculiar treatment of the self-energy. The single-particle vertex is not fully included in the sense of a Dyson series. Instead, we prescribe how many single-particle vertices appear. This step could possibly be justified through a discussion of bubbles with more and more single-particle vertices similar to how we will discuss the dot-reservoir bubbles in Sec. 4.6.3.

Steps (iii)-(v) are justified in Secs. 4.6.3 and 4.6.4: for key example diagrams, the resulting approximate values are compared with the exact values. Steps (iii.a), (iv), and (v) are fully analogous to the respective steps performed for the X-ray-edge model. In Sec. 4.6.3 we motivate the entirely new step (iii.b) pedagogically.

4.6.2 Role of the dot-dot bubbles

In Sec. 4.4.1 we have calculated the dot-dot bubbles. They are the simplest bubble diagrams because they contain no single-particle vertices and no reservoir propagators. The diagrams and their exact values are shown in Eqs. (4.23) and (4.24).

Let us gauge the importance of these diagrams. In the regime of interest formulated in Sec. 4.5.2, the dot-dot particle-particle bubble can be estimated as $-2U\sigma_1'\sigma_1$, which is minus twice the bare vertex and thus certainly not negligible. Also, it is not negligible when compared with the dot-reservoir bubbles, which we have tuned to be of the same order as the bare vertex by focusing on the leading-logarithmic regime. The dot-dot particle-hole bubble evaluates to zero. So the dot-dot particle-particle bubble seems to be important, while the dot-dot particle-hole bubble is not.

The dot-dot bubbles have no counterpart in the leading-logarithmic approximation for the X-ray-edge model; they do not even contain logarithms. Moreover, they do not seem to fit in the simple picture that Schrieffer and Wolff's insights on the Hamiltonian level can be transferred to the diagrammatic level in the form of effective Kondo vertices. The question arises whether there is some reason that makes the

dot-dot bubbles negligible or whether we could set up the diagrammatic formulation slightly differently to achieve that.

As one such change of the diagrammatic formulation that is worth considering, we can try altering the dot occupation associated with the free propagator. This occupation is encoded in the sign of the imaginary part of the frequency-dependent free propagator and originates from the choice of state that forms the expectation value in the generating functional, see Eq. (2.8). Currently, this state is given by the noninteracting ground state and the dot is doubly occupied, see Eq. (4.15). As shown in Sec. 2.11, generalizations of the zero-temperature formalism that involve other choices than the noninteracting ground state are possible. But choices with other dot occupations likely violate the convergence of time integrals. Let us say we can somehow overcome the issue of convergence.

If the free propagator is altered such that the dot is singly occupied, the dot-dot particle-particle bubble (4.23) evaluates to zero and the dot-dot particle-hole bubble (4.24) evaluates to

$$\pm U^2 \delta_{\sigma_1 \bar{\sigma}_2} \frac{1}{X + \varepsilon_{d,\sigma_1} - \varepsilon_{d,\bar{\sigma}_1} \mp \mathrm{i}\eta}, \tag{4.49}$$

depending on whether $\bar{\sigma}_1$ or σ_1 is the spin of the occupied dot state. In the regime of interest, this value is of the same order as the bare vertex. So the dot-dot bubbles again seem important – in this case not because of the particle-particle channel but because of the particle-hole channel. In the same regime, we can flip the sign of the dot-dot particle-hole bubble by flipping all its spins. While this property can cause cancellations, it can only do so for ladder subdiagrams with an odd number of dot-dot particle-hole bubbles.

And if the free propagator is altered such that the dot is empty, the values of the dot-dot bubbles are analogous to the original case with a doubly occupied dot. So neither way of altering the dot occupation renders the dot-dot bubbles negligible.

We consider the dot-dot bubbles to be less important than the comparison with the bare vertex suggests for another reason: in the regime of interest, the dot-dot bubbles depend only very weakly on frequencies and can be seen to just renormalize the bare vertex. To this end we consider, in the original diagrammatic formulation with a doubly occupied dot, the series of ladder diagrams that are composed of $n = 0, 1, 2, \ldots$ dot-dot particle-particle bubbles, where the case $n = 0$ represents the bare vertex. As this series evaluates approximately to $U\sigma_1'\sigma_1 \sum_{n=0}^{\infty}(-2)^n$, it does not converge. However, if we treated it as a converging geometric series, we could write

$$\sum_{n=0}^{\infty}(-2)^n = 1 - 2\sum_{n=1}^{\infty}(-2)^{n-1} = 1 - 2\sum_{n=0}^{\infty}(-2)^n \qquad \Leftrightarrow \qquad \sum_{n=0}^{\infty}(-2)^n = \frac{1}{3}. \tag{4.50}$$

In this sense we interpret the dot-dot bubbles as representing an improper, nonconverging series expansion of a static renormalization of the bare two-particle vertex by a factor 1/3.

We neglect the dot-dot bubbles and instead focus on the diagrams containing the leading logarithmic terms. In the end the renormalized value of the bare vertex could still be used as an afterthought to see the quantitative impact of the dot-dot bubbles on the results.

4.6.3 Approximating the dot-reservoir bubbles

In this section we motivate the approximations listed in Sec. 4.6.1 that concern the dot-reservoir bubbles, specifically the steps (iii.a), (iii.b), and (iv). We explicitly discuss the dot-reservoir particle-particle bubble $I_\sigma^{(\mathrm{pp})}(\Omega)$ defined in Eq. (4.25). The argument works analogously for the dot-reservoir particle-hole bubble $I_{\sigma'\sigma}^{(\mathrm{ph})}(X)$ defined in Eq. (4.26). In the end we confirm that the approximations yield the correct leading behavior for each of these bubbles as expected.

For convenience let us repeat the definition

$$I_\sigma^{(\mathrm{pp})}(\Omega) = \frac{\pi t}{2}\int_{-\infty}^{\infty}\frac{\mathrm{d}\omega}{2\pi}\, g_{d\bar\sigma}(\Omega-\omega)\, g_r(\omega)\big[g_{d\sigma}(\omega)\big]^2 \tag{4.51a}$$

$$= \int_{-\infty}^{\infty}\frac{\mathrm{d}\omega}{2\pi}\,\frac{1}{\Omega-\omega-\varepsilon_{d,\bar\sigma}-\mathrm{i}\eta}\left[\ln\frac{|W+\omega|}{|W-\omega|}-\mathrm{i}\pi\,\mathrm{sgn}(\omega)\Theta(W-|\omega|)\right]\frac{1}{(\omega-\varepsilon_{d,\sigma}-\mathrm{i}\eta)^2}. \tag{4.51b}$$

In the second line, we have inserted the exact expressions (4.20a) and (4.20d) for the free propagators.

We know this integral diverges logarithmically as $|\Omega-\varepsilon_{d,\bar\sigma}|/|\varepsilon_{d,\sigma}|\to 0$. Which of its features can be responsible for any kind of divergence? Since the integrand falls off as $1/\omega^4$ for $\omega\to\pm\infty$, only the singularities of the integrand at $\omega=\pm W,\varepsilon_{d,\sigma}$, $\Omega-\varepsilon_{d,\bar\sigma}$ come into question. The singularities at $\omega=\pm W$ are only logarithmic and cannot lead to a divergent integral.

Also the singularity at $\omega=\varepsilon_{d,\sigma}$ does not lead to a divergent integral. To show this we consider the interval $[3\varepsilon_{d,\sigma}/2,\varepsilon_{d,\sigma}/2]$ and expand the first two factors of the integrand around $\omega=\varepsilon_{d,\sigma}$. As no other singularity or discontinuity lies in the interval, this expansion converges. The constant and the linear term lead to an integral of the form

$$\int_{-a}^{a}\mathrm{d}x\,\frac{c_0+c_1x}{(x-\mathrm{i}\eta)^2} = c_0\int_{-a}^{a}\mathrm{d}x\,\frac{x^2-\eta^2}{(x^2+\eta^2)^2}+\mathrm{i}c_1\int_{-a}^{a}\mathrm{d}x\,\frac{2\eta x^2}{(x^2+\eta^2)^2} \tag{4.52a}$$

$$= c_0\,\frac{-x}{x^2+\eta^2}\bigg|_{-a}^{a}+\mathrm{i}c_1\left[\arctan\Big(\frac{x}{\eta}\Big)-\frac{\eta x}{x^2+\eta^2}\right]_{-a}^{a} \tag{4.52b}$$

$$= -2\,\frac{c_0}{a}+\mathrm{i}\pi c_1, \tag{4.52c}$$

where $x=\omega-\varepsilon_{d,\sigma}$, $a=|\varepsilon_{d,\sigma}|/2$, $c_0\approx -\mathrm{i}/(2\varepsilon_{d,\sigma})$, and $c_1\approx \mathrm{i}/(2\varepsilon_{d,\sigma}^2)$; this result is negligible. For the quadratic and higher-order terms, the singularity of the integrand is even removable.

Consequently, the singularity at $\omega=\Omega-\varepsilon_{d,\bar\sigma}$ must cause the integral to diverge. The mechanism is familiar from our study of the X-ray-edge model: the sign function disrupts the cancellation of the positive and negative contributions from the principal-value part of the first factor. This mechanism gives rise to a logarithm of the form $\ln(|\Omega-\varepsilon_{d,\bar\sigma}|/\omega_{\mathrm{cutoff}})$ with $|\Omega-\varepsilon_{d,\bar\sigma}|\ll\omega_{\mathrm{cutoff}}$. Here, $\pm\omega_{\mathrm{cutoff}}$ denote the frequencies at which the $1/|\omega|$-tails of the integrand, which help to build up the logarithm, are cut off in some way. Shifts of the tails or cutoff frequencies by $\Omega-\varepsilon_{d,\bar\sigma}$ are negligible.

There are two candidates for ω_{cutoff}. Like for the X-ray-edge model, we have a step function $\Theta(W-|\omega|)$ that cuts off the tails at the band edges $\pm W$. Here, we additionally have the factor

$$\frac{1}{(\omega-\varepsilon_{d,\sigma}-\mathrm{i}\eta)^2} \approx \begin{cases} 1/\varepsilon_{d,\sigma}^2, & |\omega| \ll |\varepsilon_{d,\sigma}| \\ 1/\omega^2, & |\omega| \gg |\varepsilon_{d,\sigma}|. \end{cases} \tag{4.53}$$

It effectively cuts off the tails already at $\mp\varepsilon_{d,\sigma}$. (We have shown above that the contribution from $|\omega| \approx |\varepsilon_{d,\sigma}|$ is negligible. Also the contribution from $W \geq |\omega| \gg |\varepsilon_{d,\sigma}|$ is negligible as the integrand has the form $1/|\omega|^3$.) Thus, the logarithmic divergence of the integral has the form $\ln(|\Omega-\varepsilon_{d,\bar{\sigma}}|/|\varepsilon_{d,\sigma}|)$. The dominant contribution comes from the integration region $|\omega| \ll |\varepsilon_{d,\sigma}|$, where the factor (4.53) is approximately $1/\varepsilon_{d,\sigma}^2$. These considerations motivate the replacement described by step (iii.b).

For the dot-reservoir particle-particle bubble, our approximation steps lead to

$$I_\sigma^{(\mathrm{pp})}(\Omega) \underset{\text{(iii.b)}}{\overset{\text{(iii.a)}}{\approx}} -\frac{\mathrm{i}}{2}\int_{-\infty}^{\infty}\mathrm{d}\omega \left(\mathcal{P}\frac{1}{\Omega-\omega-\varepsilon_{d,\bar{\sigma}}}\right) \operatorname{sgn}(\omega)\Theta(W-|\omega|)\,\frac{\Theta(|\varepsilon_{d,\sigma}|-|\omega|)}{\varepsilon_{d,\sigma}^2} \tag{4.54a}$$

$$= \frac{\mathrm{i}}{2\varepsilon_{d,\sigma}^2}\int_{-|\varepsilon_{d,\sigma}|-\Omega+\varepsilon_{d,\bar{\sigma}}}^{|\varepsilon_{d,\sigma}|-\Omega+\varepsilon_{d,\bar{\sigma}}}\mathrm{d}\omega' \left(\mathcal{P}\frac{1}{\omega'}\right)\operatorname{sgn}(\omega'+\Omega-\varepsilon_{d,\bar{\sigma}}) \tag{4.54b}$$

$$\overset{\text{(iv)}}{\approx} \frac{\mathrm{i}}{2\varepsilon_{d,\sigma}^2}\int_{-|\varepsilon_{d,\sigma}|}^{|\varepsilon_{d,\sigma}|}\mathrm{d}\omega' \left(\mathcal{P}\frac{1}{\omega'}\right)\operatorname{sgn}(\omega'+\Omega-\varepsilon_{d,\bar{\sigma}}) \tag{4.54c}$$

$$= \frac{-\mathrm{i}}{\varepsilon_{d,\sigma}^2}\ln\frac{|\Omega-\varepsilon_{d,\bar{\sigma}}|}{|\varepsilon_{d,\sigma}|}. \tag{4.54d}$$

We have transformed the integration variable to $\omega' = \omega - \Omega + \varepsilon_{d,\bar{\sigma}}$. The calculation shows that the dominant contribution comes from the integration region $|\Omega-\varepsilon_{d,\bar{\sigma}}| \leq |\omega'| \ll |\varepsilon_{d,\sigma}|$. For the dot-reservoir particle-hole bubble, our steps lead to

$$I_{\sigma'\sigma}^{(\mathrm{ph})}(X) = \frac{\pi t}{2}\int_{-\infty}^{\infty}\frac{\mathrm{d}\omega}{2\pi}\, g_{d\sigma'}(X+\omega)\, g_r(\omega)\big[g_{d\sigma}(\omega)\big]^2 \tag{4.55a}$$

$$\underset{\text{(iii.b)}}{\overset{\text{(iii.a)}}{\approx}} -\frac{\mathrm{i}}{2}\int_{-\infty}^{\infty}\mathrm{d}\omega \left(\mathcal{P}\frac{1}{X+\omega-\varepsilon_{d,\sigma'}}\right) \operatorname{sgn}(\omega)\Theta(W-|\omega|)\,\frac{\Theta(|\varepsilon_{d,\sigma}|-|\omega|)}{\varepsilon_{d,\sigma}^2} \tag{4.55b}$$

$$= \frac{-\mathrm{i}}{2\varepsilon_{d,\sigma}^2}\int_{-|\varepsilon_{d,\sigma}|+X-\varepsilon_{d,\sigma'}}^{|\varepsilon_{d,\sigma}|+X-\varepsilon_{d,\sigma'}}\mathrm{d}\omega' \left(\mathcal{P}\frac{1}{\omega'}\right)\operatorname{sgn}(\omega'-X+\varepsilon_{d,\sigma'}) \tag{4.55c}$$

$$\overset{\text{(iv)}}{\approx} \frac{-\mathrm{i}}{2\varepsilon_{d,\sigma}^2}\int_{-|\varepsilon_{d,\sigma}|}^{|\varepsilon_{d,\sigma}|}\mathrm{d}\omega' \left(\mathcal{P}\frac{1}{\omega'}\right)\operatorname{sgn}(\omega'-X+\varepsilon_{d,\sigma'}) \tag{4.55d}$$

$$= \frac{\mathrm{i}}{\varepsilon_{d,\sigma}^2}\ln\frac{|X-\varepsilon_{d,\sigma'}|}{|\varepsilon_{d,\sigma}|}. \tag{4.55e}$$

We have transformed the integration variable to $\omega' = \omega + X - \varepsilon_{d,\sigma'}$. The dominant contribution comes from the region $|X-\varepsilon_{d,\sigma'}| \leq |\omega'| \ll |\varepsilon_{d,\sigma}|$.

The approximate results (4.54d) and (4.55e) agree with Eqs. (4.34a) and (4.34b), which state the respective leading behavior that we determined from the exact value. We have thus confirmed that our scheme captures the leading logarithms of the dot-reservoir bubbles.

4.6.4 Approximating the crossed bubble

We calculate the crossed bubble $C(X,\omega)$ defined in Eq. (4.35) by applying the approximations listed in Sec. 4.6.1. As this diagram is composed of two dot-reservoir bubbles, we again use steps (iii.a), (iii.b), and (iv). Additionally, the crossed bubble serves as a key example for step (v) in higher-order parquet diagrams.

We will compare our result with the one of the exact calculation discussed in Sec. 4.4.3. There, we neglect the spin dependence of the dot levels, $\varepsilon_{d,\uparrow} = \varepsilon_d = \varepsilon_{d,\downarrow}$. Here, we do the same for clarity, although the calculation would stay manageable even with the spin dependence.

After the spin index of the free dot propagator has been dropped, the definition of the crossed bubble reads

$$\begin{aligned} &C(X,\omega) \\ &= \frac{\pi^2 t^2}{4} \int_{-\infty}^{\infty} \frac{\mathrm{d}\omega_o}{2\pi} \int_{-\infty}^{\infty} \frac{\mathrm{d}\omega_i}{2\pi}\, g_d(X+\omega_o)\, g_r(\omega_o) \big[g_d(\omega_o)\big]^2 g_d(\Omega_i-\omega_i)\, g_r(\omega_i) \big[g_d(\omega_i)\big]^2 \end{aligned} \tag{4.56}$$

with $\Omega_i = X+\omega+\omega_o$. Inserting the expressions specified by steps (iii.a) and (iii.b) for the free propagators and transforming the integration variables to $\omega_o' = \omega_o + X - \varepsilon_d$ and $\omega_i' = \omega_i - \Omega_i + \varepsilon_d$ leads to

$$\begin{aligned} C(X,\omega) \approx \frac{1}{4\varepsilon_d^4} &\int_{-|\varepsilon_d|+X-\varepsilon_d}^{|\varepsilon_d|+X-\varepsilon_d} \mathrm{d}\omega_o' \int_{-|\varepsilon_d|-\Omega_i+\varepsilon_d}^{|\varepsilon_d|-\Omega_i+\varepsilon_d} \mathrm{d}\omega_i' \left(\mathcal{P}\frac{1}{\omega_o'}\right) \mathrm{sgn}(\omega_o' - X + \varepsilon_d) \\ &\times \left(\mathcal{P}\frac{1}{\omega_i'}\right) \mathrm{sgn}(\omega_i' + \Omega_i - \varepsilon_d). \end{aligned} \tag{4.57}$$

The natural frequency $\Omega_i = \omega_o' + \omega + \varepsilon_d$ of the inner bubble turns out to satisfy $|\Omega_i - \varepsilon_d| \ll |\varepsilon_d|$ as far as the leading logarithms are concerned: as in Sec. 4.4.3 we assume $|\omega| \ll |\varepsilon_d|$, and the approximate calculation of the dot-reservoir particle-hole bubble in Sec. 4.6.3 shows that the dominant contribution comes from the region $|\omega_o'| \ll |\varepsilon_d|$. Applying step (iv) we set the integration boundaries of the ω_i'-integral to $\pm|\varepsilon_d|$ and obtain

$$\begin{aligned} &C(X,\omega) \\ &\approx -\frac{1}{2\varepsilon_d^4} \int_{-|\varepsilon_d|+X-\varepsilon_d}^{|\varepsilon_d|+X-\varepsilon_d} \mathrm{d}\omega_o' \left(\mathcal{P}\frac{1}{\omega_o'}\right) \mathrm{sgn}(\omega_o' - X + \varepsilon_d)\Theta(|\varepsilon_d| - |\Omega_i - \varepsilon_d|) \ln\frac{|\Omega_i - \varepsilon_d|}{|\varepsilon_d|}. \end{aligned} \tag{4.58}$$

We drop the step function because it evaluates to one for the dominant contribution or, alternatively, because we interpret it as a small shift of the integration boundaries. Again applying step (iv), we set the integration boundaries of the ω_o'-integral to $\pm|\varepsilon_d|$. The crossed bubble is now given by

$$C(X,\omega) \approx -\frac{1}{2\varepsilon_d^4} \int_{-|\varepsilon_d|}^{|\varepsilon_d|} \mathrm{d}\omega_o' \left(\mathcal{P}\frac{1}{\omega_o'}\right) \mathrm{sgn}(\omega_o' - X + \varepsilon_d) \ln\frac{|\omega_o' + \omega|}{|\varepsilon_d|}. \tag{4.59}$$

At this point we apply step (v), i.e. we replace

$$|\omega_o' + \omega| \to \max\{|\omega_o'|, |\omega|\}. \tag{4.60}$$

By appropriately decomposing the integration region, we straightforwardly solve the integral and arrive at

$$C(X,\omega) \approx \frac{1}{2\varepsilon_d^4} \begin{cases} 2\ln\frac{|\omega|}{|\varepsilon_d|}\ln\frac{|X-\varepsilon_d|}{|\varepsilon_d|} - \ln^2\frac{|\omega|}{|\varepsilon_d|}, & |\omega| \geq |X-\varepsilon_d| \\ \ln^2\frac{|X-\varepsilon_d|}{|\varepsilon_d|}, & |\omega| \leq |X-\varepsilon_d|. \end{cases} \tag{4.61}$$

This result is identical to the leading behavior (4.36) that has been extracted from the exact value of the crossed bubble. So our approximation scheme captures the leading logarithms even for parquet diagrams with crossed channels.

Finally, let us briefly discuss an alternative way of applying step (v). The logarithmic approximation looks different for the X-ray-edge model and for the SIAM, compare Eq. (3.51) with Eq. (4.60). The reason lies in the choice of the independent frequency variables. In the X-ray-edge model, they have been chosen to be the deep-state frequencies. In the SIAM they have originally been chosen to be the reservoir frequencies but have been transformed to be the dot frequencies (up to the sign and up to a shift by the dot level, the equivalent of which in the X-ray-edge model has been set to zero). To achieve a full analogy, we would have to transform ω as well, namely to $\omega' = \omega + X - \varepsilon_d$, so that step (v) would mean replacing

$$|\omega_o' + \omega' - X + \varepsilon_d| \to \max\{|\omega_o'|, |\omega'|, |X-\varepsilon_d|\}. \tag{4.62}$$

This approximation naturally leads to a case distinction involving ω' instead of ω. Just like before, the integration region $|\omega_o'| < |X-\varepsilon_d|$ gives a vanishing contribution as the integrand is odd. Outside this region the replacement (4.62) reduces to $\max\{|\omega_o'|, |\omega'|\}$ and so the result has the exact same form as the right-hand side of Eq. (4.61), just with ω' instead of ω. These two results can be shown to agree in leading logarithmic order. So both ways of applying step (v) are valid.

4.6.5 Relation of the SIAM and the Kondo model from a diagrammatic perspective

In this section we develop an effective diagrammatic formulation that incorporates some of the approximation steps from Sec. 4.6.1. It allows to express the leading-logarithmic approximation more efficiently. Here, we use it to study the relation of the SIAM and the Kondo model on the leading-logarithmic level.

First, we elaborate on the requirement made in step (ii) concerning the orientation of the dot-reservoir bubbles in parquet diagrams: with the exception of the external legs, each two-particle vertex has one incoming and one outgoing long sequence, which has two single-particle vertices, and one incoming and one outgoing short sequence, which has none. In principle other orientations are possible, e.g. causing a vertex to have two incoming long sequences and two outgoing short sequences or to have three long sequences and only one short sequence, see Fig. 4.1. But such diagrams are subleading.

The reasoning for this statement builds an intuition for the frequencies of the free propagator lines. The logarithmic divergences of the dot-reservoir particle-particle and particle-hole bubbles are located at $\Omega \approx \varepsilon_d$ and $X \approx \varepsilon_d$ and they arise from the

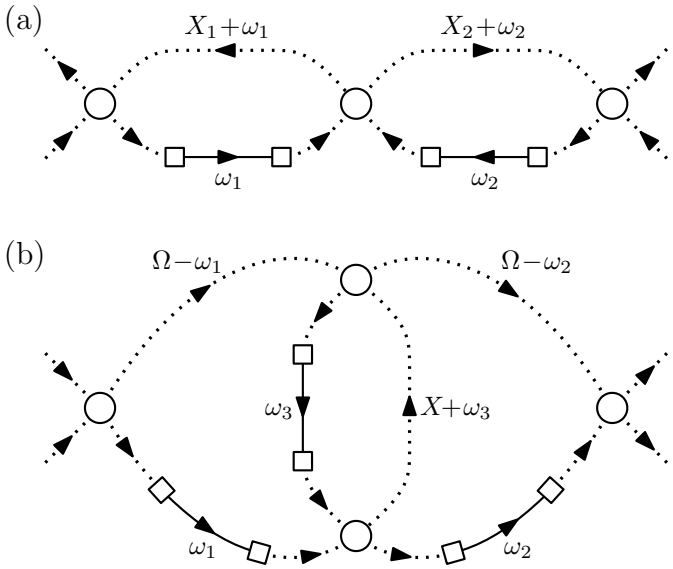

Figure 4.1: Orientations of dot-reservoir bubbles that turn out to be subleading. The frequencies satisfy $X_1 = -X_2$ and $X = \omega_1 - \omega_2$, respectively. Not all labels are shown.

integration region $|\omega| \ll |\varepsilon_d|$, where ω is the frequency of the long sequence. (Here, we write ε_d as a placeholder for $\varepsilon_{d,\uparrow}$ or $\varepsilon_{d,\downarrow}$ because we assume that the influence of the magnetic field on the dot levels is rather small.) If we require that each bubble contributes a large logarithm, we can think of its short sequence as carrying a frequency $\Omega - \omega \approx \varepsilon_d$ or $X + \omega \approx \varepsilon_d$ and of its long sequence as carrying a frequency with absolute value $|\omega| \ll |\varepsilon_d|$. As far as the leading logarithms are concerned, frequency conservation then implies the requirement made in step (ii). Diagrams that violate this requirement feature fewer than the maximum number of diverging logarithms achieved in other parquet diagrams of the same order.

As we consider only the leading parquet diagrams, we are left with one possible constellation in which the single- and two-particle vertices can appear, namely

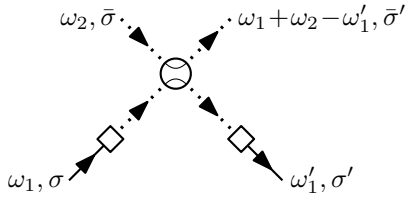

$$= U\sigma'\sigma\tau^2 g_{d\sigma}(\omega_1)\, g_{d\sigma'}(\omega_1'). \tag{4.63}$$

We have drawn the internal connections to fix the value. We now regard this constellation as an effective vertex

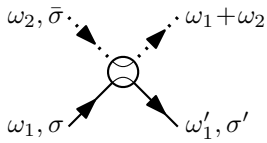

$$= U\sigma'\sigma\tau^2 \frac{\Theta(|\varepsilon_{d,\sigma}| - |\omega_1|)\Theta(|\varepsilon_{d,\sigma'}| - |\omega_1'|)}{\varepsilon_{d,\sigma}\, \varepsilon_{d,\sigma'}}. \tag{4.64}$$

As part of the definition, we have applied step (iii.b) to the free dot propagators.

To guarantee the above constellation also at the external legs, we have to attach free dot propagators and single-particle vertices. We thereby introduce an additional factor

$$\tau^2 \, \frac{\Theta(|\varepsilon_{d,\sigma}| - |\omega|)\Theta(|\varepsilon_{d,\sigma'}| - |\omega'|)}{\varepsilon_{d,\sigma}\, \varepsilon_{d,\sigma'}}, \tag{4.65}$$

where ω, ω' and σ, σ' are the frequencies and spins of the incoming and outgoing reservoir legs. We expect that the 1PI two-particle vertex function enters the calculation of an observable by being part of external dot-reservoir bubbles, similarly to Fig. 3.1 for the X-ray-edge model, and that our approximation steps can be applied once again. If this is not the case, the additional factor can simply be removed.

To complete the effective diagrammatics, we apply step (iii.a) to the remaining free propagators. According to Eq. (4.47), the dotted and full lines now have the values

$$\overset{\omega,\sigma}{\cdots\!\blacktriangleright\!\cdots} = \mathcal{P}\frac{1}{\omega - \varepsilon_{d,\sigma}} \tag{4.66a}$$

$$\overset{\omega,\sigma}{\longrightarrow} = -\mathrm{i}\frac{2}{t}\,\mathrm{sgn}(\omega)\Theta(W - |\omega|). \tag{4.66b}$$

The leading-logarithmic approximation only comprises parquet diagrams built from dot-reservoir bubbles, completely neglects the self-energy, and uses steps (iv) and (v) exactly as before.

In the following we simplify the prefactors of these parquet diagrams. Without loss of generality, we consider the reservoir legs of the 1PI two-particle vertex to be the first and the dot legs to be the second incoming and outgoing legs, i.e. we calculate a 1PI vertex function of the form $\gamma_{rd|rd}$. When choosing the internal connections in the effective vertices, we make the natural choice of connecting the reservoir legs with each other and the dot legs with each other, as we have done in Eq. (4.64). All dotted lines of a diagram then link together to form one composite line, and so do the full lines. Since the reservoir line and the dot line of each bubble are originally part of sequences with different lengths, they do not count as equivalent lines. The prefactor $\mathrm{sgn}(P)(-1)^{n_{\mathrm{loop}}}/(2^{n_{\mathrm{eq}}}S)$, see Eq. (2.45), then evaluates to one. Aside from the values of its vertices and lines, a diagram features only a factor i^{l-1}, where l is the number of vertices and the -1 comes from calculating a 1PI two-particle vertex function instead of a Green function.

Let us briefly discuss the role of the direct versus the exchange particle-hole channel. Originally, these two channels are equally important because they both feature bubbles with logarithmic divergences. As we have mentioned in Sec. 4.4, the diagrams for these channels are almost identical, differing only in the order of the external legs. But since we calculate $\gamma_{rd|rd}$, since the effective vertex has two reservoir legs and two dot legs, and since we only consider parquet diagrams built from dot-reservoir bubbles, the direct particle-hole channel does not contribute anymore; the situation is analogous in the X-ray-edge model, see the discussion after the flow equation (3.63). Note that if we would calculate $\gamma_{rd|dr}$, the exchange particle-hole channel would not contribute instead. Ultimately, we have to antisymmetrize the 1PI vertex function, thus including both these structures and restoring the channel that did not contribute.

Now we use the effective diagrammatics to compare the SIAM with the Kondo model. Treating the latter in a diagrammatic formalism is possible only after the impurity spin has been represented with a many-particle model. We consider the Kondo Hamiltonian (4.41) that Schrieffer and Wolff derive from the SIAM Hamiltonian in Ref. [SW66] and we consider the coupling strength $J_{k'k}$ to be approximated as the constant (4.42), see Sec. 4.5.1 for a brief recap. From the standpoint of the original Kondo model, this Hamiltonian constitutes a pseudo-fermion representation of the impurity spin; the dot states play the role of the pseudo-fermion states. Rigorously deriving diagrammatic rules for the Kondo model is beyond the scope of this thesis. Anyway, let us imagine that we apply the zero-temperature formalism to the Kondo model similar to how we applied it to the SIAM.

While we can define the free reservoir propagator with the factor $4/(M+1)$ and the momentum sum exactly as for the SIAM, it is not clear how we should define the free dot propagator. In contrast to a proper spin operator, the pseudo-fermion representation introduces unphysical parts to the Hilbert space, namely the subspaces with no or two pseudo fermions. The projection onto the physical Hilbert space is a delicate matter and can entail introducing a single-particle term, see Ref. [Abr65] for the Matsubara formalism and Ref. [SW10] for the Keldysh formalism. In their Hamiltonian approach, Schrieffer and Wolff treat the dot occupation-number operator as a constant, which is why we have written the Hamiltonian (4.41) without the term $\sum_\sigma \varepsilon_d\, d_\sigma^\dagger d_\sigma$. All in all, the dot levels and their occupation associated with the free propagator should be reconsidered for the Kondo model. Furthermore, it is not clear whether approximating the free propagators similarly to step (iii.a) is reasonable.

Turning our attention to the vertices, we translate the interaction part of the Kondo Hamiltonian (4.41) to

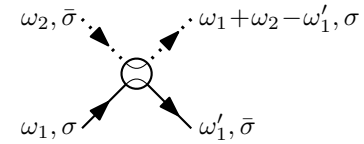

$$= -\frac{\tau^2 U}{\varepsilon_d(\varepsilon_d + U)} \tag{4.67a}$$

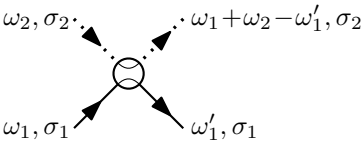

$$= -\sigma_1\sigma_2\, \frac{\tau^2 U}{2\varepsilon_d(\varepsilon_d + U)}. \tag{4.67b}$$

With regard to the stroke style and direction of the legs, both these vertices agree with the effective vertex (4.64), which we derived for the SIAM. With regard to the spins, however, only the vertex (4.67a) agrees with the effective vertex: it corresponds to the case $\sigma' = \bar\sigma$ and constitutes the spin-flip processes. The vertex (4.67b) partly corresponds to the case $\sigma' = \sigma$, but it also allows for equal spins to interact – seemingly, a stark contrast between the Kondo model and the SIAM.

Let us pinpoint the cause of this discrepancy. When Schrieffer and Wolff perform a canonical transformation to eliminate the first-order term in the coupling amplitude τ, they obtain not only the Kondo interaction but also the s-d direct interaction

[SW66]

$$H_{\mathrm{dir}} = \sum_{k'k} W_{k'k}\big(c^\dagger_{k',\uparrow}c_{k,\uparrow} + c^\dagger_{k',\downarrow}c_{k,\downarrow}\big) + \frac{1}{4}\sum_{k'k} J_{k'k}\big(c^\dagger_{k',\uparrow}c_{k,\uparrow} + c^\dagger_{k',\downarrow}c_{k,\downarrow}\big)\big(d^\dagger_\uparrow d_\uparrow + d^\dagger_\downarrow d_\downarrow\big). \tag{4.68}$$

We still consider $J_{k'k}$ to be constant. Schrieffer and Wolff treat the dot occupation-number operator as a constant and drop the entire term H_{dir}, arguing that it reduces to a single-particle potential with a negligible effect on the single-particle states and energies. If we restore the two-particle term of Eq. (4.68) by adding it to the Kondo Hamiltonian (4.41), the equal-spin interactions cancel out,

$$H_{\mathrm{Kondo}} + H^{(2)}_{\mathrm{dir}} = \sum_{k\sigma} \varepsilon_k\, c^\dagger_{k,\sigma}c_{k,\sigma} + \frac{J}{2}\sum_{k'k}\sum_{\sigma'\sigma} \sigma'\sigma\, c^\dagger_{k',\sigma'}c_{k,\sigma}d^\dagger_{\bar\sigma'}d_{\bar\sigma}. \tag{4.69}$$

The resulting interaction term is translated to

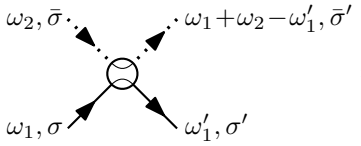

$$= \sigma'\sigma\,\frac{\tau^2 U}{\varepsilon_d(\varepsilon_d+U)}, \tag{4.70}$$

which has the same spin structure as the effective vertex (4.64). That Schrieffer and Wolff neglect the s-d direct interaction suggests that the discrepancy in the spin structure of the vertices turns out to be negligible.

With regard to the values, there remain two differences between the adjusted Kondo vertex (4.70) and the effective vertex (4.64). The former has no step functions that impose frequency windows on the reservoir lines. And it features the denominator $\varepsilon_d(\varepsilon_d + U)$ instead of ε_d^2. Since we expanded the Green functions in U and τ and treated ε_d as an independent parameter, our effective vertex can be interpreted as the leading order in U of Schrieffer and Wolff's effective Kondo coupling. Near the particle-hole symmetric point $\varepsilon_d = -U/2$, the second difference amounts approximately to a minus sign.

In summary, the Kondo diagrammatics have significant similarities to our effective diagrammatics for the SIAM. However, the abovementioned minus sign makes the difference between antiferromagnetic and ferromagnetic coupling. We therefore do not expect that our leading-logarithmic approximation correctly captures the Kondo physics exhibited by the SIAM. Some form of nonperturbative treatment of U appears to be necessary to capture the full U-dependence of the effective Kondo coupling and to thereby obtain the correct sign.

4.7 Properties of various cutoffs

The steps listed in Sec. 4.6.1 detail which diagrams to select and which approximations to apply in their calculations. For a solution of the 1PI two-particle vertex, we need to somehow resum all those approximated diagrams. The selected diagrams are parquet diagrams, so the same two ways as for the X-ray-edge model can be pursued for the resummation: via parquet equations or via FRG flow equations.

We will investigate various cutoffs. For the parquet equations, a cutoff could be useful as a mathematical trick to find an analytic solution as it was for the X-ray-edge model, see Sec. 3.4.5 and the appendix of Ref. [RGN69]. For the FRG flow equations, a cutoff is a necessary first step. The flow parameter λ is introduced into the free propagators; the initial value is $\lambda_{\mathrm{ini}} \to \infty$ and the final value is $\lambda_{\mathrm{fin}} = 0$. At this final value, the free propagators and thus the values of the diagrams are fully restored.

For each cutoff we check whether the divergences with respect to the frequencies, which are the reason why a resummation of infinitely many diagrams is necessary in the first place, are regularized during the entire flow. We also check whether the values of diagrams remain well-defined. The following discussion is restricted to the dot-reservoir bubbles with the applicable approximations from Sec. 4.6.1, i.e. the free propagators are approximated according to steps (iii.a) and (iii.b) and small shifts of the integration boundaries are neglected according to step (iv). Specifically, we show the calculation of the dot-reservoir particle-particle bubble (4.25); all statements apply to the dot-reservoir particle-hole bubble (4.26) as well.

First, we investigate a sharp infrared frequency cutoff in the free reservoir propagator,

$$g_r^\lambda(\omega) = -\mathrm{i}\frac{2}{t}\,\Theta(|\omega| - \lambda)\,\mathrm{sgn}(\omega)\Theta(W - |\omega|). \tag{4.71}$$

The dot-reservoir particle-particle bubble acquires the λ-dependence

$$\begin{aligned}
&I_\sigma^{(\mathrm{pp})\lambda}(\Omega) \\
&\approx \frac{-\mathrm{i}}{2\varepsilon_{d,\sigma}^2}\int_{-\infty}^{\infty}\mathrm{d}\omega\left(\mathcal{P}\frac{1}{\Omega-\omega-\varepsilon_{d,\bar\sigma}}\right)\Theta(|\omega|-\lambda)\,\mathrm{sgn}(\omega)\Theta(W-|\omega|)\Theta(|\varepsilon_{d,\sigma}|-|\omega|) && \text{(4.72a)}\\
&= \frac{\mathrm{i}}{2\varepsilon_{d,\sigma}^2}\,\Theta(|\varepsilon_{d,\sigma}|-\lambda)\,\mathcal{P}\left(\int_{-|\varepsilon_{d,\sigma}|}^{-\lambda}\mathrm{d}\omega\,\frac{-1}{\omega-\Omega+\varepsilon_{d,\bar\sigma}} + \int_{\lambda}^{|\varepsilon_{d,\sigma}|}\mathrm{d}\omega\,\frac{1}{\omega-\Omega+\varepsilon_{d,\bar\sigma}}\right) && \text{(4.72b)}\\
&= \frac{\mathrm{i}}{2\varepsilon_{d,\sigma}^2}\,\Theta(|\varepsilon_{d,\sigma}|-\lambda)\,\mathcal{P}\left(\int_{\lambda}^{|\varepsilon_{d,\sigma}|}\mathrm{d}\omega\,\frac{1}{\omega+|\Omega-\varepsilon_{d,\bar\sigma}|} + \int_{\lambda}^{|\varepsilon_{d,\sigma}|}\mathrm{d}\omega\,\frac{1}{\omega-|\Omega-\varepsilon_{d,\bar\sigma}|}\right). && \text{(4.72c)}
\end{aligned}$$

The cutoff has introduced a divergence with respect to the flow parameter, namely at $\lambda = |\Omega - \varepsilon_{d,\bar\sigma}|$. At this value the first integral in the last line is finite, whereas the second integral does not exist because it covers the positive part of the $1/x$-shape down to $x = 0$ but not the negative part. So values of diagrams are not well-defined for this cutoff.

Second, we investigate a sharp infrared band cutoff. To introduce it we have to resort to the expression (4.20c) for the free reservoir propagator, where the momentum integral is not yet solved. Complying with step (iii.a), we neglect the real part. The free reservoir propagator with band cutoff reads

$$\begin{aligned}
g_r^\lambda(\omega) &= \frac{2}{\pi t}\int_{-W}^{W}\mathrm{d}\varepsilon\,\Theta(|\varepsilon| - \lambda)(-\mathrm{i}\pi)\,\mathrm{sgn}(\varepsilon)\delta(\omega-\varepsilon) && \text{(4.73a)}\\
&= -\mathrm{i}\frac{2}{t}\,\Theta(|\omega| - \lambda)\,\mathrm{sgn}(\omega)\Theta(W - |\omega|). && \text{(4.73b)}
\end{aligned}$$

This cutoff is equivalent to the frequency cutoff (4.71) and so it leads to the same problem.

Third, we investigate a sharp infrared frequency cutoff in the free dot propagator,

$$g_{d\sigma}^{\lambda}(\omega) = \mathcal{P}\frac{\Theta(|\omega-\varepsilon_{d,\sigma}|-\lambda)}{\omega-\varepsilon_{d,\sigma}}. \tag{4.74}$$

The principle value is relevant only at $\lambda = 0$. We apply this cutoff only to the free dot propagator constituting the shorter sequence of a dot-reservoir bubble. It would not be reasonable to use the same expression for the two identical free dot propagators of the longer sequence because the frequency integral would not exist at the end of the flow; the importance of the individual real and imaginary parts of these free propagators can be seen in Eq. (4.52). How the flow parameter can be introduced only in certain dot propagators is a technical issue. The effective diagrammatics from Sec. 4.6.5, where the free dot propagators of the longer sequence are absorbed into the vertices, could be used as an intermediate step.

This third cutoff has the following effect on the dot-reservoir particle-particle bubble,

$$\begin{aligned}
&I_{\sigma}^{(\mathrm{pp})\lambda}(\Omega) \\
&\approx \frac{-\mathrm{i}}{2\varepsilon_{d,\sigma}^2}\int_{-\infty}^{\infty}\mathrm{d}\omega\left[\mathcal{P}\frac{\Theta(|\Omega-\omega-\varepsilon_{d,\bar{\sigma}}|-\lambda)}{\Omega-\omega-\varepsilon_{d,\bar{\sigma}}}\right]\mathrm{sgn}(\omega)\Theta(W-|\omega|)\Theta(|\varepsilon_{d,\sigma}|-|\omega|) && \text{(4.75a)}\\
&\approx \frac{\mathrm{i}}{2\varepsilon_{d,\sigma}^2}\int_{-|\varepsilon_{d,\sigma}|}^{|\varepsilon_{d,\sigma}|}\mathrm{d}\omega'\left[\mathcal{P}\frac{\Theta(|\omega'|-\lambda)}{\omega'}\right]\mathrm{sgn}(\omega'+\Omega-\varepsilon_{d,\bar{\sigma}}) && \text{(4.75b)}\\
&= \frac{\mathrm{i}}{\varepsilon_{d,\sigma}^2}\int_{|\Omega-\varepsilon_{d,\bar{\sigma}}|}^{|\varepsilon_{d,\sigma}|}\mathrm{d}\omega'\,\mathcal{P}\frac{\Theta(|\omega'|-\lambda)}{\omega'} && \text{(4.75c)}\\
&= \frac{-\mathrm{i}}{\varepsilon_{d,\sigma}^2}\,\Theta(|\varepsilon_{d,\sigma}|-\lambda)\ln\frac{\max\{\lambda,|\Omega-\varepsilon_{d,\bar{\sigma}}|\}}{|\varepsilon_{d,\sigma}|}. && \text{(4.75d)}
\end{aligned}$$

The integration variable has been transformed to $\omega' = \omega - \Omega + \varepsilon_{d,\bar{\sigma}}$, but the corresponding small shifts of the integration boundaries have been neglected. The divergence at $\Omega = \varepsilon_{d,\bar{\sigma}}$ is regularized for every $\lambda > 0$, i.e. during the entire flow.

It is crucial that the cutoff (4.74) is centered around the spin-dependent dot level. The positive and negative parts of the $1/x$-shape of the free dot propagator are thereby included symmetrically. If the cut-out frequency window would be shifted, a divergence with respect to the flow parameter would be introduced, just as with the first and second cutoff. Those affect only the free reservoir propagator, which cannot access the information where the symmetry point of the $1/x$-shape lies.

In summary, the frequency cutoff in the free reservoir propagator and the band cutoff are equivalent within the leading-logarithmic approximation. As they cause divergences during the flow, they are unsuitable. In contrast, the frequency cutoff in the free dot propagator, see Eq. (4.74), is a reasonable choice that regularizes the divergences of the dot-reservoir bubbles. This cutoff can be expected to facilitate a solution of the 1PI two-particle vertex. However, this thesis does not present such a solution for the SIAM.

4.8 Linear conductance as observable

In this section we study an observable of interest for the SIAM, namely the linear conductance across the dot. We sketch how it can be expressed in terms of Green functions in the zero-temperature formalism.

The system is prepared at half filling as described by Eq. (4.13) and at vanishing temperature with respect to the Hamiltonian H from Sec. 4.2. So the system is in its ground state, which is denoted by $|\Psi_0\rangle$. In the following we will freely switch between the representation with left and right reservoirs and the representation with even and odd reservoirs.

At the initial time $t_0 \to -\infty$, we apply the bias voltage

$$H_b(t) = \frac{qV}{2}\,(N_L - N_R)\,\mathrm{Re}\,e^{-\mathrm{i}(\omega+\mathrm{i}\eta_b)t}, \tag{4.76}$$

where $q < 0$ is the charge of an electron, V is the amplitude of the voltage, and $N_r = \sum_{k\sigma} c^\dagger_{r,k,\sigma} c_{r,k,\sigma}$ is the particle number operator for reservoir $r = L, R$. For $t > t_0$ the dynamics of the system are governed by $H_{\mathrm{tot}}(t) = H + H_b(t)$ and the electric current from left to right is

$$I(t) = -\frac{q}{2}\frac{\mathrm{d}}{\mathrm{d}t}\,\langle\Psi_0|U^\dagger_{\mathrm{tot}}(t,t_0)(N_L - N_R)U_{\mathrm{tot}}(t,t_0)|\Psi_0\rangle. \tag{4.77}$$

The bias voltage shall be applied adiabatically through the limits $t_0 \to -\infty$ and $\eta_b \to 0^+$; t shall be finite. Only then do we take the limit $\omega \to 0$ for the voltage frequency, thus guaranteeing that the system does not equilibrate. This order of limits yields the steady-state current

$$I = \lim_{\omega\to 0}\lim_{\eta_b\to 0^+}\lim_{t_0\to-\infty} I(t). \tag{4.78}$$

After using the Schrödinger equation to perform the time derivative in the current formula (4.77), we go over to the interaction picture by writing

$$U_{\mathrm{tot}}(t,t_0) = U(t,t_0)U_I(t,t_0), \tag{4.79}$$

where $U(t,t_0)$ is the time evolution operator with respect to H. The time evolution operator of the interaction picture can be expanded in the voltage amplitude,

$$U_I(t,t_0) = 1 - \mathrm{i}\int_{t_0}^{t}\mathrm{d}t'\,U^\dagger(t',t_0)H_b(t')U(t',t_0) + O(V^2). \tag{4.80}$$

The linear conductance $G = \lim_{V\to 0} I/V$ can then be written as

$$G = -\frac{q^2}{4}\lim_{\omega\to 0}\lim_{\eta_b\to 0^+}\mathrm{Re}\int_0^\infty \mathrm{d}t\,e^{\mathrm{i}(\omega+\mathrm{i}\eta_b)t}\big\langle\Psi_0\big|\big[[H, N_L-N_R](t)_H, N_L-N_R\big]\big|\Psi_0\big\rangle \tag{4.81}$$

with the notation $A(t)_H = e^{\mathrm{i}Ht}A\,e^{-\mathrm{i}Ht}$.

In the representation with even and odd reservoirs, the inner commutator is given by

$$[H, N_L - N_R] = \sum_{k\sigma}\bar{\tau}_k\big(c^\dagger_{\mathrm{odd},k,\sigma}d_\sigma - d^\dagger_\sigma c_{\mathrm{odd},k,\sigma}\big). \tag{4.82}$$

The expectation value appearing in the conductance formula (4.81) can thus be expressed in terms of expectation values of four ladder operators.

However, we can immediately calculate the effect from the odd sector. Since the Hamiltonian $H = H_{\text{even}} + H_{\text{odd}}$ does not couple the even sector to the odd sector, see Sec. 4.2.3, since we have prepared the system with fixed numbers of electrons in these sectors, see Eq. (4.13), and since H_{odd} is noninteracting, we can write the ground state in the form

$$|\Psi_0\rangle = \left(\prod_{k \text{ with } \varepsilon_k<0} c^\dagger_{\text{odd},k,\uparrow} c^\dagger_{\text{odd},k,\downarrow} \right) |\Psi_{\text{even},0}\rangle. \tag{4.83}$$

Here, $|\Psi_{\text{even},0}\rangle$ is the ground state of H_{even} for the particular filling of the even sector and is some combination of even creation operators acting on the vacuum state. The operators in the expectation values factorize with respect to the even and odd sectors and we can easily calculate the contributions from the odd operators. This leads to

$$\begin{aligned} &\big\langle \Psi_0 \big| \big[[H, N_L - N_R](t)_H, N_L - N_R \big] \big| \Psi_0 \big\rangle \\ &= \sum_{k\sigma} \bar{\tau}_k \Big[\Theta(-\varepsilon_k)\, e^{\mathrm{i}\varepsilon_k t} \langle \Psi_{\text{even},0} | d_\sigma(t)_{H_{\text{even}}} c^\dagger_{\text{even},k,\sigma} | \Psi_{\text{even},0} \rangle \\ &\qquad - \Theta(\varepsilon_k)\, e^{-\mathrm{i}\varepsilon_k t} \langle \Psi_{\text{even},0} | d^\dagger_\sigma(t)_{H_{\text{even}}} c_{\text{even},k,\sigma} | \Psi_{\text{even},0} \rangle \Big] + \text{c.c.} \end{aligned} \tag{4.84}$$

So the linear conductance reduces to an expression with only single-particle Green functions. For these remaining Green functions, one has to consider only the even sector – just as we have done in Sec. 4.3 when applying the zero-temperature formalism. The expression (4.84) does not directly depend on the 1PI two-particle vertex, which the leading-logarithmic approximation in Sec. 4.6 focuses on.

That only single-particle and no two-particle correlation functions have to be calculated for the linear conductance can be understood also in the representation with left and right reservoirs. There, the expectation value appearing in the conductance formula (4.81) assumes the form

$$\begin{aligned} &\big\langle \Psi_0 \big| \big[[H, N_L - N_R](t)_H, N_L - N_R \big] \big| \Psi_0 \big\rangle \\ &= \sum_{r=L,R} \sum_{r'=L,R} \sum_{kk'} \sum_{\sigma\sigma'} (\delta_{rL} - \delta_{rR})(\delta_{r'L} - \delta_{r'R}) \tau_k \\ &\quad \times \big\langle \Psi_0 \big| \big[c^\dagger_{r,k,\sigma}(t)_H\, d_\sigma(t)_H - d^\dagger_\sigma(t)_H\, c_{r,k,\sigma}(t)_H, c^\dagger_{r',k',\sigma'} c_{r',k',\sigma'} \big] \big| \Psi_0 \big\rangle. \end{aligned} \tag{4.85}$$

Previously, we have worked with the even and odd reservoirs and have applied the zero-temperature formalism only to the even system. Let us now imagine that we work with the left and right reservoirs and apply the formalism to the entire system. The expression (4.85) can then be translated to a linear combination of two-particle Green functions that have reservoir indices $r = L, R$.

The dependence of such Green functions on the reservoir indices is trivial. The free reservoir propagator is diagonal but otherwise independent of its reservoir indices, the single-particle vertex does not depend on its reservoir index at all, and the two-particle vertex has only dot legs. Connected Green functions, other than the

single-particle Green function, are completely independent of their reservoir indices because the lines starting or ending at external points have to enter or leave single-particle vertices. As a consequence the connected parts of the two-particle Green functions in Eq. (4.85) cancel out. The linear conductance again reduces to an expression with only single-particle Green functions.

So, no matter the representation, the presented formula (4.81) is not directly accessible from the 1PI two-particle vertex. To obtain the linear conductance from our leading-logarithmic approximation, we would first have to translate the result for the 1PI two-particle vertex into terms of the single-particle Green function.

4.9 Conclusion

The investigated SIAM describes a quantum dot with two single-particle states that is subject to an on-site interaction and tunnel-coupled to two noninteracting reservoirs. We considered the system to be half-filled, in equilibrium, at vanishing temperature, and near the particle-hole symmetric point and we considered the reservoirs to be symmetric. We transformed the basis of the reservoir states such that only one effective reservoir couples to the dot; the nontrivial part of the Hamiltonian is then analogous to the impurity version of the SIAM. The electron transport through the dot is still accessible in linear response. Specifically, we are interested in the Kondo effect.

Several FRG approaches to the SIAM exist in the literature, see Sec. 4.1 for a detailed discussion, some capturing aspects of the Kondo effect and single ones even producing good estimates for the exponential interaction dependence of the Kondo temperature. But the regime of large interaction in particular has proven difficult to describe accurately. Almost all the approaches are based on a regular perturbation theory, in which the reservoirs have been integrated out and the on-site interaction is the expansion parameter; simple low-order calculations cannot capture the emerging Kondo scale. The FRG approaches do not deal with the resummation of important terms marked by divergences and are not controlled. To gauge their reliability, they depend on comparisons to benchmark data.

This overall description of the existing FRG approaches equally applies to the existing parquet approaches to the SIAM, see Refs. [CB92, Pok+17, Ge+24]. They fall in the category of the full parquet approximation. Fittingly to the lack of divergences in the usual formulation of the perturbation theory, we are not aware of a leading-logarithmic parquet approximation for the SIAM, only of the leading-logarithmic parquet approximation of Ref. [Abr65] for the related Kondo model.

For our approach we have set up the perturbation theory differently by not integrating out the reservoirs and by expanding simultaneously in the coupling between the dot and the reservoirs as well as in the on-site interaction. Employing the zero-temperature formalism and calculating some low-order example diagrams of the 1PI two-particle vertex, we found logarithmic divergences similar to the ones in the X-ray-edge model. They appear in the parquet diagrams built from the dot-reservoir bubbles, which have exactly one reservoir propagator. To make a leading-logarithmic analysis viable, we formulated assumptions on the external frequencies such that

these bubbles are evaluated close to their divergences and on the system parameters such that the common prefactor that comes with each logarithm is small. The latter assumption coincides with the regime considered by Schrieffer and Wolff [SW66] to relate the SIAM Hamiltonian to the Kondo Hamiltonian.

We developed an approximation scheme with steps similar as for the X-ray-edge model to resum the leading logarithms of the parquet diagrams built from the dot-reservoir bubbles. This discussion cannot dismiss the importance of other kinds of diagrams. For such a parquet diagram to have the maximum number of logarithms evaluated close to their divergence, the sequences that contain a reservoir propagator must all have the same direction. The approximations that apply to individual diagrams were justified via comparisons with the leading behaviors of the exact values of the single dot-reservoir bubbles and a crossed bubble. The main difference between the dot-reservoir bubbles and the bubbles for the X-ray-edge model are the two dot propagators that surround the reservoir propagator. They effectively cut off the $1/|\omega|$-tails building the logarithms already at minus and plus the dot levels instead of at the band edges; the arguments of the logarithms differ accordingly.

We presented effective diagrammatic rules that incorporate the abovementioned leading-logarithmic approximation scheme. They provide a diagrammatic perspective on the relation between the SIAM and the Kondo model. The effective vertex constitutes a two-particle interaction between the dot and the reservoirs that conserves the respective particle numbers and is quadratic in the original coupling amplitude – just like the Kondo interaction derived from the SIAM Hamiltonian by Schrieffer and Wolff [SW66], which, in terms of the original Kondo interaction, amounts to a pseudo-fermion representation of the impurity spin. But our effective vertex does not allow particles with equal spins to interact, whereas the Kondo interaction does. This difference might turn out to be irrelevant as it can be ascribed to the s-d direct interaction being neglected in Ref. [SW66].

A difference that appears very much relevant is the extra dependence of the denominator in the Kondo interaction on the original on-site interaction U. Near the particle-hole symmetric point, it essentially changes the overall sign of the interaction so we do not expect our current approach to correctly capture the Kondo physics. Our effective vertex could be thought of as the correct leading-order term in U of the Kondo interaction only if the dot levels and the on-site interaction were treated as independent. An indication for the relevance of higher-order terms is given by the dot-dot bubbles, which have no reservoir propagator and which we neglected. One of them is actually comparable with the bare vertex and the corresponding ladder diagrams can be interpreted as representing an improper, nonconverging series expansion of a static renormalization of the bare vertex by a significant amount. An avenue of capturing the full U-dependence of the Kondo interaction is possibly given by a nonperturbative treatment similar to the extraordinary perturbation theory underlying the FRG approach of Ref. [Kin+13]: one could solve the dot subsystem exactly and integrate out its degrees of freedom to eliminate all dot-only subdiagrams in favor of effective vertices. But since those vertices would have arbitrarily many legs, some approximation or truncation would be necessary and retaining the original parquet diagrams built from the dot-reservoir bubbles would not be trivial.

Another open question is what role bubbles with more than one reservoir propagator play. As one considers cases with more and more reservoir propagators, exact calculations quickly become cumbersome if not impossible. But if the real part of the reservoir propagator is again neglected because it essentially affects only frequencies close to the band edges, analytic calculations appear straightforward. Then one can analytically calculate the bubbles even after dressing the dot propagator with the self-energy $\tau^2 g_r(\omega)$, i.e. after incorporating arbitrary numbers of reservoir propagators. The imaginary part of the reservoir propagator acts as a level broadening that regularizes the logarithmic divergences. Our choice of retaining only the dot-reservoir bubbles could be considered as the first-order approximation with respect to the level broadening. This line of thought could bridge the differences between our approach and the typical FRG approaches that integrate out the reservoirs from the start. On the other hand, our choice is necessary for the similarities to the diagrammatic elements of the Kondo model and, as long as the bubbles are not evaluated too close to the divergences, it appears justified if the level broadening is small compared to the dot levels. This condition corresponds to the regime of large interaction, where the typical FRG approaches struggle to capture the Kondo physics.

Our research into the SIAM is not finished. A resummation of the approximated diagrams for the 1PI two-particle vertex via an FRG flow or via parquet equations remains to be done. For an explicit calculation of the linear conductance, which boils down to single-particle Green functions, we will have to extend the approach such that it yields also the self-energy, e.g. by keeping track of the self-energy during the flow via its flow equation or by determining the self-energy from the final result for the 1PI two-particle vertex via the Schwinger-Dyson equation, cf. Ref. [KD18b]. We will then have to revisit the assumptions on the frequencies of the 1PI vertices. As a preparation primarily for an FRG solution, we have investigated various cutoffs, finding the best candidate in properly regularizing the divergences of the dot-reservoir bubbles to be a sharp infrared frequency cutoff in the free dot propagator – but only in the shorter sequences, which contain no reservoir propagator. To technically avoid introducing the cutoff in the longer sequences, which contain a reservoir propagator, diagrammatic rules with effective dot-reservoir vertices could be helpful.

Finally, let us point out that in our investigation the temperature is fixed to zero and cannot keep the flow from diverging as the cutoff scale approaches the Kondo temperature. In the context of Anderson's poor man's scaling for the Kondo model, the renormalization is routinely stopped by hand when the cutoff scale reaches the temperature, which is assumed to be larger than the Kondo temperature [PG04, Ren16]. The Keldysh FRG approach of Ref. [Die17] to the Kondo model shows a natural mechanism within the flow equations by which such a finite temperature serves to avoid a divergence. Eventually, one could enhance the flow with higher-order corrections that avoid a divergence even below the Kondo temperature.

Chapter 5

Conclusion and outlook

Since we have already given a detailed, separate conclusion for each of the three main chapters about the zero-temperature FRG, the X-ray-edge model, and the SIAM, let us restrict the conclusion here to the big picture and focus on the outlook.

We comprehensively set up the (1PI) FRG in the zero-temperature formalism for a general model of interacting fermions. While this formalism is designed for systems in their ground state, it can be somewhat adapted, including to specific situations occurring for the models we studied. Nonetheless, the zero-temperature formalism remains more restrictive than the Matsubara and Keldysh formalisms. But since it uses real times and frequencies on a simple contour, it is simpler in comparison and can facilitate analytic solutions or reduce numerical effort. As the Matsubara FRG and Keldysh FRG are well-established and successful tools for studying condensed-matter systems of interacting fermions, we hope that the zero-temperature FRG will be found useful beyond this thesis.

We presented a one-loop FRG approach to the X-ray-edge model that is in detail fully equivalent to the leading-logarithmic parquet approximation of Ref. [RGN69], reconfirming that the FRG can achieve leading-logarithmic accuracy with a one-loop truncation. Whether low-order FRG truncations can reproduce leading-logarithmic results had been put into question in the context of the X-ray-edge model and the multiloop FRG had been developed as a fix [KD18a, KD18c], whereas many lowest-order RG and scaling approaches to various models have been known to achieve this level of accuracy for a long time, see e.g. Refs. [AM70, FZ71, Kim73, Sól74, Sól79]. In our case the one-loop FRG and the leading-logarithmic parquet approximation can be interpreted as one and the same approximation scheme viewed from different perspectives. This equivalence of the two methods required a careful analysis and construction. It is of course not guaranteed in general as various factors come into play, e.g. some FRG cutoffs are better suited for a one-loop truncation than others.

When treating the SIAM, we expanded simultaneously in the coupling between the dot and the reservoirs as well as in the on-site interaction. Logarithmic divergences appeared in the bubbles with one reservoir propagator and we developed an approximation scheme aimed at resumming the leading logarithms of the SIAM via FRG flow equations or parquet equations in a similar way as for the X-ray-edge model. We expressed this scheme in terms of effective diagrammatic rules, finding

similarities to the Kondo model. But the differences indicate that our approach needs to be extended before it can properly capture the Kondo physics of the SIAM; a possible avenue to resolve the main difference is to treat the on-site interaction of the SIAM nonperturbatively by solving and integrating out the dot subsystem like Ref. [Kin+13]. Such a procedure would amount to the opposite of the usually employed perturbation theory with integrated-out reservoirs. One could study the effect of additional reservoir propagators in bubbles to relate our approach to the existing FRG and parquet approaches, e.g. to those of Refs. [Hed+04, KEM06, Kar+08] and [CB92, Pok+17, Ge+24], albeit at the cost of losing the abovementioned similarities to the Kondo model. As that usual perturbation theory for the SIAM is regular, the logarithms are typically not analyzed let alone resummed consistently in the traditional approaches.

For many low-dimensional condensed-matter systems, the problem of logarithmic divergences in perturbation theory is more widely known. The generic mechanism is clear: All it takes is for example a power-law behavior

$$x^{c_1 g + c_2 g^2 + \dots} = e^{(c_1 g + c_2 g^2 + \dots) \ln x} \tag{5.1}$$

of some correlation function with the small expansion parameter g appearing in the exponent. Then logarithms $\ln x$ occur in all orders. If the argument x goes to zero or infinity, they diverge and cause the breakdown of the perturbation theory. This problem can arise also from other dependences on a combination of the expansion parameter and a logarithm. The X-ray-edge model is prototypical for the whole class of (mostly zero- and one-dimensional) models for which the divergences appear in multiple two-particle channels with one logarithm per bubble. Also the SIAM belongs to this class from the perspective of our unusual perturbation theory.

The leading logarithms $g^n \ln^n x$ for all $n = 1, 2, \dots$ become important when the product of expansion parameter and logarithm becomes sizable, $|g \ln x| \lesssim 1$. While the first few coefficients c_i in the exponent could be deduced from low-order perturbation theory if the general form of the power law was known or guessed beforehand, see e.g. Ref. [Mah67], the full resummation of the leading logarithms is necessary for a proper deduction of the power law $x^{c_1 g}$ as the leading behavior of the correlation function. For the considered class of models, the leading logarithms are contained in the parquet diagrams of the relevant two-particle channels. The leading-logarithmic parquet approximation is specifically designed for this resummation. We have established that the FRG can join the ranks of other RG and scaling methods that can achieve leading-logarithmic accuracy even in a low-order truncation.

The goal of many RG and scaling approaches was to go beyond the leading-logarithmic level [GZ74, Sól79, Hew93]. Resumming the next-to-leading logarithms $g^{n+1} \ln^n x$ provides a meaningful correction as long as $|g \ln x| \lesssim 1$ still holds. And resumming all subleading logarithms $g^m \ln^n x$ with $m \leq 2n$ is sufficient for a good approximation in the regime $|g^2 \ln x| \lesssim 1$, namely $x^{c_1 g + c_2 g^2}$. Parquet-based discussions of the subleading logarithms for the X-ray-edge model are given in Refs. [NGR69, Gie+25]. According to the recent Ref. [Gie+25], the resummation of the next-to-leading logarithms is possible with the full parquet approximation if one properly includes the self-energy and all three two-particle channels, but a consistent resum-

mation of further subleading logarithms is beyond the full parquet approximation as that would require a nontrivial totally irreducible vertex. From the FRG perspective, efficient arguments are desirable that can directly decide on the level of accuracy of a given approximation step within the flow equations, without relying on the study of individual diagrams.

Let us mention that the full parquet approximation and the multiloop FRG are often used for the class of (mostly two-dimensional) models for which a bubble can yield more than one logarithm. There, an analysis of the logarithms is typically not attempted and the choice of method is determined by other aspects, like e.g. conservation laws. Our findings do not apply to that class of models.

The benefits of a priori controlled approximations are obvious. If one knows even before arriving at a result that an approximation is good in a certain regime, one does not rely on exact benchmark data to be available or on a consensus to be reached by many different methods. But FRG approaches to low-dimensional condensed-matter systems often do not focus on being controlled; approximations and in particular truncations are typically justified only perturbatively, i.e. they are correct within some low order of the expansion parameter but uncontrolled once the next order becomes important and especially once the perturbation theory breaks down entirely. Notable exceptions are Refs. [Med+02, Kar+10, KM13], where correct leading scaling behaviors are reproduced with lowest-level truncations in the context of a Luttinger liquid with an impurity and in the context of the interacting resonant-level model. General strengths of the FRG are its versatility, efficiency, and analytical accessibility. Its capability for a controlled accuracy should now be studied further.

A wide array of tasks awaits. As already described above, one should try to extend the regime of reliability by pursuing a consistent treatment of the subleading logarithms. Additionally, one should try to develop FRG approaches that focus on capturing the leading (and eventually subleading) logarithms to other models of the same class as the X-ray-edge model. The Kondo model and the one-dimensional Fermi gas model in particular could yield further methodological insights because they have been extensively studied, including with the leading-logarithmic parquet approximation [Abr65, BGD66].

Furthermore, one should try to base those approaches not only on the zero-temperature formalism but also on the Matsubara and Keldysh formalisms. Our approach to the X-ray-edge model at vanishing temperature has already been transferred to the Matsubara formalism [DJ24], which is the standard for FRG studies of condensed-matter systems. The Matsubara and Keldysh formalisms allow for a finite temperature to be considered and its regularizing effect on the logarithmic divergences to be investigated; at a sufficiently low temperature, the logarithms remain of course problematic. Reference [DJ24] briefly addresses this topic. The Keldysh formalism also allows for nonequilibrium situations to be studied, e.g. of the SIAM and the Kondo model. One could then compare the new, controlled approaches to the existing Keldysh FRG approaches of Refs. [GPM07, Jak10, JPS10, Ge+24] and [SW10, Die17], respectively.

Between the chosen accuracy, model, and formalism, the calculations might get considerably more complicated in the suggested FRG studies than in this thesis,

where all insights have been gained analytically. With the principles for controlled approximations understood, one can start to draw on numerical resources. The long-term goal is to develop the FRG further into a versatile, efficient, and analytically transparent method that is applicable to impurity, quantum-dot, and quantum-wire models, which might describe actual such setups or appear in dynamical mean-field theory calculations for lattice models, and that is reliable with an a priori controlled accuracy in a wide parameter regime, including the Kondo regime.

Appendix A

Diagonalizing a tight-binding chain

We consider the single-particle problem of a finite, spinless tight-binding chain. The ends of the chain are not linked. The Hilbert space is spanned by the orthonormal Wannier states $|s\rangle$, which describe the particle at a given site $s = 1, \ldots, M$. We allow only for a nearest-neighbor hopping with amplitude $t > 0$. The potential energy is assumed to be constant over all sites and is set to zero. The Hamiltonian reads

$$H = -t \sum_{s=1}^{M-1} \big(|s\rangle\langle s+1| + |s+1\rangle\langle s| \big). \tag{A.1}$$

We now solve the eigenvalue problem $\varepsilon_k |k\rangle = H|k\rangle$. The ansatz

$$|k\rangle = \sum_{s=1}^{M} \big(A_k \, e^{\mathrm{i}ks} + B_k \, e^{-\mathrm{i}ks} \big) |s\rangle \tag{A.2}$$

leads to

$$\begin{aligned} \varepsilon_k \sum_{s=1}^{M} \big(A_k \, e^{\mathrm{i}ks} + B_k \, e^{-\mathrm{i}ks} \big) |s\rangle = &-t \sum_{s=1}^{M-1} \big[A_k \, e^{\mathrm{i}k(s+1)} + B_k \, e^{-\mathrm{i}k(s+1)} \big] |s\rangle \\ &-t \sum_{s=2}^{M} \big[A_k \, e^{\mathrm{i}k(s-1)} + B_k \, e^{-\mathrm{i}k(s-1)} \big] |s\rangle. \end{aligned} \tag{A.3}$$

In this equation we compare the coefficients for each state $|s\rangle$. From $s = 2, \ldots, M-1$ we get

$$\varepsilon_k = -2t \cos(k). \tag{A.4}$$

From $s = 1$ we then get

$$B_k = -A_k. \tag{A.5}$$

From $s = M$ we finally obtain the discretization

$$k = \frac{\pi l}{M+1} \qquad \text{with } l \in \mathbb{Z}. \tag{A.6}$$

After restricting $l = 1, \ldots, M$, we have found M eigenstates with mutually different eigenvalues because ε_k increases strictly monotonically for $k \in (0, \pi)$. So

these states form an orthogonal eigenbasis of H. The normalization $\langle k|k\rangle = 1$ is achieved by choosing

$$A_k = \frac{-\mathrm{i}}{\sqrt{2M+2}}. \tag{A.7}$$

In total the eigenenergies and orthonormal eigenstates of H are given by

$$\varepsilon_k = -2t\cos(k) \qquad \text{with } k = \frac{\pi l}{M+1} \text{ and } l = 1, \ldots, M \tag{A.8a}$$

$$|k\rangle = \sqrt{\frac{2}{M+1}} \sum_{s=1}^{M} \sin(ks)|s\rangle. \tag{A.8b}$$

In each state $|k\rangle$, the absolute value of the momentum is fixed and equal to k. (The lattice constant is set to one.) However, these states do not represent movement in any direction and instead describe standing waves.

Appendix B

Properties of the logarithm and dilogarithm

B.1 Logarithm

Throughout this thesis the principle branch of the complex logarithm is denoted by

$$\mathrm{Log}(z) = \ln|z| + \mathrm{i}\arg(z) \qquad \text{with } z \in \mathbb{C} \setminus \{0\} \text{ and } \arg(z) \in (-\pi, \pi]. \tag{B.1}$$

Its branch cut lies on the negative real axis $(-\infty, 0]$. The logarithm has the expansion

$$\mathrm{Log}(1+z) = z - \frac{z^2}{2} + \frac{z^3}{3} + O(z^4). \tag{B.2}$$

B.2 Dilogarithm

The principle branch of the dilogarithm can be defined as [DLMF: Eq. (25.12.2)]

$$\mathrm{Li}_2(z) = -\int_0^z \mathrm{d}t\, \frac{\mathrm{Log}(1-t)}{t} \qquad \text{with } z \in \mathbb{C} \setminus (1, \infty), \tag{B.3}$$

where the integration contour must not touch the interval $(1, \infty)$. The dilogarithm is continuous at its branch point $z = 1$; the branch cut runs along $[1, \infty)$. In the region $\mathbb{C} \setminus [1, \infty)$, the dilogarithm is a holomorphic function with the derivative

$$\frac{\mathrm{d}}{\mathrm{d}z}\,\mathrm{Li}_2(z) = -\frac{\mathrm{Log}(1-z)}{z} \qquad \text{with } z \in \mathbb{C} \setminus [1, \infty). \tag{B.4}$$

The dilogarithm is identical to the series [DLMF: Eq. (25.12.1)]

$$\mathrm{Li}_2(z) = \sum_{n=1}^{\infty} \frac{z^n}{n^2} \qquad \text{with } z \in \mathbb{C} \text{ and } |z| \leq 1. \tag{B.5}$$

It evaluates to the special values

$$\mathrm{Li}_2(-1) = -\frac{\pi^2}{12}, \qquad \mathrm{Li}_2(1) = \frac{\pi^2}{6}. \tag{B.6}$$

Reference [DLMF: Eqs. (25.12.3) and (25.12.4)] provides also the identities

$$\mathrm{Li}_2(z) + \mathrm{Li}_2\left(\frac{z}{z-1}\right) = -\frac{1}{2}\,\mathrm{Log}^2(1-z) \qquad \text{with } z \in \mathbb{C} \setminus [1,\infty) \tag{B.7a}$$

$$\mathrm{Li}_2(z) + \mathrm{Li}_2\left(\frac{1}{z}\right) = -\frac{\pi^2}{6} - \frac{1}{2}\,\mathrm{Log}^2(-z) \qquad \text{with } z \in \mathbb{C} \setminus [0,\infty). \tag{B.7b}$$

In the following we derive a series expansion of the dilogarithm around its branch point. By successively using the identities (B.7a) and (B.7b), we separate the nonanalytic behavior into logarithmic terms,

$$\begin{aligned}
&\mathrm{Li}_2(1+z) \\
&= -\mathrm{Li}_2\left(\frac{1+z}{z}\right) - \frac{1}{2}\,\mathrm{Log}^2(-z) \qquad \text{if } 1+z \in \mathbb{C} \setminus [1,\infty) && \text{(B.8a)} \\
&= \mathrm{Li}_2\left(\frac{z}{1+z}\right) + \frac{\pi^2}{6} + \frac{1}{2}\,\mathrm{Log}^2\left(-\frac{1+z}{z}\right) - \frac{1}{2}\,\mathrm{Log}^2(-z) \qquad \text{if } \frac{1+z}{z} \in \mathbb{C} \setminus [0,\infty). && \text{(B.8b)}
\end{aligned}$$

The two restrictions in this equation are equivalent to $z \in \mathbb{C} \setminus \big\{(-\infty,-1] \cup [0,\infty)\big\}$. As we are interested in the behavior close to the branch point, we further restrict $z \in \mathbb{C} \setminus [0,1)$ with $|z| < 1$. We can then write

$$\begin{aligned}
&\mathrm{Log}\left(-\frac{1+z}{z}\right) \qquad \text{with } z \in \mathbb{C} \setminus [0,1) \text{ and } |z| < 1 \\
&= \mathrm{Log}\left(\frac{1}{z}+1\right) + \begin{cases} +\mathrm{i}\pi, & \mathrm{Im}(z) > 0 \\ -\mathrm{i}\pi, & \mathrm{Im}(z) < 0 \text{ or } z \in (-1,0) \end{cases} && \text{(B.9a)} \\
&= \mathrm{Log}(1+z) + \mathrm{Log}\left(\frac{1}{z}\right) + \begin{cases} +\mathrm{i}\pi, & \mathrm{Im}(z) > 0 \\ -\mathrm{i}\pi, & \mathrm{Im}(z) < 0 \text{ or } z \in (-1,0) \end{cases} && \text{(B.9b)} \\
&= \mathrm{Log}(1+z) - \mathrm{Log}(z) + \begin{cases} +\mathrm{i}\pi, & \mathrm{Im}(z) > 0 \text{ or } z \in (-1,0) \\ -\mathrm{i}\pi, & \mathrm{Im}(z) < 0 \end{cases} && \text{(B.9c)} \\
&= \mathrm{Log}(1+z) - \mathrm{Log}(-z). && \text{(B.9d)}
\end{aligned}$$

Inserting this into Eq. (B.8) gives

$$\begin{aligned}
&\mathrm{Li}_2(1+z) \qquad \text{with } z \in \mathbb{C} \setminus [0,1) \text{ and } |z| < 1 \\
&= \mathrm{Li}_2\left(\frac{z}{1+z}\right) + \frac{\pi^2}{6} + \frac{1}{2}\,\mathrm{Log}^2(1+z) - \mathrm{Log}(1+z)\,\mathrm{Log}(-z). && \text{(B.10)}
\end{aligned}$$

Aside from the factor $\mathrm{Log}(-z)$, which contains the nonanalytic behavior for $z \in [0,1)$ that is inherent to $\mathrm{Li}_2(1+z)$, we can now straightforwardly perform a series expansion around $|z| \ll 1$ to arrive at

$$\begin{aligned}
&\mathrm{Li}_2(1+z) \qquad \text{with } z \in \mathbb{C} \setminus [0,1) \text{ and } |z| < 1 && \text{(B.11)} \\
&= \frac{\pi^2}{6} + z\big[1 - \mathrm{Log}(-z)\big] + z^2\left[-\frac{1}{4} + \frac{1}{2}\,\mathrm{Log}(-z)\right] + z^3\left[\frac{1}{9} - \frac{1}{3}\,\mathrm{Log}(-z)\right] + O(z^4 \ln|z|).
\end{aligned}$$

Appendix C

Some useful integrals

C.1 Very simple integrals

We solve the following integral by rewriting it as a contour integral in the complex plane,

$$\begin{aligned} &\int_a^b \mathrm{d}x \, \frac{1}{x - y - \mathrm{i}\eta} \qquad \text{with } a, b, y, \eta \in \mathbb{R} \text{ and } \eta \neq 0 \\ &= \int_\gamma \mathrm{d}z \, \frac{1}{z} = \mathrm{Log}(z)\Big|_{\gamma(a)}^{\gamma(b)} = \mathrm{Log}(x - y - \mathrm{i}\eta)\Big|_{x=a}^{x=b} \end{aligned} \tag{C.1}$$

with the contour $\gamma : [a, b] \to \mathbb{C}$, $x \mapsto x - y - \mathrm{i}\eta$, which does not cross the branch cut of $\mathrm{Log}(z)$.

Analogously, we solve the integral

$$\begin{aligned} &\int_a^b \mathrm{d}x \, \frac{1}{(x - y - \mathrm{i}\eta)^2} \qquad \text{with } a, b, y, \eta \in \mathbb{R} \text{ and } \eta \neq 0 \\ &= \int_\gamma \mathrm{d}z \, \frac{1}{z^2} = \frac{-1}{z}\Big|_{\gamma(a)}^{\gamma(b)} = \frac{-1}{x - y - \mathrm{i}\eta}\Big|_{x=a}^{x=b} \end{aligned} \tag{C.2}$$

with the contour $\gamma : [a, b] \to \mathbb{C}$, $x \mapsto x - y - \mathrm{i}\eta$, which does not cross the pole of $1/z$.

C.2 Integral over $\mathrm{Log}(x - x_1 - \mathrm{i}\eta)/(x - x_2 - \mathrm{i}\eta)$

We will solve the integral

$$\int_a^b \mathrm{d}x \, \frac{\mathrm{Log}(x - x_1 - \mathrm{i}\eta)}{x - x_2 - \mathrm{i}\eta} \qquad \text{with } a, b, x_1, x_2, \eta \in \mathbb{R} \text{ and } x_1 \neq x_2 \text{ and } \eta > 0. \tag{C.3}$$

We rewrite the logarithm by using

$$x - x_1 - \mathrm{i}\eta = (x_2 - x_1)\left(1 - \frac{x - x_2 - \mathrm{i}\eta}{x_1 - x_2}\right) \tag{C.4}$$

and

$$\begin{aligned}&\arg\left[(x_2-x_1)\left(1-\frac{x-x_2-\mathrm{i}\eta}{x_1-x_2}\right)\right]\\&=\arg(x_2-x_1)+\arg\left(1-\frac{x-x_2-\mathrm{i}\eta}{x_1-x_2}\right)-2\pi\Theta(x_1-x_2).\end{aligned}\tag{C.5}$$

Equation (C.5) holds trivially up to multiples of 2π. For $x_2-x_1>0$ it holds because $\arg(x_2-x_1)=0$. In the case $x_2-x_1<0$, we have $\arg(x_2-x_1)=\pi$ and $\arg\big[1-(x-x_2-\mathrm{i}\eta)/(x_1-x_2)\big]\in(0,\pi)$ so both sides of the equation lie in $(-\pi,0)$. We can now write

$$\mathrm{Log}(x-x_1-\mathrm{i}\eta)=\mathrm{Log}(x_2-x_1)+\mathrm{Log}\left(1-\frac{x-x_2-\mathrm{i}\eta}{x_1-x_2}\right)-2\pi\mathrm{i}\Theta(x_1-x_2)\tag{C.6a}$$

$$=\mathrm{Log}(x_2-x_1-\mathrm{i}0^+)+\mathrm{Log}\left(1-\frac{x-x_2-\mathrm{i}\eta}{x_1-x_2}\right).\tag{C.6b}$$

Inserting this into Eq. (C.3) yields

$$\begin{aligned}&\int_a^b\mathrm{d}x\,\frac{\mathrm{Log}(x-x_1-\mathrm{i}\eta)}{x-x_2-\mathrm{i}\eta}\\&=\mathrm{Log}(x_2-x_1-\mathrm{i}0^+)\int_a^b\mathrm{d}x\,\frac{1}{x-x_2-\mathrm{i}\eta}+\int_a^b\mathrm{d}x\,\frac{\mathrm{Log}\big(1-\frac{x-x_2-\mathrm{i}\eta}{x_1-x_2}\big)}{x-x_2-\mathrm{i}\eta}.\end{aligned}\tag{C.7}$$

The first of the remaining integrals is of the form (C.1). The second integral can be rewritten as

$$\begin{aligned}&\int_a^b\mathrm{d}x\,\frac{\mathrm{Log}\big(1-\frac{x-x_2-\mathrm{i}\eta}{x_1-x_2}\big)}{x-x_2-\mathrm{i}\eta}\\&=\int_\gamma\mathrm{d}z\,\frac{\mathrm{Log}(1-z)}{z}=-\mathrm{Li}_2(z)\Big|_{\gamma(a)}^{\gamma(b)}=-\mathrm{Li}_2\left(\frac{x-x_2-\mathrm{i}\eta}{x_1-x_2}\right)\Big|_{x=a}^{x=b}\end{aligned}\tag{C.8}$$

with the contour $\gamma:[a,b]\to\mathbb{C}$, $x\mapsto(x-x_2-\mathrm{i}\eta)/(x_1-x_2)$, which has a constant, nonvanishing imaginary part so it does not cross the branch cut of the dilogarithm, see Eq. (B.3). In total we obtain the solution

$$\begin{aligned}&\int_a^b\mathrm{d}x\,\frac{\mathrm{Log}(x-x_1-\mathrm{i}\eta)}{x-x_2-\mathrm{i}\eta}\qquad\text{with } a,b,x_1,x_2,\eta\in\mathbb{R}\text{ and }x_1\neq x_2\text{ and }\eta>0\\&=\mathrm{Log}(x_2-x_1-\mathrm{i}0^+)\,\mathrm{Log}(x-x_2-\mathrm{i}\eta)\Big|_{x=a}^{x=b}-\mathrm{Li}_2\left(\frac{x-x_2-\mathrm{i}\eta}{x_1-x_2}\right)\Big|_{x=a}^{x=b}.\end{aligned}\tag{C.9}$$

If η is infinitesimal, we can just as well write η instead of 0^+.

C.3 Integral over $\mathrm{Log}(x-x_1-\mathrm{i}\eta)/(x-x_2-\mathrm{i}\eta)^2$

We will solve the integral

$$\int_a^b\mathrm{d}x\,\frac{\mathrm{Log}(x-x_1-\mathrm{i}\eta)}{(x-x_2-\mathrm{i}\eta)^2}\qquad\text{with } a,b,x_1,x_2,\eta\in\mathbb{R}\text{ and }x_1\neq x_2\text{ and }\eta\neq0.\tag{C.10}$$

The function

$$F(z) = \frac{(z - x_1 - \mathrm{i}\eta)\,\mathrm{Log}(z - x_1 - \mathrm{i}\eta) - (z - x_2 - \mathrm{i}\eta)\,\mathrm{Log}(z - x_2 - \mathrm{i}\eta)}{(x_1 - x_2)(z - x_2 - \mathrm{i}\eta)} \tag{C.11}$$

is holomorphic in the region $\{z \in \mathbb{C} |\ |\mathrm{Im}(z)| < \eta\}$ with the derivative

$$\frac{\mathrm{d}F}{\mathrm{d}z} = \frac{\mathrm{Log}(z - x_1 - \mathrm{i}\eta)}{(z - x_2 - \mathrm{i}\eta)^2}. \tag{C.12}$$

With the contour $\gamma : [a, b] \to \mathbb{C}$, $x \mapsto x$ lying in the region $\{z \in \mathbb{C} |\ |\mathrm{Im}(z)| < \eta\}$, we find

$$\int_a^b \mathrm{d}x\, \frac{\mathrm{Log}(x - x_1 - \mathrm{i}\eta)}{(x - x_2 - \mathrm{i}\eta)^2} = \int_\gamma \mathrm{d}z\, \frac{\mathrm{Log}(z - x_1 - \mathrm{i}\eta)}{(z - x_2 - \mathrm{i}\eta)^2} = F(z)\Big|_{\gamma(a)}^{\gamma(b)} \tag{C.13}$$

and thus

$$\begin{aligned} &\int_a^b \mathrm{d}x\, \frac{\mathrm{Log}(x - x_1 - \mathrm{i}\eta)}{(x - x_2 - \mathrm{i}\eta)^2} \qquad \text{with } a, b, x_1, x_2, \eta \in \mathbb{R} \text{ and } x_1 \neq x_2 \text{ and } \eta \neq 0 \\ &= \left[\frac{x - x_1 - \mathrm{i}\eta}{(x_1 - x_2)(x - x_2 - \mathrm{i}\eta)}\, \mathrm{Log}(x - x_1 - \mathrm{i}\eta) - \frac{1}{x_1 - x_2}\, \mathrm{Log}(x - x_2 - \mathrm{i}\eta) \right]_{x=a}^{x=b}. \end{aligned} \tag{C.14}$$

Appendix D

Crossed bubble in the SIAM

D.1 Calculating the exact value

We calculate the crossed bubble defined in Eq. (4.35). Instead of the original expression $C(X,\omega)$, we consider

$$\tilde{C}(X,\omega) = -C(X,\omega - X). \tag{D.1}$$

This is done exclusively to salvage an older version of the calculation. We now have to perform the integrals in the expression

$$\begin{aligned}
&\tilde{C}(X,\omega) \\
&= -\int_{-\infty}^{\infty}\frac{\mathrm{d}\omega_o}{2\pi}\int_{-\infty}^{\infty}\frac{\mathrm{d}\omega_i}{2\pi}\int_{-W}^{W}\mathrm{d}\varepsilon_o\int_{-W}^{W}\mathrm{d}\varepsilon_i\,\frac{1}{X+\omega_o-\varepsilon_d-\mathrm{i}\eta}\,\frac{1}{\omega_o-\varepsilon_o+\mathrm{i}\eta\,\mathrm{sgn}\,\varepsilon_o} \\
&\quad\times\frac{1}{(\omega_o-\varepsilon_d-\mathrm{i}\eta)^2}\,\frac{1}{\omega+\omega_o-\omega_i-\varepsilon_d-\mathrm{i}\eta}\,\frac{1}{\omega_i-\varepsilon_i+\mathrm{i}\eta\,\mathrm{sgn}\,\varepsilon_i}\,\frac{1}{(\omega_i-\varepsilon_d-\mathrm{i}\eta)^2}.
\end{aligned} \tag{D.2}$$

We close the ω_i-integral in the lower half plane, apply the residue theorem, and use a partial fraction decomposition with respect to ε_i. These steps are fully analogous to the ones we performed for the dot-reservoir particle-particle bubble, see Eqs. (4.27) through (4.29), because the inner bubble is of this kind. However, we do not yet exploit that η is infinitesimal. We obtain

$$\begin{aligned}
&\tilde{C}(X,\omega) \\
&= \mathrm{i}\int_{-\infty}^{\infty}\frac{\mathrm{d}\omega_o}{2\pi}\int_{-W}^{W}\mathrm{d}\varepsilon_o\int_{-W}^{W}\mathrm{d}\varepsilon_i\,\frac{1}{X+\omega_o-\varepsilon_d-\mathrm{i}\eta}\,\frac{1}{\omega_o-\varepsilon_o+\mathrm{i}\eta\,\mathrm{sgn}\,\varepsilon_o}\,\frac{1}{(\omega_o-\varepsilon_d-\mathrm{i}\eta)^2} \\
&\quad\times\Bigg[\Theta(-\varepsilon_i)\,\frac{1}{\varepsilon_i-\omega-\omega_o+\varepsilon_d+2\mathrm{i}\eta}\,\frac{1}{(\omega+\omega_o-2\varepsilon_d-2\mathrm{i}\eta)^2} \\
&\qquad+\Theta(\varepsilon_i)\,\frac{1}{\varepsilon_i-\varepsilon_d-2\mathrm{i}\eta}\,\frac{1}{(\omega+\omega_o-2\varepsilon_d-2\mathrm{i}\eta)^2} \\
&\qquad+\Theta(\varepsilon_i)\,\frac{1}{(\varepsilon_i-\varepsilon_d-2\mathrm{i}\eta)^2}\,\frac{1}{\omega+\omega_o-2\varepsilon_d-2\mathrm{i}\eta}\Bigg].
\end{aligned} \tag{D.3}$$

Next, we close the ω_o-integral in the lower half plane and apply the residue theorem to get

$$\begin{aligned}\tilde{C}(X,\omega) = \int_{-W}^{W} \mathrm{d}\varepsilon_o \int_{-W}^{W} \mathrm{d}\varepsilon_i\, \Theta(\varepsilon_o)\, \frac{1}{X+\varepsilon_o-\varepsilon_d-2\mathrm{i}\eta}\, \frac{1}{(\varepsilon_o-\varepsilon_d-2\mathrm{i}\eta)^2} \\ \times\Bigg[\Theta(-\varepsilon_i)\, \frac{1}{\varepsilon_i-\omega-\varepsilon_o+\varepsilon_d+3\mathrm{i}\eta}\, \frac{1}{(\omega+\varepsilon_o-2\varepsilon_d-3\mathrm{i}\eta)^2} \\ + \Theta(\varepsilon_i)\, \frac{1}{\varepsilon_i-\varepsilon_d-2\mathrm{i}\eta}\, \frac{1}{(\omega+\varepsilon_o-2\varepsilon_d-3\mathrm{i}\eta)^2} \\ + \Theta(\varepsilon_i)\, \frac{1}{(\varepsilon_i-\varepsilon_d-2\mathrm{i}\eta)^2}\, \frac{1}{\omega+\varepsilon_o-2\varepsilon_d-3\mathrm{i}\eta}\Bigg].\end{aligned} \tag{D.4}$$

As η is infinitesimal, its role is to specify the way in which poles and branch cuts are navigated. The factors 2 and 3 in the η-terms are irrelevant for this, so we drop them. Note that while we performed the ω_i- and ω_o-integrals, the η-terms only accumulated and did not compete with each other. The only exception to this occurred for the ω_i-integral, where the problematic terms immediately canceled each other, see the lines after Eq. (4.28).

To perform the remaining two integrations, we rewrite the individual terms such that they match one of the general integrals that are solved in Appendix C. To this end we redefine $\varepsilon_i \to -\varepsilon_i$ in the first term of Eq. (D.4). The crossed bubble then reads

$$\begin{aligned}\tilde{C}(X,\omega) = \int_{0}^{W} \mathrm{d}\varepsilon_o \int_{0}^{W} \mathrm{d}\varepsilon_i \Bigg[\left(\frac{-1}{\varepsilon_i+\varepsilon_o+\omega-\varepsilon_d-\mathrm{i}\eta}+\frac{1}{\varepsilon_i-\varepsilon_d-\mathrm{i}\eta}\right) \\ \times \frac{1}{\varepsilon_o+X-\varepsilon_d-\mathrm{i}\eta}\, \frac{1}{(\varepsilon_o-\varepsilon_d-\mathrm{i}\eta)^2}\, \frac{1}{(\varepsilon_o+\omega-2\varepsilon_d-\mathrm{i}\eta)^2} \\ + \frac{1}{(\varepsilon_i-\varepsilon_d-\mathrm{i}\eta)^2}\, \frac{1}{\varepsilon_o+X-\varepsilon_d-\mathrm{i}\eta}\, \frac{1}{(\varepsilon_o-\varepsilon_d-\mathrm{i}\eta)^2}\, \frac{1}{\varepsilon_o+\omega-2\varepsilon_d-\mathrm{i}\eta}\Bigg].\end{aligned} \tag{D.5}$$

We perform the individual ε_i-integrals by applying the general formulas (C.1) and (C.2). Simultaneously, we perform partial fraction decompositions with respect to ε_o

for the second and third line. This yields

$$
\begin{aligned}
&\tilde{C}(X,\omega)\\
&=\int_0^W \mathrm{d}\varepsilon_o \Bigg\{ \big[-\operatorname{Log}(W+\varepsilon_o+\omega-\varepsilon_d-\mathrm{i}\eta)+\operatorname{Log}(\varepsilon_o+\omega-\varepsilon_d-\mathrm{i}\eta)\\
&\qquad\qquad +\operatorname{Log}(W-\varepsilon_d-\mathrm{i}\eta)-\operatorname{Log}(-\varepsilon_d-\mathrm{i}\eta)\big]\\
&\quad\times\Bigg[\frac{1}{\varepsilon_o+X-\varepsilon_d-\mathrm{i}\eta}\,\frac{1}{X^2(\omega-X-\varepsilon_d)^2}+\frac{1}{\varepsilon_o-\varepsilon_d-\mathrm{i}\eta}\,\frac{-\omega-2X+\varepsilon_d}{X^2(\omega-\varepsilon_d)^3}\\
&\qquad+\frac{1}{(\varepsilon_o-\varepsilon_d-\mathrm{i}\eta)^2}\,\frac{1}{X(\omega-\varepsilon_d)^2}+\frac{1}{\varepsilon_o+\omega-2\varepsilon_d-\mathrm{i}\eta}\,\frac{-3\omega+2X+3\varepsilon_d}{(\omega-X-\varepsilon_d)^2(\omega-\varepsilon_d)^3}\\
&\qquad+\frac{1}{(\varepsilon_o+\omega-2\varepsilon_d-\mathrm{i}\eta)^2}\,\frac{-1}{(\omega-X-\varepsilon_d)(\omega-\varepsilon_d)^2}\Bigg]\\
&\quad+\left(-\frac{1}{W-\varepsilon_d-\mathrm{i}\eta}+\frac{1}{-\varepsilon_d-\mathrm{i}\eta}\right)\\
&\quad\times\Bigg[\frac{1}{\varepsilon_o+X-\varepsilon_d-\mathrm{i}\eta}\,\frac{1}{X^2(\omega-X-\varepsilon_d)}+\frac{1}{\varepsilon_o-\varepsilon_d-\mathrm{i}\eta}\,\frac{-\omega-X+\varepsilon_d}{X^2(\omega-\varepsilon_d)^2}\\
&\qquad+\frac{1}{(\varepsilon_o-\varepsilon_d-\mathrm{i}\eta)^2}\,\frac{1}{X(\omega-\varepsilon_d)}+\frac{1}{\varepsilon_o+\omega-2\varepsilon_d-\mathrm{i}\eta}\,\frac{-1}{(\omega-X-\varepsilon_d)(\omega-\varepsilon_d)^2}\Bigg]\Bigg\}.
\end{aligned}
\tag{D.6}
$$

Finally, we perform the individual ε_o-integrals by applying the general formulas (C.1), (C.2), (C.9), and (C.14). We arrive at the exact value of the crossed bubble

$$
\begin{aligned}
&\tilde{C}(X,\omega)\\
&=\frac{1}{X^2(\omega-X-\varepsilon_d)^2}\\
&\quad\times\Bigg\{-\operatorname{Log}(-X+W+\omega-\mathrm{i}\eta)\left[\operatorname{Log}(W+X-\varepsilon_d-\mathrm{i}\eta)-\operatorname{Log}(X-\varepsilon_d-\mathrm{i}\eta)\right]\\
&\qquad+\operatorname{Li}_2\!\left(\frac{W+X-\varepsilon_d-\mathrm{i}\eta}{-W-\omega+X}\right)-\operatorname{Li}_2\!\left(\frac{X-\varepsilon_d-\mathrm{i}\eta}{-W-\omega+X}\right)\\
&\qquad+\operatorname{Log}(-X+\omega-\mathrm{i}\eta)\left[\operatorname{Log}(W+X-\varepsilon_d-\mathrm{i}\eta)-\operatorname{Log}(X-\varepsilon_d-\mathrm{i}\eta)\right]\\
&\qquad-\operatorname{Li}_2\!\left(\frac{W+X-\varepsilon_d-\mathrm{i}\eta}{-\omega+X}\right)+\operatorname{Li}_2\!\left(\frac{X-\varepsilon_d-\mathrm{i}\eta}{-\omega+X}\right)\\
&\qquad+\left[\operatorname{Log}(W-\varepsilon_d-\mathrm{i}\eta)-\operatorname{Log}(-\varepsilon_d-\mathrm{i}\eta)\right]\left[\operatorname{Log}(W+X-\varepsilon_d-\mathrm{i}\eta)-\operatorname{Log}(X-\varepsilon_d-\mathrm{i}\eta)\right]\Bigg\}\\
&\quad+\frac{-\omega-2X+\varepsilon_d}{X^2(\omega-\varepsilon_d)^3}\\
&\quad\times\Bigg\{-\operatorname{Log}(W+\omega-\mathrm{i}\eta)\left[\operatorname{Log}(W-\varepsilon_d-\mathrm{i}\eta)-\operatorname{Log}(-\varepsilon_d-\mathrm{i}\eta)\right]\\
&\qquad+\operatorname{Li}_2\!\left(\frac{W-\varepsilon_d-\mathrm{i}\eta}{-W-\omega}\right)-\operatorname{Li}_2\!\left(\frac{-\varepsilon_d-\mathrm{i}\eta}{-W-\omega}\right)\\
&\qquad+\operatorname{Log}(\omega-\mathrm{i}\eta)\left[\operatorname{Log}(W-\varepsilon_d-\mathrm{i}\eta)-\operatorname{Log}(-\varepsilon_d-\mathrm{i}\eta)\right]\\
&\qquad-\operatorname{Li}_2\!\left(\frac{W-\varepsilon_d-\mathrm{i}\eta}{-\omega}\right)+\operatorname{Li}_2\!\left(\frac{-\varepsilon_d-\mathrm{i}\eta}{-\omega}\right)
\end{aligned}
\tag{D.7}
$$

$$
\begin{aligned}
&\quad + \big[\mathrm{Log}(W-\varepsilon_d-\mathrm{i}\eta) - \mathrm{Log}(-\varepsilon_d-\mathrm{i}\eta)\big]\big[\mathrm{Log}(W-\varepsilon_d-\mathrm{i}\eta) - \mathrm{Log}(-\varepsilon_d-\mathrm{i}\eta)\big]\Big\} \\
&+ \frac{1}{X(\omega-\varepsilon_d)^2} \\
&\times\Big\{ - \frac{2W+\omega-\varepsilon_d-\mathrm{i}\eta}{(-W-\omega)(W-\varepsilon_d-\mathrm{i}\eta)}\,\mathrm{Log}(2W+\omega-\varepsilon_d-\mathrm{i}\eta) + \frac{\mathrm{Log}(W-\varepsilon_d-\mathrm{i}\eta)}{-W-\omega} \\
&\quad + \frac{W+\omega-\varepsilon_d-\mathrm{i}\eta}{(-W-\omega)(-\varepsilon_d-\mathrm{i}\eta)}\,\mathrm{Log}(W+\omega-\varepsilon_d-\mathrm{i}\eta) - \frac{\mathrm{Log}(-\varepsilon_d-\mathrm{i}\eta)}{-W-\omega} \\
&\quad + \frac{W+\omega-\varepsilon_d-\mathrm{i}\eta}{(-\omega)(W-\varepsilon_d-\mathrm{i}\eta)}\,\mathrm{Log}(W+\omega-\varepsilon_d-\mathrm{i}\eta) - \frac{\mathrm{Log}(W-\varepsilon_d-\mathrm{i}\eta)}{-\omega} \\
&\quad - \frac{\omega-\varepsilon_d-\mathrm{i}\eta}{(-\omega)(-\varepsilon_d-\mathrm{i}\eta)}\,\mathrm{Log}(\omega-\varepsilon_d-\mathrm{i}\eta) + \frac{\mathrm{Log}(-\varepsilon_d-\mathrm{i}\eta)}{-\omega} \\
&\quad + \big[\mathrm{Log}(W-\varepsilon_d-\mathrm{i}\eta) - \mathrm{Log}(-\varepsilon_d-\mathrm{i}\eta)\big]\left(-\frac{1}{W-\varepsilon_d-\mathrm{i}\eta} + \frac{1}{-\varepsilon_d-\mathrm{i}\eta}\right)\Big\} \\
&+ \frac{-3\omega+2X+3\varepsilon_d}{(\omega-X-\varepsilon_d)^2(\omega-\varepsilon_d)^3} \\
&\times\Big\{ - \mathrm{Log}(W+\varepsilon_d-\mathrm{i}\eta)\,\big[\mathrm{Log}(W+\omega-2\varepsilon_d-\mathrm{i}\eta) - \mathrm{Log}(\omega-2\varepsilon_d-\mathrm{i}\eta)\big] \\
&\quad + \mathrm{Li}_2\left(\frac{W+\omega-2\varepsilon_d-\mathrm{i}\eta}{-W-\varepsilon_d}\right) - \mathrm{Li}_2\left(\frac{\omega-2\varepsilon_d-\mathrm{i}\eta}{-W-\varepsilon_d}\right) \\
&\quad + \mathrm{Log}(\varepsilon_d-\mathrm{i}\eta)\,\big[\mathrm{Log}(W+\omega-2\varepsilon_d-\mathrm{i}\eta) - \mathrm{Log}(\omega-2\varepsilon_d-\mathrm{i}\eta)\big] \\
&\quad - \mathrm{Li}_2\left(\frac{W+\omega-2\varepsilon_d-\mathrm{i}\eta}{-\varepsilon_d}\right) + \mathrm{Li}_2\left(\frac{\omega-2\varepsilon_d-\mathrm{i}\eta}{-\varepsilon_d}\right) \\
&\quad + \big[\mathrm{Log}(W-\varepsilon_d-\mathrm{i}\eta) - \mathrm{Log}(-\varepsilon_d-\mathrm{i}\eta)\big]\,\big[\mathrm{Log}(W+\omega-2\varepsilon_d-\mathrm{i}\eta) - \mathrm{Log}(\omega-2\varepsilon_d-\mathrm{i}\eta)\big]\Big\} \\
&+ \frac{-1}{(\omega-X-\varepsilon_d)(\omega-\varepsilon_d)^2} \\
&\times\Big\{ - \frac{2W+\omega-\varepsilon_d-\mathrm{i}\eta}{(-W-\varepsilon_d)(W+\omega-2\varepsilon_d-\mathrm{i}\eta)}\,\mathrm{Log}(2W+\omega-\varepsilon_d-\mathrm{i}\eta) + \frac{\mathrm{Log}(W+\omega-2\varepsilon_d-\mathrm{i}\eta)}{-W-\varepsilon_d} \\
&\quad + \frac{W+\omega-\varepsilon_d-\mathrm{i}\eta}{(-W-\varepsilon_d)(\omega-2\varepsilon_d-\mathrm{i}\eta)}\,\mathrm{Log}(W+\omega-\varepsilon_d-\mathrm{i}\eta) - \frac{\mathrm{Log}(\omega-2\varepsilon_d-\mathrm{i}\eta)}{-W-\varepsilon_d} \\
&\quad + \frac{W+\omega-\varepsilon_d-\mathrm{i}\eta}{(-\varepsilon_d)(W+\omega-2\varepsilon_d-\mathrm{i}\eta)}\,\mathrm{Log}(W+\omega-\varepsilon_d-\mathrm{i}\eta) - \frac{\mathrm{Log}(W+\omega-2\varepsilon_d-\mathrm{i}\eta)}{-\varepsilon_d} \\
&\quad - \frac{\omega-\varepsilon_d-\mathrm{i}\eta}{(-\varepsilon_d)(\omega-2\varepsilon_d-\mathrm{i}\eta)}\,\mathrm{Log}(\omega-\varepsilon_d-\mathrm{i}\eta) + \frac{\mathrm{Log}(\omega-2\varepsilon_d-\mathrm{i}\eta)}{-\varepsilon_d} \\
&\quad + \big[\mathrm{Log}(W-\varepsilon_d-\mathrm{i}\eta) - \mathrm{Log}(-\varepsilon_d-\mathrm{i}\eta)\big]\left(-\frac{1}{W+\omega-2\varepsilon_d-\mathrm{i}\eta} + \frac{1}{\omega-2\varepsilon_d-\mathrm{i}\eta}\right)\Big\} \\
&+ \left(-\frac{1}{W-\varepsilon_d-\mathrm{i}\eta} + \frac{1}{-\varepsilon_d-\mathrm{i}\eta}\right) \\
&\times\Big\{ \frac{1}{X^2(\omega-X-\varepsilon_d)}\,\big[\mathrm{Log}(W+X-\varepsilon_d-\mathrm{i}\eta) - \mathrm{Log}(X-\varepsilon_d-\mathrm{i}\eta)\big]
\end{aligned}
$$

$$
\begin{aligned}
&+ \frac{-\omega - X + \varepsilon_d}{X^2(\omega - \varepsilon_d)^2} \left[\mathrm{Log}(W - \varepsilon_d - \mathrm{i}\eta) - \mathrm{Log}(-\varepsilon_d - \mathrm{i}\eta)\right] \\
&+ \frac{1}{X(\omega - \varepsilon_d)} \left(- \frac{1}{W - \varepsilon_d - \mathrm{i}\eta} + \frac{1}{-\varepsilon_d - \mathrm{i}\eta} \right) \\
&+ \frac{-1}{(\omega - X - \varepsilon_d)(\omega - \varepsilon_d)^2} \left[\mathrm{Log}(W + \omega - 2\varepsilon_d - \mathrm{i}\eta) - \mathrm{Log}(\omega - 2\varepsilon_d - \mathrm{i}\eta)\right] \Bigg\}.
\end{aligned}
$$

Certainly, there are ways to simplify this expression. However, we are interested only in the leading behavior in a regime where many terms turn out to be negligible anyway. We will therefore expand the lengthy Eq. (D.7) directly.

D.2 Extracting the leading behavior

We now determine the leading behavior of the crossed bubble by expanding its exact value. In Sec. 4.6 we develop an efficient approximation scheme; there, we would like to have a reference value of $C(X, \omega)$ for

$$
|X - \varepsilon_d|, |\omega| \ll |\varepsilon_d| \ll W. \tag{D.8}
$$

This regime translates into various small quantities, in which we have to expand.

Here, we make assumptions that are stricter than the regime (D.8) by specifying how some of the small quantities compare with each other. We formulate these assumptions for $\tilde{C}(X, \omega)$ instead of $C(X, \omega)$, i.e. we account for the redefinition of the second argument described by Eq. (D.1). We assume

$$
|X - \varepsilon_d|, |\omega - \varepsilon_d| \ll |\varepsilon_d| \ll \frac{|\omega - \varepsilon_d|^3}{|\varepsilon_d|^3} W \tag{D.9a}
$$

$$
\frac{|\omega - \varepsilon_d|}{|\varepsilon_d|} \ln^2 \frac{W}{|\varepsilon_d|} \ll 1. \tag{D.9b}
$$

Additionally, we assume that none of the factors

$$
\ln \frac{W}{|X - \varepsilon_d|}, \ \ln \frac{W}{|\omega - \varepsilon_d|}, \ \ln \frac{W}{|\omega - X|} \tag{D.10}
$$

is so large that it can change the relations if it is inserted somewhere in Eq. (D.9a).

We neglect terms that are smaller than $1/\varepsilon_d^4$. The assumptions above are designed such that we have to keep only terms of very low order in the individual expansions. Ultimately, we will see that the leading terms have the form $\ln^2/\varepsilon_d^4$ with two large logarithms.

We start by exploiting that W is by far the largest of the energies and frequencies. Technically, we achieve this by identifying in the individual terms and factors, which appear in the exact value (D.7) of the crossed bubble, small quantities of the form $O(X, \omega, \varepsilon_d)/W$. Using the general equations and expansions of the logarithm and dilogarithm stated in Appendix B, we expand in these quantities and have to keep

only the large logarithms and the constant terms. The crossed bubble is then given by

$$
\begin{aligned}
&\tilde{C}(X,\omega)\\
&\approx \frac{1}{X^2(\omega-X-\varepsilon_d)^2}\left\{\big[\mathrm{Log}(-X+\omega-\mathrm{i}\eta)-\ln|\varepsilon_d|\big]\big[\ln W-\mathrm{Log}(X-\varepsilon_d-\mathrm{i}\eta)\big]\right.\\
&\qquad\left.-\frac{\pi^2}{12}+\frac{\pi^2}{6}+\frac{1}{2}\,\mathrm{Log}^2\!\left(-\frac{W-\mathrm{i}\eta}{-\omega+X}\right)+\mathrm{Li}_2\!\left(\frac{X-\varepsilon_d-\mathrm{i}\eta}{-\omega+X}\right)\right\}\\
&+\frac{-\omega-2X+\varepsilon_d}{X^2(\omega-\varepsilon_d)^3}\left\{\big[\mathrm{Log}(\omega-\mathrm{i}\eta)-\ln|\varepsilon_d|\big]\big[\ln W-\ln|\varepsilon_d|\big]-\frac{\pi^2}{12}+\frac{\pi^2}{6}\right.\\
&\qquad\left.+\frac{1}{2}\,\mathrm{Log}^2\!\left(-\frac{W-\mathrm{i}\eta}{-\omega}\right)+\mathrm{Li}_2\!\left(\frac{-\varepsilon_d-\mathrm{i}\eta}{-\omega}\right)\right\}\\
&+\frac{1}{X(\omega-\varepsilon_d)^2}\left\{\left(\frac{1}{\omega}-\frac{1}{\varepsilon_d}\right)\big[\mathrm{Log}(\omega-\varepsilon_d-\mathrm{i}\eta)-\ln|\varepsilon_d|\big]\right\}\\
&+\frac{-3\omega+2X+3\varepsilon_d}{(\omega-X-\varepsilon_d)^2(\omega-\varepsilon_d)^3}\left\{-\mathrm{i}\pi\big[\ln W-\mathrm{Log}(\omega-2\varepsilon_d-\mathrm{i}\eta)\big]-\frac{\pi^2}{12}+\frac{\pi^2}{6}\right.\\
&\qquad\left.+\frac{1}{2}\,\mathrm{Log}^2\!\left(-\frac{W-\mathrm{i}\eta}{-\varepsilon_d}\right)+\mathrm{Li}_2\!\left(\frac{\omega-2\varepsilon_d-\mathrm{i}\eta}{-\varepsilon_d}\right)\right\}\\
&+\frac{-1}{(\omega-X-\varepsilon_d)(\omega-\varepsilon_d)^2}\left\{\frac{\omega-\varepsilon_d}{\varepsilon_d(\omega-2\varepsilon_d-\mathrm{i}\eta)}\,\mathrm{Log}(\omega-\varepsilon_d-\mathrm{i}\eta)-\frac{1}{\varepsilon_d}\,\mathrm{Log}(\omega-2\varepsilon_d-\mathrm{i}\eta)\right.\\
&\qquad\left.-\frac{1}{\omega-2\varepsilon_d-\mathrm{i}\eta}\ln|\varepsilon_d|\right\}\\
&+\frac{1}{-\varepsilon_d}\left\{\frac{1}{X^2(\omega-X-\varepsilon_d)}\big[\ln W-\mathrm{Log}(X-\varepsilon_d-\mathrm{i}\eta)\big]\right.\\
&\qquad+\frac{-\omega-X+\varepsilon_d}{X^2(\omega-\varepsilon_d)^2}\big[\ln W-\ln|\varepsilon_d|\big]+\frac{1}{X(\omega-\varepsilon_d)(-\varepsilon_d)}\\
&\qquad\left.+\frac{-1}{(\omega-X-\varepsilon_d)(\omega-\varepsilon_d)^2}\big[\ln W-\mathrm{Log}(\omega-2\varepsilon_d-\mathrm{i}\eta)\big]\right\}.
\end{aligned}
\tag{D.11}
$$

Next, we expand in the two quantities $(\omega-\varepsilon_d)/\varepsilon_d$ and $(\omega-\varepsilon_d)/X$ around zero. Since $|X-\varepsilon_d|\ll|\varepsilon_d|$, they are comparably small. Again, we use the general equations and expansions of the logarithm and dilogarithm stated in Appendix B. Here, they lead to the following specific expansions of individual terms, where we show only the orders that will turn out to be relevant,

$$
\begin{aligned}
\mathrm{Log}(\omega-\mathrm{i}\eta)-\ln|\varepsilon_d| &= \mathrm{Log}\!\left(1+\frac{\omega-\varepsilon_d-\mathrm{i}\eta}{\varepsilon_d}\right)-\mathrm{i}\pi \qquad\qquad (\mathrm{D.12a})\\
&= \frac{\omega-\varepsilon_d}{\varepsilon_d}-\frac{1}{2}\,\frac{(\omega-\varepsilon_d)^2}{\varepsilon_d^2}+\frac{1}{3}\,\frac{(\omega-\varepsilon_d)^3}{\varepsilon_d^3}+O\!\left[\frac{(\omega-\varepsilon_d)^4}{\varepsilon_d^4}\right]-\mathrm{i}\pi
\end{aligned}
$$

$$
\begin{aligned}
&\frac{1}{2}\operatorname{Log}^2\!\left(-\frac{W-\mathrm{i}\eta}{-\omega}\right) \qquad \text{with } \omega<0\\
&=\frac{1}{2}\left[\ln\frac{W}{|\varepsilon_d|}+\mathrm{i}\pi-\ln\!\left(1+\frac{\omega-\varepsilon_d}{\varepsilon_d}\right)\right]^2 \qquad \text{(D.12b)}\\
&=\frac{1}{2}\left(\ln\frac{W}{|\varepsilon_d|}+\mathrm{i}\pi\right)^2-\left(\ln\frac{W}{|\varepsilon_d|}+\mathrm{i}\pi\right)\left[\frac{\omega-\varepsilon_d}{\varepsilon_d}-\frac{1}{2}\frac{(\omega-\varepsilon_d)^2}{\varepsilon_d^2}+\frac{1}{3}\frac{(\omega-\varepsilon_d)^3}{\varepsilon_d^3}\right]\\
&\quad+\frac{1}{2}\frac{(\omega-\varepsilon_d)^2}{\varepsilon_d^2}-\frac{1}{2}\frac{(\omega-\varepsilon_d)^3}{\varepsilon_d^3}+O\!\left[\ln\frac{W}{|\varepsilon_d|}\frac{(\omega-\varepsilon_d)^4}{\varepsilon_d^4},\ \frac{(\omega-\varepsilon_d)^4}{\varepsilon_d^4}\right]
\end{aligned}
$$

$$
\begin{aligned}
&\mathrm{Li}_2\!\left(\frac{-\varepsilon_d-\mathrm{i}\eta}{-\omega}\right) \qquad \text{with } \omega<0\\
&=-\frac{\pi^2}{6}-\mathrm{Li}_2\!\left(1+\frac{\omega-\varepsilon_d}{\varepsilon_d}+\mathrm{i}\eta\right)-\frac{1}{2}\left[\ln\!\left(1+\frac{\omega-\varepsilon_d}{\varepsilon_d}\right)-\mathrm{i}\pi\right]^2\\
&=\frac{\pi^2}{6}+\frac{\omega-\varepsilon_d}{\varepsilon_d}\left[-1+\mathrm{i}\pi+\operatorname{Log}\!\left(\frac{\omega-\varepsilon_d-\mathrm{i}\eta}{|\varepsilon_d|}\right)\right] \qquad \text{(D.12c)}\\
&\quad+\frac{(\omega-\varepsilon_d)^2}{\varepsilon_d^2}\left[-\frac{1}{4}-\frac{1}{2}\mathrm{i}\pi-\frac{1}{2}\operatorname{Log}\!\left(\frac{\omega-\varepsilon_d-\mathrm{i}\eta}{|\varepsilon_d|}\right)\right]\\
&\quad+\frac{(\omega-\varepsilon_d)^3}{\varepsilon_d^3}\left[\frac{7}{18}+\frac{1}{3}\mathrm{i}\pi+\frac{1}{3}\operatorname{Log}\!\left(\frac{\omega-\varepsilon_d-\mathrm{i}\eta}{|\varepsilon_d|}\right)\right]+O\!\left[\frac{(\omega-\varepsilon_d)^4}{\varepsilon_d^4}\ln\frac{|\omega-\varepsilon_d|}{|\varepsilon_d|}\right]
\end{aligned}
$$

$$
\frac{1}{\omega}=\frac{1}{\varepsilon_d}\left\{1-\frac{\omega-\varepsilon_d}{\varepsilon_d}+\frac{(\omega-\varepsilon_d)^2}{\varepsilon_d^2}+O\!\left[\frac{(\omega-\varepsilon_d)^3}{\varepsilon_d^3}\right]\right\} \qquad \text{(D.12d)}
$$

$$
\frac{1}{(\omega-X-\varepsilon_d)^2}=\frac{1}{X^2}\left\{1+2\frac{\omega-\varepsilon_d}{X}+3\frac{(\omega-\varepsilon_d)^2}{X^2}+4\frac{(\omega-\varepsilon_d)^3}{X^3}+O\!\left[\frac{(\omega-\varepsilon_d)^4}{X^4}\right]\right\} \qquad \text{(D.12e)}
$$

$$
\begin{aligned}
\operatorname{Log}(\omega-2\varepsilon_d-\mathrm{i}\eta)-\ln|\varepsilon_d| &= \operatorname{Log}\!\left(1-\frac{\omega-\varepsilon_d}{\varepsilon_d}-\mathrm{i}\eta\right) \qquad \text{(D.12f)}\\
&=-\frac{\omega-\varepsilon_d}{\varepsilon_d}-\frac{1}{2}\frac{(\omega-\varepsilon_d)^2}{\varepsilon_d^2}-\frac{1}{3}\frac{(\omega-\varepsilon_d)^3}{\varepsilon_d^3}+O\!\left[\frac{(\omega-\varepsilon_d)^4}{\varepsilon_d^4}\right]
\end{aligned}
$$

$$
\begin{aligned}
&\mathrm{Li}_2\left(\frac{\omega-2\varepsilon_d-\mathrm{i}\eta}{-\varepsilon_d}\right)\\
&=\mathrm{Li}_2\left(1-\frac{\omega-\varepsilon_d}{\varepsilon_d}-\mathrm{i}\eta\right) \qquad \text{(D.12g)}\\
&=\frac{\pi^2}{6}+\frac{\omega-\varepsilon_d}{\varepsilon_d}\left[-1+\mathrm{Log}\left(\frac{\omega-\varepsilon_d-\mathrm{i}\eta}{\varepsilon_d}\right)\right]+\frac{(\omega-\varepsilon_d)^2}{\varepsilon_d^2}\left[-\frac{1}{4}+\frac{1}{2}\,\mathrm{Log}\left(\frac{\omega-\varepsilon_d-\mathrm{i}\eta}{\varepsilon_d}\right)\right]\\
&\quad+\frac{(\omega-\varepsilon_d)^3}{\varepsilon_d^3}\left[-\frac{1}{9}+\frac{1}{3}\,\mathrm{Log}\left(\frac{\omega-\varepsilon_d-\mathrm{i}\eta}{\varepsilon_d}\right)\right]+O\left[\frac{(\omega-\varepsilon_d)^4}{\varepsilon_d^4}\ln\frac{|\omega-\varepsilon_d|}{|\varepsilon_d|}\right]
\end{aligned}
$$

$$
\frac{1}{\omega-X-\varepsilon_d}=\frac{-1}{X}\left\{1+\frac{\omega-\varepsilon_d}{X}+\frac{(\omega-\varepsilon_d)^2}{X^2}+O\left[\frac{(\omega-\varepsilon_d)^3}{X^3}\right]\right\} \qquad \text{(D.12h)}
$$

$$
\frac{1}{\omega-2\varepsilon_d-\mathrm{i}\eta}=\frac{1}{-\varepsilon_d}\left\{1+\frac{\omega-\varepsilon_d}{\varepsilon_d}+\frac{(\omega-\varepsilon_d)^2}{\varepsilon_d^2}+O\left[\frac{(\omega-\varepsilon_d)^3}{\varepsilon_d^3}\right]\right\}. \qquad \text{(D.12i)}
$$

Inserting these expansions into the expression (D.11) for the crossed bubble, we obtain

$$
\begin{aligned}
&\tilde{C}(X,\omega)\\
&\approx\frac{1}{X^4}\left\{\left[\mathrm{Log}(-X+\omega-\mathrm{i}\eta)-\ln|\varepsilon_d|\right]\left[\ln W-\mathrm{Log}(X-\varepsilon_d-\mathrm{i}\eta)\right]+\frac{\pi^2}{12}\right. \qquad \text{(D.13)}\\
&\qquad\left.+\frac{1}{2}\,\mathrm{Log}^2\left(-\frac{W-\mathrm{i}\eta}{-\omega+X}\right)+\mathrm{Li}_2\left(\frac{X-\varepsilon_d-\mathrm{i}\eta}{-\omega+X}\right)\right\}\\
&\quad+\left[\frac{-2}{X}\,\frac{1}{(\omega-\varepsilon_d)^3}+\frac{-1}{X^2}\,\frac{1}{(\omega-\varepsilon_d)^2}\right]\\
&\quad\times\left\{\left[-\mathrm{i}\pi+\frac{\omega-\varepsilon_d}{\varepsilon_d}-\frac{1}{2}\,\frac{(\omega-\varepsilon_d)^2}{\varepsilon_d^2}+\frac{1}{3}\,\frac{(\omega-\varepsilon_d)^3}{\varepsilon_d^3}\right]\left[\ln W-\ln|\varepsilon_d|\right]\right.\\
&\qquad+\frac{\pi^2}{12}+\frac{1}{2}\left(\ln\frac{W}{|\varepsilon_d|}+\mathrm{i}\pi\right)^2-\left(\ln\frac{W}{|\varepsilon_d|}+\mathrm{i}\pi\right)\left[\frac{\omega-\varepsilon_d}{\varepsilon_d}-\frac{1}{2}\,\frac{(\omega-\varepsilon_d)^2}{\varepsilon_d^2}+\frac{1}{3}\,\frac{(\omega-\varepsilon_d)^3}{\varepsilon_d^3}\right]\\
&\qquad+\frac{1}{2}\,\frac{(\omega-\varepsilon_d)^2}{\varepsilon_d^2}-\frac{1}{2}\,\frac{(\omega-\varepsilon_d)^3}{\varepsilon_d^3}+\frac{\pi^2}{6}+\frac{\omega-\varepsilon_d}{\varepsilon_d}\left[-1+\mathrm{i}\pi+\mathrm{Log}\left(\frac{\omega-\varepsilon_d-\mathrm{i}\eta}{|\varepsilon_d|}\right)\right]\\
&\qquad+\frac{(\omega-\varepsilon_d)^2}{\varepsilon_d^2}\left[-\frac{1}{4}-\frac{\mathrm{i}\pi}{2}-\frac{1}{2}\,\mathrm{Log}\left(\frac{\omega-\varepsilon_d-\mathrm{i}\eta}{|\varepsilon_d|}\right)\right]\\
&\qquad\left.+\frac{(\omega-\varepsilon_d)^3}{\varepsilon_d^3}\left[\frac{7}{18}+\frac{\mathrm{i}\pi}{3}+\frac{1}{3}\,\mathrm{Log}\left(\frac{\omega-\varepsilon_d-\mathrm{i}\eta}{|\varepsilon_d|}\right)\right]\right\}\\
&\quad+\frac{1}{X}\,\frac{1}{(\omega-\varepsilon_d)^2}\,\frac{1}{\varepsilon_d}\left[-\frac{\omega-\varepsilon_d}{\varepsilon_d}+\frac{(\omega-\varepsilon_d)^2}{\varepsilon_d^2}\right]\mathrm{Log}\left(\frac{\omega-\varepsilon_d-\mathrm{i}\eta}{|\varepsilon_d|}\right)\\
&\quad+\frac{1}{X^2}\left[1+2\,\frac{\omega-\varepsilon_d}{X}+3\,\frac{(\omega-\varepsilon_d)^2}{X^2}+4\,\frac{(\omega-\varepsilon_d)^3}{X^3}\right]\left[2X\,\frac{1}{(\omega-\varepsilon_d)^3}-3\,\frac{1}{(\omega-\varepsilon_d)^2}\right]
\end{aligned}
$$

$$
\begin{aligned}
&\times\Bigg\{-\mathrm{i}\pi\ln\frac{W}{|\varepsilon_d|}+\mathrm{i}\pi\left[-\frac{\omega-\varepsilon_d}{\varepsilon_d}-\frac{1}{2}\frac{(\omega-\varepsilon_d)^2}{\varepsilon_d^2}-\frac{1}{3}\frac{(\omega-\varepsilon_d)^3}{\varepsilon_d^3}\right]+\frac{\pi^2}{12}+\frac{1}{2}\left(\ln\frac{W}{|\varepsilon_d|}+\mathrm{i}\pi\right)^2\\
&\quad+\frac{\pi^2}{6}+\frac{\omega-\varepsilon_d}{\varepsilon_d}\left[-1+\mathrm{Log}\left(\frac{\omega-\varepsilon_d-\mathrm{i}\eta}{\varepsilon_d}\right)\right]+\frac{(\omega-\varepsilon_d)^2}{\varepsilon_d^2}\left[-\frac{1}{4}+\frac{1}{2}\mathrm{Log}\left(\frac{\omega-\varepsilon_d-\mathrm{i}\eta}{\varepsilon_d}\right)\right]\\
&\quad+\frac{(\omega-\varepsilon_d)^3}{\varepsilon_d^3}\left[-\frac{1}{9}+\frac{1}{3}\mathrm{Log}\left(\frac{\omega-\varepsilon_d-\mathrm{i}\eta}{\varepsilon_d}\right)\right]\Bigg\}\\
&+\frac{1}{X}\left[1+\frac{\omega-\varepsilon_d}{X}+\frac{(\omega-\varepsilon_d)^2}{X^2}\right]\frac{1}{(\omega-\varepsilon_d)^2}\\
&\times\Bigg\{\frac{1}{-\varepsilon_d}\left(1+\frac{\omega-\varepsilon_d}{\varepsilon_d}\right)\frac{\omega-\varepsilon_d}{\varepsilon_d}\mathrm{Log}(\omega-\varepsilon_d-\mathrm{i}\eta)-\frac{1}{\varepsilon_d}\left[\ln|\varepsilon_d|-\frac{\omega-\varepsilon_d}{\varepsilon_d}-\frac{1}{2}\frac{(\omega-\varepsilon_d)^2}{\varepsilon_d^2}\right]\\
&\quad-\frac{1}{-\varepsilon_d}\left[1+\frac{\omega-\varepsilon_d}{\varepsilon_d}+\frac{(\omega-\varepsilon_d)^2}{\varepsilon_d^2}\right]\ln|\varepsilon_d|\Bigg\}\\
&+\frac{-1}{\varepsilon_d}\Bigg\{\frac{1}{X^2}\frac{-1}{X}\left[\ln W-\mathrm{Log}(X-\varepsilon_d-\mathrm{i}\eta)\right]+\left[-\frac{1}{X}\frac{1}{(\omega-\varepsilon_d)^2}-\frac{1}{X^2}\frac{1}{\omega-\varepsilon_d}\right]\ln\frac{W}{|\varepsilon_d|}\\
&\qquad+\frac{1}{X}\left[1+\frac{\omega-\varepsilon_d}{X}+\frac{(\omega-\varepsilon_d)^2}{X^2}\right]\frac{1}{(\omega-\varepsilon_d)^2}\left[\ln\frac{W}{|\varepsilon_d|}+\frac{\omega-\varepsilon_d}{\varepsilon_d}+\frac{1}{2}\frac{(\omega-\varepsilon_d)^2}{\varepsilon_d^2}\right]\\
&\qquad+\frac{1}{X(\omega-\varepsilon_d)(-\varepsilon_d)}\Bigg\}.
\end{aligned}
$$

As before, we neglect terms that are smaller than $1/\varepsilon_d^4$; at this stage many terms cancel out or can be seen to be negligible. The expression for the crossed bubble thereby reduces to

$$
\begin{aligned}
&\tilde{C}(X,\omega)\\
&\approx-\frac{1}{X^4}\mathrm{Log}\left(\frac{\omega-X-\mathrm{i}\eta}{|\varepsilon_d|}\right)\mathrm{Log}\left(\frac{X-\varepsilon_d-\mathrm{i}\eta}{|\varepsilon_d|}\right)+\frac{1}{X^4}\frac{\pi^2}{3}+\frac{1}{X^4}\frac{1}{2}\mathrm{Log}^2\left(\frac{\omega-X-\mathrm{i}\eta}{|\varepsilon_d|}\right)\\
&\quad+\frac{1}{X^4}\mathrm{Li}_2\left(\frac{X-\varepsilon_d-\mathrm{i}\eta}{-\omega+X}\right)-\frac{1}{X^2\varepsilon_d^2}\frac{1}{2}-\frac{1}{X^3\varepsilon_d}\mathrm{Log}\left(\frac{X-\varepsilon_d-\mathrm{i}\eta}{|\varepsilon_d|}\right).
\end{aligned}
\tag{D.14}
$$

Now, we perform the last expansion on the crossed bubble, namely in $(X-\varepsilon_d)/\varepsilon_d$ around zero. This leads to

$$
\begin{aligned}
\tilde{C}(X,\omega)\approx\frac{1}{\varepsilon_d^4}\Bigg[&-\mathrm{Log}\left(\frac{\omega-X-\mathrm{i}\eta}{|\varepsilon_d|}\right)\mathrm{Log}\left(\frac{X-\varepsilon_d-\mathrm{i}\eta}{|\varepsilon_d|}\right)+\frac{1}{2}\mathrm{Log}^2\left(\frac{\omega-X-\mathrm{i}\eta}{|\varepsilon_d|}\right)\\
&+\mathrm{Li}_2\left(\frac{X-\varepsilon_d-\mathrm{i}\eta}{-\omega+X}\right)-\mathrm{Log}\left(\frac{X-\varepsilon_d-\mathrm{i}\eta}{|\varepsilon_d|}\right)+\frac{\pi^2}{3}-\frac{1}{2}\Bigg].
\end{aligned}
\tag{D.15}
$$

We have made no assumption about the relation of X and ω. We now distinguish the complementary cases $|\omega-X|\geq|X-\varepsilon_d|$ and $|\omega-X|\leq|X-\varepsilon_d|$ to approximate the remaining dilogarithm by using its series expansion (B.5) and its identity (B.7b). At this point, we see that the leading terms have two large logarithmic factors and we neglect all other terms to find

$$
\tilde{C}(X,\omega)\approx-\frac{1}{2\varepsilon_d^4}\begin{cases}2\ln\frac{|\omega-X|}{|\varepsilon_d|}\ln\frac{|X-\varepsilon_d|}{|\varepsilon_d|}-\ln^2\frac{|\omega-X|}{|\varepsilon_d|}, & |\omega-X|\geq|X-\varepsilon_d|\\ \ln^2\frac{|X-\varepsilon_d|}{|\varepsilon_d|}, & |\omega-X|\leq|X-\varepsilon_d|.\end{cases}
\tag{D.16}
$$

Finally, we unravel the redefinition of the crossed bubble made in Eq. (D.1). The crossed bubble $C(X,\omega)$ without tilde is defined in Eq. (4.35). Its leading behavior, resulting from proper expansions of its exact value, is

$$C(X,\omega) \approx \frac{1}{2\varepsilon_d^4} \begin{cases} 2\ln\frac{|\omega|}{|\varepsilon_d|}\ln\frac{|X-\varepsilon_d|}{|\varepsilon_d|} - \ln^2\frac{|\omega|}{|\varepsilon_d|}, & |\omega| \geq |X-\varepsilon_d| \\ \ln^2\frac{|X-\varepsilon_d|}{|\varepsilon_d|}, & |\omega| \leq |X-\varepsilon_d|. \end{cases} \tag{D.17}$$

This result is based on the assumptions stated in the paragraph around Eqs. (D.9) and (D.10). Note that those assumptions are formulated for $\tilde{C}(X,\omega)$. In the main body of this thesis, we formulate them for $C(X,\omega)$ instead, see Sec. 4.4.3.

Bibliography

[Abr65] A. A. Abrikosov. *Electron scattering on magnetic impurities in metals and anomalous resistivity effects.* Phys. Phys. Fiz. **2**, 5 (1965).

[AGD63] A. A. Abrikosov, L. P. Gorkov, and I. E. Dzyaloshinski. *Methods of quantum field theory in statistical physics.* Prentice-Hall, Englewood Cliffs, 1963.

[AGU20] Y. Ashida, Z. Gong, and M. Ueda. *Non-Hermitian physics.* Adv. Phys. **69**, 249 (2020).

[AM70] A. A. Abrikosov and A. A. Migdal. *On the theory of the Kondo effect.* J. Low Temp. Phys. **3**, 519 (1970).

[And+08] S. Andergassen, T. Enss, C. Karrasch, and V. Meden. *A gentle introduction to the functional renormalization group: The Kondo effect in quantum dots.* In: *Quantum magnetism*, p. 1. Springer, Dordrecht, 2008.

[And61] P. W. Anderson. *Localized magnetic states in metals.* Phys. Rev. **124**, 41 (1961).

[And70] P. W. Anderson. *A poor man's derivation of scaling laws for the Kondo problem.* J. Phys. C **3**, 2436 (1970).

[Bar+09] L. Bartosch, H. Freire, J. J. R. Cardenas, and P. Kopietz. *A functional renormalization group approach to the Anderson impurity model.* J. Phys.: Condens. Matter **21**, 305602 (2009).

[BBD03] B. Binz, D. Baeriswyl, and B. Douçot. *Weakly interacting electrons and the renormalization group.* Ann. Phys. (Leipzig) **12**, 704 (2003).

[BCP08] R. Bulla, T. A. Costi, and T. Pruschke. *Numerical renormalization group method for quantum impurity systems.* Rev. Mod. Phys. **80**, 395 (2008).

[BDL11] S. Bravyi, D. P. DiVincenzo, and D. Loss. *Schrieffer–Wolff transformation for quantum many-body systems.* Ann. Phys. (N. Y.) **326**, 2793 (2011).

[BGD66] Y. A. Bychkov, L. P. Gor'kov, and I. E. Dzyaloshinskii. *Possibility of superconductivity type phenomena in a one-dimensional system.* Zh. Eksp. Teor. Fiz. **50**, 738 (1966). [Sov. Phys. JETP **23**, 489 (1966)]

[Bic91] N. E. Bickers. *Parquet equations for numerical self-consistent-field theory.* Int. J. Mod. Phys. B **5**, 253 (1991).

[BS92] N. E. Bickers and D. J. Scalapino. *Critical behavior of electronic parquet solutions.* Phys. Rev. B **46**, 8050 (1992).

[Cam+22] G. Camacho, C. Klöckner, D. M. Kennes, and C. Karrasch. *Review of recent developments of the functional renormalization group for systems out of equilibrium*. Eur. Phys. J. B **95**, 195 (2022).

[CB92] C.-X. Chen and N. E. Bickers. *Numerical solution of parquet equations for the Anderson impurity model*. Solid State Commun. **82**, 311 (1992).

[Cha+22] P. Chalupa-Gantner, F. B. Kugler, C. Hille, J. von Delft, S. Andergassen, and A. Toschi. *Fulfillment of sum rules and Ward identities in the multi-loop functional renormalization group solution of the Anderson impurity model*. Phys. Rev. Res. **4**, 023050 (2022).

[Die17] J. Diekmann. *Functional renormalization group approach to transport through a Kondo quantum dot*. Master's thesis. RWTH Aachen University, 2017.

[DJ21] J. Diekmann and S. G. Jakobs. *Parquet approximation and one-loop renormalization group: Equivalence on the leading-logarithmic level*. Phys. Rev. B **103**, 155156 (2021).

[DJ24] J. Diekmann and S. G. Jakobs. *Leading-logarithmic approximation by one-loop renormalization group within Matsubara formalism*. Phys. Rev. B **109**, 115134 (2024).

[DLMF] *NIST digital library of mathematical functions*. https://dlmf.nist.gov/, Release 1.2.3 of 2024-12-15. F. W. J. Olver, A. B. Olde Daalhuis, D. W. Lozier, B. I. Schneider, R. F. Boisvert, C. W. Clark, B. R. Miller, B. V. Saunders, H. S. Cohl, and M. A. McClain, eds.

[FC12] H. Freire and E. Corrêa. *A functional generalization of the field-theoretical renormalization group approach for the single-impurity Anderson model*. J. Low Temp. Phys. **166**, 192 (2012).

[FW71] A. L. Fetter and J. D. Walecka. *Quantum theory of many-particle systems*. McGraw-Hill, New York, 1971.

[FZ71] M. Fowler and A. Zawadowski. *Scaling and the renormalization group in the Kondo effect*. Solid State Commun. **9**, 471 (1971).

[Ge+24] A. Ge, N. Ritz, E. Walter, S. Aguirre, J. von Delft, and F. B. Kugler. *Real-frequency quantum field theory applied to the single-impurity Anderson model*. Phys. Rev. B **109**, 115128 (2024).

[Geo+96] A. Georges, G. Kotliar, W. Krauth, and M. J. Rozenberg. *Dynamical mean-field theory of strongly correlated fermion systems and the limit of infinite dimensions*. Rev. Mod. Phys. **68**, 13 (1996).

[Gie+25] M. Gievers, R. Schmidt, J. von Delft, and F. B. Kugler. *Subleading logarithmic behavior in the parquet formalism*. Phys. Rev. B **111**, 085151 (2025).

[Gol+98] D. Goldhaber-Gordon, H. Shtrikman, D. Mahalu, D. Abusch-Magder, U. Meirav, and M. A. Kastner. *Kondo effect in a single-electron transistor*. Nature **391**, 156 (1998).

[GPM07] R. Gezzi, T. Pruschke, and V. Meden. *Functional renormalization group for nonequilibrium quantum many-body problems.* Phys. Rev. B **75**, 045324 (2007).

[GR88] L. I. Glazman and M. E. Raikh. *Resonant Kondo transparency of a barrier with quasilocal impurity states.* Pis'ma Zh. Eksp. Teor. Fiz. **47**, 378 (1988). [Sov. Phys. JETP Lett. **47**, 452 (1988)]

[GZ74] G. Grüner and A. Zawadowski. *Magnetic impurities in non-magnetic metals.* Rep. Prog. Phys. **37**, 1497 (1974).

[Hed+04] R. Hedden, V. Meden, T. Pruschke, and K. Schönhammer. *A functional renormalization group approach to zero-dimensional interacting systems.* J. Phys.: Condens. Matter **16**, 5279 (2004).

[Hel07] K. Held. *Electronic structure calculations using dynamical mean field theory.* Adv. Phys. **56**, 829 (2007).

[Hew93] A. C. Hewson. *The Kondo problem to heavy fermions.* Cambridge University Press, Cambridge, 1993.

[HH07] J. E. Han and R. J. Heary. *Imaginary-time formulation of steady-state nonequilibrium: Application to strongly correlated transport.* Phys. Rev. Lett. **99**, 236808 (2007).

[Hil+20a] C. Hille, F. B. Kugler, C. J. Eckhardt, Y.-Y. He, A. Kauch, C. Honerkamp, A. Toschi, and S. Andergassen. *Quantitative functional renormalization group description of the two-dimensional Hubbard model.* Phys. Rev. Res. **2**, 033372 (2020).

[Hil+20b] C. Hille, D. Rohe, C. Honerkamp, and S. Andergassen. *Pseudogap opening in the two-dimensional Hubbard model: A functional renormalization group analysis.* Phys. Rev. Res. **2**, 033068 (2020).

[HJ96] H. Haug and A.-P. Jauho. *Quantum kinetics in transport and optics of semiconductors.* Springer, Berlin, 1996.

[IKK01] V. Y. Irkhin, A. A. Katanin, and M. I. Katsnelson. *Effects of van Hove singularities on magnetism and superconductivity in the $t - t'$ Hubbard model: A parquet approach.* Phys. Rev. B **64**, 165107 (2001).

[Isi+10] A. Isidori, D. Roosen, L. Bartosch, W. Hofstetter, and P. Kopietz. *Spectral function of the Anderson impurity model at finite temperatures.* Phys. Rev. B **81**, 235120 (2010).

[Jak10] S. G. Jakobs. *Functional renormalization group studies of quantum transport through mesoscopic systems.* Dissertation. RWTH Aachen University, 2010.

[Jak19] S. Jakobs. *Functional RG for nonequilibrium transport through mesoscopic systems.* Lecture notes. RWTH Aachen University, winter term 2019/2020.

[JG96] M. Jarrell and J. E. Gubernatis. *Bayesian inference and the analytic continuation of imaginary-time quantum Monte Carlo data.* Phys. Rep. **269**, 133 (1996).

[JMS07] S. G. Jakobs, V. Meden, and H. Schoeller. *Nonequilibrium functional renormalization group for interacting quantum systems.* Phys. Rev. Lett. **99**, 150603 (2007).

[JPS10] S. G. Jakobs, M. Pletyukhov, and H. Schoeller. *Nonequilibrium functional renormalization group with frequency-dependent vertex function: A study of the single-impurity Anderson model.* Phys. Rev. B **81**, 195109 (2010).

[Kad76] L. P. Kadanoff. *Scaling, universality and operator algebras.* Ph. Transit. Crit. Phenom. **5a**, 1 (1976).

[Kar+08] C. Karrasch, R. Hedden, R. Peters, T. Pruschke, K. Schönhammer, and V. Meden. *A finite-frequency functional renormalization group approach to the single impurity Anderson model.* J. Phys.: Condens. Matter **20**, 345205 (2008).

[Kar+10] C. Karrasch, M. Pletyukhov, L. Borda, and V. Meden. *Functional renormalization group study of the interacting resonant level model in and out of equilibrium.* Phys. Rev. B **81**, 125122 (2010).

[Kat04] A. A. Katanin. *Fulfillment of Ward identities in the functional renormalization group approach.* Phys. Rev. B **70**, 115109 (2004).

[Kat09] A. A. Katanin. *Two-loop functional renormalization group approach to the one- and two-dimensional Hubbard model.* Phys. Rev. B **79**, 235119 (2009).

[KBS10] P. Kopietz, L. Bartosch, and F. Schütz. *Introduction to the functional renormalization group.* Springer, Berlin, 2010.

[KD18a] F. B. Kugler and J. von Delft. *Multiloop functional renormalization group that sums up all parquet diagrams.* Phys. Rev. Lett. **120**, 057403 (2018).

[KD18b] F. B. Kugler and J. von Delft. *Multiloop functional renormalization group for general models.* Phys. Rev. B **97**, 035162 (2018).

[KD18c] F. B. Kugler and J. von Delft. *Fermi-edge singularity and the functional renormalization group.* J. Phys.: Condens. Matter **30**, 195501 (2018).

[KD18d] F. B. Kugler and J. von Delft. *Derivation of exact flow equations from the self-consistent parquet relations.* New J. Phys. **20**, 123029 (2018).

[KEM06] C. Karrasch, T. Enss, and V. Meden. *Functional renormalization group approach to transport through correlated quantum dots.* Phys. Rev. B **73**, 235337 (2006).

[KH13] M. Kinza and C. Honerkamp. *Two-particle correlations in a functional renormalization group scheme using a dynamical mean-field theory approach.* Phys. Rev. B **88**, 195136 (2013).

[Kie+22] D. Kiese, T. Müller, Y. Iqbal, R. Thomale, and S. Trebst. *Multiloop functional renormalization group approach to quantum spin systems.* Phys. Rev. Res. **4**, 023185 (2022).

[Kim73] M. Kimura. *Renormalization group theory for a one-dimensional Fermi system.* Prog. Theor. Phys. **49**, 697 (1973).

[Kin+13] M. Kinza, J. Ortloff, J. Bauer, and C. Honerkamp. *Alternative functional renormalization group approach to the single impurity Anderson model.* Phys. Rev. B **87**, 035111 (2013).

[KL60] W. Kohn and J. M. Luttinger. *Ground-state energy of a many-fermion system.* Phys. Rev. **118**, 41 (1960).

[KM13] D. M. Kennes and V. Meden. *Interacting resonant-level model in nonequilibrium: Finite-temperature effects.* Phys. Rev. B **87**, 075130 (2013).

[Lan+15] P. Lange, C. Drukier, A. Sharma, and P. Kopietz. *Summing parquet diagrams using the functional renormalization group: X-ray problem revisited.* J. Phys. A **48**, 395001 (2015).

[LW60] J. M. Luttinger and J. C. Ward. *Ground-state energy of a many-fermion system. II.* Phys. Rev. **118**, 1417 (1960).

[Mah67] G. D. Mahan. *Excitons in metals: Infinite hole mass.* Phys. Rev. **163**, 612 (1967).

[Med+02] V. Meden, W. Metzner, U. Schollwöck, and K. Schönhammer. *A single impurity in a Luttinger liquid: How it "cuts" the chain.* J. Low Temp. Phys. **126**, 1147 (2002).

[Met+12] W. Metzner, M. Salmhofer, C. Honerkamp, V. Meden, and K. Schönhammer. *Functional renormalization group approach to correlated fermion systems.* Rev. Mod. Phys. **84**, 299 (2012).

[Mor94] T. R. Morris. *The exact renormalization group and approximate solutions.* Int. J. Mod. Phys. A **9**, 2411 (1994).

[ND69] P. Nozières and C. T. De Dominicis. *Singularities in the X-ray absorption and emission of metals. III. One-body theory exact solution.* Phys. Rev. **178**, 1097 (1969).

[NGR69] P. Nozières, J. Gavoret, and B. Roulet. *Singularities in the X-ray absorption and emission of metals. II. Self-consistent treatment of divergences.* Phys. Rev. **178**, 1084 (1969).

[NL88] T. K. Ng and P. A. Lee. *On-site Coulomb repulsion and resonant tunneling.* Phys. Rev. Lett. **61**, 1768 (1988).

[NO88] J. W. Negele and H. Orland. *Quantum many-particle systems.* Addison-Wesley, Reading, 1988.

[PG04] M. Pustilnik and L. Glazman. *Kondo effect in quantum dots.* J. Phys.: Condens. Matter **16**, R513 (2004).

[PHT13] C. Platt, W. Hanke, and R. Thomale. *Functional renormalization group for multi-orbital Fermi surface instabilities.* Adv. Phys. **62**, 453 (2013).

[Pok+17] V. Pokorný, M. Žonda, A. Kauch, and V. Janiš. *Simplified parquet equations for the Anderson impurity model: Comparison with numerically exact solutions.* Acta Phys. Pol. A **131**, 1042 (2017).

[Ren16] J. F. Rentrop. *Paradigmatic extensions of the functional renormalization group approach.* Dissertation. RWTH Aachen University, 2016.

[RGN69] B. Roulet, J. Gavoret, and P. Nozières. *Singularities in the X-ray absorption and emission of metals. I. First-order parquet calculation.* Phys. Rev. **178**, 1072 (1969).

[RMJ16] J. F. Rentrop, V. Meden, and S. G. Jakobs. *Renormalization group flow of the Luttinger-Ward functional: Conserving approximations and application to the Anderson impurity model.* Phys. Rev. B **93**, 195160 (2016).

[Roh+18] G. Rohringer, H. Hafermann, A. Toschi, A. A. Katanin, A. E. Antipov, M. I. Katsnelson, A. I. Lichtenstein, A. N. Rubtsov, and K. Held. *Diagrammatic routes to nonlocal correlations beyond dynamical mean field theory.* Rev. Mod. Phys. **90**, 025003 (2018).

[Sha94] R. Shankar. *Renormalization-group approach to interacting fermions.* Rev. Mod. Phys. **66**, 129 (1994).

[SIK13] S. Streib, A. Isidori, and P. Kopietz. *Solution of the Anderson impurity model via the functional renormalization group.* Phys. Rev. B **87**, 201107 (2013).

[Sól74] J. Sólyom. *Renormalization and scaling in the X-ray absorption and Kondo problems.* J. Phys. F **4**, 2269 (1974).

[Sól79] J. Sólyom. *The Fermi gas model of one-dimensional conductors.* Adv. Phys. **28**, 201 (1979).

[Sud56] V. V. Sudakov. *Meson-meson scattering in meson field theory.* Dokl. Akad. Nauk SSSR **111**, 338 (1956). [Sov. Phys.-Dokl. **1**, 662 (1956)]

[SW10] H. Schmidt and P. Wölfle. *Transport through a Kondo quantum dot: Functional RG approach.* Ann. Phys. (Berl.) **19**, 60 (2010).

[SW66] J. R. Schrieffer and P. A. Wolff. *Relation between the Anderson and Kondo Hamiltonians.* Phys. Rev. **149**, 491 (1966).

[SZ74] J. Sólyom and A. Zawadowski. *Are the scaling laws for the Kondo problem exact?* J. Phys. F **4**, 80 (1974).

[Tag+19] A. Tagliavini, C. Hille, F. B. Kugler, S. Andergassen, A. Toschi, and C. Honerkamp. *Multiloop functional renormalization group for the two-dimensional Hubbard model: Loop convergence of the response functions.* SciPost Phys. **6**, 9 (2019).

[Tho+20] J. Thoenniss, M. K. Ritter, F. B. Kugler, J. von Delft, and M. Punk. *Multiloop pseudofermion functional renormalization for quantum spin systems: Application to the spin-$\frac{1}{2}$ kagome Heisenberg model.* arXiv:2011.01268 [cond-mat.str-el], 2020.

[TKH07] A. Toschi, A. A. Katanin, and K. Held. *Dynamical vertex approximation: A step beyond dynamical mean-field theory.* Phys. Rev. B **75**, 045118 (2007).

[TKK18] D. Tarasevych, J. Krieg, and P. Kopietz. *A rich man's derivation of scaling laws for the Kondo model.* Phys. Rev. B **98**, 235133 (2018).

[TW83] A. M. Tsvelick and P. B. Wiegmann. *Exact results in the theory of magnetic alloys*. Adv. Phys. **32**, 453 (1983).

[Voi95] J. Voit. *One-dimensional Fermi liquids*. Rep. Prog. Phys. **58**, 977 (1995).

[VT97] Y. M. Vilk and A.-M. S. Tremblay. *Non-perturbative many-body approach to the Hubbard model and single-particle pseudogap*. J. Phys. I France **7**, 1309 (1997).

[Wen+20] N. Wentzell, G. Li, A. Tagliavini, C. Taranto, G. Rohringer, K. Held, A. Toschi, and S. Andergassen. *High-frequency asymptotics of the vertex function: Diagrammatic parametrization and algorithmic implementation*. Phys. Rev. B **102**, 085106 (2020).

[Wet93] C. Wetterich. *Exact evolution equation for the effective potential*. Phys. Lett. B **301**, 90 (1993).

[Wie+00] W. G. van der Wiel, S. De Franceschi, T. Fujisawa, J. M. Elzerman, S. Tarucha, and L. P. Kouwenhoven. *The Kondo effect in the unitary limit*. Science **289**, 2105 (2000).

[Wil75] K. G. Wilson. *The renormalization group: Critical phenomena and the Kondo problem*. Rev. Mod. Phys. **47**, 773 (1975).

[YJ22] J. Yan and V. Janiš. *Single-impurity Anderson model out of equilibrium: A two-particle semianalytic approach*. Phys. Rev. B **105**, 085122 (2022).